NPS

1

AD-A240 862

GLOBAL ISOTOPIC SIGNATURES OF OCEANIC ISLAND BASALTS

by

LYNN A. OSCHMANN
A.B. BRYN MAWR COLLEGE (1989)

SUBMITTED IN PARTIAL FULFILLMENT OF THE
REQUIREMENTS FOR THE DEGREE OF
MASTER OF SCIENCE IN OCEANOGRAPHY

at the

MASSACHUSETTS INSTITUTE OF TECHNOLOGY

and the

WOODS HOLE OCEANOGRAPHIC INSTITUTION
August 1991

91-10912

Signature of Author Lynn A. Oschmann
Joint Program in Oceanography
Massachusetts Institute of Technology/
Woods Hole Oceanographic Institution

Certified by Stanley R. Hart
Dr. Stanley R. Hart
Senior Scientist, Woods Hole Oceanographic Institution
Thesis Supervisor

Accepted by G. P. Lohmann
Dr. G. Pat Lohman
Chairman, Joint Committee for Geology and Geophysics,
Massachusetts Institute of Technology/
Woods Hole Oceanographic Institution

91 [illegible] 20

GLOBAL ISOTOPIC SIGNATURES OF OCEANIC ISLAND BASALTS

by

LYNN A. OSCHMANN

Submitted to the Department of Earth, Atmospheric and Planetary Sciences
Massachusetts Institute of Technology
and
the Department of Geology and Geophysics
Woods Hole Oceanographic Institution
August 9, 1991
in partial fulfillment of the requirements for the degree of
MASTER OF SCIENCE IN OCEANOGRAPHY

ABSTRACT

Sr, Nd and Pb isotopic analyses of 477 samples representing 30 islands or island groups, 3 seamounts or seamount chains, 2 oceanic ridges and 1 oceanic plateau [for a total of 36 geographic features] are compiled to form a comprehensive oceanic island basalt [OIB] data set. These samples are supplemented by 90 selected mid-ocean ridge basalt [MORB] samples to give adequate representation to MORB as an oceanic basalt end-member. This comprehensive data set is used to infer information about the Earth's mantle. Principal component analysis of the OIB+MORB data set shows that the first three principal components account for 97.5% of the variance of the data. Thus, only four mantle end-member components [EMI, EMII, HIMU and DMM] are required to completely encompass the range of known isotopic values. Each sample is expressed in terms of percentages of the four mantle components, assuming linear mixing. There is significant correlation between location and isotopic signature within geographic features, but not between them, so discrimination analysis of the viability of separating the oceanic islands into those lying inside and outside Hart's (1984, 1988) DUPAL belt is performed on the feature level and yields positive results.

A "continuous layer model" is applied to the mantle component percentage data to solve for the spherical harmonic coefficients using approximation methods. Only the degrees 0-5 coefficients can be solved for since there are only 36 features. The EMI and HIMU percentage data sets must be filtered to avoid aliasing. Due to the nature of the data, the coefficients must be solved for using singular value decomposition [SVD], versus the least squares method. The F-test provides an objective way to estimate the number of singular values to retain when solving with SVD. With respect to the behavior of geophysics control data

sets, only the degree 2 spherical harmonic coefficients for the mantle components can be estimated with a reasonable level of confidence with this method.

Applying a "delta-function model" removes the problem of aliasing and simplifies the spherical harmonic coefficient solutions from integration on the globe to summation over the geographic features due to the properties of delta-functions. With respect to the behavior of geophysics control data sets, at least the degree 2 spherical harmonic coefficients for the mantle components can be estimated with confidence, if not the degrees 3 and 4 as well. Delta-function model solutions are, to some extent, controlled by the nonuniform feature distribution, while the continuous layer model solutions are not.

The mantle component amplitude spectra, for both models, show power at all degrees, with no one degree dominating. The DUPAL components [EMI, EMII and HIMU], for both models, correlate well with the degree 2 geoid, indicating a deep origin for the components since the degrees 2-3 geoid is inferred to result from topography at the core-mantle boundary. The DUPAL and DMM components, for both models, correlate well [and negatively] at degree 3 with the velocity anomalies of the Clayton-Comer seismic tomography model in the 2500-2900 km depth range [immediately above the core-mantle boundary]. The EMII component correlates well [and positively] at degree 5 with the velocity anomalies of the Clayton-Comer model in the 700-1200 km depth range, indicating a subduction related origin. Similar positive correlations for the geoid in the upper lower mantle indicate that subducted slabs extend beyond the 670 km seismic discontinuity and support a whole-mantle convection model.

Thesis Supervisor: Dr. Stanley R. Hart
Title: Senior Scientist, Woods Hole Oceanographic Institution

TABLE OF CONTENTS

ACKNOWLEDGEMENTS

I am indebted to Stan Hart for getting me started on this project, oh so long ago [it's been a lot of fun!], and for providing abundant enthusiasm and support along the way. Many thanks to Brad Hager for guiding me through the labyrinth that is spherical harmonics and for shedding the light of experience on many a sticky geophysics problem. Quite a few staff members at the Woods Hole Oceanographic Institution were generous with their time and help, but most noteworthy are: Andy Solow, who helped with the understanding and application of statistics, Peter Shaw who explained and provided information on the F-test, Carl Bowin who cleared up a few geoid questions and provided some helpful figures and papers, John Goff who gave freely of his knowledge of mathematics and his Apollo terminal, Debbie Smith who provided a little disk space when it was needed and Warren Sass who was there to answer that late night computer question. Thanks are extended to Dave Bercovici [lounging somewhere on a beach in Hawaii, no doubt] for walking me through many an equation in my quest to understand spherical harmonics and inverse modeling [I am not an uprooted carrot!]. C programming was made a little less painful with the help of Brendan Reilly. Just the right amount of commiseration and procrastination was provided by fellow grad students Cecily Wolfe, Chris Bradley, Elise Ralph, Gail Christeson, Gary Jaroslow and Chris Weidman. My officemate JoAnn Muramoto was always willing to take a break from her own thesis and put up with a lot of unusual office behavior. Housemate Laura Praderio always had a willing ear and an open kitchen policy. As always, Mom and Dad were there all along, listening to the incomprehensible babble of geochemistry and math that spewed forth along the phone lines and providing that no-matter-what-happens-we're-proud-of-you support. Finally, I owe my sanity to Pat Munson for dragging me away from the computer every now and then to remind me that it is indeed summer.

Officially, support for graduate study in the MIT/WHOI Joint Program in Oceanography was provided by the US Navy under the CIVINS program.

CHAPTER 1

INTRODUCTION

PREVIOUS WORK

That the Earth's mantle is heterogeneous is no longer a subject of controversy among geochemists, but the composition, the location and the geometry of these heterogeneities is very much in question. Direct sampling is not an option for studying the chemistry of most of the mantle, so products of indirect sampling, such as oceanic island basalts [OIB's] and mid-ocean ridge basalts [MORB], are invaluable for revealing the nature of the inaccessible mantle. Though the OIB's may be contaminated by interactions with the lithosphere or may sample large vertical sections of the mantle, they still retain the signature of their original source.

Using various statistical methods and models, previous workers have defined what they believe to be the number of mantle component end-members required to represent the variation in the oceanic mantle data [OIB+MORB]. Early on, Zindler *et al.* (1982) used factor analysis to evaluate the oceanic data in five dimensions. Their analysis indicated that the oceanic data define a plane [the "mantle plane"], described by the mixing of three chemically independent components, two undifferentiated or slightly enriched mantle components and one MORB-type or depleted mantle component.

Other workers have chosen five groups or components to represent the data. Using a series of two-dimensional isotopic plots, White (1985) divided the oceanic data into five distinct basalt groups [MORB, St. Helena, Kerguelen, Society, and Hawaii]. He concedes that the five groups may be end-members which mix to form intermediate compositions, but he believes that each group either represents a distinct, internally homogeneous reservoir or that each group is composed of a number of isotopically similar reservoirs. Likewise, Li *et al.* (1991) proposed fives extremes, using non-linear mapping: Atlantic MORB [DMM], St. Helena [HIMU], Walvis [EMI], Samoa [EMII] and D_5 [EMIII]. Non-linear mapping approximately preserves the geometric structure of the data by maintaining interpoint distances. Four of the five extremes of Li *et al.* (1991) are based solidly on samples trends from islands, but the D_5 extreme is based only on that one sample. More data is needed to substantiate their fifth extreme.

By far the majority of analyses indicate the existence of four end-member components for the oceanic mantle data. Using two-dimensional plots, Zindler and Hart (1986) defined the following four end-member components: depleted MORB mantle [DMM], high U/Pb mantle [HIMU], and two enriched mantle components [EMI and EMII], with possibly two other components prevalent mantle composition [PREMA] and bulk silicate Earth [BSE]. Eigenvector analyses by Allègre *et al.* (1987) agree with the four component model of Zindler and Hart (1986). The four extremes of Allègre *et al.* (1987) are [correspond to]: extreme MORB [DMM]; St. Helena, Tubuaï and Mangaï islands [HIMU]; Kerguelen, Gough, Tristan da Cunha and Raratonga islands [EMI]; and São Miguel and Atui islands [EMII]. Hart (1988), using an augmented data set and two-dimensional plots, concluded that the four end-members proposed by Zindler and Hart (1986) are valid representations of the extremes of the oceanic data. He resolves White's (1985) groupings into his own four component system as follows [White = Hart]: MORB = DMM, Society = EMII, St. Helena = HIMU, Hawaii = EMI, with the suggestion that White's fifth group, Kerguelen, is a mixture of EMI and EMII. In addition, Li *et al.* (1991) also noted a tetrahedral structure to the data, when using factor analysis with varimax rotation, with the following four extremes: Atlantic MORB [DMM], Mangaia [HIMU], Samoa [EMII] and Walvis[EMI].

One scenario for the genesis of the three unusual mantle components is put forth by Hart (1988). He proposes that HIMU, enriched in U, is probably generated by intra-mantle metasomatism, that EMI corresponds to a slightly modified bulk-earth compositon and that EMII can be explained by the recycling of sediments during subduction. The proposed formation mechanisms in no way limit the geometry of the mantle needed to generate the heterogeneities and, as such, a wide variety of models have been proposed. A whole mantle convection model might portray the enriched mantle components as blobs floating around in a depleted mantle matrix (Zindler and Hart, 1986) or perhaps as an accumulated layer of subducted oceanic crust and sediment at the core-mantle boundary that reaches the surface in mantle plumes (Hofmann and White, 1982). A two-layer convection model might rely on a depleted upper mantle feeding the mid-ocean ridges and an enriched lower mantle feeding oceanic islands via mantle plumes (Dupre and Allègre, 1983) or require a depleted upper mantle, a primitive lower mantle and an accumulated layer of subducted oceanic crust and sediment at the 670 km discontinuity that supplies the enriched components via mantle plumes (White, 1985; Allègre and Turcotte, 1985). Anderson (1985) even proposes a three-layer convective model with the geochemical contrasts occurring only in the upper mantle with a depleted lower part that supplies the mid-ocean ridges and an enriched upper part from subduction of oceanic crust and sediment.

A deep origin for the enriched components is indicated by Hart's (1984) large-scale isotopic anomaly, the DUPAL anomaly, characterized by the concentration of the enriched mantle components in a band from 2° S to 60° S. Qualitatively, countours of the anomaly criteria [Δ7/4, Δ8/4 and ΔSr (Hart, 1984)] correspond to long-wavelength [and thus deep] geophysical quantities (Hart, 1988). Other researchers oppose this deep origin interpretation, citing the nonuniform distribution of hotspots as the reason for the pattern (White, 1985) or arguing that the DUPAL compositions occur in scattered locations and do not cover a coherent geographic area (Allègre *et al.*, 1987).

The purpose of this thesis is three-fold: (1) to address once again the issue of the number of mantle end-member components needed to represent the oceanic mantle data, (2) to statistically test the viability of the DUPAL distinction as a means of characterizing the OIB data and (3) to try to pinpoint the source depth of the enriched mantle components by expanding their relative abundances in spherical harmonics and comparing their expansions to those of known geophysical quantities.

DATA

The majority of this study focuses on Sr, Nd and Pb isotopic analyses of volcanic rocks from oceanic islands, seamounts, ridges, and plateaus. All of these geographic features overlie oceanic crust, with the exception of Nunivak Island on the Alaskan Continental Shelf, and none of them is directly associated with seafloor spreading, with the exception of Iceland, which has a mixture of mid-ocean ridge and hotspot influences. Essentially, the data set is that compiled by Zindler et al. (1982) and later augmented by Hart (1988), with some additional recent analyses (Appendix). Samples in the data set are mainly basalt, with some gabbros and trachybasalts; trachytes and other silica-rich rocks relative to basalt [roughly $SiO_2 > 50\%$] are excluded. The majority of the samples are of Cenozoic age, with the exception of the Walvis Ridge, Rio Grande Rise and New England Seamounts samples, with ages up to 100 Ma. If a choice is given, analyses of leached samples are preferred over analyses of unleached samples. In addition, only single samples for which there are Sr, Nd and Pb analyses are included. For consistency, Sr data is adjusted to 0.70800 [E&A standard] or 0.71022 [NBS SRM 987 standard] and Nd data is adjusted to

0.512640 [BCR-1 standard] or 0.511862 [La Jolla standard] or 0.511296 [Spex standard].

In this data set, referred to as the OIB data set, there are 477 samples representing 30 islands or island groups, 3 seamounts or seamount chains, 2 aseismic oceanic ridges and 1 oceanic plateau (Figure 1.1 and Table 1.1). The isotopic means and standard deviations for the OIB data are listed in Table 1.2.

Since MORB is considered to be one of the mantle component end-members (Zindler *et al.*, 1982; White, 1985; Zindler and Hart, 1986; Hart, 1988), any attempt to choose end-members should include MORB data. For this reason, a second data set is created using the OIB data and a selection of 90 MORB samples (Appendix), the OIB+MORB data set (Table 1.3). The criteria for choosing OIB samples applies to the MORB samples as well. Isotopic means and standard deviations for the OIB+MORB data are listed in Table 1.2.

ORGANIZATION

The main thust of this work is to characterize the OIB data and to search for possible correlations between the geochemical signatures of OIB's and geophysical quantities, such as the geoid and seismic tomography, that might help pinpoint the depth[s] of the OIB reservoir[s].

Chapter 2 explores the nature of the OIB isotope data. With the help of principal component analysis, the data is expressed in terms of percentages of four mantle component end-members. Spatial correlation testing reveals the relationship between geographic distance from island to island and feature to feature and the "isotopic distance" between samples. Discrimination analysis, both nearest-neighbor and graphical, is used to test the viability of separating the oceanic islands into two groups, inside and outside the DUPAL belt.

Chapter 3 applies a "continuous layer model" to the mantle component data, as an assumed geometry for the OIB reservoir, in orJer to solve for the spherical harmonic coefficients. The problem of aliasing is addressed with the relationship of variation in mantle components to distance between features. Approximation methods are used to solve for the coefficients. Geophysical data sets are constructed, using GEM-L2 geoid coefficients, to serve as controls against which to judge the success of the approximation methods.

Chapter 4 applies a "delta-function model" to the mantle component data to provide a mathematically more robust solution for the spherical harmonic coefficients. The delta-function approximation removes the problem of aliasing, but generates a solution dependent upon feature location. The same geophysical data sets are used again to judge the success of the delta-function approximation.

Chapter 5 compares the mantle component spherical harmonic solutions for the two models in terms of their amplitude spectra, how well they correlate with the geoid, how they are affected by the nonuniform feature distribution and how well they correlate with the Clayton-Comer seismic tomography model. The implications of these results and recommendations for further research are discussed.

Table 1.1. Geographic features represented in the OIB data set, with their components, number of samples [in braces] and references indicated.

Feature	Components	References[1]
Ascension [5]		7,34,35
Amsterdam/St. Paul [11]		
	Amsterdam [5]	38
	St. Paul [6]	38
Azores [6]		
	Faial [1]	22
	São Miguel [5]	1,8
Balleny [3]		19
Cameroon Line [18]		
	Bioko [5]	17,18
	Pagalu [1]	18
	Principe [3]	18
	São Tomé [9]	17,18
Cape Verde Islands [41]		
	Fogo [6]	14
	Maio [9]	8,14
	Sao Antao [10]	8,14
	Sao Tiago [13]	14
	Sao Vincente [3]	14
Christmas [13]		19
Cocos [3]		3
Comores Archipelago [14]		38
Cook-Austral Islands [26]		
	Aitutaki [4]	1,21
	Atui [6]	1,21
	Mangia [5]	1,21
	Mauke [3]	1,21
	Raratonga [8]	1,21,23
Crozet Islands [9]		38
Fernando de Noronha [16]		1,13
Galapagos Islands [11]		39
Gough [2]		1
Hawaiian Islands [73]		
	Hawaii [14]	28,32
	Kahoolawe [13]	37
	Kauai [2]	28
	Lanai [4]	37

Table 1.1. Continued.

Feature	Components	References
Hawaiian Islands [73]		
	Loihi [15]	27
	Maui [3]	28
	Molokai [5]	28
	Oahu [17]	29
Iceland [7]		20
Juan Fernandez Islands [4]		15
Kerguelen Plateau [41]		
	Heard Island [9]	2,30
	Kerguelen Island [20]	12,30,38
	Kerguelen Plateau [12]	26,36
Louisville Seamount Chain [4]		6
Marion/Prince Edward [4]		19
Marquesas Archipelago [11]		10,11,33
Mascareignes [8]		
	Mauritius [1]	1
	Réunion [7]	38
New England Seamounts [6]		31
Nunivak [2]		25
Pitcairn [19]		41
Ponape [1]		19
Sala Y Gomez [1]		?
Samoa Islands [34]		
	Manu'a [4]	42
	Savai'i [8]	42
	Tutuila [9]	23,42
	Upolu [13]	23,42
San Felix/San Ambrosio [5]		
	San Felix [4]	15
	San Ambrosio [1]	15
Shimada Seamount [1]		16
Society Ridge [9]		
	Mehetia [2]	9
	Moua Pihaa [1]	9
	Tahaa [1]	40
	Teahitia [4]	9
	dredge [1]	9
St. Helena [31]		?,1,4,7,22

Table 1.1. Continued.

Feature	Components	References
Trinidade [1]		1
Tristan de Cunha [5]		7,22
Tubuai-Austral Islands [22]		
	Marotiri [1]	5
	Raevavae [1]	1
	Rapa [3]	5,23
	Rimatara [4]	?,21
	Rurutu [4]	21,23
	Tubuai [9]	5
Walvis Ridge [10]		24

[1]In the reference column, a "?" indicates a sample with an unknown reference.

Reference guide: [1] Allègre *et al.*, 1987; [2] Barling and Goldstein, 1990; [3] Castillo *et al.*, 1988; [4] Chaffey *et al.*, 1989; [5] Chauvel *et al.*, 1991; [6] Cheng *et al.*, 1988; [7] Cohen and O'Nions, 1982a; [8] Davies *et al.*, 1989; [9] Devey *et al.*, 1990; [10] Duncan *et al.*, 1986; [11] Dupuy *et al.*, 1987; [12] Gautier *et al.*, 1990; [13] Gerlach *et al.*, 1987; [14] Gerlach *et al.*, 1988; [15] Gerlach *et al.*, 1986; [16] Graham, 1987; [17] Halliday *et al.*, 1990; [18] Halliday *et al.*, 1988; [19] Hart, 1988; [20] Hart, unpublished; [21] Nakamura and Tatsumoto, 1988; [22] Newsom *et al.*, 1986; [23] Palacz and Saunders, 1986; [24] Richardson *et al.*, 1982; [25] Roden, 1982; [26] Salters, 1989; [27] Staudigel *et al.*, 1984; [28] Stille *et al.*, 1986; [29] Stille *et al.*, 1983; [30] Storey *et al.*, 1988; [31] Taras and Hart, 1987; [32] Tatsumoto, 1978; [33] Vidal *et al.*, 1984; [34] Weis, 1983; [35] Weis *et al.*, 1987; [36] Weis *et al.*, 1989; [37] West *et al.*, 1987; [38] White, unpublished; [39] White and Hofmann, 1982; [40] White *et al.*, 1989; [41] Woodhead and McColloch, 1989; [42] Wright and White, 1987.

Table 1.2. Isotopic means and standard deviations[1] for the OIB and the OIB+MORB data sets.

	Sr	Nd	6/4Pb	7/4Pb	8/4Pb
OIB[2]					
Mean	0.703943	0.512825	19.065	15.586	38.965
Std Dev	0.000892	0.000145	0.880	0.093	0.693
OIB+MORB[3]					
Mean	0.703752	0.512869	18.939	15.571	38.799
Std Dev	0.000936	0.000170	0.870	0.093	0.748

[1]Isotopic variance is the square of the standard deviation.
[2]Mean and standard deviation based on 477 samples.
[3]Mean and standard deviation based on 567 samples.

Table 1.3. Sample locations for the MORB data in the OIB+MORB data set, with the number of samples [in braces] and references indicated.

Location	References
Atlantic Ocean [22]	2,5
Pacific Ocean	
East Pacific Rise [6]	5,7
Galapagos Ridge [13]	5,7
Gorda Ridge [8]	7
Juan de Fuca Ridge [6]	7
Indian Ocean [10]	1,5
E Indian Ridge [7]	4
SE Indian Ridge [12]	6
SW Indian Ridge [6]	3

Reference guide: [1] Cohen and O'Nions, 1982b; [2] Cohen *et al.*, 1980; [3] Hamelin and Allègre, 1985; [4] Hamelin *et al.*, 1986; [5] Ito *et al.*, 1987; [6] Klein *et al.*, 1988; [7] White *et al.*, 1987.

ISTRIBUTION

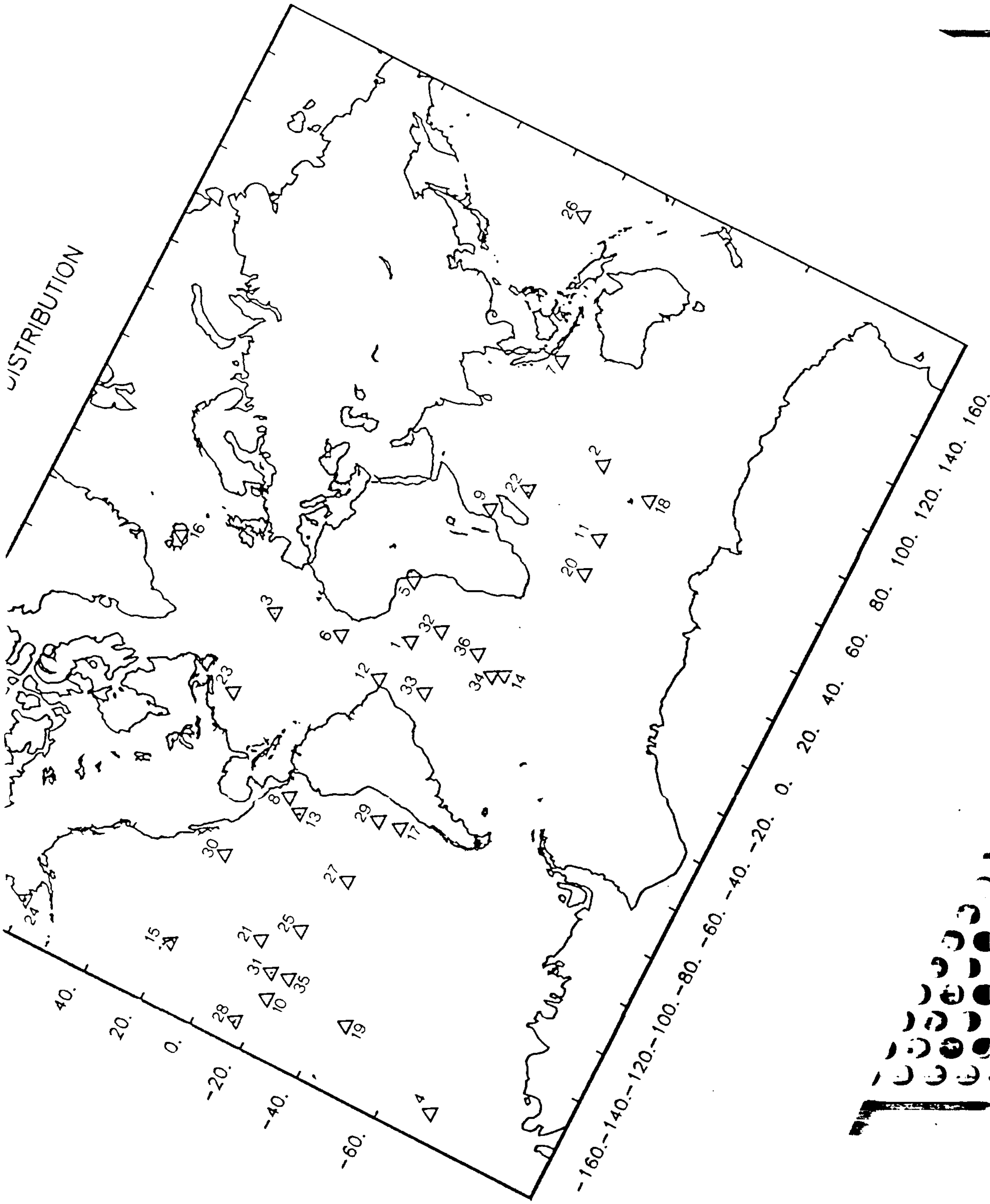

Fig. 1.1. Global distribution of oceanic island basalt samples. The triangles represent the 36 geographic features with the following number key: [1] Ascension, [2] Amsterdam/St. Paul, [3] Azores, [4] Balleny, [5] Cameroon Line, [6] Cape Verde Islands, [7] Christmas, [8] Cocos, [9] Comores Archipelago, [10] Cook-Austral Islands, [11] Crozet Islands, [12] Fernando de Noronha, [13] Galapagos Islands, [14] Gough, [15] Hawaiian Islands, [16] Iceland, [17] Juan Fernandez Islands, [18] Kerguelen Plateau, [19] Louisville Seamount Chain, [20] Marion/Prince Edward, [21] Marquesas Archipelago, [22] Mascareignes, [23] New England Seamounts, [24] Nunivak, [25] Pitcairn, [26] Ponape, [27] Sala Y Gomez, [28] Samoa Islands, [29] San Felix/San Ambrosio, [30] Shimada Seamount, [31] Society Ridge, [32] St. Helena, [33] Trinidade, [34] Tristan de Cunha, [35] Tubuai-Austral Islands, [36] Walvis Ridge.

CHAPTER 2

MATHEMATICAL AND STATISTICAL METHODS OF DATA ANALYSIS

INTRODUCTION

When dealing with a multidimentional data set with dimension greater than three, it is impossible to visualize the shape of the data in that space. This makes it difficult to choose "end-members" for the data, where end-members are interpreted as the vertices of the smallest simplex, with linear or nonlinear edges, that completely encloses all the data points. Previous work using two-dimensional plots to estimate the groups or end-members (Zindler *et al.*, 1982; White, 1985; Zindler and Hart, 1986) can be misleading since those plots are projections of a higher-dimensional shape. For this study, it is possible to reduce the dimensionality of the OIB+MORB data set, via principal component analysis, and still retain its general shape, making it possible to choose end-members in three-dimensions.

For the OIB data set, the data locations [oceanic islands] are not distributed evenly about the globe. This prompts the question as to whether there is any relationship between location and isotopic signature. To address this, a spatial correlation test (Mantel, 1967) is used to test for a correlation between the geographic distance and the "isotopic distance" between samples. In addition, a count is kept of the number of times a sample's isotopic "nearest-neighbor" occurs within the same island and within the same geographic feature.

Finally, the globe has been divided by Hart (1984, 1988) into the islands lying inside the DUPAL belt, from 2° S to 60° S, and those lying outside. To see if there is statistical justification for separating the data into these two different populations, isotopic nearest-neighbor discriminant analysis is performed on the data set to obtain a misclassification error rate. The significance of this error rate is based upon a randomization test of Solow (1990). While giving promising results, the randomization test for significance is inconclusive because spatial correlation within geographic features has not been accounted for. As an alternative, discrimination between isotopic signatures on the scale of geographic features inside and outside the DUPAL belt is addressed graphically.

PRINCIPAL COMPONENT ANALYSIS

Theory

Principal component analysis can be viewed as a coordinate system transformation, but one that has particular properties. It generates a new set of variables, the principal components, that are linear combinations of the original variables:

$$Z_i = \sum_{j=1}^{5} e_{ij} X_j \qquad\qquad i = 1,\ldots,5$$

where the Z_i's are the principal components, the e_{ij}'s are the transformation coefficients, and the X_j's are the original isotope measurements ($X_1 = {}^{87}Sr/{}^{86}Sr$, $X_2 = {}^{143}Nd/{}^{144}Nd$, $X_3 = {}^{206}Pb/{}^{204}Pb$, $X_4 = {}^{207}Pb/{}^{204}Pb$, $X_5 = {}^{208}Pb/{}^{204}Pb$).

The principal components have the following properties:

(1) Z_i and Z_j are uncorrelated, for all i, j

(2) $\text{Variance}(Z_1) \geq \text{Variance}(Z_2) \geq \ldots \geq \text{Variance}(Z_5)$

(3) for all i, $\sum_{j=1}^{5} e_{ij}^2 = 1$

The transformation coefficients are the elements of the unit eigenvectors of the 5 x 5 data covariance matrix. Because the isotopic ratios are on different scales, the data set must be normalized in order for all of the isotopes to be treated equally in the analysis. One way to do this is to take each sample and for every isotope subtract the mean and divide by the standard deviation (Table 1.2):

$$Y_{ij} = \frac{X_{ij} - \overline{X}_j}{\sigma_j}$$

where X_{ij} is the jth isotopic ratio for the ith . ›mple, etc. This method weights the information provided by all five isotopes equally. Alternatively, Allègre *et al.* (1987) develop their own empirical norm, the "geologic norm", that takes analytical errors into account and is designed to give equal weight to all isotopes except $^{207}Pb/^{204}Pb$, which has the largest analytical error.

Application to the OIB+MORB Data Set

Because DMM [depleted MORB mantle] is one of the proposed mantle end-member components, I have chosen to do principal component analysis using all of the oceanic island data [477 samples] plus a wide selection of MORB data [90 samples]. The covariance matrix for the OIB+MORB data set and its eigenvectors and eigenvalues are shown in Table 2.1. The sum of the eigenvalues is the trace of the covariance matrix, ie. the sum of the diagonal elements. This is equal to 5 because the diagonal elements of the covariance matrix, the scaled isotope variances, are all 1. To find out how much of the variance of the scaled data set is accounted for by each eigenvector, and thus each principal component, divide the corresponding eigenvalue by 5. The first three principal components account for 97.5% of the variance of the data set. Therefore it is reasonable to use the three-dimension principal component data set to select end-member components. This has important implications for the OIB+MORB data set. In n-dimensional space, the polygon containing the fewest vertices $[n+1]$ is a simplex. Thus, the OIB+MORB data set would require six end-member components to completely define it, if it spanned the entire five-dimensional space. The fact that it can be adequately represented in three-dimensions implies that the OIB+MORB data set requires only four end-member components.

A comparison of eigenvalues and corresponding percentages of variance from this study and from Allègre *et al.* (1987) for OIB+ MORB and OIB data sets is presented in Table 2.2. It should be noted that the OIB eigenvalues from this study are found using a separate covariance matrix derived from the 477 OIB samples alone, as is done by Allègre *et al.* (1987). Their analysis yielded similar results for a three-dimensional fit to the data [OIB+MORB: 99.2% versus 97.5%; OIB: 98.8% versus 97.3%]. Part of the small difference that does exist may be due to the fact that they used a smaller data set [OIB+MORB: 91 samples versus 567 samples; OIB: 53 samples versus 477], in addition to the different methods used to scale the data.

The procedure outlined above for computing principal components is compacted into matrix form, **Z** = **EY**, with exact solutions:

$$\begin{bmatrix} Z_{11} \ldots\ldots Z_{1N} \\ Z_{21} \ldots\ldots Z_{2N} \\ Z_{31} \ldots\ldots Z_{3N} \\ Z_{41} \ldots\ldots Z_{4N} \\ Z_{51} \ldots\ldots Z_{5N} \end{bmatrix} = \begin{bmatrix} e_{11}\, e_{12}\, e_{13}\, e_{14}\, e_{15} \\ \vdots \qquad\qquad \vdots \\ e_{51}\, e_{52}\, e_{53}\, e_{54}\, e_{55} \end{bmatrix} \begin{bmatrix} Y_{11} \ldots\ldots Y_{1N} \\ Y_{21} \ldots\ldots Y_{2N} \\ Y_{31} \ldots\ldots Y_{3N} \\ Y_{41} \ldots\ldots Y_{4N} \\ Y_{51} \ldots\ldots Y_{5N} \end{bmatrix}$$

where N = the number of samples [567], the Y_{ij}'s are the normalized isotopic values and the eigenvectors are the rows of the matrix **E**. Three two-dimensional plots of the first three principal components, with general end-member regions indicated, (Figs. 2.1, 2.2 and 2.3) are presented for comparison with those of Allègre *et al.* (1987) (Fig. 2.4). Plotting the principal component values for the samples versus each other is the same as plotting the projection of the OIB+MORB population onto its eigenvector planes as they have done. The two sets of plots are very similar, but mirror images of each other. This is simply because the eigenvectors used were of opposite sign, in no way affecting the validity of either set of plots.

Mantle End-Member Components

In three-dimensional space the principal component data form a tetrahedron (Fig. 2.5). It should be noted that the tetrahedron is not aligned with the principal component axes, so two-dimensional plots of the principal component data do not give an exact indication of the location of the extreme points. End-member component values are chosen by eye at the extremes of the tetrahedron using a rotating three-dimensional plotting program.

First, the "nonlinear" end-member points are chosen, those that just form the vertices of the tetrahedron (Table 2.3). These end-members are referred to as "nonlinear" because they define the vertices of the smallest simplex enclosing the data points which has linear and nonlinear edges. In geometry, a simplex is defined as a polygon with planar faces, but I am extending this definition to encompass polygons containing nonplanar faces as well. The purpose of choosing particular end-member points is to be able to express all of the sample points as a combination of the four end-member components, for later use in spherical harmonic expansions. Though linear mixing is believed to exist between HIMU and EMI (Hart *et al.*, 1986) and HIMU and DMM (Hart, 1988), more complicated mixing arrays are probable amongst the other components. Since no models exist for the nonlinear mixing arrays, it is easiest to represent the sample points as a linear combination of the end-member points. Thus, it is necessary to find the vertices of the smallest simplex with planar faces that encloses as many data points as possible; these vertices are the "linear" end-members. These end-members are chosen by rotating the figure to look at the four sides of the tetrahedron edge on and moving out the "nonlinear" end-members until the planar-sided tetrahedron defined by linear mixing expands to contain as many sample points as possible, without becoming overly extreme (Table 2.4). This is an admittedly subjective process, but more accurate than choosing end-members using two dimensional plots. Figures 2.6 - 2.9 show the four views normal to each of the tetrahedron faces.

When assuming linear mixing, the simplex defined by the final chosen "linear" end-member points excludes only 13 OIB data points, out of 477, and 3 MORB data points out of 90 (Table 2.5), compared to the 85 OIB and 49 MORB data points excluded when using the "nonlinear" end-member values. The excluded points will have negative amounts of some of the end-members and will not be used in spherical harmonic expansions.

The end-member values selected in principal component space are converted back into normalized isotope values (Tables 2.3 and 2.4) by substituting zeros [the mean value for each principal component] for the fourth and fifth principal components in the **Z** matrix:

$$\begin{bmatrix} C_{11} \ldots\ldots C_{14} \\ C_{21} \ldots\ldots C_{24} \\ C_{31} \ldots\ldots C_{34} \\ C_{41} \ldots\ldots C_{44} \\ C_{51} \ldots\ldots C_{54} \end{bmatrix} = \begin{bmatrix} e_{11}\; e_{12}\; e_{13}\; e_{14}\; e_{15} \\ \vdots \qquad\qquad\qquad \vdots \\ \vdots \qquad\qquad\qquad \vdots \\ e_{51}\; e_{52}\; e_{53}\; e_{54}\; e_{55} \end{bmatrix}^{-1} \begin{bmatrix} Z_{11} \ldots\ldots Z_{14} \\ Z_{21} \ldots\ldots Z_{24} \\ Z_{31} \ldots\ldots Z_{34} \\ 0 \ldots\ldots\ldots 0 \\ 0 \ldots\ldots\ldots 0 \end{bmatrix}$$

where C_{1i} is the normalized $^{87}Sr/^{86}Sr$ ratio for the ith end-member component, and so forth. There is some error involved in this process, but because the variances of the fourth and fifth principal components are small, the error is small. To compute these errors, the entire OIB+MORB data set is transformed into principal components; the fourth and fifth principal components are dropped; the approximate normalized isotope values are computed as above; and these values are then unnormalized and compared to the actual isotope values. The average absolute errors for this transformation are fairly small compared to the isotope standard deviations (Table 2.6). Compared to the range of analytical errors, all of the transformation errors are reasonable except the one for $^{206}Pb/^{204}Pb$, which is approximately 6x larger than its analytical error (Table 2.6).

Finally, the samples are computed as percentages of the four "linear" end-members:

$$\begin{bmatrix} C_{11} \ldots\ldots C_{14} \\ C_{21} \ldots\ldots C_{24} \\ C_{31} \ldots\ldots C_{34} \\ C_{41} \ldots\ldots C_{44} \\ C_{51} \ldots\ldots C_{54} \\ 1 \ldots\ldots\ldots 1 \end{bmatrix} \begin{bmatrix} p_{1j} \\ p_{2j} \\ p_{3j} \\ p_{4j} \end{bmatrix} = \begin{bmatrix} Y_{1j} \\ Y_{2j} \\ Y_{3j} \\ Y_{4j} \\ Y_{5j} \\ 1 \end{bmatrix}$$

where p_{ij} is the percentage of the ith end-member component for the jth sample and Y_{ij} is the ith normalized isotope value for the jth sample. The C matrix is the normalized end-member isotope value matrix computed from above with an additional row of ones. This row of ones and the one included in the **Y** vector define a constraint that the sum of the percentages add up to 1. This is necessary to provide useful positive results between 0 and 1 since the tetrahedron is not a four-component composition diagram, but resides in Euclidean space. QR decomposition is used to solve this over-determined system of equations. It decomposes the **C** matrix into two matrices: **Q** [orthogonal] and **R** [upper triangular]: $\mathbf{QRp} = \mathbf{Y}$, with solutions: $\mathbf{p}^{est} = \mathbf{R}^{-1}\mathbf{Q}^{T}\mathbf{Y}$.

SPATIAL CORRELATION TESTING

Methodology

In order to check for spatial correlation, a paired distance approach is employed, as outlined in Mantel (1967), using geographic and isotopic distances. The geographic distance used is that of an arc on a sphere connecting any two sample locations, ie. a great circle distance (Turcotte and Schubert, 1982). The angle Δ_{ij} between the two locations *I* and *J* on the sphere (Fig. 2.10) is given by:

$$\Delta_{ij} = \cos^{-1}[\cos\theta_j \cos\theta_i + \sin\theta_j \sin\theta_i \cos(\varphi_j - \varphi_i)]$$

where θ_i and φ_i are the colatitude and longitude of location *I* and θ_j and φ_j are the colatitude and longitude of location *J*. The surface distance *s* between *I* and *J* is:

$$s_{ij} = R\Delta_{ij}$$

where *R* is the radius of the earth [R = 6378.139 km]. The isotopic distance used is the generalized Euclidean distance in multidimensions scaled by the variances of the isotopic ratios. Scaling by the variances of the isotopic ratios is necessary to keep the distance measurement from being dominated by the isotopic ratio with the largest variance, $^{206}Pb/^{204}Pb$ (Table 1.2). For any two samples $\mathbf{X}_i$ and $\mathbf{X}_j$, the isotopic distance between them, *d*, is:

$$d_{ij} = \sqrt{(\mathbf{X}_i - \mathbf{X}_j)^T \mathbf{V}^{-1} (\mathbf{X}_i - \mathbf{X}_j)}$$

where

$$\mathbf{X}_i = \begin{bmatrix} X_{1i} \\ X_{2i} \\ X_{3i} \\ X_{4i} \\ X_{5i} \end{bmatrix}$$

is the isotope vector for *i*th sample [$\mathbf{X}_{1i}$ is the $^{87}Sr/^{86}Sr$ ratio of the *i*th sample, etc.] and **V** is the diagonal variance matrix. A similar distance measurement, called Mahalanobis distance (Manly, 1986) was considered, but not used because it utilizes the covariance matrix. Covariance is a meaningful measurement when the data is normally distributed (elliptical) in space. From the three-dimensional principal component plots (Figs. 2.5-2.9), it is apparent that the data set is not elliptical, so covariance is a meaningless measurement concerning the nature of the data.

Next, the correlation between the two distances for all the samples is calculated. The key to Mantel's (1967) technique is to determine the significance of this observed correlation by creating random pairings of the sample locations and isotopic signatures, calculating the appropriate distances, and computing their correlation, thus constructing a distribution against which the observed value can be judged. This distribution is that of the correlation under the null hypothesis that the geographic distances are matched to the isotopic distances at random.

Zindler and Hart (1986) noted a relationship between the scale length of a geographic feature and the isotopic range of that feature. Basically, they concluded that the largest isotopic ranges occur in the largest geographic features, while small isotopic ranges may occur in small or large features. This implies a correlation between the within-feature geographic distance and the within-feature isotopic distance. The paired distance correlation method outlined above computes the correlation between geographic and isotopic distances both within features and between features. In using this method, it is possible that any correlation within the features may be masked by a lack of correlation between the features. As an additonal check for within-feature correlation, a count is kept of the number of times a sample's isotopic nearest-neighbor [the sample that is the smallest isotopic distance from the sample in question] occurs within the same island and within the same island group [or island, if an island is not part of a larger group]. The counts are performed both for the observed data and for the random permutations. Those from the random permutations can be used, as before, to judge the significance of the observed counts. The larger scale geographic divisions of the data set into island groups and the remaining solitary islands (Table 2.7) will be referred to from this point on as features.

Application to the OIB Data Set

For this application, the OIB data is used since only oceanic island interrelationships are of interest. Two 477 x 477 distance matrices are calculated for the geographic and isotopic distances between samples. For the observed data, the correlation between the distance matrices is 0.1756 and the within island and feature nearest-neighbor occurrence rates are 61.4% and 76.7%, respectively (Table 2.8). The occurrence rates within islands and features appear significant and are confirmed so by randomization, as none of the generated occurrence rates are as large as the observed rates for 100 permutations (Table 2.8). The correlation, on the other hand, is small, but attains significance compared to the randomization values which are all less than the observed value (Table 2.8) Thus, both methods indicate that there is spatial correlation between sample location and isotopic signature and the correlation that exists between samples within the same geographic feature seems to dominate.

Treating the samples inside and outside the DUPAL belt separately and then testing for spatial correlation yields results similar to those obtained with the whole data set (Table 2.8).

It is not clear if all of the spatial correlation is due to the correlation within the features. There may be some additional spatial correlation between features. To check this, the appropriate samples are averaged to get an average isotopic signature and location for each feature (Table 2.7). Using all of the features both inside and outside the DUPAL belt, the observed correlation is 0.1584 with a significance level of 0.13 [there are 13 permutations, out of 100, that have correlations higher than the observed correlation] (Table 2.8). Thus, it appears that there is spatial correlation between features. However, if there is a distinction between features inside and outside the DUPAL belt, this distinction may manifest itself as spatial correlation when testing all of the features at once. Testing the features inside and outside the DUPAL belt separately results in correlations of 0.0685 and 0.2645 with significance levels of 0.95 and 0.51, respectively (Table 2.8). These results indicate that there is no significant spatial correlation between the features, but that there is a distinction between features inside and outside the DUPAL belt.

DISCRIMINANT ANALYSIS

Isotopic Nearest-Neighbor Discriminant Analysis

Methodology. Without taking account of spatial correlation, the validity of the division of the OIB data into samples inside and outside the DUPAL belt is addressed using isotopic nearest-neighbor as a discrimination rule. Using the isotopic distance measure outlined earlier, a given sample's isotopic nearest-neighbor is the sample that is the smallest isotopic distance away.

For the discriminant analysis, the assumption is made that the selected sample's location is unknown, so it is assigned the location of its isotopic nearest-neighbor. This assigned location is compared to the actual location; if they are different, it is a misclassification. A count is kept of the number of misclassifications to calculate an error rate.

Solow (1990) proposes a randomization technique for judging the estimated misclassification probability or error rate. The importance of the misclassification error rate is to test the null hypothesis that there is no difference between the samples inside and outside the DUPAL belt. This is a trivial matter if the sampling distribution of the error rate under the null hypothesis is known, but in this case it is not. A simple but effective way to judge the significance of the observed error rate is to construct a randomization distribution under the null hypothesis that the pairing of isotopic signatures and locations inside or outside the DUPAL belt occurs by chance. Applying the randomization technique to the data, the samples retain their isotopic signature, so their isotopic nearest-neighbor remains the same, but they are randomly assigned to locations inside and outside the belt. The discriminant analysis is done, as described above, with this new randomly constructed data set to get its misclassification error rate. Then the process is repeated to construct the distribution.

Application to the OIB data set. For the OIB data set, the observed misclassification rate is 7.3% and the randomization error rate ranges from 35.2% to 53.7%. Superficially, it appears that describing the data as two populations residing inside and outside the DUPAL belt is viable. However, the within-feature spatial correlation has not been accounted for in this analysis. If 76.7% of the time, a sample's isotopic nearest-neighbor is located within the same geographic feature, then it seems obvious that the misclassification error rate would be small. The observed error rate itself is not incorrect, but the randomization distribution of error rates against which it is being judged is incorrect. In order for the significance of the observed error rate to be properly judged, the spatial correlation must be preserved in the randomization process. In this case, preserving the spatial correlation is too complicated to pursue when other methods may provide the desired information.

Graphical Discrimination of Geographic Features

As shown earlier, the correlation between isotopic distance and the geographic distance within features is very strong. A way around this spatial correlation is to look for differences between populations inside and outside the DUPAL belt on the feature level. The averaged isotopic values for the features (Table 2.7) are scaled by the mean and standard deviation of the isotopes derived from the entire OIB+MORB data set (Table 1.2) and expressed in terms of principal components using the eigenvectors of the OIB+MORB correlation matrix (Table 2.1).

The first three principal components are plotted to look for differences in features inside and outside the DUPAL belt, with the general direction of the end-members indicated (Figs. 2.11-2.13). On all of the plots, but especially Z_3 versus Z_2, most of the features outside the belt cluster in a band between DMM and HIMU, with the exception of the Hawaiian islands [the Koolau volcanics on Oahu show a strong EMI signature (Hart, 1988)], Shimada Seamount [which also has an EMI signature (Hart, 1988)], and the Azores [São Miguel has a strong EMII signature (Hart, 1988)]. Essentially, the features outside the DUPAL belt, with few exceptions, occupy only part of the available isotopic space, while features inside the belt occupy all of the available isotopic space, including some overlap with features outside. This is essentially the relationship found by Hart

(1988), not that the two populations are totally separated, but that one population contains isotopic signatures that the other does not. It is important that this two population distinction is still valid on the feature level. Since it is still apparent at this larger scale [not just sample to sample] the geochemical signatures of the oceanic island basalts do have a long wavelength component to them, making it feasible to attempt to quantify these signatures using spherical harmonic expansions.

In addition to this graphical presentation, the discrimination analysis can also be done on the feature level, but the variances of the isotopes within each feature must be accounted for in some way.

SUMMARY

Mathematical and statistical methods to explore and characterize the OIB and MORB data reveal these main points:

- OIB+MORB data require only four mantle end-member components to completely span the range of known isotopic values.

- Choosing the mantle end-member components can be made easier [and more accurate] with the use of principal component analysis.

- Within geographic features, there is a significant correlation between location and isotopic signature, but between geographic features, there is not.

- Graphical discrimination of geographic features shows that the distinction between islands inside and outside the DUPAL belt is viable.

- The existence of the DUPAL anomaly on the feature level indicates that the anomaly has a long wavelength component to it.

Table 2.1. Covariance matrix[1] of the five isotopes with its eigenvectors and eigenvalues.

	Covariance Matrix				
Isotope	**Y_1**	**Y_2**	**Y_3**	**Y_4**	**Y_5**
Y_1	1.000000	-0.796442	-0.273004	-0.019107	0.061599
Y_2		1.000000	0.054987	-0.170370	-0.295078
Y_3			1.000000	0.901205	0.894577
Y_4				1.000000	0.901429
Y_5					1.000000

	Eigenvector Matrix				
Isotope	**I**	**II**	**III**	**IV**	**V**
Y_1	-0.017647	0.699432	0.682362	-0.174033	-0.120738
Y_2	-0.122196	-0.683457	0.679315	-0.179201	0.156120
Y_3	0.565079	-0.195210	0.019019	-0.235936	-0.765867
Y_4	0.574974	-0.006763	0.249290	0.753093	0.200145
Y_5	0.578661	0.074352	-0.102014	-0.561051	0.578307
Eigenvalues	2.830	1.861	0.183	0.091	0.035
Percentage of total variance accounted for by each eigenvector					
	56.6	37.2	3.7	1.8	0.7

[1]Only the upper half of the covariance matrix is shown since it is symmetric.

All eigenvector values are rounded to six decimal places from the fourteen decimal accuracy used in the calculations.

Covariance matrix is calculated using 477 OIB and 90 MORB samples.

Table 2.2. Comparison of eigenvalues and percentages of variance accounted for by the corresponding eigenvectors from this study and from Allègre *et al.* (1987)[1] for OIB+MORB and OIB data sets.

OIB+MORB	I	II	III	IV	V
[2]	2.830 [56.6%]	1.861 [37.2%]	0.183 [3.7%]	0.091 [1.8%]	0.035 [0.7%]
[3]Allègre *et al.*	3.20 [64.0%]	1.61 [32.2%]	0.15 [3.0%]	0.03 [0.6%]	0.01 [0.2%]
OIB	**I**	**II**	**III**	**IV**	**V**
[4]	3.047 [60.9%]	1.568 [31.4%]	0.249 [5.0%]	0.099 [2.0%]	0.037 [0.7%]
[5]Allègre *et al.*	2.85 [57.0%]	1.87 [37.4%]	0.22 [4.4%]	0.05 [1.0%]	0.01 [0.2%]

[1]Eigenvalues from Allègre *et al.* (1987) are converted to scaled eigenvalues that add up to 5 for comparison with eigenvalues from this study.

Percentages of variance accounted for by the corresponding eigenvectors are indicated in parentheses.

[2]Based on 567 samples.
[3]Based on 91 samples.
[4]Based on 477 samples.
[5]Based on 53 samples.

Table 2.3. "Nonlinear" end-member component values in principal component space and the transformed values in isotope space.

End-Members in Principal Component Space

	Z1	Z2	Z3
EMI	-2.0	3.6	-1.3
EMII	1.0	4.0	2.2
HIMU	5.0	-1.3	-0.25
DMM	-3.75	-2.9	0.4

End-Members in Isotope Space

	X1	X2	X3	X4	X5
EMI	0.705311	0.512343	17.322	15.431	38.232
EMII	0.707759	0.512638	18.788	15.673	39.287
HIMU	0.702659	0.512887	21.615	15.833	40.911
DMM	0.702171	0.513329	17.594	15.381	36.983

Table 2.4. "Linear" end-member component values, based upon linear mixing, in principal component space and the transformed values in isotope space.

End-Members in Principal Component Space

	Z1	Z2	Z3
EMI	-2.4	3.6	-1.6
EMII	1.8	4.5	2.6
HIMU	6.0	-1.9	-0.6
DMM	-4.3	-3.7	0.35

End-Members in Isotope Space

	X1	X2	X3	X4	X5
EMI	0.705126	0.512316	17.121	15.403	38.082
EMII	0.708329	0.512609	19.103	15.724	39.630
HIMU	0.702026	0.512896	22.203	15.879	41.337
DMM	0.701624	0.513428	17.459	15.351	36.704

Table 2.5. Samples excluded from linear mixing tetrahedral volume.[1]

Location	Sample Number	Row Number[2]
Azores, São Miguel	SM1D	32
	SM49	36
Galapagos	E35	173
Gough	10	175
Hawaii	69Tan2	200
Kerguelen Plateau	DR02/12	279
	DR08	282
	747c-12r-4-45-46	292
	747c-16r-2-81-84	294
Marquesas	uap11	329
Pitcairn, Pulwana	642	370
St. Helena	37	469
	237	482
Atlantic Ocean	AD3-3	535
SW Indian Ridge	D1	536
	D5	539

[1]OIB samples excluded from the volume will not be used in spherical harmonic expansions.

[2]Indicates row number of the data set included in Appendix A.

Table 2.6. Average absolute errors in transforming three-dimensional principal component data into five-dimensional isotope data, with their ratio to isotope standard deviations and comparison to analytical errors.

	X1	X2	X3	X4	X5
Average absolute error [for 567 samples]					
	0.000041	0.000008	0.111	0.016	0.111
Ratio of average absolute error to standard deviation[1]					
	0.043802	0.047124	0.128	0.170	0.149

	Absolute Error Percentage Range[2]	Analytical Error Range
X1	0.00580 to 0.00584%	0.003 to 0.01%
X2	0.001558 to 0.001561%	0.003 to 0.01%
X3	0.225 to 0.330%/amu	0.03 to 0.05%/amu
X4	0.0337 to 0.0347%/amu	0.03 to 0.05%/amu
X5	0.068 to 0.075%/amu	0.03 to 0.05%/amu

[1]Isotopic standard deviations for the OIB+MORB data set are indicated in Table 1.2.

[2]Absolute error percentage ranges are calculated using the average absolute errors and the ranges of the isotopes in the OIB+MORB data set:

X1	0.702290 to 0.707400
X2	0.512376 to 0.513290
X3	16.943 to 21.755
X4	15.406 to 15.862
X5	37.235 to 40.619

Table 2.7. Average isotopic signatures and locations of the geographic features [island groups, islands, ridges, seamounts] represented in the OIB data set with the number of samples [in braces].

Feature	Sr	Nd	6/4Pb	7/4Pb	8/4Pb	Lat	Long
Ascension [5]	0.702830	0.513036	19.421	15.612	38.916	-7.95	-14.37
Amsterdam/St. Paul [11]	0.703733	0.512879	18.879	15.585	39.131	-38.33	77.59
Azores [6]	0.704572	0.512806	19.707	15.703	39.810	38.50	-28.00
Balleny [3]	0.702938	0.512967	19.752	15.600	39.359	-67.53	-168.88
Cameroon Line [18]	0.703143	0.512901	20.020	15.672	39.758	1.03	6.10
Cape Verde Islands [41]	0.703414	0.512839	19.254	15.580	39.026	15.80	-24.24
Christmas [13]	0.704403	0.512690	18.639	15.605	38.742	-10.50	105.67
Cocos [3]	0.703030	0.512991	19.234	15.589	38.973	5.54	-87.08
Comores Archipelago [14]	0.703415	0.512817	19.615	15.609	39.479	-12.09	43.76
Cook-Austral Islands [26]	0.704124	0.512774	19.565	15.623	39.412	-20.37	-158.56
Crozet Islands [9]	0.703997	0.512849	18.929	15.587	39.037	-46.45	52.00

Table 2.7. Continued.

Feature	Sr	Nd	6/4Pb	7/4Pb	8/4Pb	Lat	Long
Fernando de Noronha [16]	0.704111	0.512809	19.409	15.634	39.331	-3.83	-32.42
Galapagos Islands [11]	0.703118	0.512988	19.076	15.564	38.692	-0.39	-90.70
Gough [2]	0.705095	0.512538	18.445	15.624	38.990	-40.33	-10.00
Hawaiian Islands [73]	0.703760	0.512934	18.188	15.462	37.899	19.76	-156.09
Iceland [7]	0.703106	0.513037	18.453	15.484	38.106	64.75	-17.65
Juan Fernandez Islands [4]	0.703659	0.512842	19.121	15.604	38.961	-33.62	-78.83
Kerguelen Plateau [41]	0.705061	0.512660	18.259	15.555	38.646	-52.92	73.15
Louisville Seamount Chain [4]	0.703576	0.512916	19.271	15.610	38.991	-45.22	-154.40
Marion/Prince Edward [4]	0.703298	0.512930	18.562	15.540	38.367	-46.92	37.75
Marquesas Archipelago [11]	0.704239	0.512805	19.362	15.604	39.258	-9.09	-139.84
Mascareignes [8]	0.704143	0.512853	18.855	15.580	38.919	-20.75	56.50

Table 2.7. Continued.

Feature	Sr	Nd	6/4Pb	7/4Pb	8/4Pb	Lat	Long
New England Seamounts [6]	0.703373	0.512850	20.155	15.629	39.907	37.86	-61.61
Nunivak [2]	0.702900	0.513110	18.588	15.471	38.088	60.00	-166.00
Pitcairn [19]	0.703994	0.512714	18.132	15.490	38.879	-20.07	-130.10
Ponape [1]	0.703287	0.512973	18.462	15.489	38.289	6.93	158.32
Sala Y Gomez [1]	0.703220	0.512898	19.865	15.640	39.670	-26.47	-105.47
Samoa Islands [34]	0.705535	0.512753	18.914	15.607	39.071	-14.08	-171.10
San Felix/San Ambrosio [5]	0.704089	0.512610	19.079	15.581	39.029	-26.42	-79.98
Shimada Seamount [1]	0.704843	0.512640	19.046	15.681	39.354	16.87	-117.47
Society Ridge [9]	0.704811	0.512795	19.128	15.592	38.915	-17.57	-149.14
St. Helena [31]	0.702874	0.512908	20.682	15.764	39.983	-15.97	-5.72
Trinidade[1]	0.703803	0.512708	19.116	15.601	39.110	-20.50	-29.42

Table 2.7. *Continued.*

Feature	Sr	Nd	6/4Pb	7/4Pb	8/4Pb	Lat	Long
Tristan de Cunha [5]	0.705004	0.512545	18.476	15.518	38.867	-37.10	-12.28
Tubuai-Austral Islands [22]	0.703110	0.512882	20.533	15.733	39.876	-23.84	-148.26
Walvis Ridge [10]	0.704696	0.512542	17.885	15.492	38.430	-30.28	-7.05

Table 2.8. Correlations between geographic and isotopic distance matrices and island/feature isotopic nearest-neighbor occurrence rates for all samples in the OIB data set and samples inside and outside the DUPAL belt. Correlations for all the geographic features and those inside and outside the DUPAL belt are also given.

	Correlation	Randomization Range[1]
OIB	0.1756	-0.0077 to 0.0224
Inside DUPAL	0.0641	-0.0035 to 0.0343
Outside DUPAL	0.6142	-0.0045 to 0.0699

	Island Occurrence Rate	Randomization Range[1]
OIB	61.4%	1.0% to 3.6%
Inside DUPAL	63.6%	1.6% to 6.2%
Outside DUPAL	47.1%	1.7% to 11.0%

	Feature Occurrence Rate	Randomization Range[1]
OIB	76.7%	3.4% to 10.0%
Inside DUPAL	71.5%	4.2% to 11.1%
Outside DUPAL	75.6%	19.2% to 35.5%

	Correlation	Randomization Range[1]	Significance Level
Features	0.1584	0.0369 to 0.2075	0.13
Inside DUPAL	0.0685	0.0350 to 0.2807	0.95
Outside DUPAL	0.2645	0.0649 to 0.6602	0.51

[1]Randomization ranges based upon 100 random permutations.

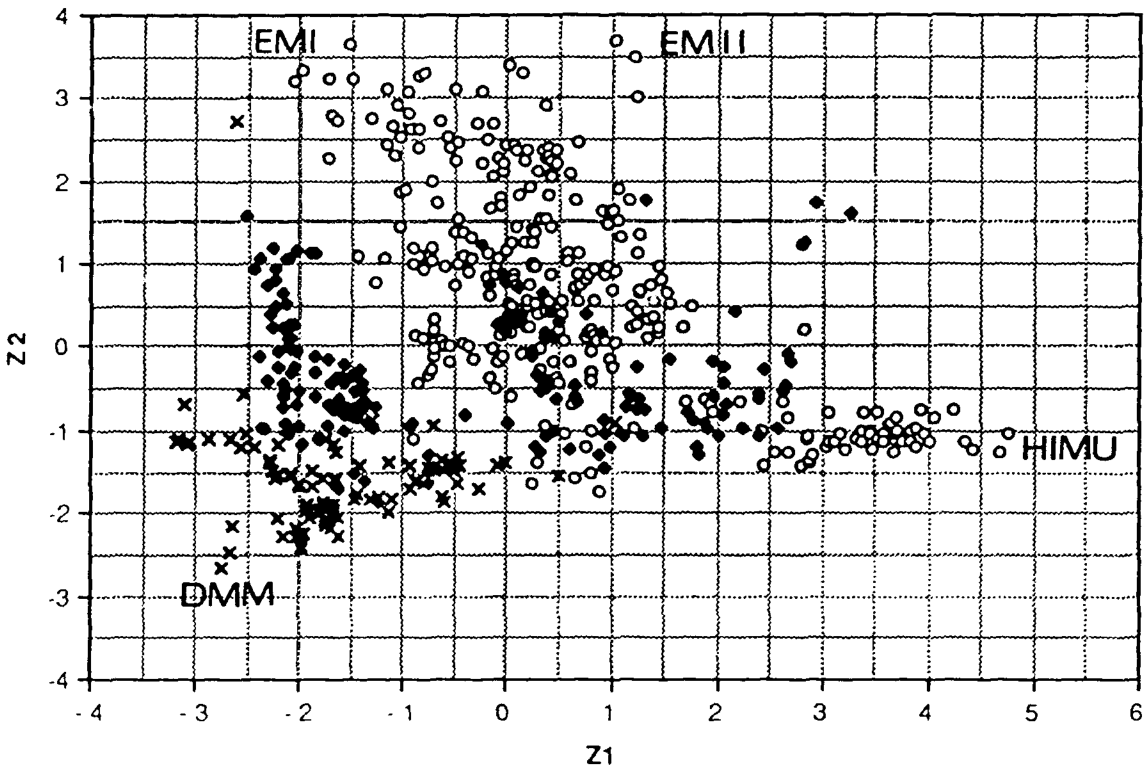

Fig. 2.1. Plot of the second principal component versus the first principal component for the OIB+MORB data set. Symbols: x = MORB data, open circle = OIB samples inside the DUPAL belt, black diamond = samples outside the DUPAL belt. General mantle end-member component regions are indicated.

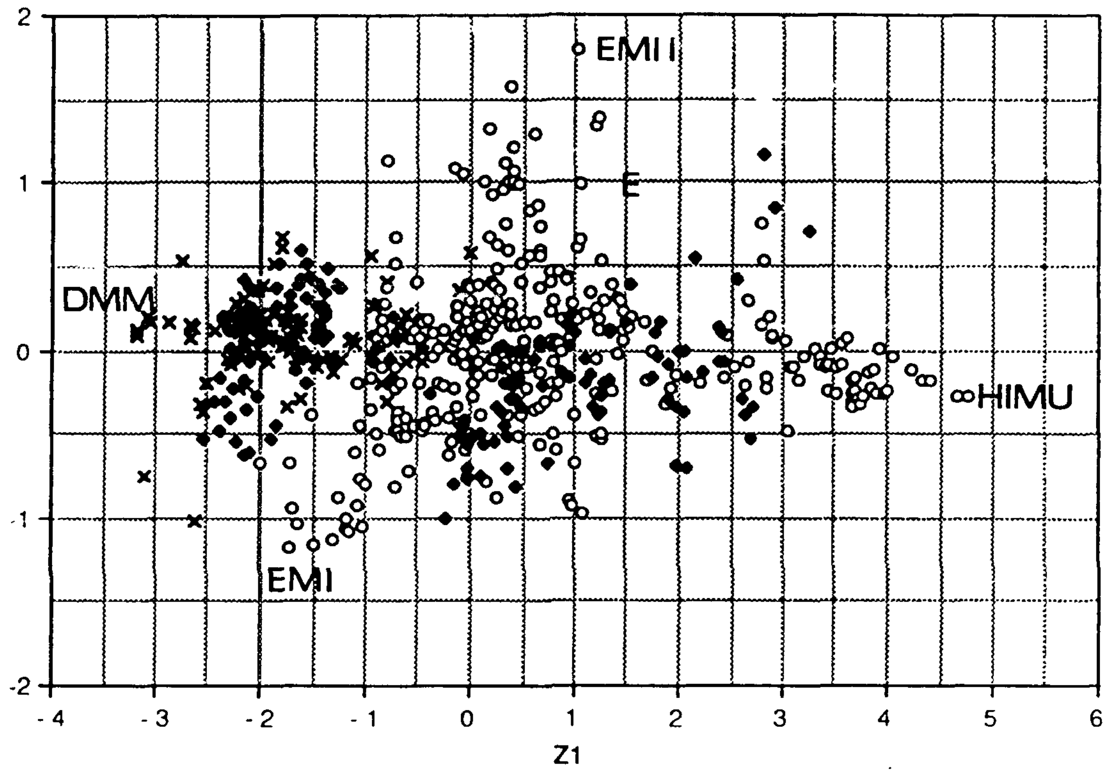

Fig. 2.2. Plot of the third principal component versus the first principal component for the OIB+MORB data set. Symbols: x = MORB data, open circle = OIB samples inside the DUPAL belt, black diamond = samples outside the DUPAL belt. General mantle end-member component regions are indicated.

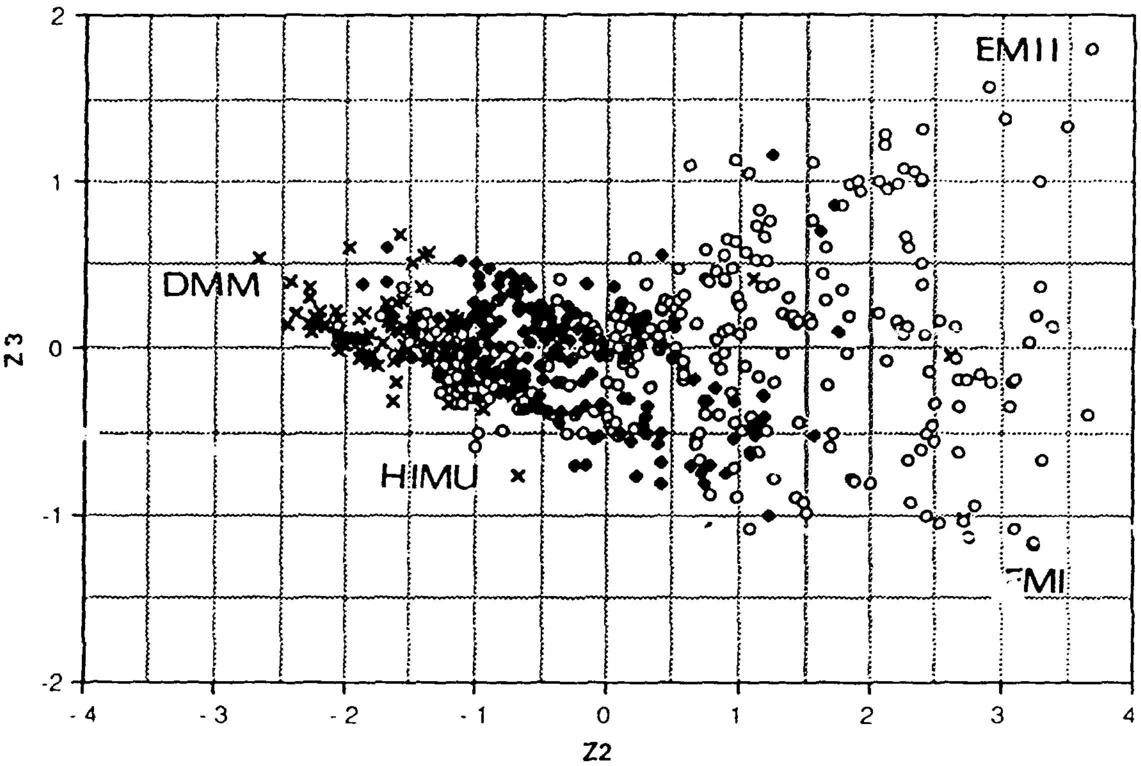

Fig. 2.3. Plot of the third principal component versus the second principal component for the OIB+MORB data set. Symbols: x = MORB data, open circle = OIB samples inside the DUPAL belt, black diamond = samples outside the DUPAL belt. General mantle end-member component regions are indicated.

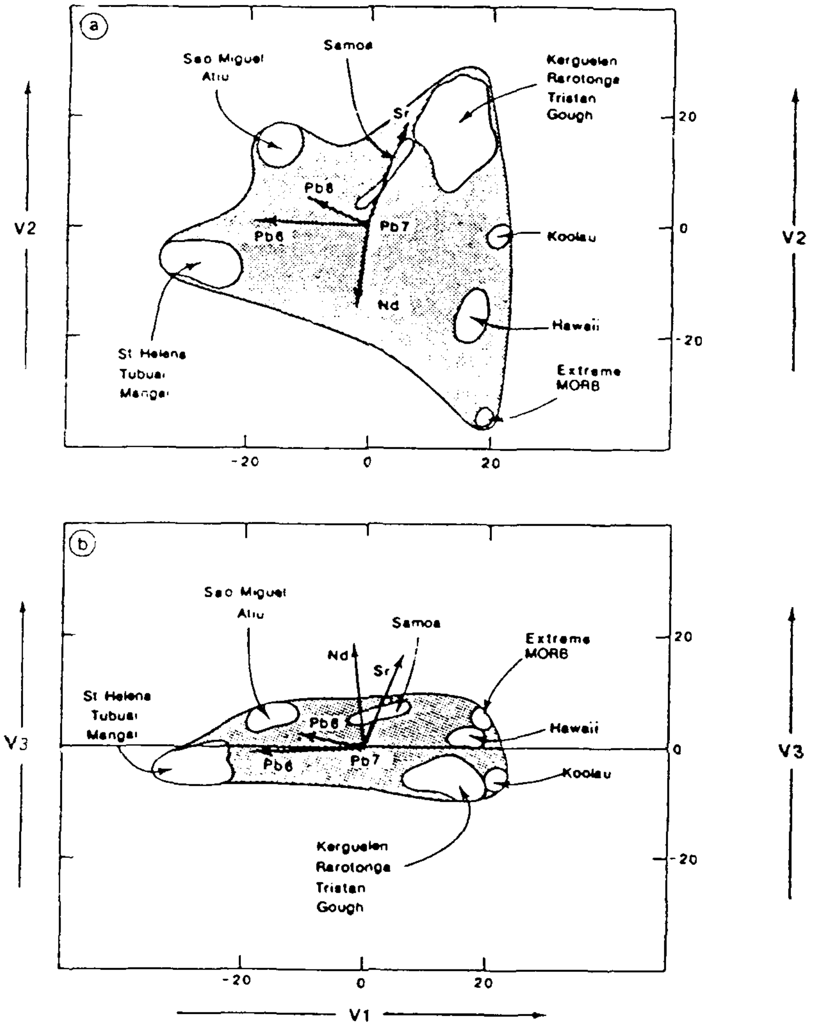

Fig. 2.4. Plots of the second principal [V2] component versus the first [V1] and the third principal component [V3] versus the first [V1] for a smaller OIB+MORB data set from an analysis done by Allègre *et al.* (1987). These plots are the mirror images of the ones done for this analysis because the chosen eigenvectors for the two analyses are of opposite sign.

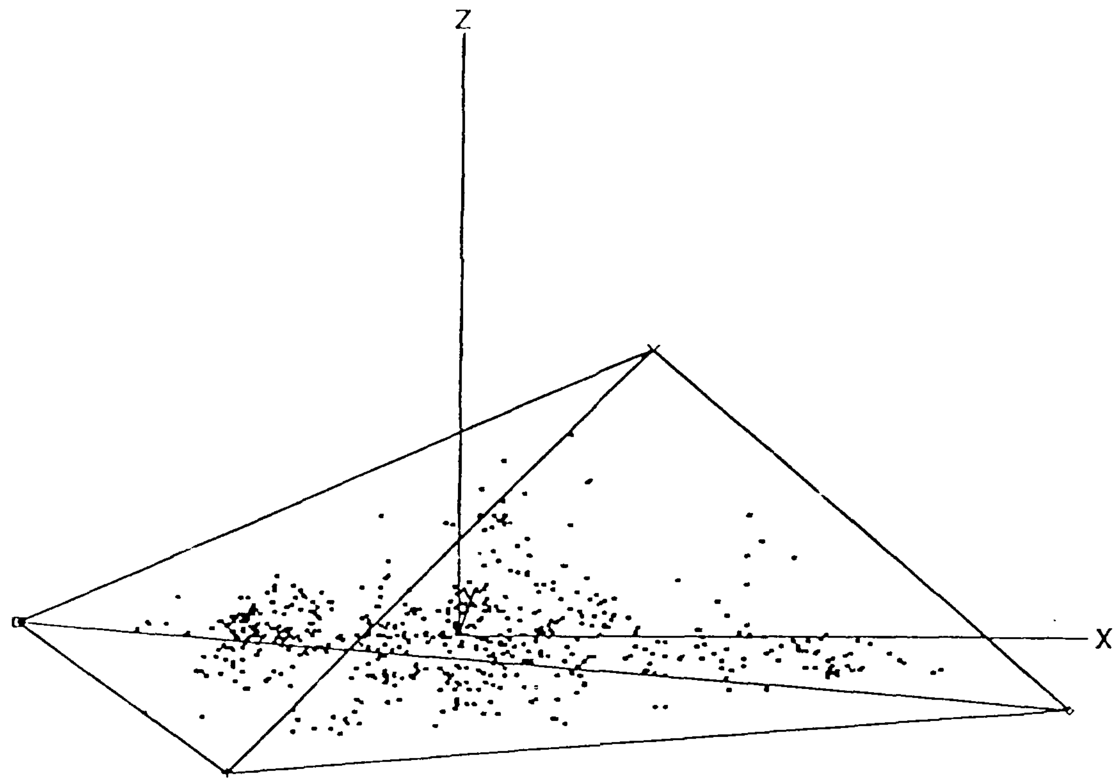

Fig. 2.5. Three-dimensional view of the OIB+MORB principal component data. Axes: X = Z1, Y = Z2, Z = Z3. Symbols for the end-member components: + = EMI, x = EMII, diamond = HIMU, square = DMM.

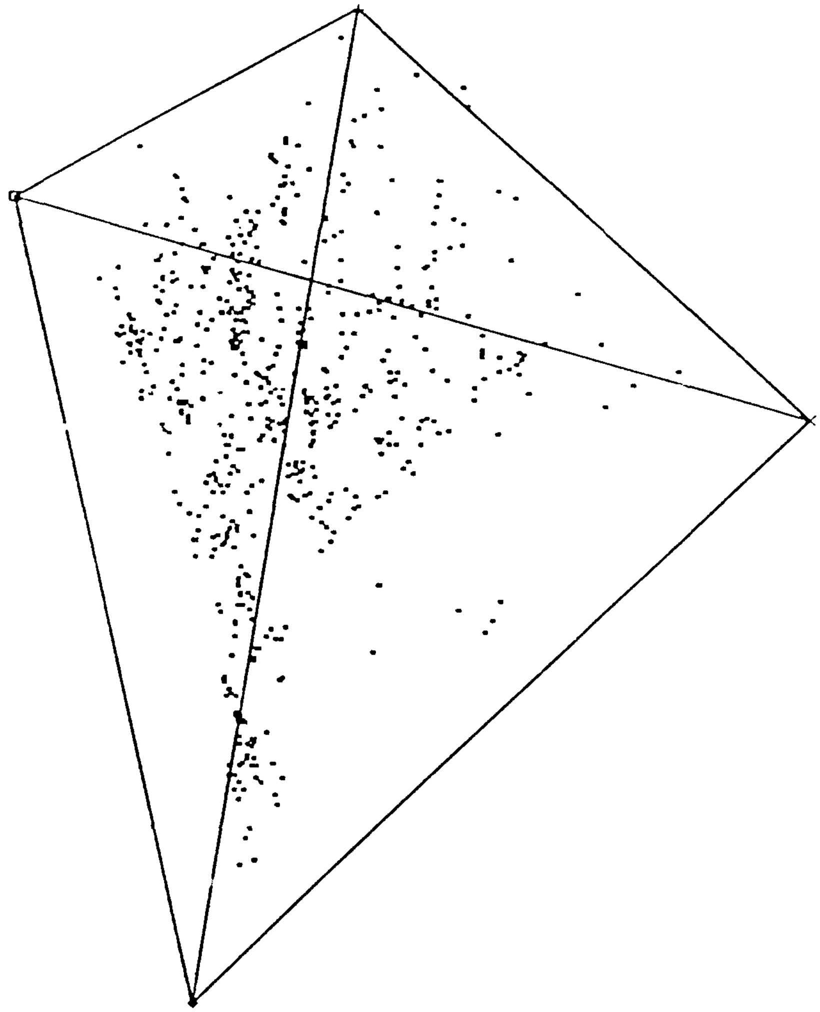

Fig. 2.6. Three-dimensional view of the OIB+MORB principal component data parallel to the EMI-EMII-HIMU plane. Symbols for the end-member components: + = EMI, x = EMII, diamond = HIMU, square = DMM.

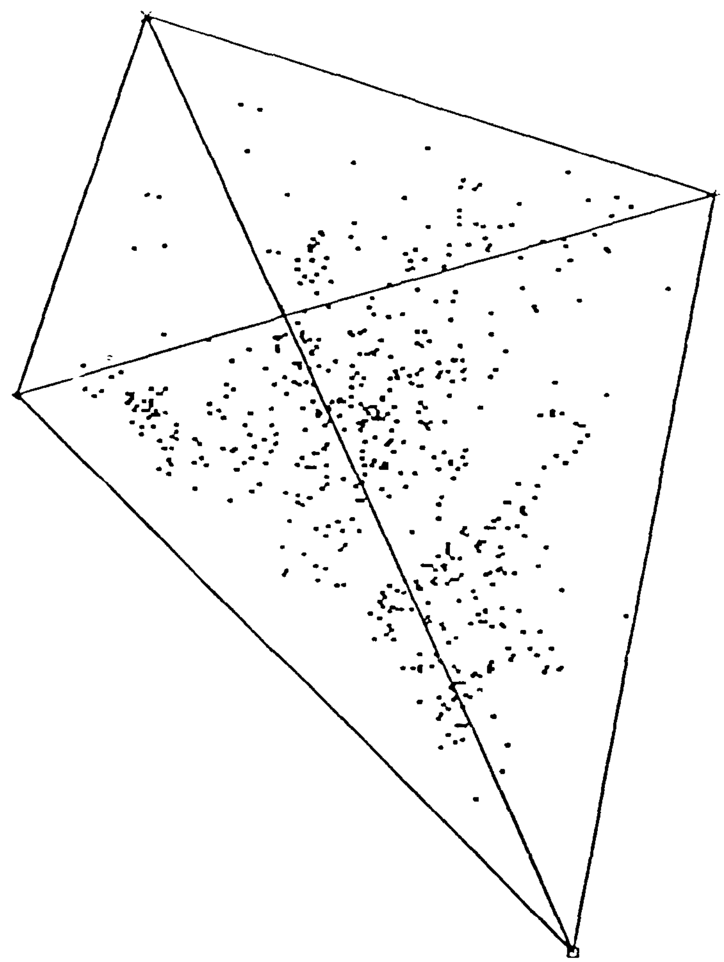

Fig. 2.7. Three-dimensional view of the OIB+MORB principal component data parallel to the EMI-EMII-DMM plane. Symbols for the end-member components: + = EMI, x = EMII, diamond = HIMU, square = DMM.

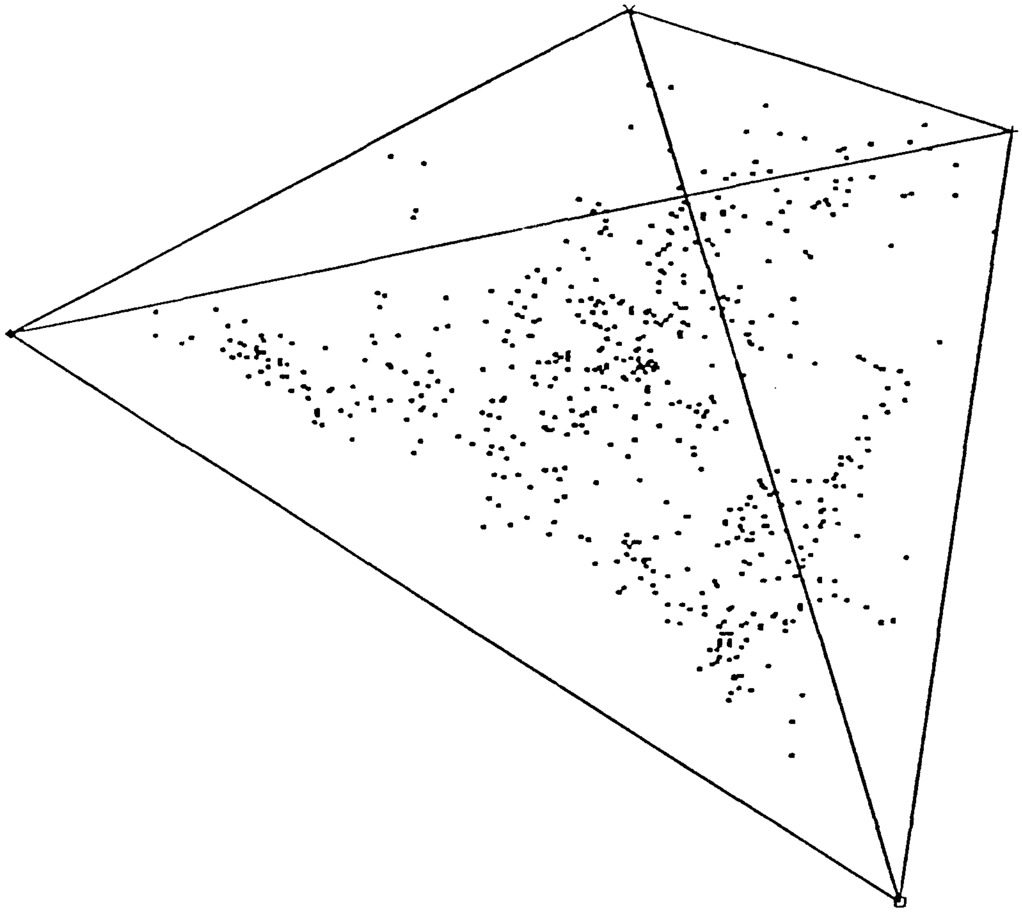

Fig. 2.8. Three-dimensional view of the OIB+MORB principal component data parallel to the EMI-HIMU-DMM plane. Symbols for the end-member components: + = EMI, x = EMII, diamond = HIMU, square = DMM.

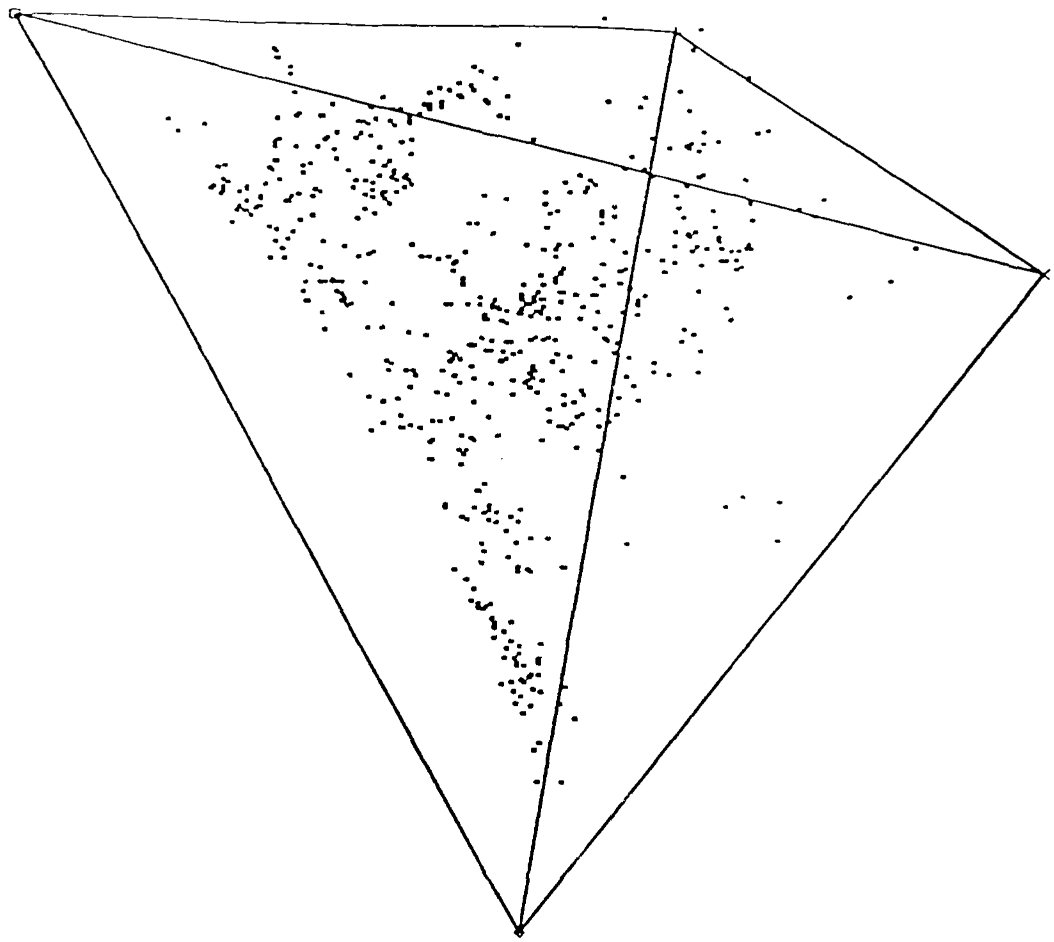

Fig. 2.9. Three-dimensional view of the OIB+MORB principal component data parallel to the EMII-HIMU-DMM plane. Symbols for the end-member components: + = EMI, x = EMII, diamond = HIMU, square = DMM.

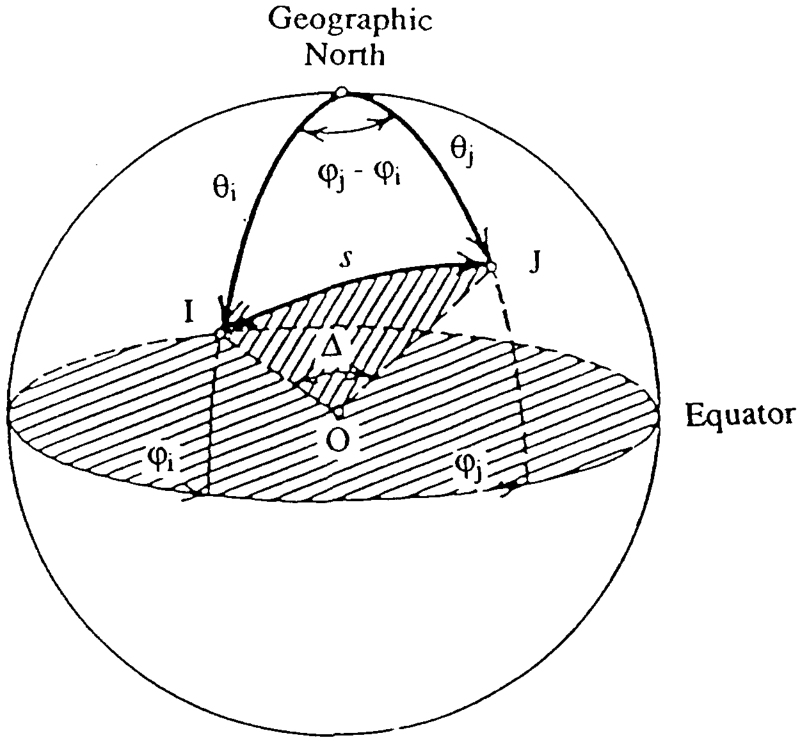

Fig. 2.10. Geometry for determining the surface distance s between locations I and J on the globe, where θ and φ are colatitude and longitude and Δ is the angle between the two locations taken from the center of the Earth. From Turcotte and Schubert (1982).

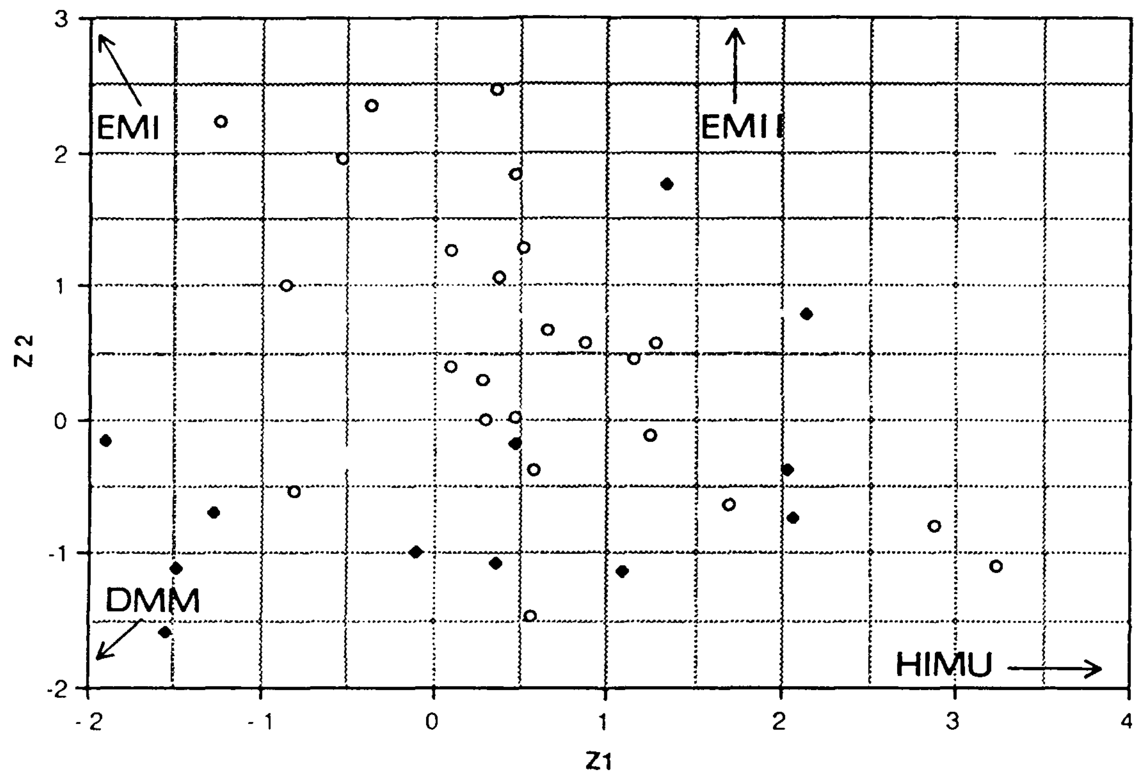

Fig. 2.11. Plot of the second principal component versus the first principal component for the 36 geographic features. Symbols: open circle = features inside the DUPAL belt, black diamond = features outside the DUPAL belt. Labeled points: 1 = Hawaiian Islands, 2 = Shimada Seamount, 3 = Azores. The general directions of the mantle end-member component regions are indicated.

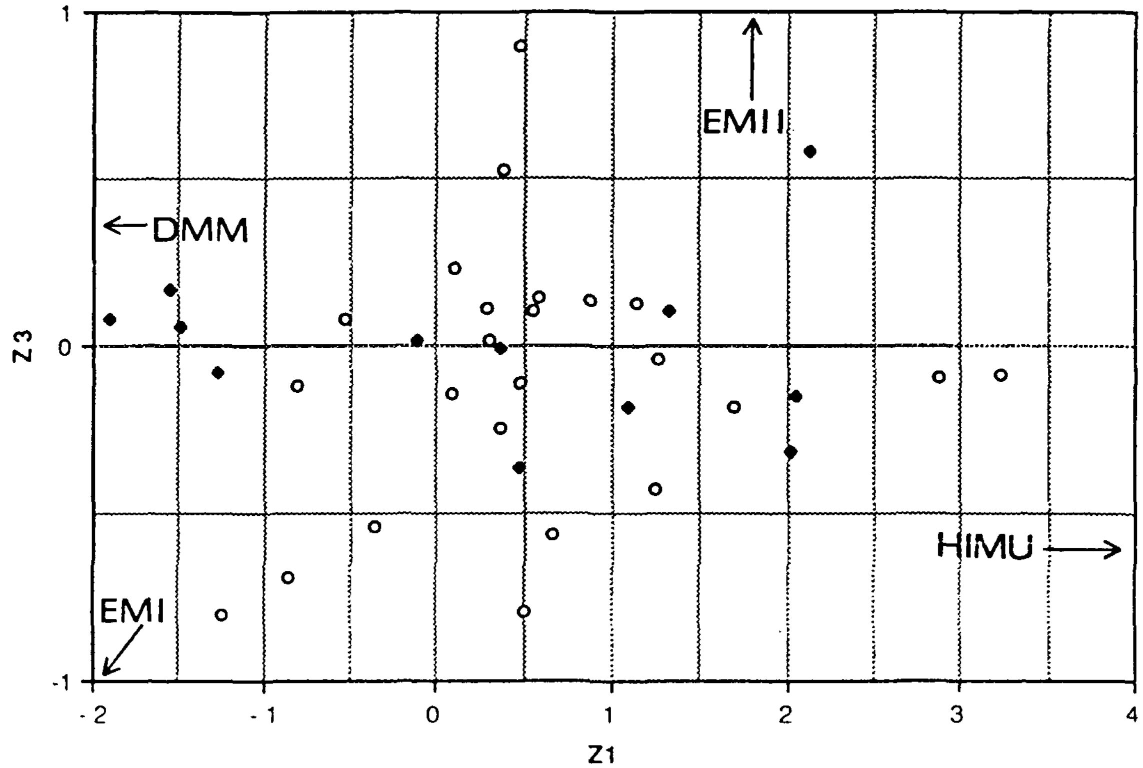

Fig. 2.12. Plot of the third principal component versus the first principal component for the 36 geographic features. Symbols: open circle = features inside the DUPAL belt, black diamond = features outside the DUPAL belt. Labeled points: 1 = Hawaiian Islands, 2 = Shimada Seamount, 3 = Azores. The general directions of the mantle end-member component regions are indicated.

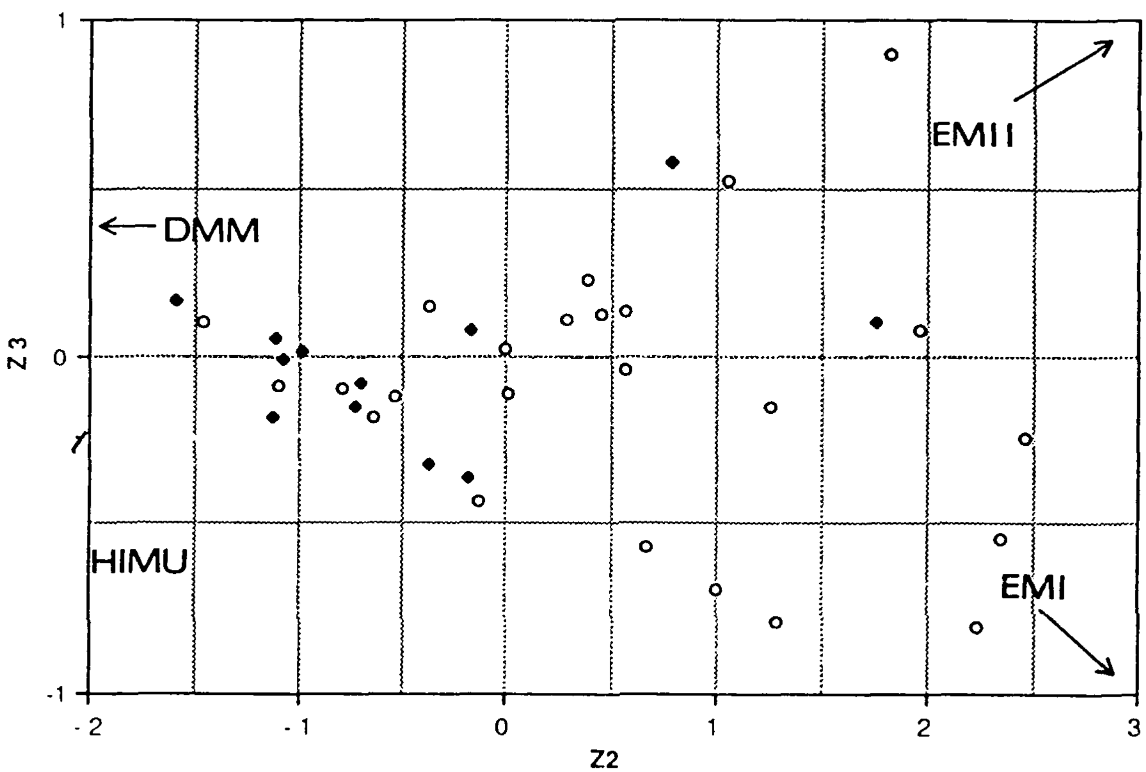

Fig. 2.13. Plot of the third principal component versus the second principal component for the 36 geographic features. Symbols: open circle = features inside the DUPAL belt, black diamond = features outside the DUPAL belt. Labeled points: 1 = Hawaiian Islands, 2 = Shimada Seamount, 3 = Azores. The general directions of the mantle end-member component regions are indicated.

CHAPTER 3

SPHERICAL HARMONIC REPRESENTATION OF ISOTOPIC SIGNATURES: THE CONTINUOUS LAYER MODEL

INTRODUCTION

Hart (1984) contoured world maps of OIB isotope data for his three DUPAL anomaly criteria [$\Delta Sr > 40$; $\Delta 7/4 > 3$; $\Delta 8/4 > 40$]. These maps show a concentrated band spanning approximately 60° of latitude, centered on 30°-40°S, with pronounced highs for the anomaly criteria in a region from the South Atlantic to the Indian Ocean [ΔSr, $\Delta 7/4$, $\Delta 8/4$] and in the central Pacific [ΔSr, $\Delta 8/4$]. Qualitatively, Hart (1984, 1988) believes this geochemical anomaly correlates with other geophysical anomalies: the slab-corrected geoid (Hager, 1984), deep mantle P-wave tomography maps (Dziewonski, 1984), slow P-wave regions at the core/mantle boundary (Creager and Jordan, 1986) and equatorial anomalies in the core (Le Mouël *et al.*, 1985). These geophysical anomaly patterns are typically expanded in terms of spherical harmonics, therefore any attempt to make a quantitative comparison between geochemical and geophysical patterns requires expanding the geochemistry data in spherical harmonics as well.

Expansion of the geochemistry data is approached in two ways, based upon an assumed geometry for the OIB geochemical reservoir. The first approach, the "continuous layer model" discussed in this chapter, assumes that the OIB reservoir is a continuous layer [not ruling out heterogeneities within this layer] and tries to reconstruct this layer. Plumes from this layer only sample the continuous geochemical "function" in discrete locations. With the geochemistry "function" unknown, the spherical harmonic coefficients must be solved for using least squares, singular value decomposition or a similar method that will approximate the values of the geochemistry "function" where there is no data.

The second approach, the "delta-function model" discussed in Chapter 4, assumes that the OIB reservoir is composed of a series of point sources, each feeding a separate plume. In this case, the geochemistry "function" is known and can be represented as a series of delta-functions. The spherical harmonic coefficients can be solved for directly with the simplification from integration to summation allowed by the delta-function approximation.

The continuous layer model and the delta-function model are not meant to suggest two end-member possibilities for OIB source geometry. Rather, the delta-function model can be regarded as an approximation of the continuous layer model that gives a mathematically robust solution for the spherical harmonic coefficients. In regard to the oceanic crust model of Hofmann and White (1982), the continuous layer model corresponds to the accumulated layer of subducted oceanic crust, with the plume-forming instabilities occurring at discrete locations within this layer. The delta-function model can also be reconciled with the accumulated layer model, with the stipulation that discrete pockets [point sources] within this layer form and feed individual instabilities.

For the purposes of minimizing small scale variations [ie. variations within a single island or island chain] in the geochemistry "function" that cannot be accurately represented with the incomplete global data coverage, this spherical harmonic study is based on the averaged isotopic signatures of the 36 geographic features (Table 2.6). These average isotopic values are converted to mantle-end member component percentages (Table 3.1), as outlined in Chapter 2, to form the data matrices used in the expansions.

SPHERICAL HARMONIC BASICS

Spherical harmonics, $Y_l^m(\theta,\varphi)$, are a set of orthonormal functions over the unit sphere:

$$Y_l^m(\theta,\varphi) = \sqrt{\frac{(2l+1)(l-m)!}{4\pi(l+m)!}}\ P_l^m(\cos\theta)\, e^{im\varphi}$$

where l is the degree of the expansion, m is the order of the expansion, θ is colatitude [$\theta = \pi/2$ - latitude; $0 \le \theta \le \pi$] and φ is longitude [$-\pi \le \varphi \le \pi$]. The functions $e^{im\varphi}$ form a complete set of orthogonal functions in the index m on the interval $-\pi \le \varphi \le \pi$ and the associated Legendre polynomials $P_l^m(\cos\theta)$ form a similar set in the index l for each m value on the interval $-1 \le \cos\theta \le 1$ (Jackson, 1975). Therefore their product forms a complete orthogonal set on the surface of the unit sphere in the two indices l,m. The spherical harmonic functions used in this analysis are normalized by the square root term so that their integrated square over the sphere is unity [in most geophysics applications, the functions are normalized so that the integrated square over the sphere is 4π]:

$$\int_0^{2\pi} d\varphi \int_{-1}^{1} d(\cos\theta) Y_{l'}^{m'}(\theta,\varphi)^* \, Y_l^m(\theta,\varphi) = \delta_{l'l}\delta_{m'm}$$

where the asterisk denotes complex conjugation.

Any function $f(\theta,\varphi)$ can be expanded in spherical harmonics:

$$f(\theta,\varphi) = \sum_{l=0}^{L} \sum_{m=-l}^{l} C_l^m Y_l^m(\theta,\varphi)$$

where L is the maximum degree of the expansion and C_l^m are complex spherical harmonic coefficients. Written in a more explicit form, the equation becomes:

$$f(\theta,\varphi) = \sum_{l=0}^{L} \sum_{m=0}^{l} \sqrt{\frac{(2l+1)(l-m)!}{4\pi(l+m)!}}\ P_l^m(\cos\theta)\left[A_l^m \cos m\varphi + B_l^m \sin m\varphi\right]$$

where A_l^m and B_l^m are real spherical harmonic coefficients. When expanding a function from degrees 0 to L, the number of coefficients that need to be calculated is: $\sum_{l=0}^{L} 2l+1$ There are actually an additional $[L+1]$ coefficients involved, but for $m = 0$, $\sin m\varphi = 0$, so $B_l^0 = 0$. It is important to realize that only having 36 features limits the possible spherical harmonic expansion to degree 5, in order to avoid a purely underdetermined problem.

MANTLE END-MEMBER COMPONENTS

When attempting to use inverse methods to solve for the harmonic coefficients of an unknown function, careful attention must be paid to the variation of the data as a function of distance to avoid the problem of aliasing. For a simple two-dimensional case, aliasing occurs if the sampling interval is longer than half the shortest wavelength of the function sampled, causing the sampled points to show a periodicity that does not exist in the original data. The minimum distance between any two geographic features in the OIB feature data set is 33.396 km, but the distance between features is not constant. Plots of data variation versus distance between data locations make it possible to select a mininum sampling distance based on the shortest distance required to get the maximum data variation. This minimum sampling distance then controls the minimum degree to which the data must be expanded in order to adequately represent the data in spherical harmonics without aliasing. The relationship between wavelength and degree is:

$$\lambda = \frac{2\pi R}{\sqrt{l(l+1)}}$$

where λ is the wavelength [λ = 2*(sampling distance)], R is the radius of the earth [R = 6378.139 km] and l is degree. Solving for degree in terms of wavelength:

$$l = \frac{-1 + \sqrt{1 + 4\left(\frac{2\pi R}{\lambda}\right)^2}}{2}$$

Variation-Distance Relationships

For variation-distance relationships, the distance measure is the angle Δ_{ij} [in degrees] from the center of the earth between any two locations I and J [see Chapter 2] and the variation measure is the absolute value of the difference between the mantle component percentages at those locations. The angle Δ_{ij} can be transformed into a great circle distance in km by converting Δ_{ij} to radians and multiplying by the radius of the earth R.

Plots of absolute difference versus angle for the four mantle components (Figs. 3.1-3.4) show the maximum variation in the components occurring on very short distance scales for the EMI and HIMU components and moderate distance scales for the EMII and DMM components. Based upon these plots, the minimum sampling distances [in degrees] are ~ 14.5° for EMI and HIMU, ~ 39° for EMII and ~ 57° for DMM. These correspond to expansions out to degrees 12, 4 and 3, respectively. For the current problem, the EMII and DMM data sets can be expanded in spherical harmonics as they are, but the EMI and HIMU data sets require some additional manipulation.

Variation Reduction by Categorizing Features

Separation of the geographic features into populations located inside and outside the DUPAL belt [2°S to 60°S] does not result in two distinct isotopic populations [Chapter 2]. Essentially, one population [outside the belt] defines a small field in isotopic space, while the other population [inside the belt] defines a larger field that overlaps with the smaller field (Fig. 3.5). A possible source of the large, small-scale isotopic variation exhibited by the EMI and HIMU data sets is the juxtaposition, due to the overlap in isotope space, of features having a strong DUPAL signature next to those that do not. If it is possible to separate DUPAL-type features [those features showing a strong DUPAL signature] from DMM-type features, this separation might reduce the small-scale variation within these two populations and thus reduce the degree to which the population data must be expanded.

Since the goal is to separate DUPAL-type features from DMM-type features, a logical starting place is to look at the spatial distribution of different percentage categories of the DMM component in three-dimensional principal component space (Fig. 3.6). Six DMM percentage categories [<10%, 10-20%, 20-30%, 30-40%, 40-50%, >50%] can be distinguished as six separate point groupings. Most striking is a large spatial separation that occurs within the 30-40% category for a small percentage difference [Louisville - 31.84%, Balleny - 32.17%, Cocos - 38.53%]. This is a reasonable place to separate the DUPAL-type features from the DMM-type features, with a boundary value of 32% DMM, for simplicity. The resulting 27 DUPAL-type features and 9 DMM-type features, with their percentage of the DMM component are listed in Table 3.2.

There are too few DMM-type features to draw any conclusions from plots of absolute difference versus angle. For the DUPAL-type features, plots of absolute difference versus angle of the DUPAL components [EMI, EMII and HIMU] show no reduction in the small-scale variation, while that of DMM does, with an increase in sampling distance from ~ 57° to 89° (Figs. 3.7-3.10). In retrospect, this is an obvious result of the artificial separation performed. The percentage categories are basically parallel slices through the tetrahedron that move from a broad base of lower percentages to a peak of high percentages approaching an end-member component apex on the tetrahedron [like a ternary diagram]. It is true that these slices can separate DMM-type features from DUPAL-type features, but only the variation of the DMM percentages are reduced. To reduce the variation of the individual DUPAL components using this method, EMI-type features would have to be distinguished from non-EMI-type features, etc. This would generate four different, though overlapping, sets of features to use to characterize the four different components. Manipulation of the data set in this way is not desirable, so another method must be pursued in the attempt to reduce small-scale data variation.

Variation Reduction by Filtering

Another method to reduce small-scale variation [and hopefully enhance any long wavelength component] is to filter the data set in some way. Here, a simple circular filter, of fixed radius, is applied to each feature location. The new data values assigned to that feature location are the means of the mantle component percentages of the feature locations that fall within the circle. To ensure that there are always at least two features falling within the circle, the radius of this circle is determined by the longest distance to the nearest feature location. Nunivak Island is the most isolated feature with the nearest feature being the Hawaiian Islands at an angular distance [from the center of the earth] of 40.86°. The circle radius is then 40.9°, for simplicity.

Plots of absolute difference versus angle for the filtered data set yield interesting results (Figs. 3.11-3.14). All of the mantle component data sets show a reduction in small-scale variation, except EMII, which shows an increase in variation, with a decrease in angular sampling distance from ~ 39° to 27° [expansions to degrees 4 and 7, respectively]. The remaining plots show an increase in angular sampling distance from ~ 14.5° to 37° [expansions to degrees 12 and 5, respectively] for EMI, an increase from ~ 57° to 102° [expansions to degrees 3 and 2, respectively] for DMM and a dramatic increase from ~ 14.5° to 83° [expansions to degrees 12 and 2, respectively] for HIMU. Now that the small-scale variation has been significantly reduced by filtering, the filtered EMI and HIMU data sets can also be expanded in spherical harmonics.

INSIGHTS FROM GEOPHYSICAL DATA

It is unclear how accurate the spherical harmonic expansions of the OIB feature data set will be due to the limited global coverage and the highly variable nature of the data. In an attempt to address these problems, three geophysical data sets, with different variance characteristics, are constructed with the same limited coverage to provide a sort of control set against which qualitative comparisons can be made. Geoid, gravity and gravity gradient anomalies are the chosen geophysical measures because their coefficients are well known and they form a kind of continuum from the long wavelength [low degree] dominance in the geoid signature to the short wavelength [high degree] dominance in the gravity gradient signature (Fig. 3.15). Techniques applied to the mantle component data, to solve for the spherical harmonic coefficients, are also applied these constructed data sets to see how closely the actual geophysical fficients can be approximated.

truction of Geophysical Data Sets

The gravitational potential V, in spherical harmonics as a function of listance r, is given by:

$$V = -\frac{GM}{R}\left\{\frac{R}{r} + \sum_{l=2}^{\infty}\left(\frac{R}{r}\right)^{l+1}\sum_{m=0}^{l}\sqrt{\frac{(2l+1)(l-m)!}{4\pi(l+m)!}}\ P_l^m(\cos\theta)\left[A_l^m\cos m\varphi + B_l^m\sin m\varphi\right]\right\}$$

where G is the gravitational constant [$G = 6.6726\times10^{-11}$ m^3/kg•s^2], M is the mass of the earth [$M = 5.973\times10^{24}$ kg] and R is the radius of the earth in meters (Stacey, 1977). The gravitational potential anomaly [$\delta V = V_{\text{observed}} - V_{\text{theoretical}}$] is:

$$\delta V = -\frac{GM}{R}\left\{\sum_{l=2}^{\infty}\left(\frac{R}{r}\right)^{l+1}\sum_{m=0}^{l}\sqrt{\frac{(2l+1)(l-m)!}{4\pi(l+m)!}}\ P_l^m(\cos\theta)\left[A_l^m\cos m\varphi + B_l^m\sin m\varphi\right]\right\}$$

which can be converted to the geoid anomaly δN (in m) by dividing by $g = -GM/R^2$:

$$\delta N = \frac{\delta V}{g} = R\left\{\sum_{l=2}^{\infty}\left(\frac{R}{r}\right)^{l+1}\sum_{m=0}^{l}\sqrt{\frac{(2l+1)(l-m)!}{4\pi(l+m)!}}\ P_l^m(\cos\theta)\left[A_l^m\cos m\varphi + B_l^m\sin m\varphi\right]\right\}$$

The geoid anomalies calculated here are referenced to a theoretical hydrostatic sphere to remove the effect of the earth's rotation (Hager, 1984). Gravity is the derivative of the gravitational potential with respect to radial distance, so the radial gravity anomaly is:

$$\begin{aligned}\delta g_r &= \frac{\partial(\delta V)}{\partial r}\\ &= \frac{GM}{R}\left\{\sum_{l=2}^{\infty}\frac{(l+1)}{R}\left(\frac{R}{r}\right)^{l+2}\sum_{m=0}^{l}\sqrt{\frac{(2l+1)(l-m)!}{4\pi(l+m)!}}\ P_l^m(\cos\theta)\left[A_l^m\cos m\varphi + B_l^m\sin m\varphi\right]\right\}\end{aligned}$$

Gravity gradient is the derivative of gravity with respect to radial distance, so the radial gravity gradient anomaly is:

$$\delta\Gamma_{rr} = \frac{\partial(\delta g_r)}{\partial r}$$
$$= -\frac{GM}{R}\left\{\sum_{l=2}^{\infty} \frac{(l+1)(l+2)}{R^2}\left(\frac{R}{r}\right)^{l+3} \sum_{m=0}^{l} \sqrt{\frac{(2l+1)(l-m)!}{4\pi(l+m)!}}\, P_l^m(\cos\theta)\left[A_l^m \cos m\varphi + B_l^m \sin m\varphi\right]\right\}$$

Evaluating at r = R and using the spherical harmonic coefficients 2-20 from the GEM-L2 model (Lerch *et al.*, 1982), the equations simplify to:

$$\delta N = R\left\{\sum_{l=2}^{20} \sum_{m=0}^{l} \sqrt{\frac{(2l+1)(l-m)!}{4\pi(l+m)!}}\, P_l^m(\cos\theta)\left[A_l^m \cos m\varphi + B_l^m \sin m\varphi\right]\right\}$$

$$\delta g_r = \frac{GM}{R^2}\left\{\sum_{l=2}^{20} (l+1) \sum_{m=0}^{l} \sqrt{\frac{(2l+1)(l-m)!}{4\pi(l+m)!}}\, P_l^m(\cos\theta)\left[A_l^m \cos m\varphi + B_l^m \sin m\varphi\right]\right\}$$

$$\delta\Gamma_{rr} = -\frac{GM}{R^3}\left\{\sum_{l=2}^{20} (l+1)(l+2) \sum_{m=0}^{l} \sqrt{\frac{(2l+1)(l-m)!}{4\pi(l+m)!}}\, P_l^m(\cos\theta)\left[A_l^m \cos m\varphi + B_l^m \sin m\varphi\right]\right\}$$

It is important to note that the GEM-L2 coefficients must be multiplied by $\sqrt{4\pi}$ before they are plugged into these equations to be consistent with the spherical harmonic normalization used in this study. The three geophysical control data sets are constructed by calculating the values of the geoid, gravity and gravity gradient anomalies at the 36 feature locations (Table 3.3).

Variation-Distance Relationships

The different characteristics of the contructed geophysical data sets are apparent in plots of absolute difference versus angle (Figs. 3.16-3.18). The geoid plot shows a clean and fairly symmetric degree 2 pattern, with an angular sampling distance of ~ 102°. The gravity plot is a little more dispersed, with weaker symmetry and an angular sampling distance of ~ 95° [expansion to degree 2]. Finally, the gravity gradient plot shows even more dispersion and an angular sampling distance of ~ 67° [expansion to degree 3]. A comparison of these plots to those for the mantle components clearly illustrates the complexity of the geochemistry data. Even the gravity gradient data [dominated by short wavelength energy] appears to have less small-scale variation [larger angular sampling distance] than all of the mantle component data sets.

Variation Reduction by Filtering

The same circular filter technique outlined above is applied to the geophysics data to see its effect (Figs. 3.19-3.21). The filtered geoid data set retains its strong degree 2 signature [angular sampling distance ~ 93°], but there is a slight increase in the dispersion of the data points. Like the geoid, the filtered gravity data maintains its angular sampling distance [~ 93°] and it shows a slight decrease in data dispersion. The gravity gradient data is most affected by the filtering process. The data dispersion due to large variation at small and large angles is reduced. In addition, the angular sampling distance is increased to ~ 77°, corresponding to spherical harmonic expansion to degree 2.

EXPANSION OF GEOPHYSICAL AND GEOCHEMICAL DATA SETS

By choosing the sampling distances based upon the inherent variation-distance relationships of the different data sets, the problem of aliasing is eliminated. Of course, the location patterns that result from spherical harmonic expansions may not represent the true patterns as they exist in the mantle, but without a more extensive global data set, there is no way to better approximate the true pattern. Coefficients will be found for all six geophysical data sets [filtered and unfiltered], for the EMII and DMM data sets and for the filtered EMI and HIMU data sets.

Solving for the spherical harmonic coefficients needed to expand a given function is a linear inverse problem. More specifically, the expansion of the mantle components or geophysical measures is a discrete linear inverse problem, since the data are discrete observations. The terminology and symbology used here to discuss inverse problems is that of Menke (1989). Values of the mantle components or geophysical measures at the feature locations form a vector of data values **d** [$N \times 1$]. The unknown spherical harmonic coefficients form a vector of model parameters **m** [$M \times 1$]. Relating the two is the data kernel matrix **G** [$N \times M$], composed of Legendre polynomials [functions of colatitude] combined with sine and cosines [functions of longitude]. In matrix form the equation is: **Gm** = **d**, or written out more explicitly:

$$\begin{bmatrix} \surd\, P_0^0(\cos\theta_0) \ldots \surd\, P_L^L(\cos\theta_0) \cos L\varphi_0 & \surd\, P_L^L(\cos\theta_0) \sin L\varphi_0 \\ \vdots & \\ \surd\, P_0^0(\cos\theta_N) \ldots \surd\, P_L^L(\cos\theta_N) \cos L\varphi_N & \surd\, P_L^L(\cos\theta_N) \sin L\varphi_N \end{bmatrix} \begin{bmatrix} A_0^0 \\ \vdots \\ A_L^L \\ B_L^L \end{bmatrix} = \begin{bmatrix} d_0 \\ \vdots \\ d_N \end{bmatrix}$$

where L is the maximum degree of the expansion, N is the number of data observations and $\surd$ is the normalization factor mentioned earlier.

Least Squares Method

Theory. If the equation **Gm** = **d** provides enough information to uniquely determine the model parameters or the best fit to the model parameters, then solving for the spherical harmonic coefficients from degrees 0 to 5 is an even-determined problem [$N = 36$, $M = 36$] and solving for the coefficients from degrees 0 to <5 is an overdetermined problem [$N = 36$, $M < 36$]. For an overdetermined system of equations $\mathbf{Gm} = \mathbf{d}$, with more equations than unknowns, there is no exact solution. The least squares method finds the model parameters that minimize the error between the observed data and the predicted data, ie. it minimizes the L_2 norm of the prediction error:

$$L_2 \text{ norm: } \|e\|_2 = \sqrt{\sum_{i=1}^{N} |e_i|^2} \text{ , where } e_i = d_i^{obs} - d_i^{pre}$$

When solving for the model parameters $\mathbf{m}$ [spherical harmonic coefficients], it is best to use QR decompositon. The normal equations $\mathbf{G}^T\mathbf{Gm} = \mathbf{G}^T\mathbf{d}$ lead to the solution: $\mathbf{m}^{est} = (\mathbf{G}^T\mathbf{G})^{-1}\mathbf{G}^T\mathbf{d}$, but if $\mathbf{G}^T\mathbf{G}$ is ill-conditioned, then taking its inverse leads to inaccurate solutions. QR decomposition is more accurate than the normal equations for ill-conditioned matrices. It decomposes the data kernel matrix $\mathbf{G}$ into two matrices: $\mathbf{Q}$ [orthogonal] and $\mathbf{R}$ [upper triangular]: $\mathbf{QRm} = \mathbf{d}$, with solutions: $\mathbf{m}^{est} = \mathbf{R}^{-1}\mathbf{Q}^T\mathbf{d}$.

Application. As a test of the viability of the least squares method, the spherical harmonic coefficients for the EMII percentage data and the geoid anomaly data are solved for in nested groupings from degrees 0-1 up to degrees 0-5. As the data is expanded out to greater degrees, the coefficients should decrease smoothly. Table 3.4 shows how the degree 2 coefficients vary as the two data sets are expanded out to progressively higher degrees. Only the A_2^0 and A_2^2 coefficients for the geoid and the A_2^0 coefficient for EMII decrease smoothly for the degrees 0-2 through degrees 0-4 expansions. The other coefficients either get larger or oscillate. When solving the even-determined system [degrees 0-5], all of the coefficients experience a large increase or decrease, indicating a very unstable solution.

Since the geoid coefficients are known, the correlations [by degree] between the actual coefficients and the computed coefficients for the nested groupings can be calculated. The correlation coefficient r_l for two sets of coefficients [A1,B1] and [A2,B2] is given by the ratio of covariance to variance at each harmonic degree (Richards and Hager, 1988):

$$r_l = \frac{\sum_{m=0}^{l} \left[A1_l^m A2_l^m + B1_l^m B2_l^m \right]}{\sqrt{\sum_{m=0}^{l} \left[(A1_l^m)^2 + (B1_l^m)^2 \right] \sum_{m=0}^{l} \left[(A2_l^m)^2 + (B2_l^m)^2 \right]}}$$

Correlations with the actual geoid coefficients can only be made at degrees 2 and higher since the actual degree 0 and 1 coefficients are zero. Correlations of the actual geoid coefficients to those calculated using least squares are:

Expansion	**Correlation Coefficient [r_l]**			
	Degree 2	**Degree 3**	**Degree 4**	**Degree 5**
Degrees 0-2	0.046	---	---	---
Degrees 0-3	0.960	0.794	---	---
Degrees 0-4	0.884	0.469	0.597	---
Degrees 0-5	-0.219	-0.105	-0.035	0.031

The expansion for degrees 0-3 shows the best correlation, but there is no consistency from expansion to expansion. Since the least squares solutions do not exhibit consistent, stable behavior, it appears that the system **Gm** = **d** does not provide enough information to uniquely determine the model parameters [or a best estimate for them]. This indicates that the system is not even- or overdetermined, but mixed-determined [neither completely overdetermined nor completely underdetermined] and requires a more sophisticated method to solve for the coefficients.

Singular Value Decompositon Method

Theory. Singular value decompositon, or SVD, is one way to solve a mixed-determined problem. Its purpose is to partition the system of equations into an overdetermined part [that can be solved in the least squares sense] and an underdetermined part [that can be solved assuming some a priori information]. For the general equation $\mathbf{Gm} = \mathbf{d}$, it is like a transformation to the system $\mathbf{G'm'} = \mathbf{d'}$, where $\mathbf{m'}$ is composed of an overdetermined part, $\mathbf{m}^{o}$ and an underdetermined part $\mathbf{m}^{u}$ (Menke, 1989):

$$\mathbf{Gm} = \mathbf{d} \rightarrow \mathbf{G'm'} = \mathbf{d'} \rightarrow \begin{bmatrix} \mathbf{G}^{o'} & 0 \\ 0 & \mathbf{G}^{u'} \end{bmatrix} \begin{bmatrix} \mathbf{m}^{o'} \\ \mathbf{m}^{u'} \end{bmatrix} = \begin{bmatrix} \mathbf{d}^{o'} \\ \mathbf{d}^{u'} \end{bmatrix}$$

SVD decomposes the data kernel matrix $\mathbf{G}$ into three matrices: $\mathbf{G} = \mathbf{U}\Lambda\mathbf{V}^{T}$. The matrix $\mathbf{U}$ is an $N \times N$ matrix of orthonormal [orthogonal and of unit length] eigenvectors that span the data space $S(\mathbf{d})$. Similarly, the matrix $\mathbf{V}$ is an $M \times M$ matrix of orthonormal vectors that span the model parameter space $S(\mathbf{m})$. The matrix Λ is an $N \times M$ diagonal eigenvector matrix with nonnegative diagonal elements called singular values, arranged in order of decreasing size. Some of the singular values may be zero, making it easy to partition the matrix into a submatrix Λ_p, with p nonzero singular values, and several zero matrices: $\Lambda = \begin{bmatrix} \Lambda_p & 0 \\ 0 & 0 \end{bmatrix}$. This simplifies the data kernel decomposition to: $\mathbf{G} = \mathbf{U}_p\Lambda_p\mathbf{V}_p^{T}$ where $\mathbf{U}_p$ and $\mathbf{V}_p$ are the first p columns of $\mathbf{U}$ and $\mathbf{V}$, respectively.

For the equations $\mathbf{Gm} = \mathbf{d}$, the solution is: $\mathbf{m}^{est} = \mathbf{V}_p \Lambda_p^{-1} \mathbf{U}_p^T \mathbf{d}$, called the natural solution (Menke, 1989). If the equation $\mathbf{GM} = \mathbf{d}$ is to some degree underdetermined, Λ_p specifies the combinations of model parameters for which the equation does provide information; these combinations lie in a subspace of the model parameter space $S_p(\mathbf{m})$. On the other hand, if $\mathbf{GM} = \mathbf{d}$ is to some degree overdetermined, then Λ_p specifies the combinations of model parameters that the product $\mathbf{Gm}$ is capable of resolving; these products span a subspace of the data space $S_p(\mathbf{d})$. If none of the singular values are zero, there are undoubtedly some very close to zero that are affecting the solution variance. One way to reduce the solution variance is to select a cutoff size for the singular values and exclude any singular values smaller than this [ie. artificially decide the size of p, the number of nonzero singular values]. This is equivalent to throwing away some combinations of the model parameters [thus reducing the sizes of $\mathbf{U}_p$ and $\mathbf{V}_p$]. However, if the singular values excluded are small, then the solution will be close to the natural solution, though the data and model resolution will be worse. This is a classic trade off situation between resolution and variance (Menke, 1989).

It is also possible to dampen the smaller singular values instead of throwing them away [equivalent to the damped least squares method]. The drawbacks to this method are that the solution is no longer close to the natural solution, the data and model resolution are worse and the damping parameter must be determined by trial-and-error. For this study, various methods are used to try to determine the optimum number of singular values to keep [p] and all singular values with index $> p$ are dropped.

Desired number of singular values. The first step in determining the desired number of singular values is to look at the data kernel spectrums [plots of the size of the singular values versus their index] for the mantle component data kernel and the geophysical data kernels (Figs. 3.22-3.25). For the mantle components, the data kernel **G** is only a function of location, so it is the same for all four components. For the geophysical data, the data kernels are constructed differently, so that all three equations with geoid, gravity and gravity gradient data are solving for the same spherical harmonic coefficients. With respect to the mantle component data kernel, terms in the geoid, gravity and gravity gradient data kernels are multiplied by the additional factors of R, $\frac{GM}{R^2}(l+1)$ and $-\frac{GM}{R^3}(l+1)(l+2)$, respectively.

For comparison, spectrums for the degrees 0-1, 0-2, 0-3, 0-4 and 0-5 expansions are all plotted, but the emphasis here will be on getting reasonable results using the degrees 0-5 expansion. All three geophysical spectrums and the geochemical spectrum for this expansion show the singular values gradually decreasing in value, with the last five or so singular values being very close to zero. There is no obvious cutoff size for the singular values apparent in these plots, so other methods must be used to estimate p.

For the geophysical control set, it is possible to find the number of singular values p needed to most closely approximate the actual coefficients. The root mean square error between the actual and estimated geophysical coefficients is given by:

$$\text{coefficient rms error} = \sqrt{\frac{\sum_{i=1}^{M}\left(m_i^{act} - m_i^{est}\right)^2}{M}}$$

where M is the number of coefficients (model parameters). A plot of coefficient rms error versus the number of singular values retained (Fig. 3.26) indicates that 30, 26 and 14 singular values should be retained, for geoid, gravity and gravity gradient, respectively, to most closely approximate the actual coefficients. These values are indicated on the data kernel spectrum plots (Figs. 3.22-3.24). It is important to note that the more a field is dominated by high degree energy, the fewer singular values it takes for the rms error to explode [at least for these sparse data sets].

Since the coefficients for the geochemistry data are not known, there is no way to measure how closely the estimated coefficients match the actual coefficients. What can be done is to try to match the observed data as closely as possible, while keeping the solution variance at a minimum. As a first step, trade-off curves are constructed to bracket the range of p values that balance the size of the model variance and the spread of the model resolution (Figs. 3.27-3.30). The size of the model variance is based upon the unit covariance matrix of the model parameters, which characterizes the degree of error amplification that occurs in the mapping from data to model parameters (Menke, 1989). Assuming that the data within the four mantle component vectors and the three geophysical vectors are uncorrelated and have uniform variance σ_d^2 [a reasonable assumption for the mantle component vectors based upon the findings in Chapter 2], the covariance matrix of the model parameters is given by:

$$[\mathrm{cov}\ \mathbf{m}^{\mathrm{est}}] = \mathbf{G}^{-g}[\mathrm{cov}\ \mathbf{d}]\mathbf{G}^{-g\mathrm{T}} = \sigma_d^2\mathbf{G}^{-g}\mathbf{G}^{-g\mathrm{T}}$$

where $\mathbf{G}^{-g}$ is the generalized inverse, which for singular value decomposition is:

$$\mathbf{G}^{-g} = \mathbf{V}_p\Lambda_p^{-1}\mathbf{U}_p^{\mathrm{T}}$$

The unit covariance matrix is:

$$[\mathrm{cov_u}\ \mathbf{m}^{\mathrm{est}}] = \sigma_d^{-2}[\mathrm{cov}\ \mathbf{m}^{\mathrm{est}}] = \mathbf{G}^{-g}\mathbf{G}^{-g\mathrm{T}} = \mathbf{V}_p\Lambda_p^{-2}\mathbf{V}_p^{\mathrm{T}}$$

Finally, the size of the model variance is:

$$\mathrm{size}([\mathrm{cov}\ \mathbf{m}^{\mathrm{est}}]) = \left\|\sqrt{\mathrm{var_u}\ \mathbf{m}^{\mathrm{est}}}\right\|_2^2 = \sum_{i=1}^{M}[\mathrm{var_u}\ \mathbf{m}^{\mathrm{est}}]_i = \sum_{i=1}^{M}[\mathrm{cov_u}\ \mathbf{m}^{\mathrm{est}}]_{ii}$$

where M is the number of model parameters. To summarize, the size of the model variance is the sum of the variances of the model parameters, which are the diagonal elements of the model parameter covariance matrix. With increasing values of p, the size of the model variance will increase.

Since resolution is optimal when the resolution matrices are identity matrices, it is possible to quantify the spread of model resolution based on the size of the off-diagonal elements of the model resolution matrix **R** (Menke, 1989):

$$\text{spread}(\mathbf{R}) = \|\mathbf{R} - \mathbf{I}\|_2^2 = \sum_{i=1}^{M} \sum_{j=1}^{M} [R_{ij} - I_{ij}]^2$$

where **I** is the identity matrix and $\mathbf{R} = \mathbf{V}_p\mathbf{V}_p^T$, $[\mathbf{m}^{est} = \mathbf{R}\mathbf{m}^{true}]$. With increasing values of p, the spread of the model resolution will decrease.

Trade-off curves of size of model variance versus spread of model resolution, as a function of the number of singular values retained, show two asymptotes [retaining all 36 singular values gives the largest model variance size] (Figs. 3.27-3.30). The ideal range for p, to balance the two measures, is in the transition between the asymptotes (Table 3.5).

Another way to try and pin down the desired number of singular values [to most closely approximate the data] is to look at plots of model rms error and a variance measure versus the number of singular values retained (Figs. 3.31-3.34). Model rms error is given by:

$$\text{model rms error} = \sqrt{\frac{\sum_{i=1}^{N} \left(d_i^{obs} - d_i^{pre}\right)^2}{N}}$$

where

$$\mathbf{d}^{pre} = \mathbf{G}\mathbf{m}^{est} = \mathbf{G}\mathbf{G}^{-g}\mathbf{d}^{obs} = \left(\mathbf{U}_p\Lambda_p\mathbf{V}_p^T\right)\left(\mathbf{V}_p\Lambda_p^{-1}\mathbf{U}_p^T\right)\mathbf{d}^{obs} = \mathbf{U}_p\mathbf{U}_p^T\mathbf{d}^{obs}$$

While $\mathbf{V}_p^T\mathbf{V}_p$ and $\mathbf{U}_p^T\mathbf{U}_p$ are the identity matrix, $\mathbf{V}_p\mathbf{V}_p^T$ and $\mathbf{U}_p\mathbf{U}_p^T$ are not necessarily the identity matrix, since $\mathbf{U}_p$ and $\mathbf{V}_p$ do not in general span the complete data and model spaces (Menke, 1989). The variance measure used is:

$$\text{variance measure} = \sum_{i=1}^{p} \left[\Lambda_p^{-2}\right]_{ii}$$

since the solution variance is proportional to Λ_p^{-2}. Again , the goal is to use the plots of these two quantities to select p so that the model rms error and the solution variance are balanced (Table 3.5).

Choosing ranges for p using trade-off curves and the model rms/variance curves is a subjective process. The ranges of values are chosen by eye and there is no objective way to select an optimal value of p from these methods. To make the process more objective, Jacobson and Shaw (1991) suggest applying a sequential F-test to SVD problems to find the statistically optimal solution. Given a null model with q parameters and a larger general model with b parameters $[b > q]$, testing the null hypothesis that the additional $[b - q]$ parameters in the general model do not improve the fit to the data [compared to the null model] requires the use of the **F**-statistic:

$$\mathbf{F} = \frac{(\mathrm{RSS}_q - \mathrm{RSS}_b)}{(b - q)} \cdot \frac{(n - b)}{\mathrm{RSS}_b}$$

where RSS_q and RSS_b denote the residual sum of squares for the null and general models, respectfully, and n is the total number of parameters. **F** has an F-distribution with $(b - q, n - b)$ degrees of freedom. The residual sum of squares for a given model is defined as:

$$\mathrm{RSS} = \sum_{i=1}^{N} \left(\mathrm{d}_i^{\mathrm{obs}} - \mathrm{d}_i^{\mathrm{pre}}\right)^2$$

Values of **F** can be converted into the probability that the null hypothesis is true, ie. that the extra parameters do not result in a better fit. Then the quantity [1 - prob(null hypothesis true)] is the significance level of the additional parameters.

For SVD, the sequential F-test starts by testing the significance of a model retaining one singular value against a model retaining no singular values, then continues to test models retaining incrementally more singular values against the current null model. When a model has reached the 95% significance level [chosen for this application] or higher, it becomes the null model against which subsequent models are to be tested, until another model also reaches or surpasses 95% significance and takes its place. Figures 3.35-3.41 show the F-test results for the geophysical and geochemical data sets and Table 3.5 lists the resulting optimal p values. In general, it appears that the smoother functions [longer wavelength] have higher numbers of significant singular values.

For determining the value of p, the three different methods agree quite well (Table 3.5). The trade-off curves define the largest interval for p, which is constrained further by the model rms/variance curves. For every data set, except filtered gravity, the value of p determined by the F-test falls within the chosen range of the model rms/variance curves. Even so, the F-test p value for filtered gravity does not fall far outside the model rms/variance range [$p = 29$ compared to 25] and it does fall within the trade-off range. Since the F-test p values are in agreement with the other methods and are by far the most objective estimate from the three methods, these values will be used in calculating the spherical harmonic coefficients.

Application. How well the estimated spherical harmonic coefficients of the constructed geophysical data sets correlate with the actual GEM-L2 coefficients is an indicator of how closely the estimated geochemistry coefficients may be expected to approximate their true coefficients. Three sets of geophysical SVD coefficient solutions are all correlated with the GEM-L2 coefficients: those that minimize the coefficient rms error and those that minimize the model error [selected p values from the F-test] for the filtered and unfiltered data sets (Table 3.6). Remember that the data kernel matrices **G** for gravity and gravity gradient are modified so that their spherical harmonic coefficients are also estimates of the GEM-L2 coefficients. The correlation coefficients r_l are calculated as outlined above. Plots of r_l versus degree include confidence levels based upon a student's t-test. The test statistic for the t-test is:

$$\mathbf{T} = \frac{r_l\sqrt{n-2}}{\sqrt{1-r_l^2}} = \frac{r_l\sqrt{2l}}{\sqrt{1-r_l^2}}$$

where n is the number of coefficients at that particular degree $[(n-2) = 2l]$. **T** has a t-distribution with $(n - 2)$ or $2l$ degrees of freedom. Given a desired significance level and the degrees of freedom, the value of **T** can be looked up in a table. Then the value that r_l should have to achieve that significance level can be calculated and plotted as confidence levels:

$$r_l = \frac{\mathbf{T}}{\sqrt{2l + \mathbf{T}^2}}$$

For the plots of r_l versus l, the geophysical coefficients estimated by minimizing the coefficient rms error correlate better than those estimated by minimizing the model error and, of those, the unfiltered data set correlates better than the filtered data set. All three sets of coefficients correlate well with the actual GEM-L2 coefficients at degree 2, except for filtered gravity (Figs. 3.42-3.44). In all cases, the geoid coefficient estimates correlate the best. In general, gravity and gravity gradient correlate better at even degrees, with the exception of the filtered coefficients. For the mantle component coefficients, all this implies that the degree 2 coefficients are probably good, but beyond that there is no guarantee. Of the four mantle component percentage data sets that are expanded, the filtered HiMU data set is unique in that it most closely resembles the geoid data set in the variation-distance plots (Figs. 3.13 and 3.16). Thus, there is a good possibility that at least the degree 3 coefficients for this data set are reasonable as well.

Correlation coefficients for the actual GEM-L2 coefficients and the estimated coefficients cannot be calculated at degrees 0 and 1 because those GEM-L2 coefficients are equal to zero. In contrast, the estimates of these coefficients from the constructed geophysical data sets are all positive numbers the same order of magnitude as the rest of the estimated coefficients. This discrepancy is caused by a sampling bias due to the fact that the oceanic islands are all hotspot related and hotspots are associated with geoid highs [Richards *et al.*, 1988]; no geoid lows are sampled to balance these highs. It is unclear how this bias may affect the estimates of the other coefficients.

The continuous layer model degree 2 "functions" for the constructed geoid data set and the mantle component percentages are reconstructed on a five degree grid over the globe from $10 \leq \theta \leq 170$ and $-180 \leq \varphi \leq 180$ using the calculated coefficients and the appropriate equations (Figs. 3.45-3.49). It should be noted that the contoured values are not actual geoid anomaly values or component percentages, but are deviations from the average [degree 0] geoid anomaly value or component percentage [average constructed geoid = 13.7 m; average filtered EMI = 0.27; average EMII = 0.17; average filtered HIMU = 0.31; average DMM = 0.25]. For comparison, the actual degree 2 geoid is constructed in the same way using the GEM-L2 coefficients [average geoid = 0.0 m] (Fig. 3.50). The constructed geoid field agrees well with the actual degree 2 geoid, as already indicated by the correlation coefficients. For the mantle components, HIMU resembles the actual geoid field with two essentially equatorial highs in approximately the same locations; EMI and EMII also have two highs that undulate above and below the equator with a longitudinal shift of ~35° to the east with respect to the actual geoid [EMII has less offset than EMI]; and DMM, with its two highs and two lows resembles none of the other degree 2 expansions.

Of all the mantle component data sets, filtered HIMU has the best chance of getting reasonable values for the degree 3 coefficients. The degrees 2-3 function for filtered HIMU is reconstructed as before (Fig. 3.51). This can be compared to the degrees 2-3 geoid reconstructed from the GEM-L2 coefficients (Fig. 3.52).

SUMMARY

Viewing the distribution of the OIB reservoir as a continuous layer in the mantle and using approximation methods to solve for the spherical harmonic coefficients of its expansion reveals the following:

- The mantle end-member component percentage data have a lot of short wavelength energy relative to equally limited geoid, gravity and gravity gradient control data sets.

- With the currently available data, solving for the spherical harmonic coefficients is a mixed-determined problem, requiring the use of singular value decomposition [SVD] to get viable solutions.

- The F-test is a simple, objective way to determine the number of singular values to retain in SVD for the statistically optimal solution.

- With the current data coverage, only the degree 2 spherical harmonic coefficients can be estimated with a reasonable level of confidence using SVD.

- Continuous layer model degree 2 HIMU closely resembles the degree 2 geoid.

- Continuous layer model degree 2 EMI and EMII resemble a longitude-shifted, undulating degree 2 geoid.

- Continuous layer model degree 2 DMM does not resemble the degree 2 geoid or the degree 2 expansion of any other mantle component.

Table 3.1. Mantle end-member component percentages[1] for the average isotopic signatures of the geographic features [island groups, islands, ridges, seamounts] represented in the OIB data set with their locations and the number of samples for each feature [in braces].

Feature	%EMI	%EMII	%HIMU	%DMM	Lat	Long
Ascension [5]	7.71	11.96	38.64	41.69	-7.95	-14.37
Amsterdam/St. Paul [11]	23.12	17.88	29.80	29.20	-29.46	66.48
Azores [6]	11.11	36.26	38.88	13.74	38.50	-28.00
Balleny [3]	14.94	8.21	44.68	32.17	-67.53	-168.88
Cameroon Line [18]	14.25	12.02	51.98	21.75	1.03	6.10
Cape Verde Islands [41]	29.52	8.83	35.59	26.06	15.80	-24.24
Christmas [13]	38.67	21.09	23.00	17.25	-10.50	105.67
Cocos [3]	14.08	11.53	35.86	38.53	5.54	-87.08
Comores Archipelago [14]	28.59	8.54	43.50	19.37	-12.09	43.76
Cook-Austral Islands [26]	26.04	20.88	36.86	16.22	-20.37	-158.56

Table 3.1. Continued.

Feature	%EMI	%EMII	%HIMU	%DMM	Lat	Long
Crozet Islands [9]	23.73	21.49	27.44	27.34	-46.45	52.00
Fernando de Noronha [16]	21.68	23.69	34.82	19.80	-3.83	-32.42
Galapagos Islands [11]	16.09	11.95	30.64	41.32	-0.39	-90.70
Gough [2]	50.11	25.99	20.70	3.20	-40.33	-10.00
Hawaiian Islands [73]	28.18	16.09	8.55	47.18	19.76	-156.09
Iceland [7]	19.13	10.71	17.35	52.81	64.75	-17.65
Juan Fernandez Islands [4]	25.41	15.53	32.43	26.63	-33.62	-78.83
Kerguelen Plateau [41]	41.82	29.23	11.57	17.39	-52.92	73.15
Louisville Seamount Chain [4]	16.07	18.90	33.18	31.84	-45.22	-154.40
Marion/Prince Edward [4]	25.43	10.87	22.81	40.88	-46.92	37.75
Marquesas Archipelago [11]	23.54	24.18	31.55	20.72	-9.09	-139.84
Mascareignes [8]	22.64	24.39	24.10	28.87	-20.75	56.50

Table 3.1. Continued.

Feature	%EMI	%EMII	%HIMU	%DMM	Lat	Long
New England Seamounts [6]	21.27	10.35	51.38	17.00	37.86	-61.61
Nunivak [2]	12.66	10.45	18.16	58.73	60.00	-166.00
Pitcairn [19]	51.65	6.98	19.79	21.57	-20.07	-130.10
Ponape [1]	24.90	10.26	18.69	46.14	6.93	158.32
Sala Y Gomez [1]	17.13	11.47	48.22	23.18	-26.47	-105.47
Samoa Islands [34]	19.15	47.12	14.85	18.88	-14.08	-171.10
San Felix/San Ambrosio [5]	51.55	7.74	32.63	8.08	-26.42	-79.98
Shimada Seamount [1]	33.05	30.47	30.46	6.01	16.87	-117.47
Society Ridge [9]	21.01	34.70	20.98	23.31	-17.57	-149.14
St. Helena [31]	5.53	12.58	64.64	17.25	-15.97	-5.72
Trinidade[1]	40.69	9.44	35.03	14.84	-20.50	-29.42

Table 3.1. Continued.

Feature	%EMI	%EMII	%HIMU	%DMM	Lat	Long
Tristan de Cunha [5]	58.53	18.05	16.72	6.70	-37.10	-12.28
Tubuai-Austral Islands [22]	9.56	13.82	59.70	16.93	-23.84	-148.26
Walvis Ridge [10]	66.28	10.85	11.07	11.80	-30.28	-7.05

[1]Percentages may not add up to 100 due to rounding.

Table 3.2. Separation of the OIB feature data set into 27 Dupal-type features and 9 DMM-type features, based upon the percentage of the DMM mantle component.

Dupal-type Features	%DMM
Gough	3.20
Shimada Seamount	6.01
Tristan de Cunha	6.70
San Felix/San Ambrosio	8.08
Walvis Ridge	11.80
Azores	13.74
Trinidade	14.84
Cook-Austral Islands	16.22
Tubuai-Austral Islands	16.93
New England Seamounts	17.00
Christmas	17.25
St. Helena	17.25
Kerguelen Plateau	17.39
Samoa Islands	18.88
Comores Archipelago	19.37
Fernando de Noronha	19.80
Marquesas Archipelago	20.72
Pitcairn	21.57
Cameroon Line	21.75
Sala Y Gomez	23.18
Society Ridge	23.31
Cape Verde Islands	26.06
Juan Fernandez Islands	26.63
Crozet Islands	27.34
Mascareignes	28.87
Amsterdam/St. Paul	29.20
Louisville Seamount Chain	31.84

Table 3.2. Continued.

DMM-type Features	%DMM
Balleny	32.17
Cocos	38.53
Marion/Prince Edward	40.88
Galapagos Islands	41.32
Ascension	41.69
Ponape	46.14
Hawaiian Islands	47.18
Iceland	52.81
Nunivak	58.73

Table 3.3. Geoid, gravity and gravity gradient anomaly values, calculated using the degrees 2-20 GEM-L2 spherical harmonic coefficients, at the geographic features [island groups, islands, ridges, seamounts] represented in the OIB data set with their locations.

Feature	Geoid[1]	Gravity[2]	Gravity Gradient[3]	Lat	Long
Ascension	66.1	29.2	-0.138	-7.95	-14.37
Amsterdam/St. Paul	-5.0	0.5	-0.072	-38.33	77.59
Azores	4.6	-2.0	0.098	38.50	-28.00
Balleny	-43.5	-23.6	0.206	-67.53	-168.88
Cameroon Line	40.8	11.3	0.039	1.03	6.10
Cape Verde Islands	44.8	13.9	0.043	15.80	-24.24
Christmas	48.5	40.8	-0.556	-10.50	105.67
Cocos	-5.9	1.8	-0.216	5.54	-87.08
Comores Archipelago	23.1	9.6	-0.023	-12.09	43.76
Cook-Austral Islands	39.5	29.2	-0.397	-20.37	-158.56

Table 3.3. Continued.

Feature	Geoid[1]	Gravity[2]	Gravity Gradient[3]	Lat	Long
Crozet Islands	-25.9	-12.5	0.148	-46.45	52.00
Fernando de Noronha	80.8	43.0	-0.287	-3.83	-32.42
Galapagos Islands	-17.5	-14.9	0.134	-0.39	-90.70
Gough	6.5	7.2	-0.100	-40.33	-10.00
Hawaiian Islands	27.7	12.2	-0.079	19.76	-156.09
Iceland	-39.8	-15.4	0.037	64.75	-17.65
Juan Fernandez Islands	-19.4	-20.3	0.320	-33.62	-78.83
Kerguelen Plateau	-35.8	-14.1	0.046	-52.92	73.15
Louisville Seamount Chain	11.6	6.6	0.012	-45.22	-154.40
Marion/Prince Edward	-26.2	-11.0	0.093	-46.92	37.75
Marquesas Archipelago	8.6	-7.8	0.265	-9.09	-139.84
Mascareignes	16.4	9.8	-0.088	-20.75	56.50

Table 3.3. Continued.

Feature	Geoid[1]	Gravity[2]	Gravity Gradient[3]	Lat	Long
New England Seamounts	-3.5	2.9	-0.110	37.86	-61.61
Nunivak	-15.0	-12.0	0.223	60.00	-166.00
Pitcairn	17.3	11.9	-0.163	-20.07	-130.10
Ponape	41.1	21.5	-0.181	6.93	158.32
Sala Y Gomez	9.3	11.9	-0.140	-26.47	-105.47
Samoa Islands	38.4	17.8	-0.126	-14.08	-171.10
San Felix/San Ambrosio	-14.3	-19.0	0.307	-26.42	-79.98
Shimada Seamount	-19.0	-12.9	0.141	16.87	-117.47
Society Ridge	24.0	7.5	0.011	-17.57	-149.14
St. Helena	67.5	44.8	-0.507	-15.97	-5.72
Trinidade	62.4	36.7	-0.326	-20.50	-29.42

Table 3.3. Continued.

Feature	Geoid[1]	Gravity[2]	Gravity Gradient[3]	Lat	Long
Tristan de Cunha	16.3	9.6	-0.065	-37.10	-12.28
Tubuai-Austral Islands	27.1	12.6	-0.056	-23.84	-148.26
Walvis Ridge	41.9	29.0	-0.298	-30.28	-7.05

[1]Geoid anomaly values in meters.
[2]Gravity anomaly values in milligals, where mgal = 10^{-5} m/s^2.
[3]Gravity gradient values in eotvos units [EU], where EU = 10^{-9} 1/s^2.

Table 3.4. Change in degree 2 spherical harmonic coefficients for the EMII percentage data and the geoid anomaly data as the data sets are expanded to progressively higher degrees.

Expansions	A_2^0	A_2^1	B_2^1	A_2^2	B_2^2
Geoid					
Degrees 0-2	-1.491E-05	-1.049E-06	-4.116E06	1.001E-05	-6.258E-06
Degrees 0-3	-1.511E-05	2.881E-06	1.551E-06	6.610E-06	-8.569E-06
Degrees 0-4	-1.825E-05	-7.480E-06	3.639E-06	6.044E-06	-1.108E-06
Degrees 0-5	3.946E-05	3.357E-05	-4.237E-04	-1.436E-04	-3.682E-06
EMII					
Degrees 0-2	-0.065243	-0.063197	0.269622	0.108911	-0.008334
Degrees 0-3	-0.076403	-0.203182	0.466347	0.148947	0.053770
Degrees 0-4	-0.170987	-0.221924	0.785142	0.167714	0.087842
Degrees 0-5	2.543222	10.864696	-30.064709	-20.805890	-10.644588

Table 3.5. Optimal values or ranges of values for p [the number of singular values retained] for the best approximations of the observed data that keep solution variance to a minimum, as determined by three different methods: trade-off curves, model rms error and variance curves, and the F-test.

Data Sets	Trade-Off Curves	Model RMS Error & Variance	F-Test
Geophysics[1]			
Geoid	$15 \leq p \leq 30$	$21 \leq p \leq 25$	$p = 25$
Gravity	$9 \leq p \leq 29$	$20 \leq p \leq 25$	$p = 20$
Gravity Gradient	$8 \leq p \leq 26$	$20 \leq p \leq 25$	$p = 20$
Filtered Geoid	$15 \leq p \leq 30$	$21 \leq p \leq 25$	$p = 24$
Filtered Gravity	$9 \leq p \leq 29$	$20 \leq p \leq 25$	$p = 29$
Filtered Gravity Gradient	$8 \leq p \leq 26$	$20 \leq p \leq 25$	$p = 24$
Geochemistry			
Filtered EMI	$15 \leq p \leq 30$	$16 \leq p \leq 21$	$p = 20$
EMII	$15 \leq p \leq 30$	$16 \leq p \leq 20$	$p = 16$
Filtered HIMU	$15 \leq p \leq 30$	$18 \leq p \leq 23$	$p = 23$
DMM	$15 \leq p \leq 30$	$19 \leq p \leq 22$	$p = 22$

[1] The optimal values of p for the best approximations to the actual GEM-L2 coefficients are 30 [geoid], 26 [gravity] and 14 [gravity gradient].

Table 3.6. Summary of correlation coefficients between the GEM-L2 coefficients and three sets of estimated geophysical coefficients that minimize the coefficient rms error and that minimize the model error for filtered and unfiltered data sets.

Data Set	*p* Value	Degree 2	Degree 3	Degree 4	Degree 5
Minimizing coefficient rms error					
geoid	30	0.988	0.909	0.744	0.705
gravity	26	0.981	0.605	0.734	0.310
gravity gradient	14	0.926	0.399	0.457	-0.014
Minimizing model error (F-test) - unfiltered					
geoid	25	0.988	0.863	0.726	-0.031
gravity	20	0.891	0.264	0.394	-0.145
gravity gradient	20	0.779	-0.084	0.543	0.085
Minimizing model error (F-test) - filtered					
geoid	24	0.629	0.537	-0.256	0.016
gravity	29	0.356	0.723	-0.331	-0.333
gravity gradient	24	0.709	0.334	-0.720	-0.491

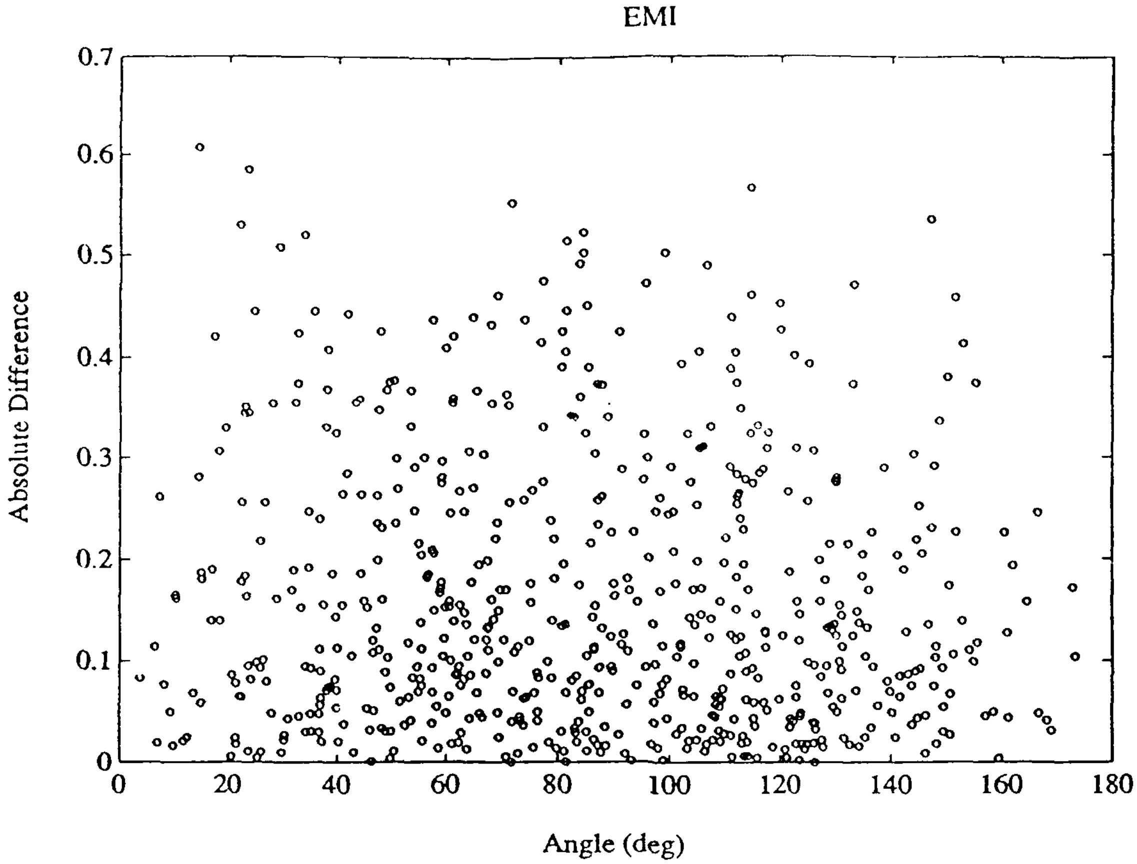

Fig. 3.1. Variation-distance plot for the EMI mantle component showing the range of variation in the component percentage with angular distance between the feature locations. To account for the variation requires a minimum sampling distance of ~ 14.5° [degree 12 expansion].

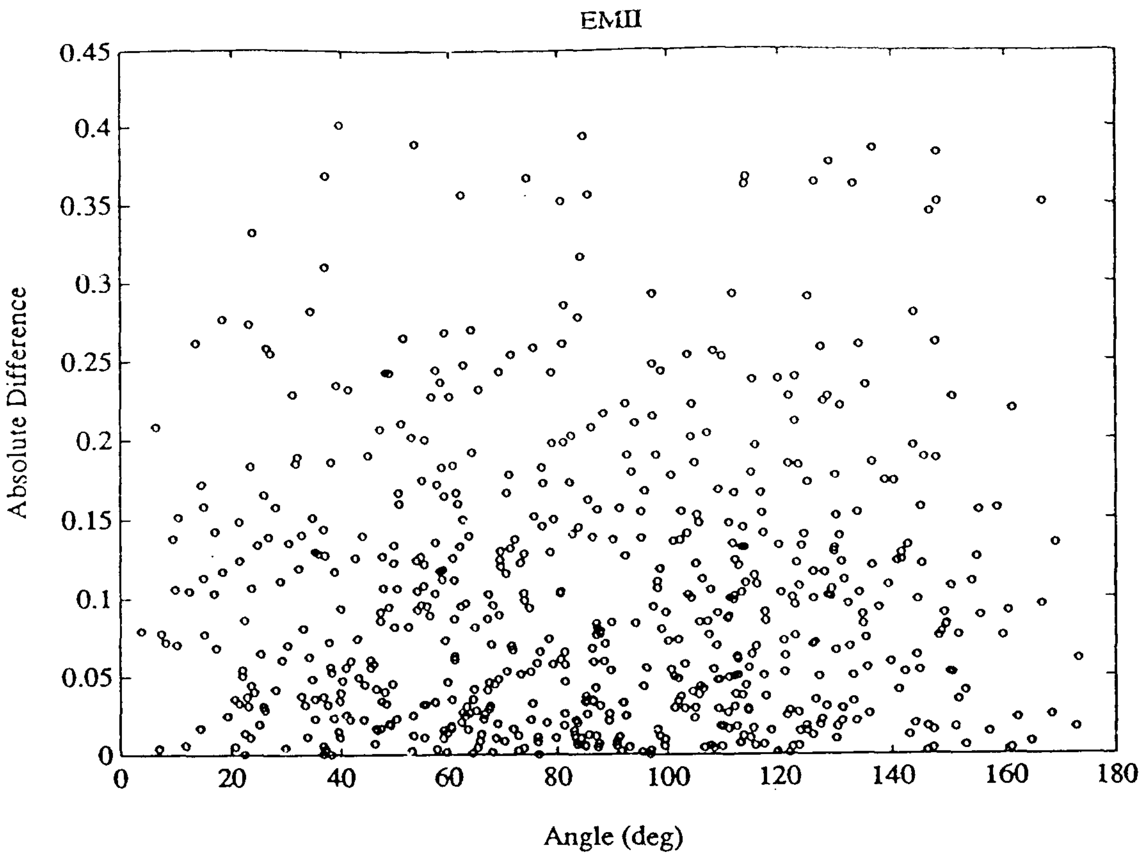

Fig. 3.2. Variation-distance plot for the EMII mantle component showing the range of variation in the component percentage with angular distance between the feature locations. To account for the variation requires a minimum sampling distance of ~ 39° [degree 4 expansion].

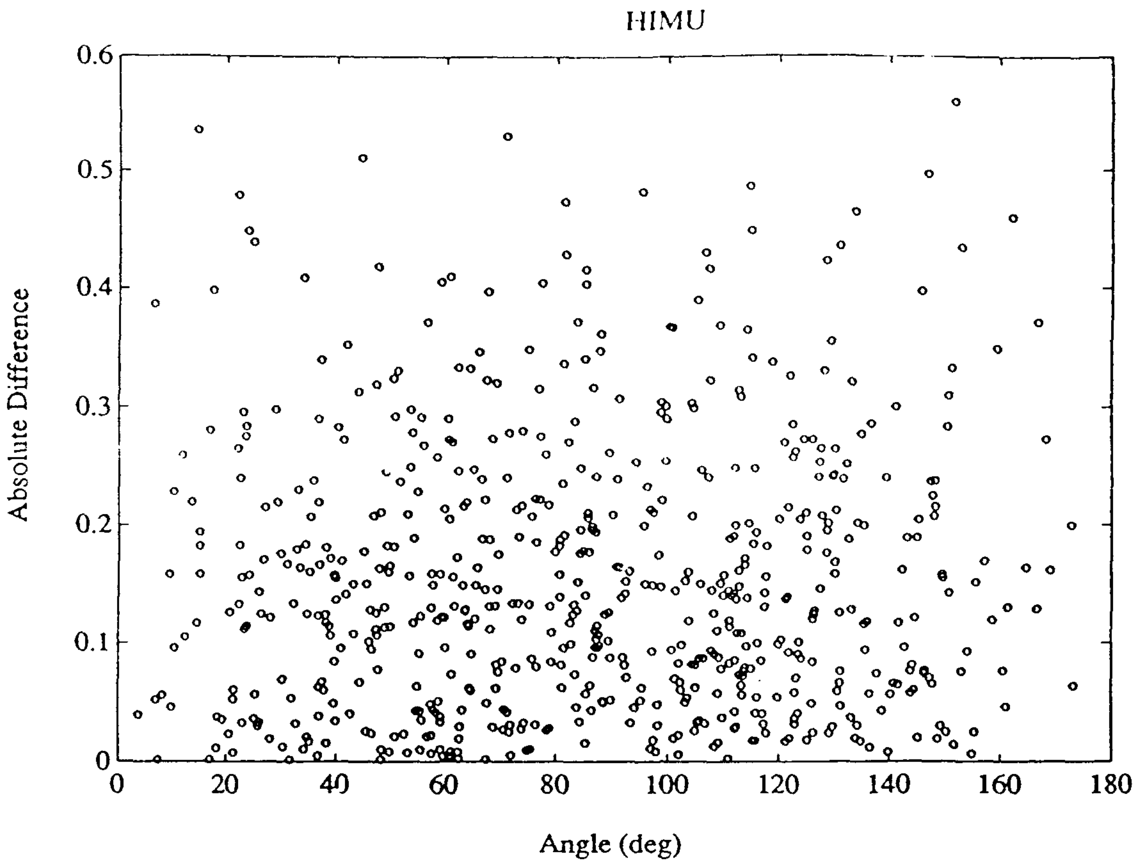

Fig. 3.3. Variation-distance plot for the HIMU mantle component showing the range of variation in the component percentage with angular distance between the feature locations. To account for the variation requires a minimum sampling distance of ~ 14.5° [degree 12 expansion].

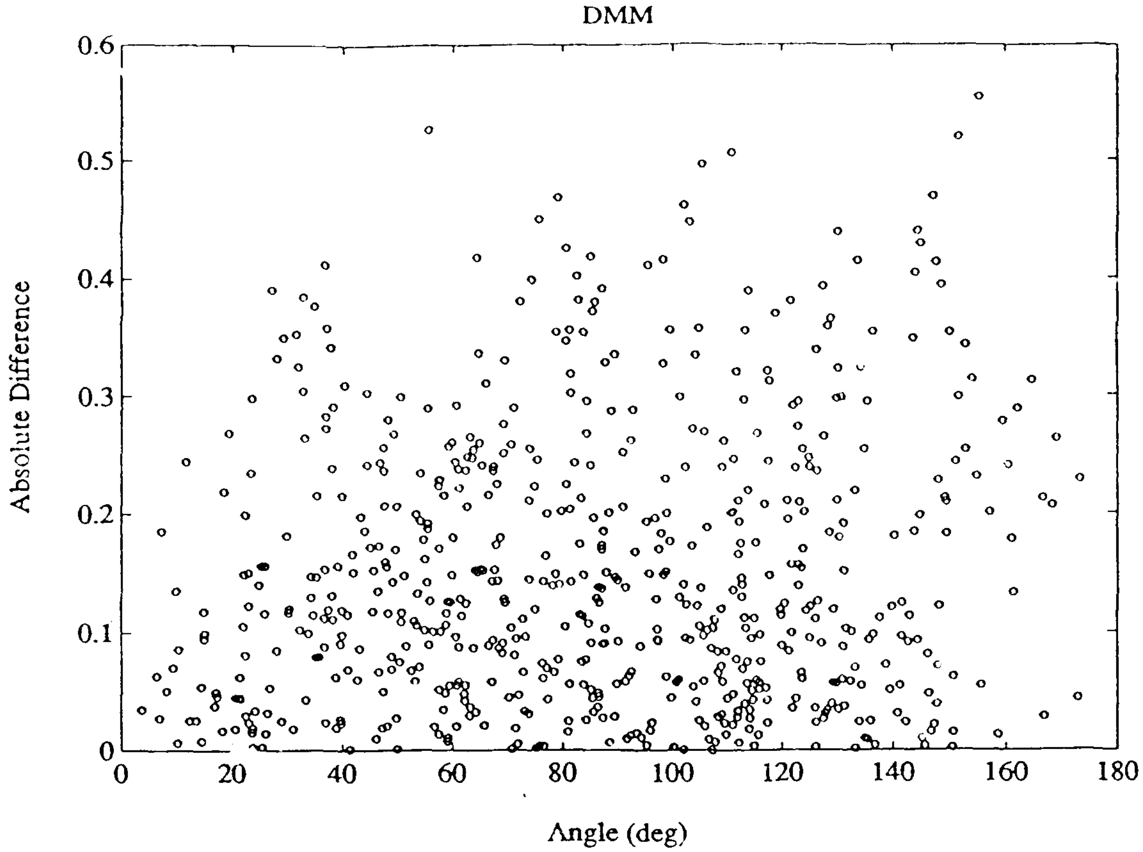

Fig. 3.4 Variation-distance plot for the DMM mantle component showing the range of variation in the component percentage with angular distance between the feature locations. To account for the variation requires a minimum sampling distance of ~ 57° [degree 3 expansion].

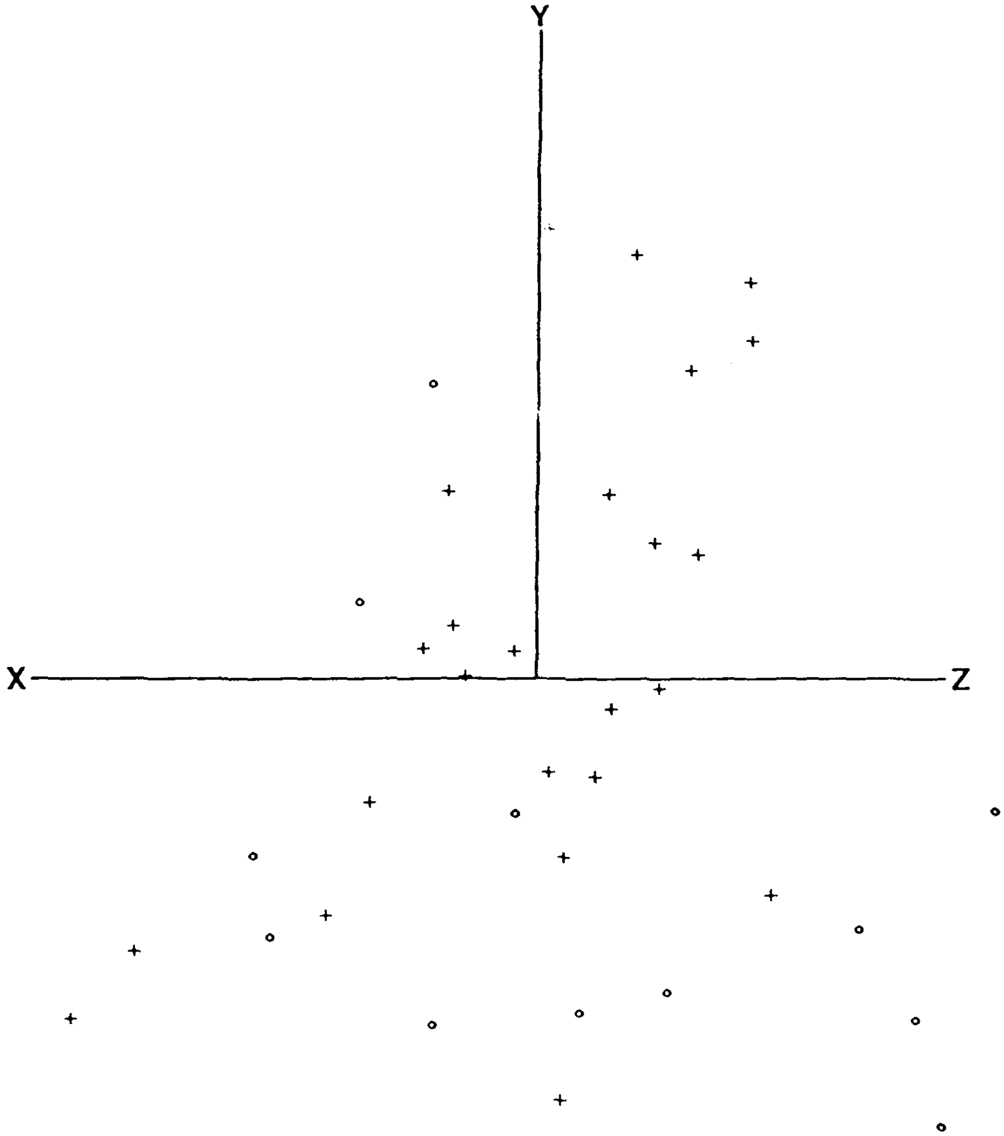

Fig. 3.5. Three-dimensional plot of the geographic feature principal component data. Axes: X = Z1, Y = Z2, Z = Z3. Symbols: + = features inside the DUPAL belt, o = features outside the DUPAL belt.

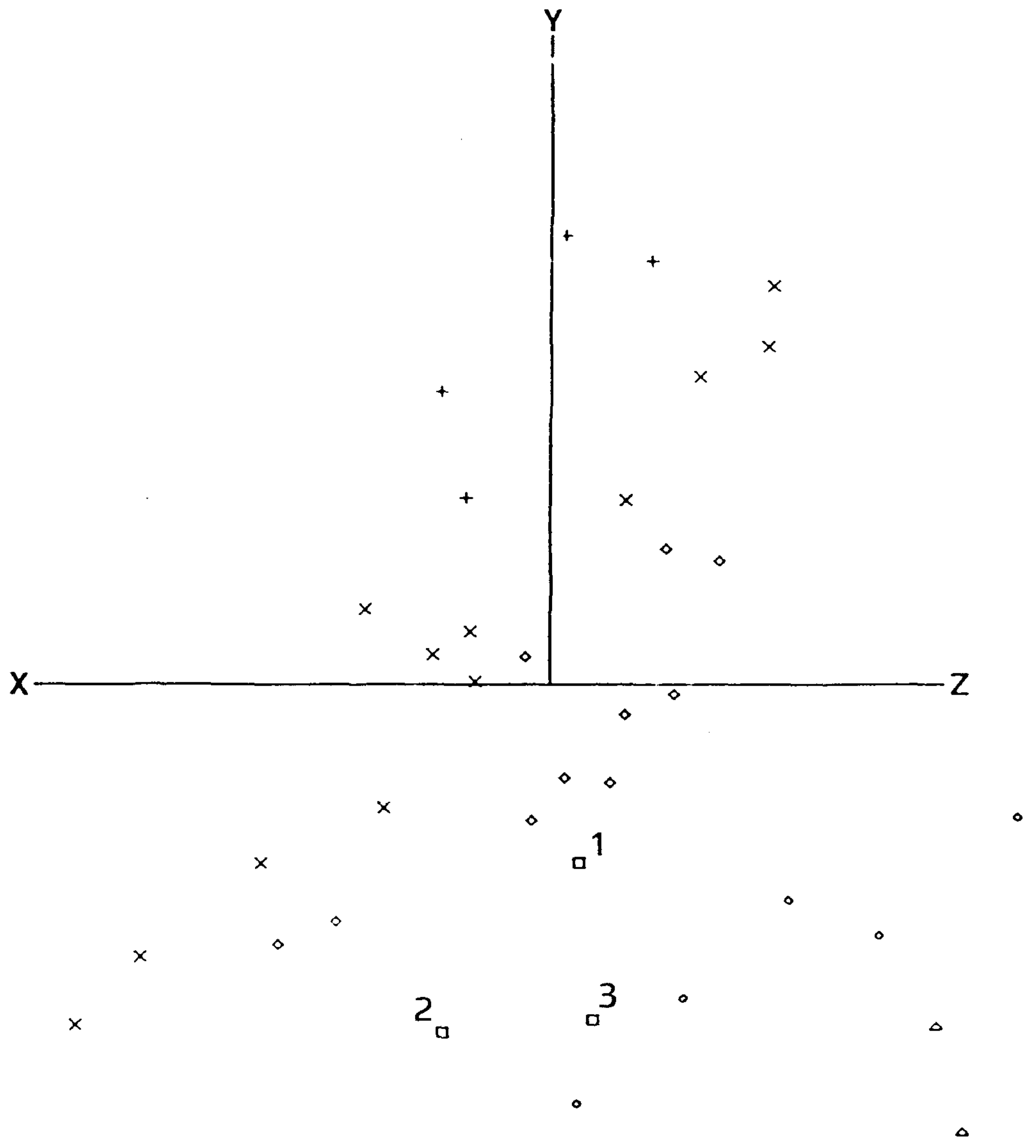

Fig. 3.6. Three-dimensional plot of the geographic feature principal component data, with symbols distinguishing percentages of the DMM component. Axes: X = Z1, Y = Z2, Z = Z3. Symbols: + = <10% DMM, x = 10-20% DMM, diamond = 20-30% DMM, square = 30-40% DMM, o = 40-50% DMM, Δ = >50% DMM. Most striking is the large spatial separation in the 30-40% category between: [1] Louisville = 31.84%, [2] Balleny = 32.17%, [3] Cocos = 38.53%.

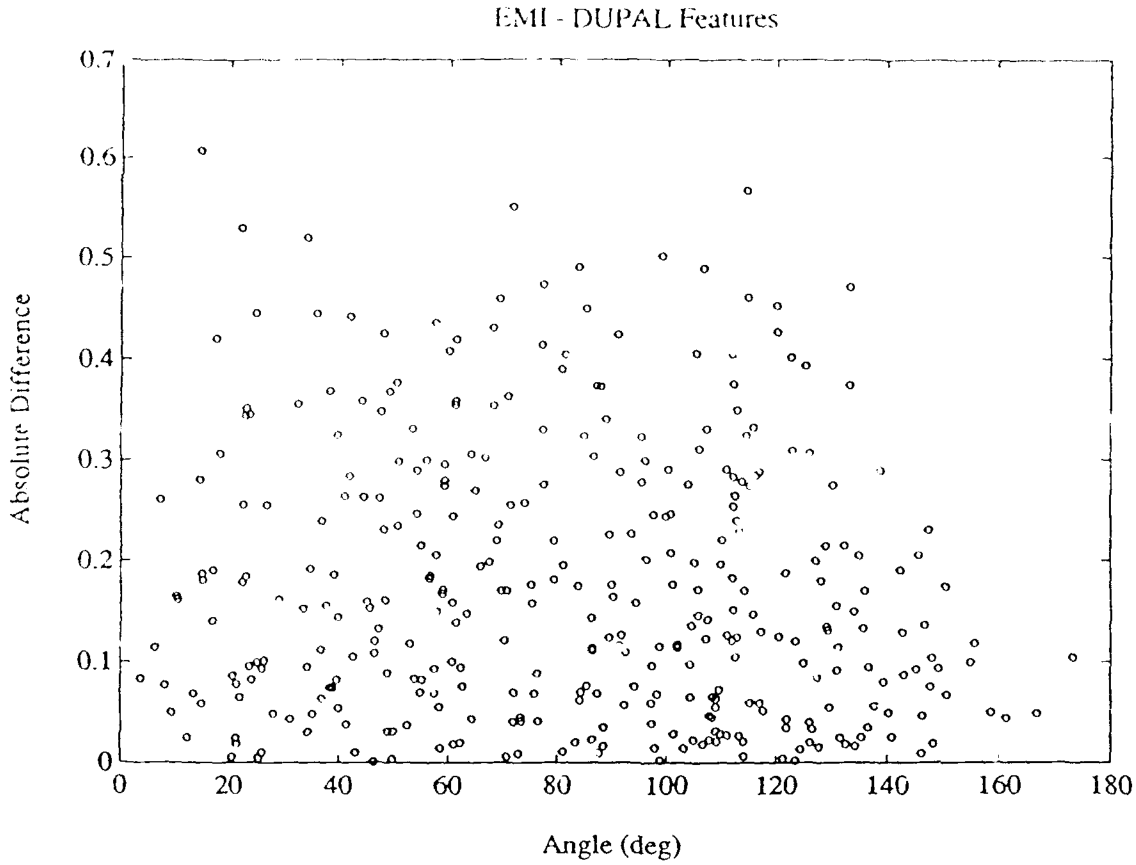

Fig. 3.7. Variation-distance plot for the EMI mantle component for the DUPAL features only [<32% DMM], showing the range of variation in the component percentage with angular distance between the feature locations. Using the DUPAL features only shows no reduction in the small-scale variation for the EMI component.

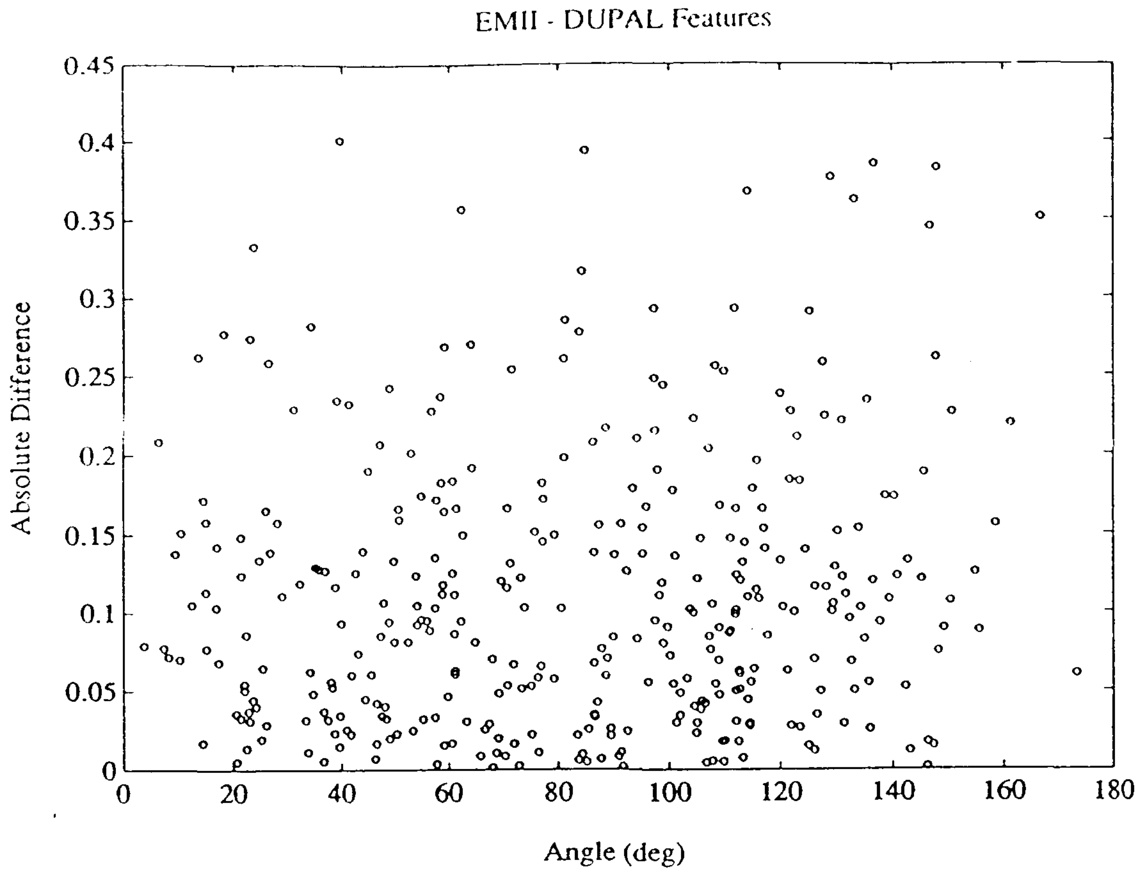

Fig. 3.8. Variation-distance plot for the EMII mantle component for the DUPAL features only [<32% DMM], showing the range of variation in the component percentage with angular distance between the feature locations. Using the DUPAL features only shows no reduction in the small-scale variation for the EMII component.

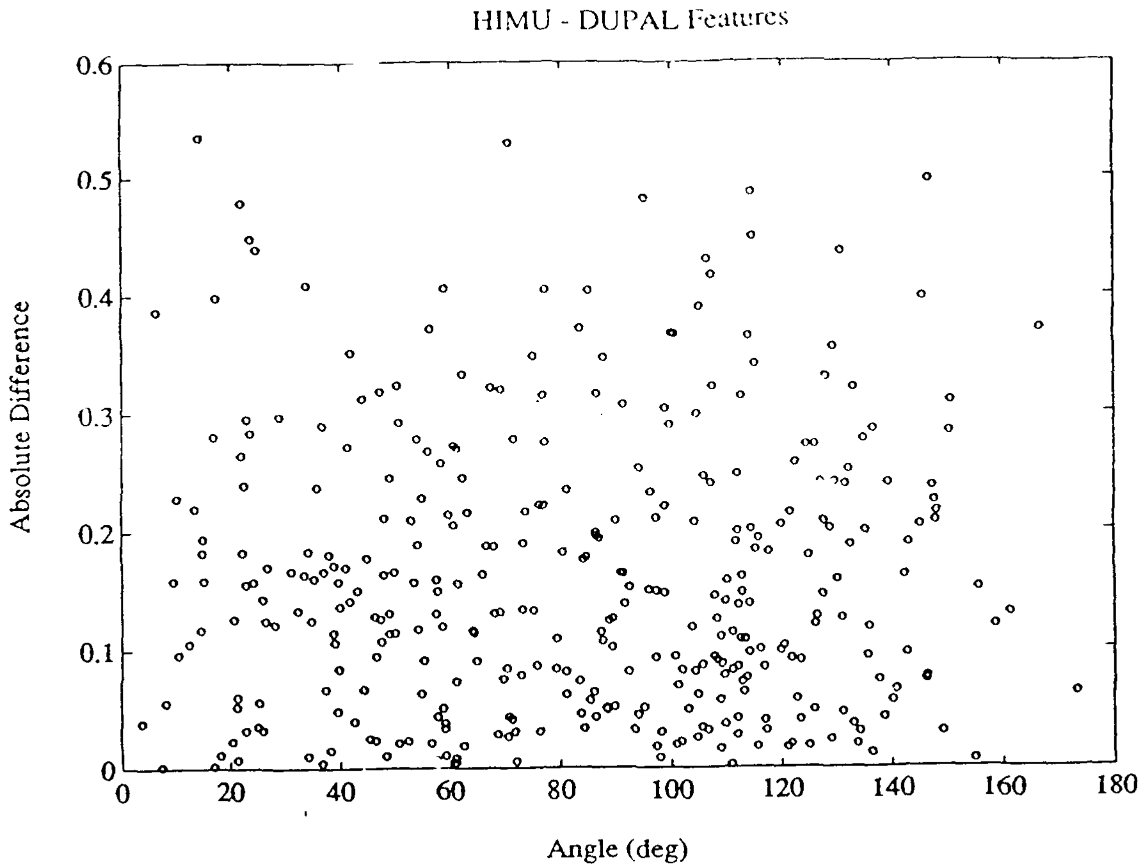

Fig. 3.9. Variation-distance plot for the HIMU mantle component for the DUPAL features only [<32% DMM], showing the range of variation in the component percentage with angular distance between the feature locations. Using the DUPAL features only shows no reduction in the small-scale variation for the HIMU component.

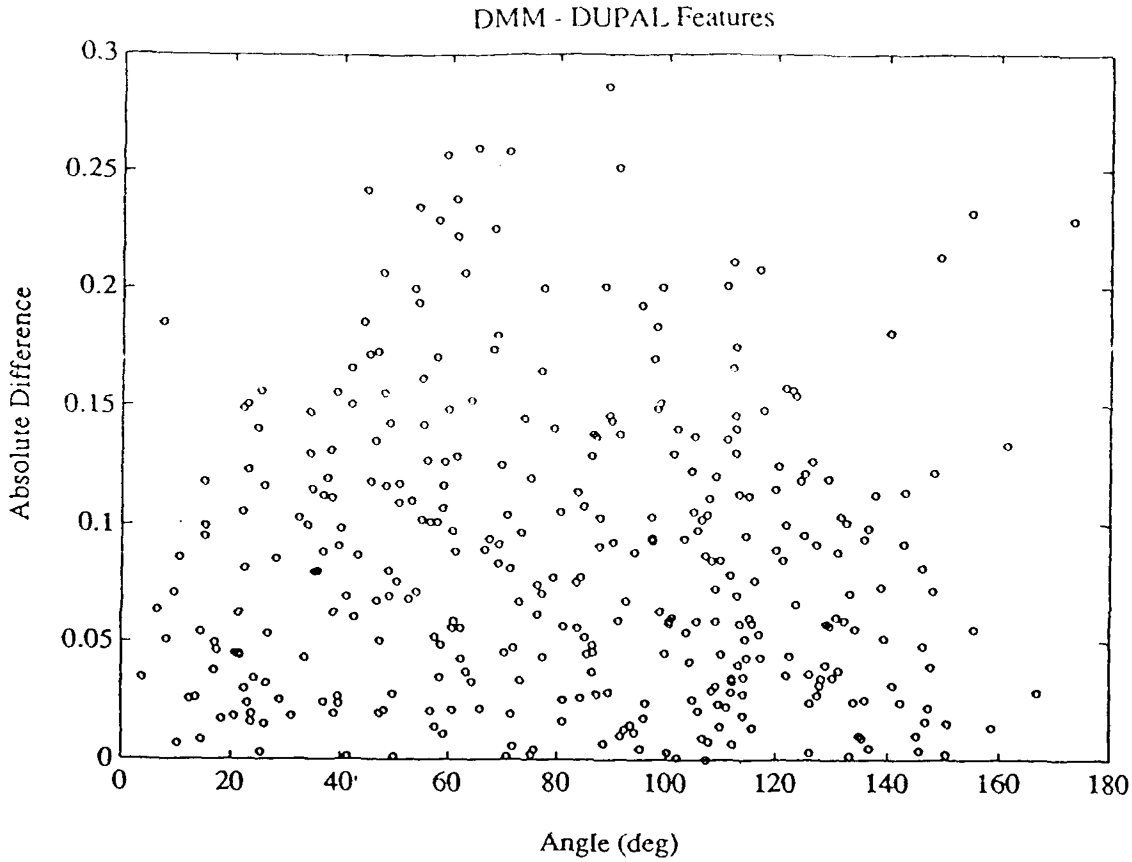

Fig. 3.10. Variation-distance plot for the DMM mantle component for the DUPAL features only [<32% DMM], showing the range of variation in the component percentage with angular distance between the feature locations. Using the DUPAL features only does show a reduction in the small-scale variation for the DMM component, with an increase in minimum sampling distance from ~ 57° to 89°.

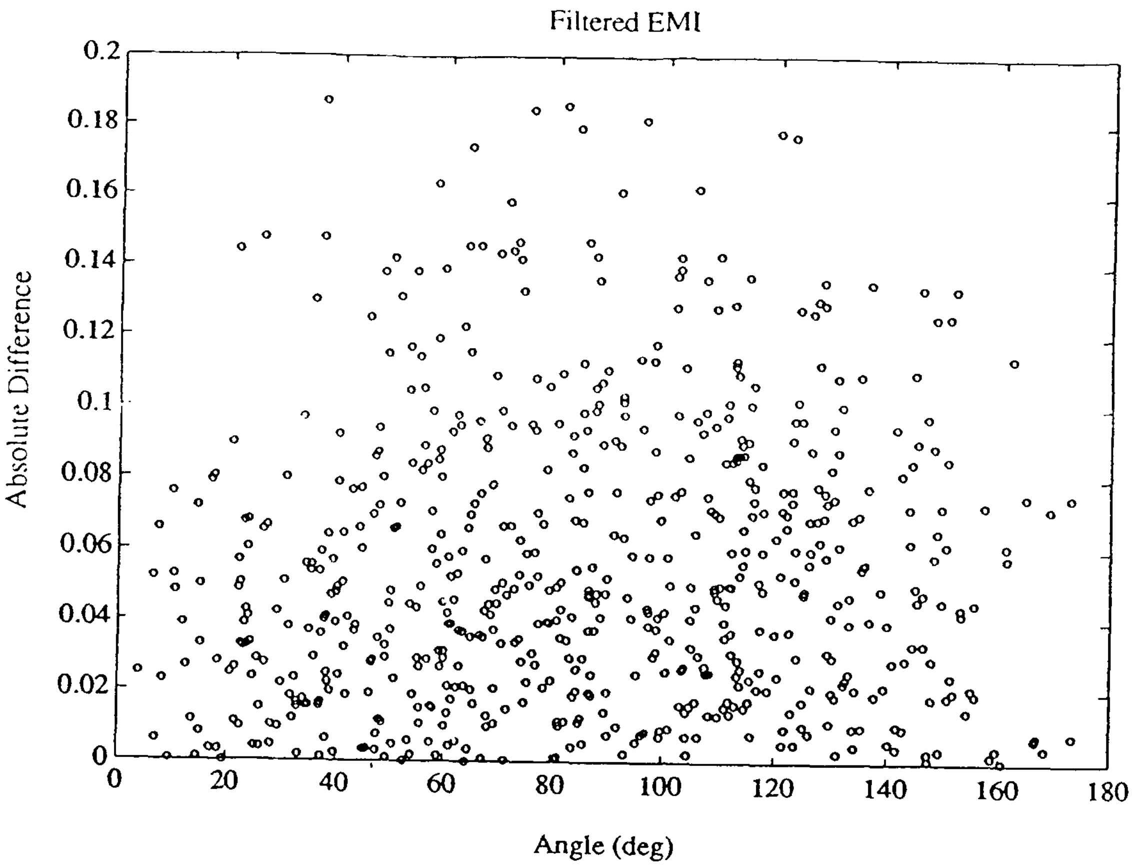

Fig. 3.11. Variation-distance plot for the filtered EMI data set, showing the range of variation in the component percentage with angular distance after the circular filter is applied. The result is a reduction in the small-scale variation, with an increase in minimum sampling distance from ~ 14.5° to 37° [expansions to degrees 12 and 5, respectively].

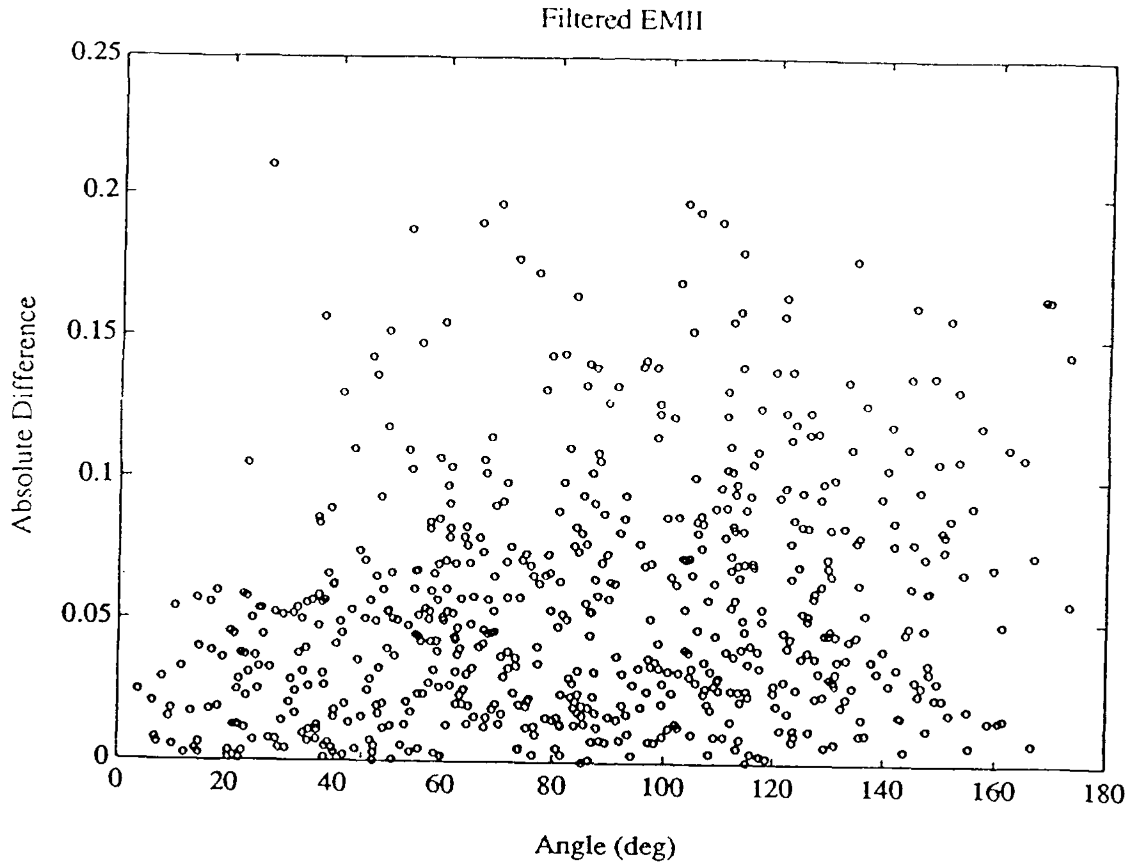

Fig. 3.12. Variation-distance plot for the filtered EMII data set, showing the range of variation in the component percentage with angular distance after the circular filter is applied. The result is an increase in the small-scale variation, with a decrease in minimum sampling distance from ~ 39° to 27° [expansions to degrees 4 and 7, respectively].

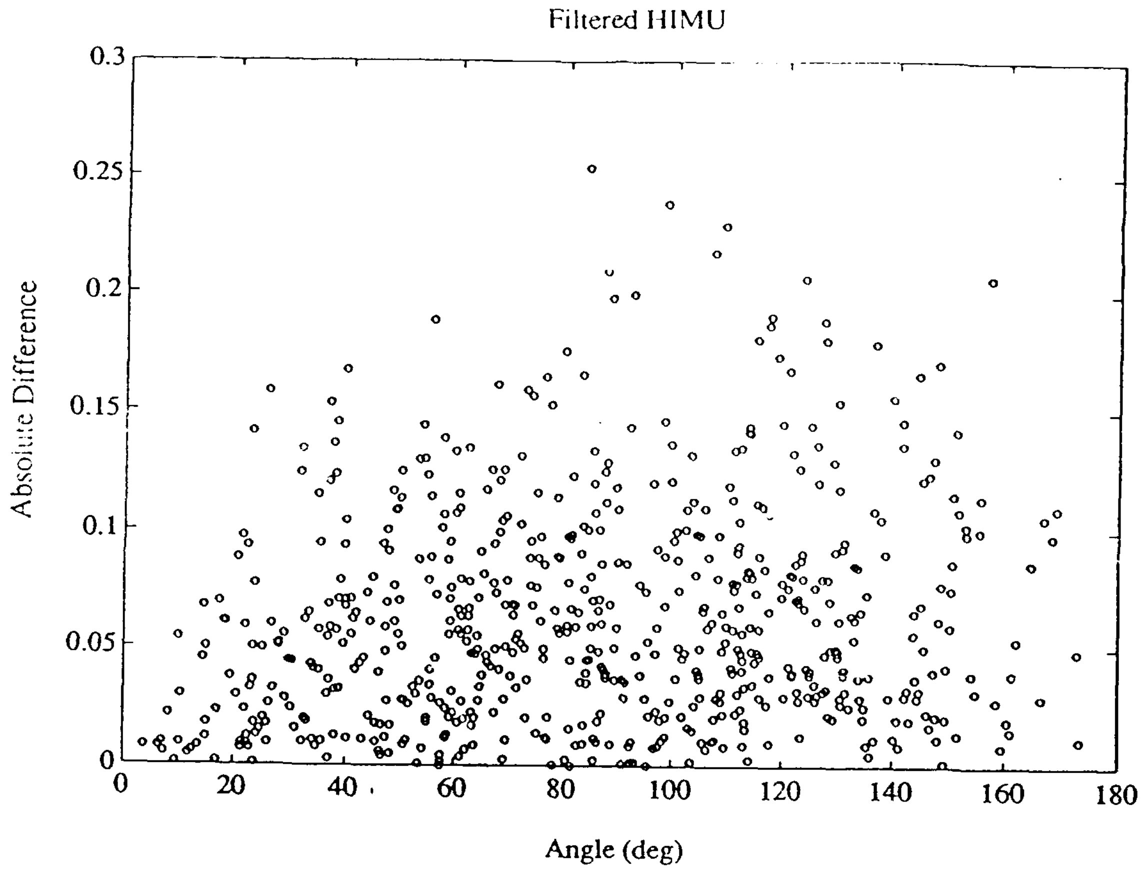

Fig. 3.13. Variation-distance plot for the filtered HIMU data set, showing the range of variation in the component percentage with angular distance after the circular filter is applied. The result is a dramatic decrease in the small-scale variation, with an increase in minimum sampling distance from ~ 14.5° to 83° [expansions to degrees 12 and 2, respectively].

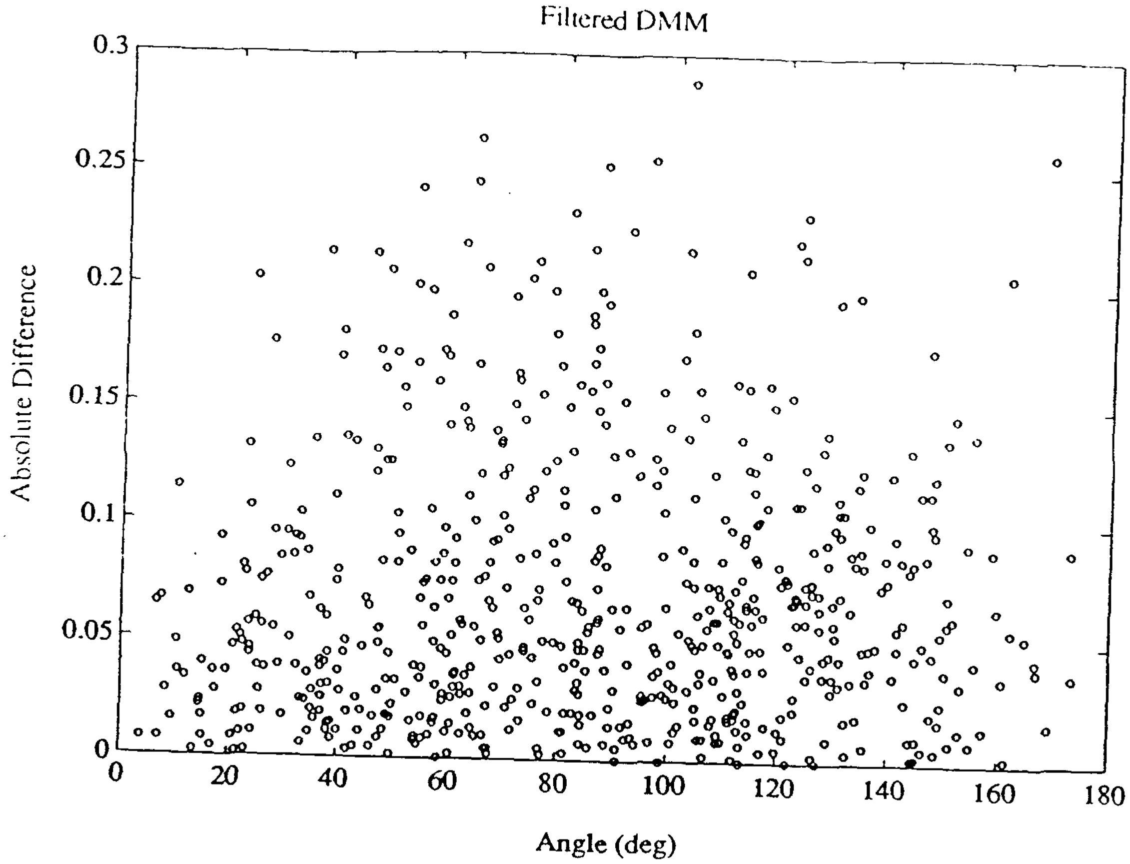

Fig. 3.14. Variation-distance plot for the filtered DMM data set, showing the range of variation in the component percentage with angular distance after the circular filter is applied. The result is a decrease in the small-scale variation, with an increase in minimum sampling distance from ~ 57° to 102° [expansions to degrees 3 and 2, respectively].

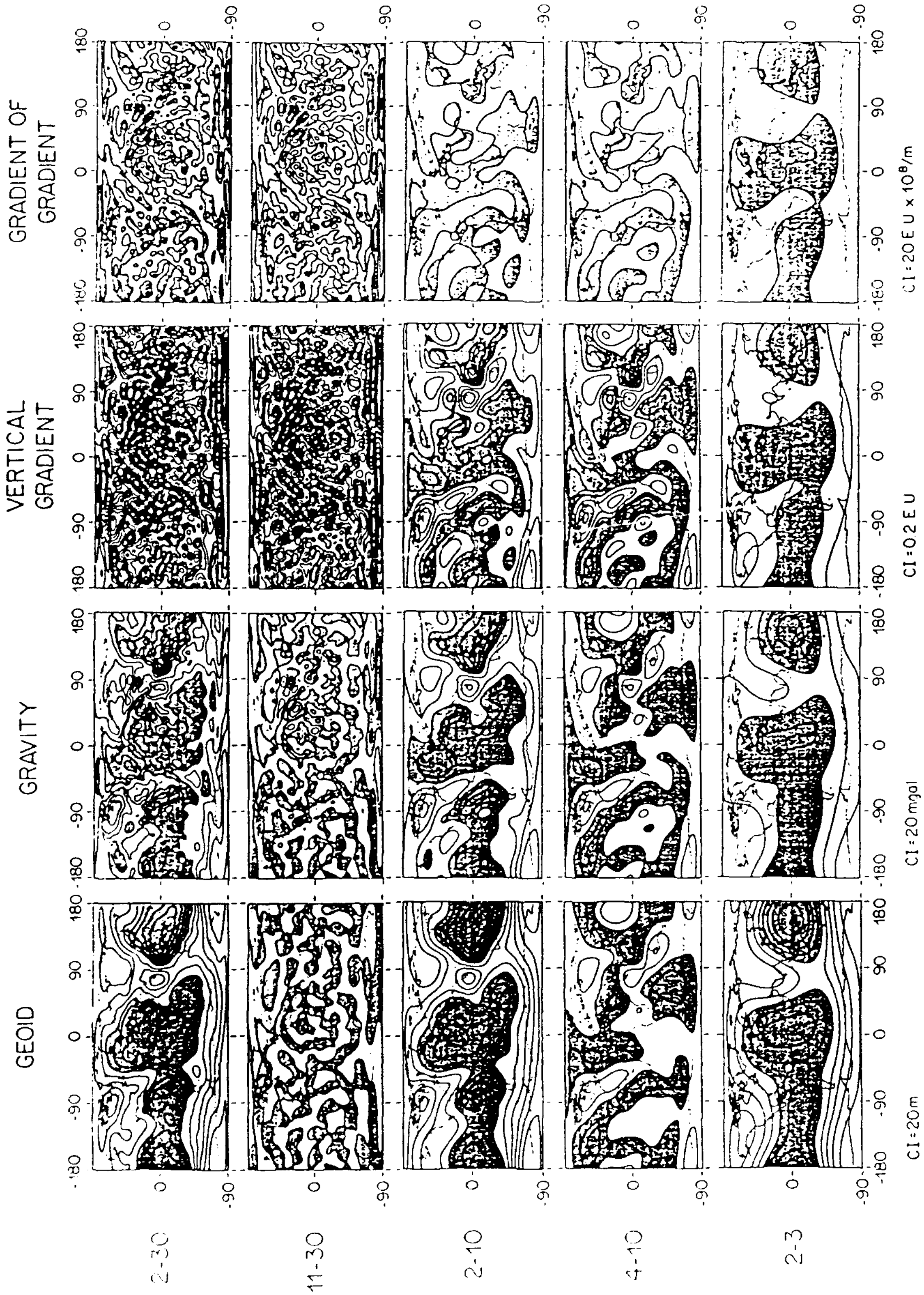

GEOID
GRAVITY
VERTICAL GRADIENT
GRADIENT OF GRADIENT
2-30
11-30
2-10
4-10
2-3
CI = 20m
CI = 20 mgal
CI = 0.2 E U
CI = 20 E U x 10^8/m

Fig. 3.15. Spherical harmonic plots of the geoid, gravity, gravity gradient and the gradient of the gradient. The degrees 2-30 plots show the appearance of the total fields. Other plots, separating this total field into contributions by high and low degrees, show the transition from long wavelength [low degree] dominance in the geoid to the short wavelength [high degree] dominance in the gravity gradient. Courtesy of Carl Bowin (1991b).

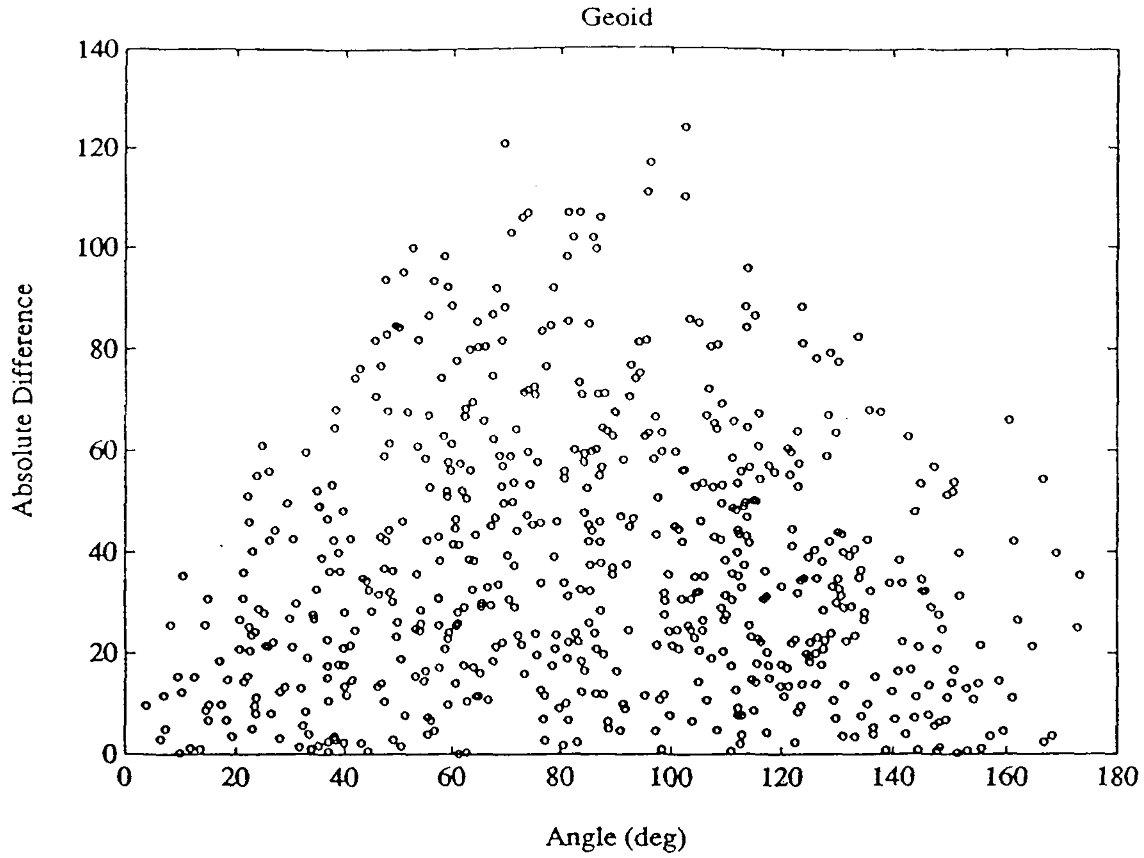

Fig. 3.16. Variation-distance plot for the constructed geoid data set showing the range of variation in the geoid with angular distance between the feature locations. To account for the variation requires a minimum sampling distance of ~ 102° [degree 2 expansion].

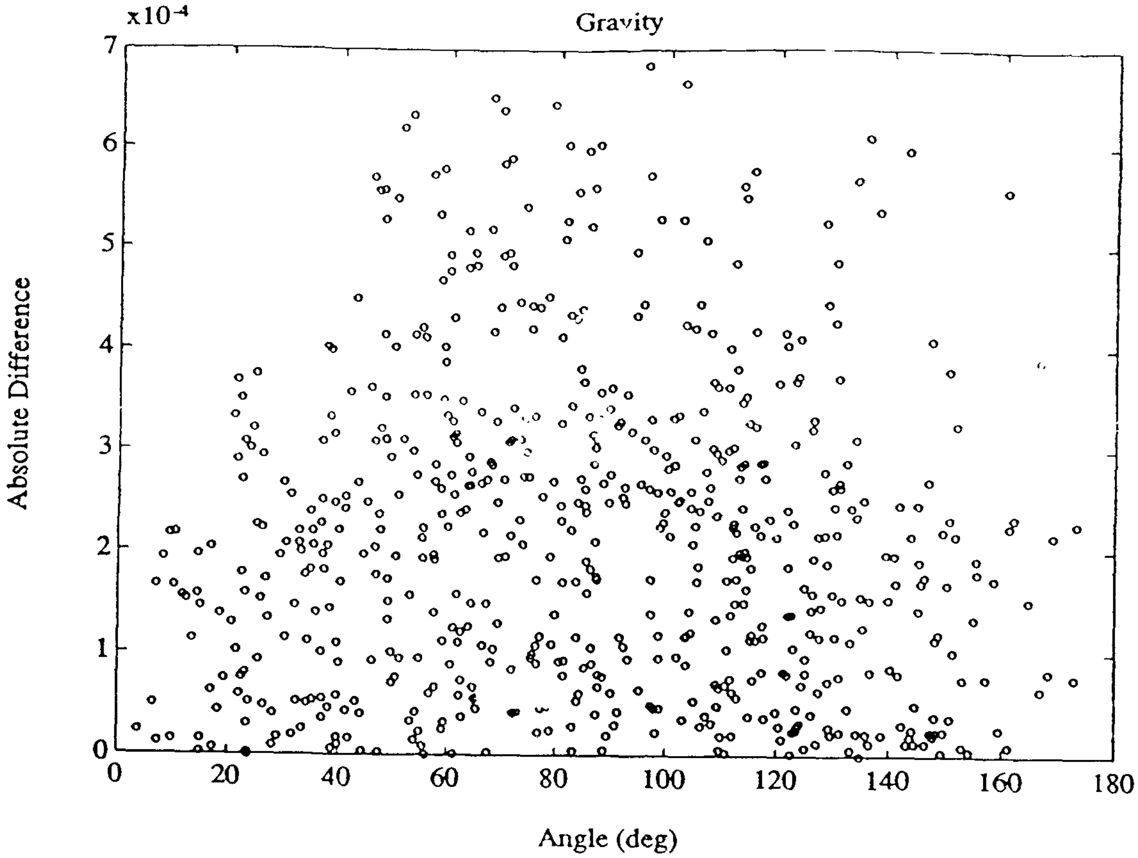

Fig. 3.17. Variation-distance plot for the constructed gravity data set showing the range of variation in gravity with angular distance between the feature locations. To account for the variation requires a minimum sampling distance of ~ 95° [degree 2 expansion].

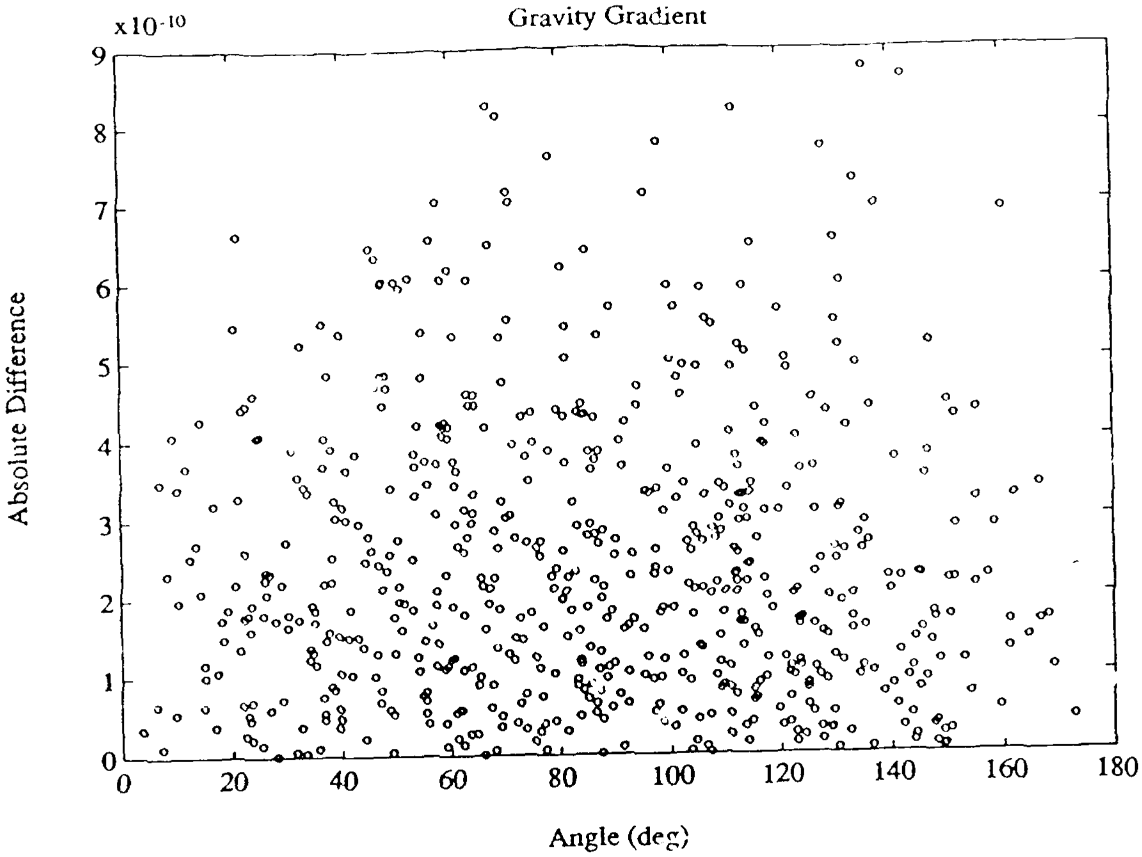

Fig. 3.18. Variation-distance plot for the constructed gravity gradient data set showing the range of variation in the gravity gradient with angular distance between the feature locations. To account for the variation requires a minimum sampling distance of ~ 67° [degree 3 expansion].

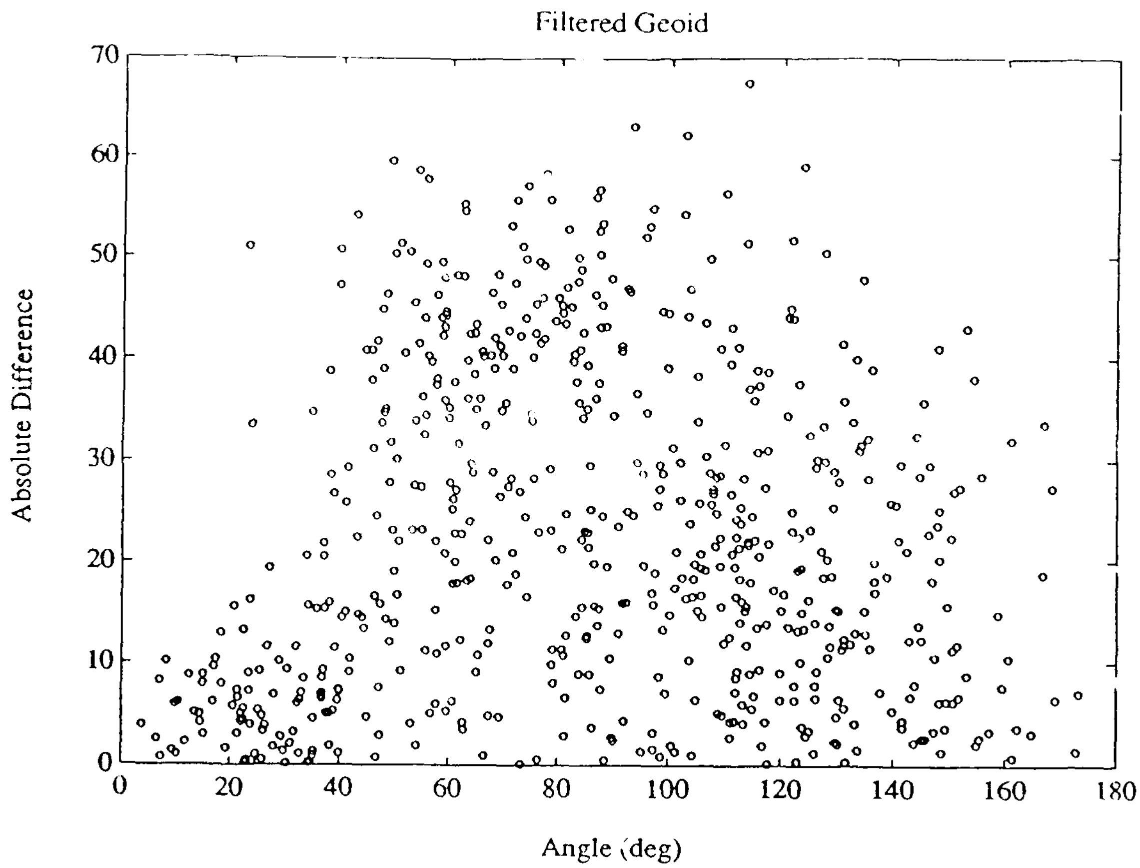

Fig. 3.19. Variation-distance plot for the filtered geoid data set, showing the range of variation in the geoid with angular distance after the circular filter is applied. The filtered geoid data set retains essentially the same angular sampling distance [~ 93°].

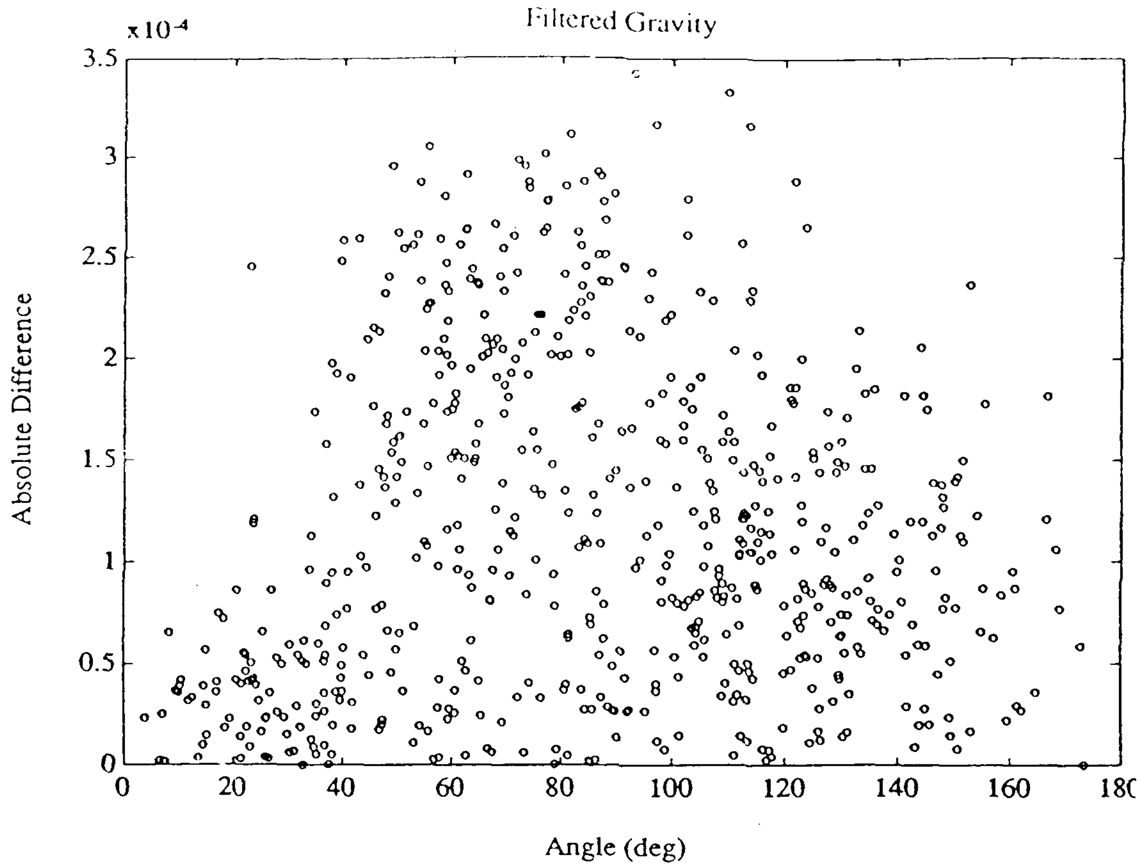

Fig. 3.20. Variation-distance plot for the filtered gravity data set, showing the range of variation in gravity with angular distance after the circular filter is applied. The filtered gravity data set retains essentially the same angular sampling distance [~ 93°].

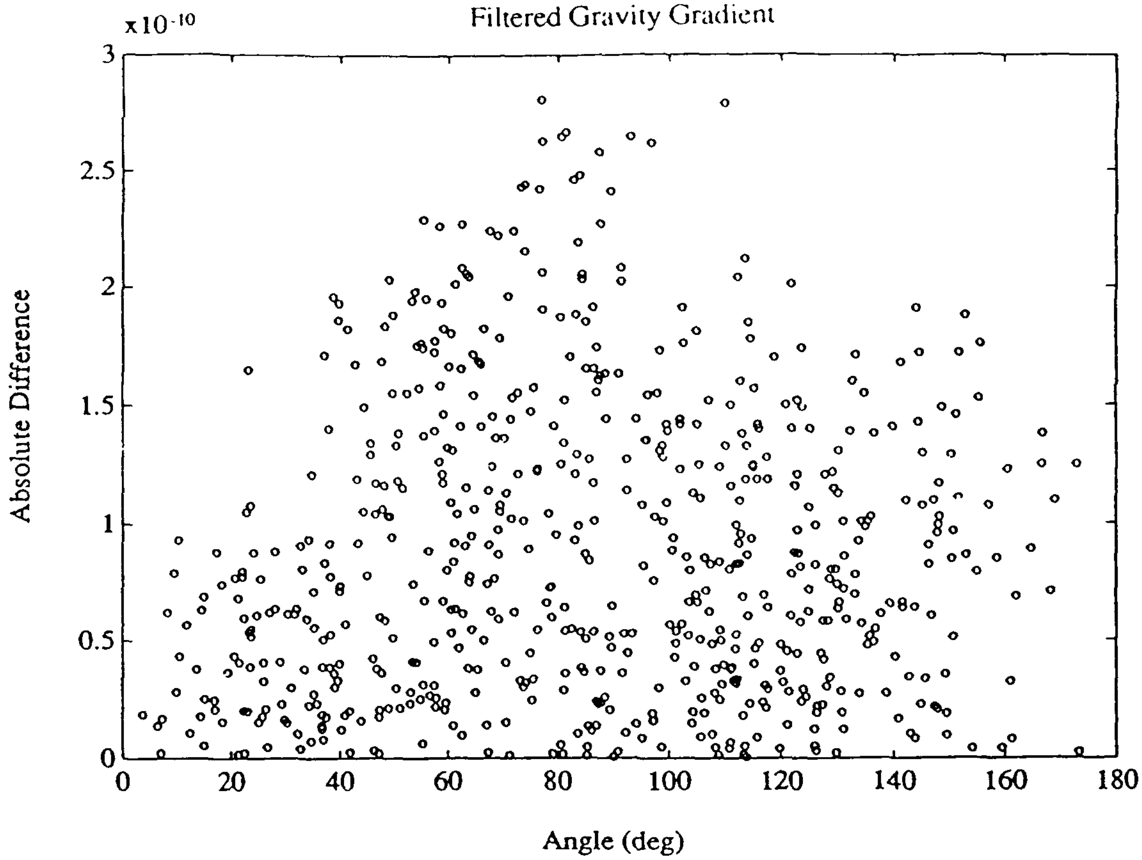

Fig. 3.21. Variation-distance plot for the filtered gravity gradient data set, showing the range of variation in the gravity gradient with angular distance after the circular filter is applied. Filtering reduces the small-scale varition in the gravity gradient data set, with an increase of angular sampling distance from ~ 67° to 77° [expansions to degrees 3 and 2, respectively].

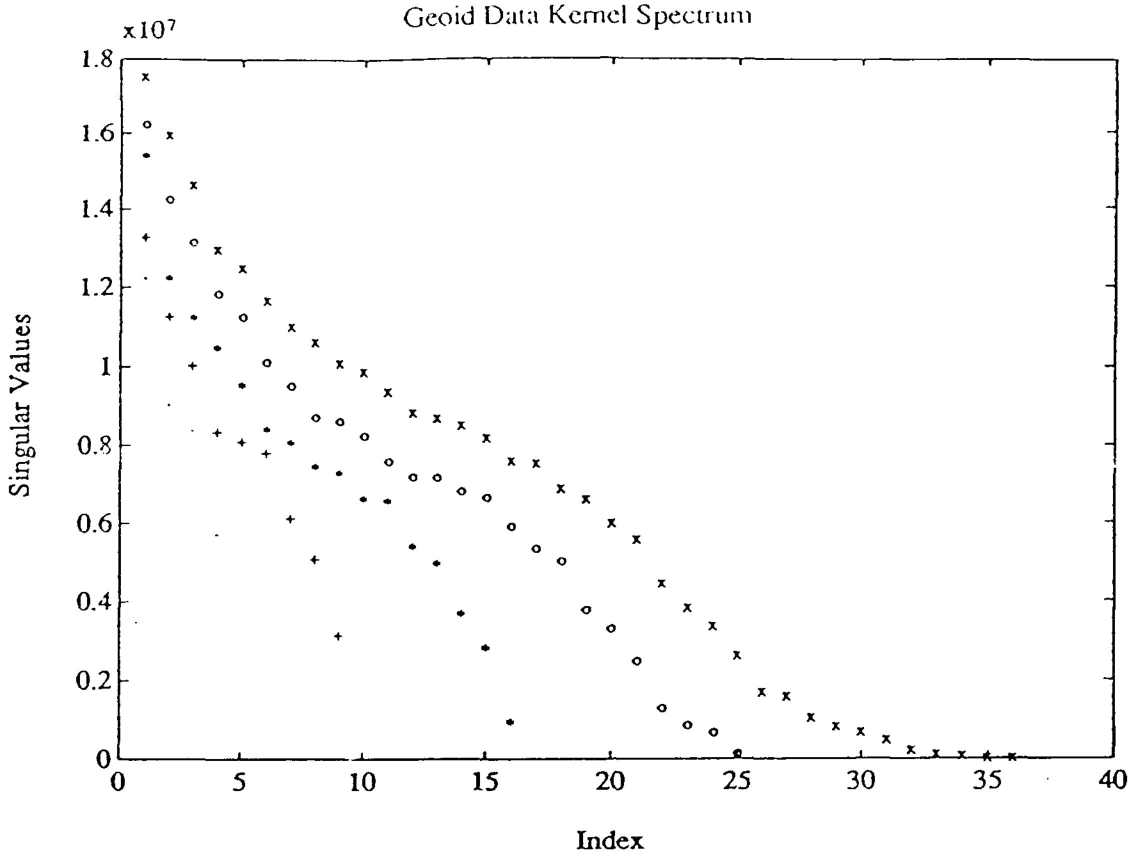

Fig. 3.22. Data kernel spectrums for the constructed geoid data kernel **G**. Symbols for the different expansions: · = degrees 0-1, + = degrees 0-2, * = degrees 0-3, o = degrees 0-4, x = degrees 0-5. For the degrees 0-5 expansion, the singular values approach zero, but there is no obvious cutoff value.

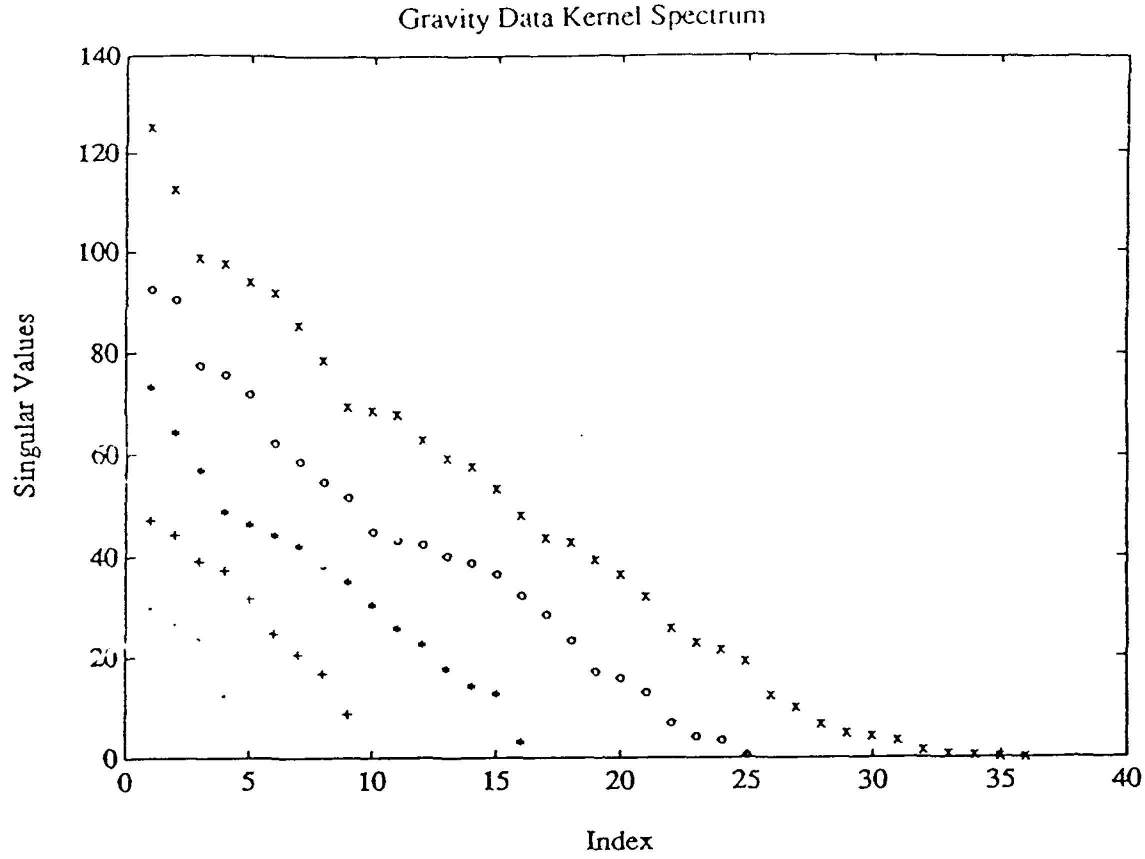

Fig. 3.23. Data kernel spectrums for the constructed gravity data kernel **G**. Symbols for the different expansions: · = degrees 0-1, + = degrees 0-2, * = degrees 0-3, o = degrees 0-4, x = degrees 0-5. For the degrees 0-5 expansion, the singular values approach zero, but there is no obvious cutoff value.

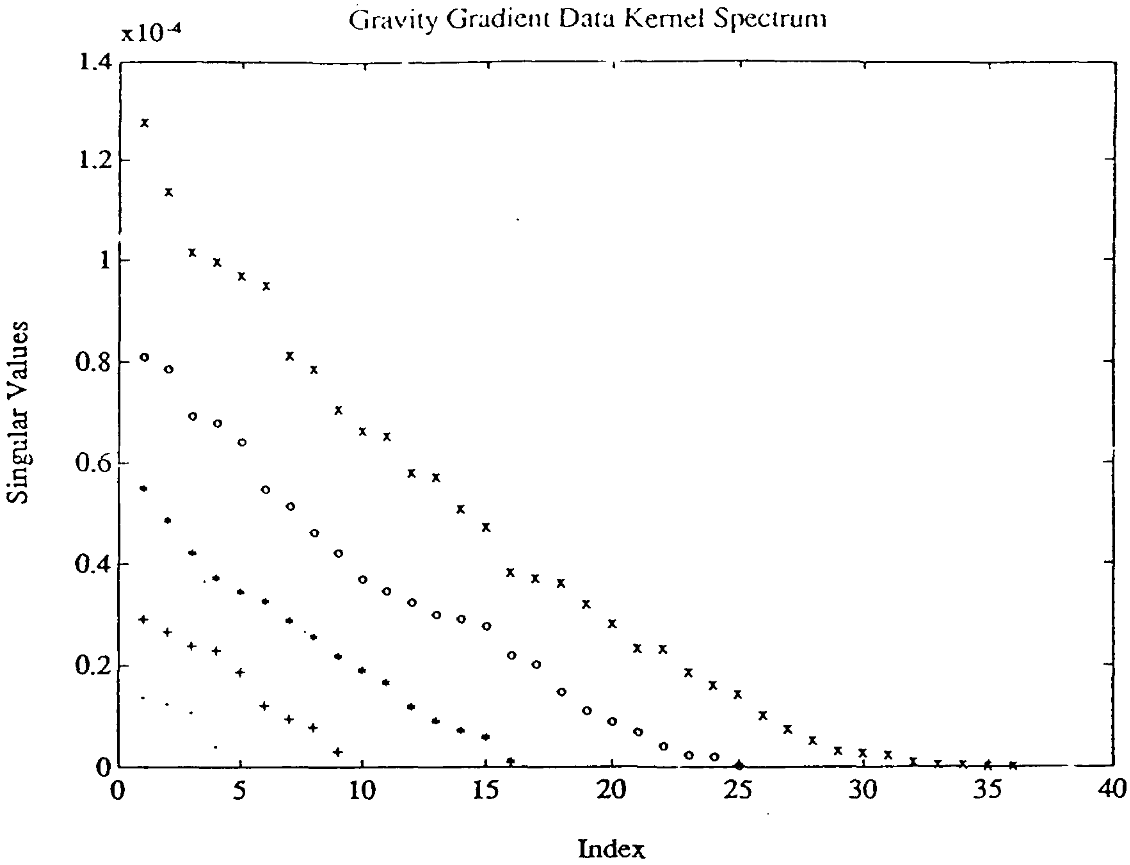

Fig. 3.24. Data kernel spectrums for the constructed gravity gradient data kernel **G**. Symbols for the different expansions: · = degrees 0-1, + = degrees 0-2, * = degrees 0-3, o = degrees 0-4, x = degrees 0-5. For the degrees 0-5 expansion, the singular values approach zero, but there is no obvious cutoff value.

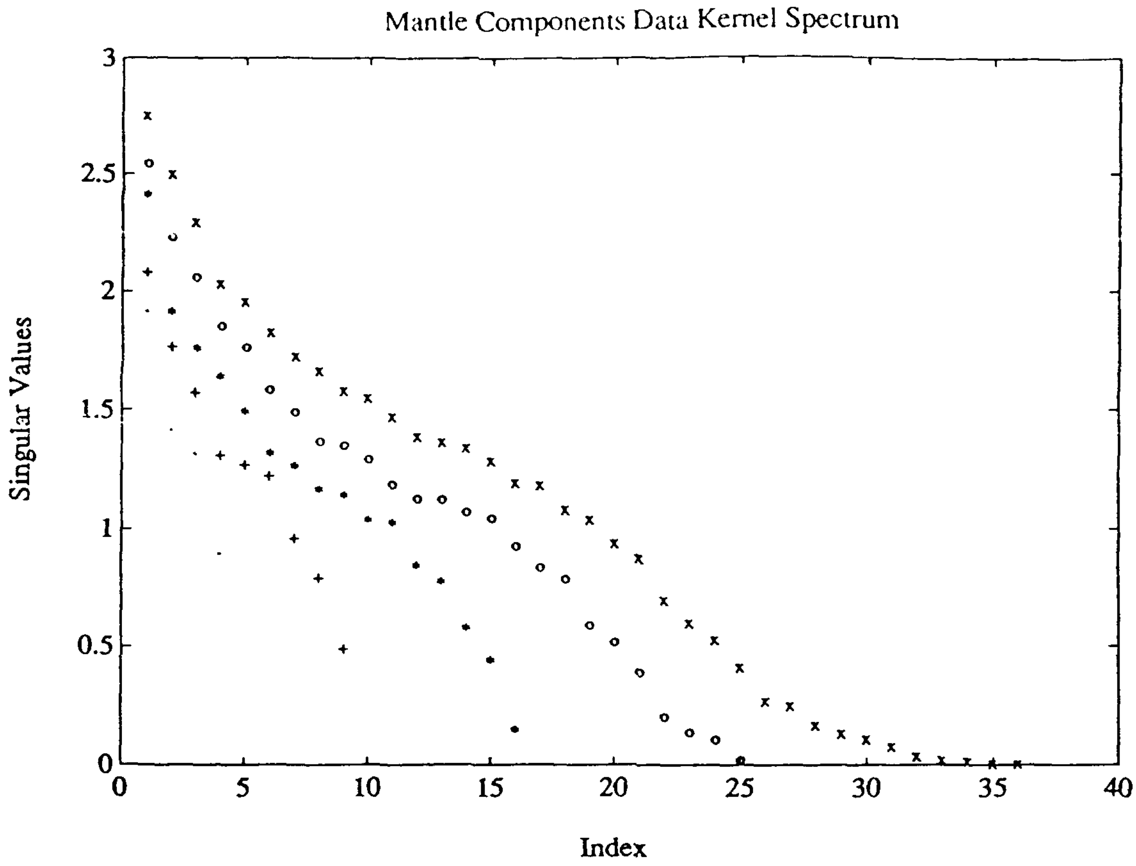

Fig. 3.25. Data kernel spectrums for the mantle component data kernel G. Symbols for the different expansions: · = degrees 0-1, + = degrees 0-2, * = degrees 0-3, o = degrees 0-4, x = degrees 0-5. For the degrees 0-5 expansion, the singular values approach zero, but there is no obvious cutoff value.

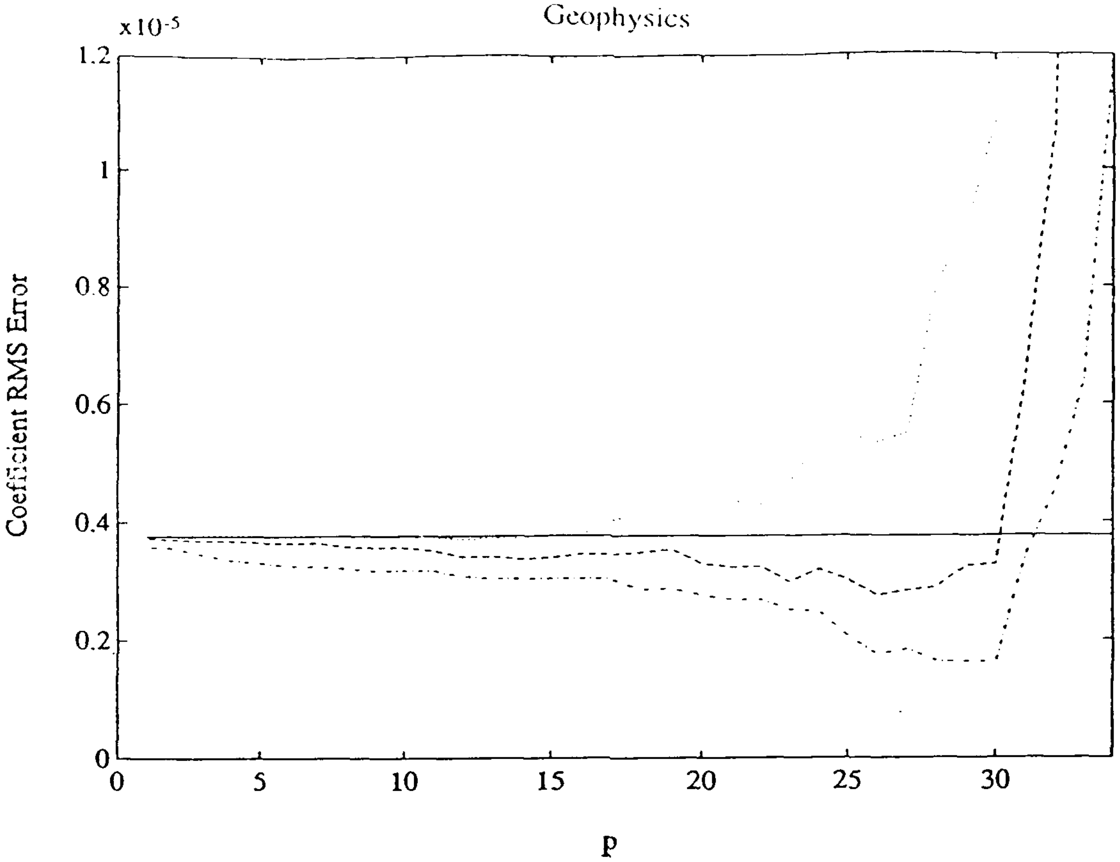

Fig. 3.26. Plot of the root mean square error [rms error], as a function of the number of singular values retained, between the actual GEM-L2 coefficients and those coefficients estimated by the constructed geoid, gravity and gravity gradient data sets. Line symbols: – . – . = geoid, - - - - = gravity, · · · · = gravity gradient, —— = root mean square of the GEM-L2 coefficients. *P* values minimizing coefficient rms error: geoid = 30, gravity = 26, gravity gradient = 14.

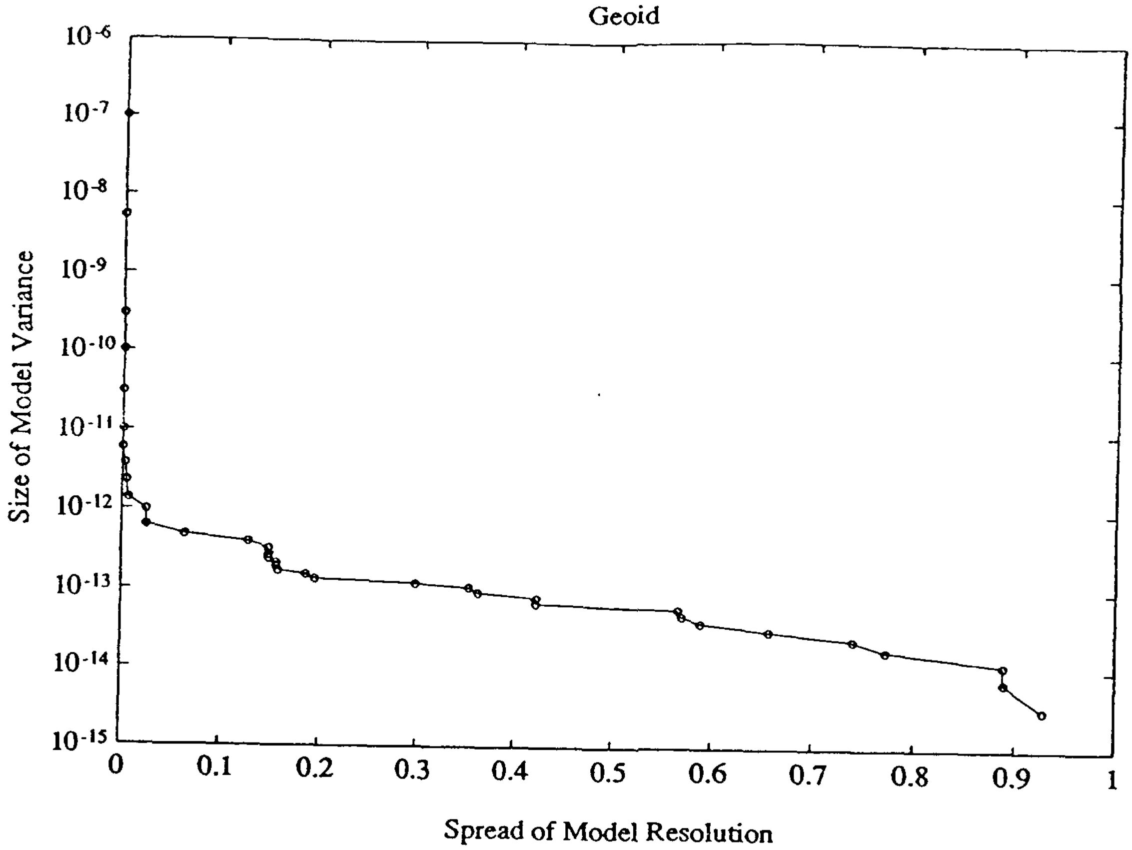

Fig. 3.27. Trade-off curve between model variance and model resolution, as a function of the number of singular values retained, for the constructed geoid data set. Range for p that balances the two measures is: $15 \leq p \leq 30$. Note that trade-off curves are determined by the data kernel matrices and so are the same for filtered and unfiltered data sets.

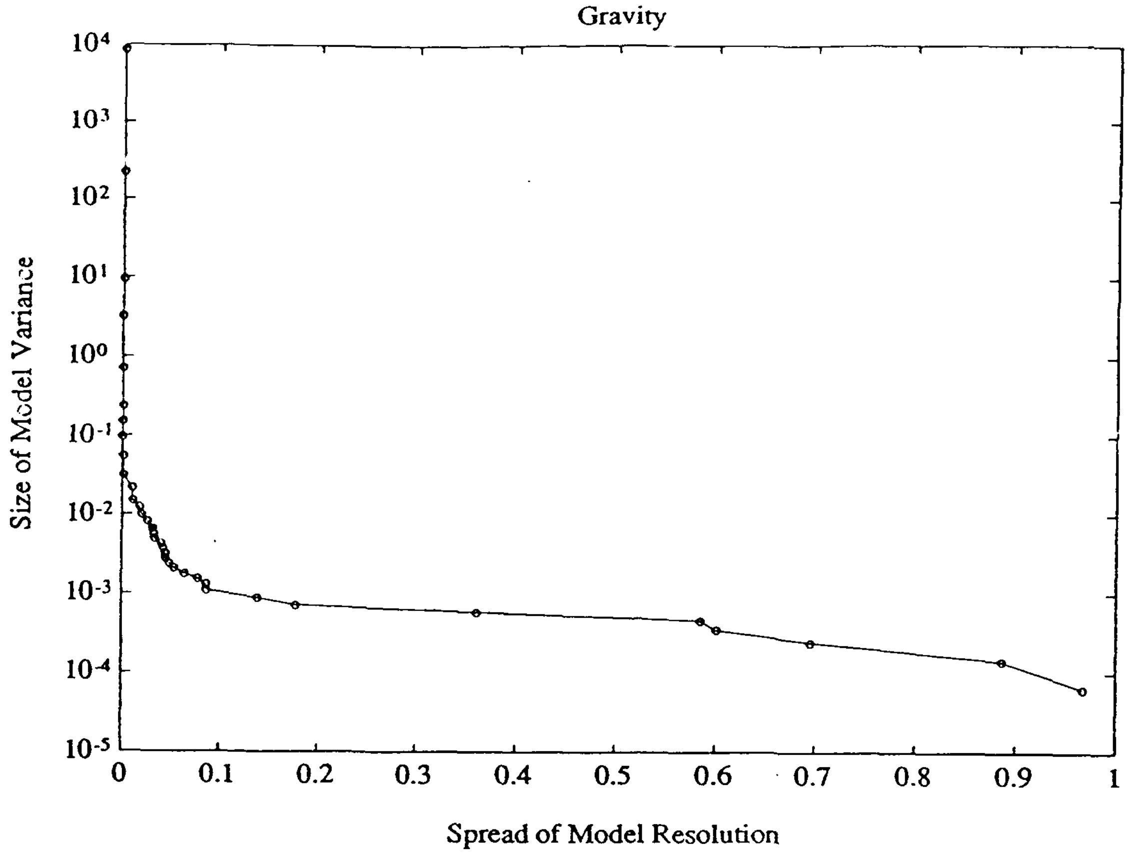

Fig. 3.28. Trade-off curve between model variance and model resolution, as a function of the number of singular values retained, for the constructed gravity data set. Range for p that balances the two measures is: $9 \leq p \leq 29$. Note that trade-off curves are determined by the data kernel matrices and so are the same for filtered and unfiltered data sets.

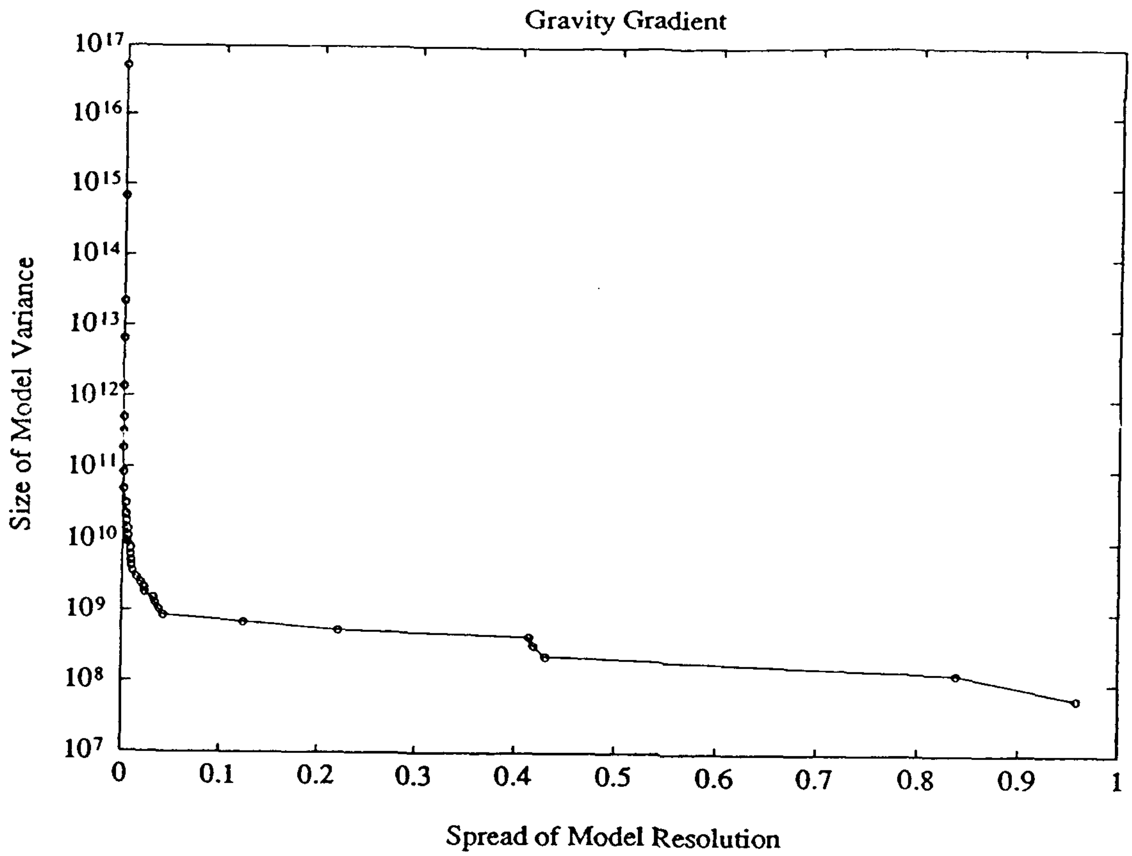

Fig. 3.29. Trade-off curve between model variance and model resolution, as a function of the number of singular values retained, for the constructed gravity gradient data set. Range for p that balances the two measures is: $8 \leq p \leq 26$. Note that trade-off curves are determined by the data kernel matrices and so are the same for filtered and unfiltered data sets.

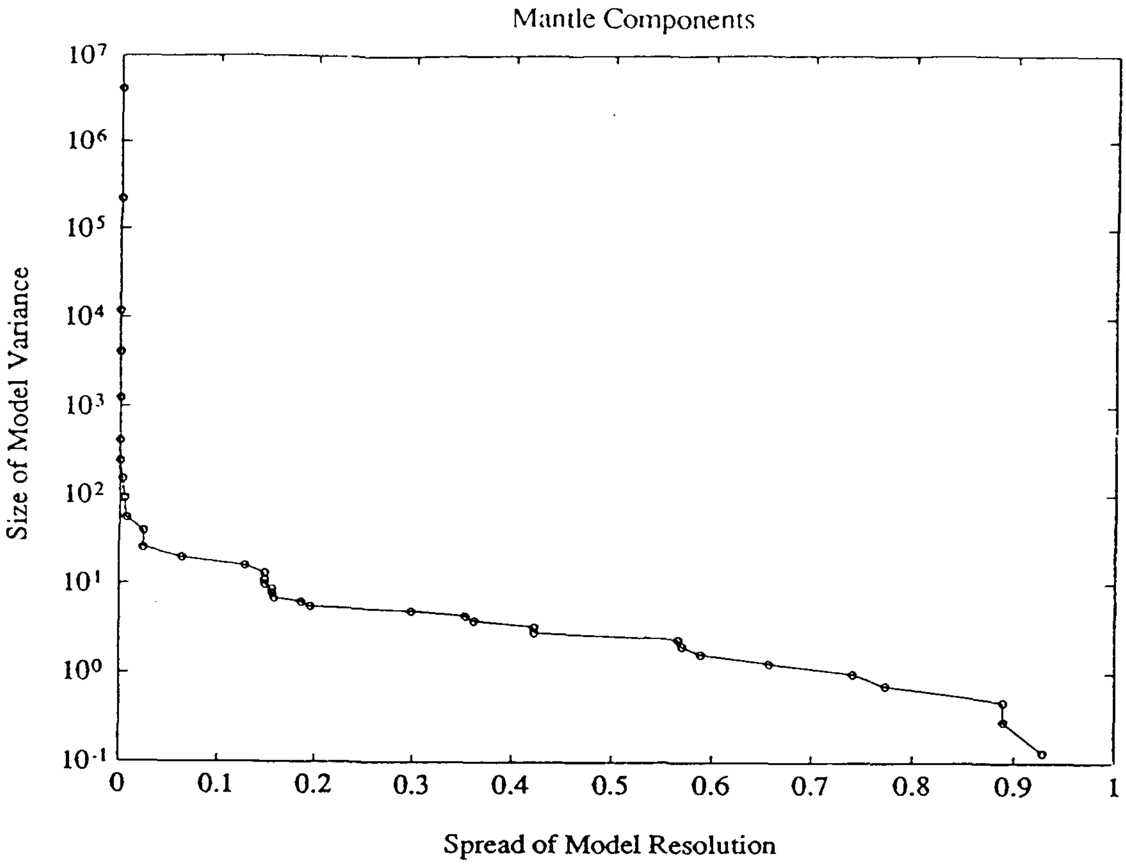

Fig. 3.30. Trade-off curve between model variance and model resolution, as a function of the number of singular values retained, for the mantle component data set. Range for p that balances the two measures is: $15 \leq p \leq 30$. Note that trade-off curves are determined by the data kernel matrices and so are the same for filtered and unfiltered data sets.

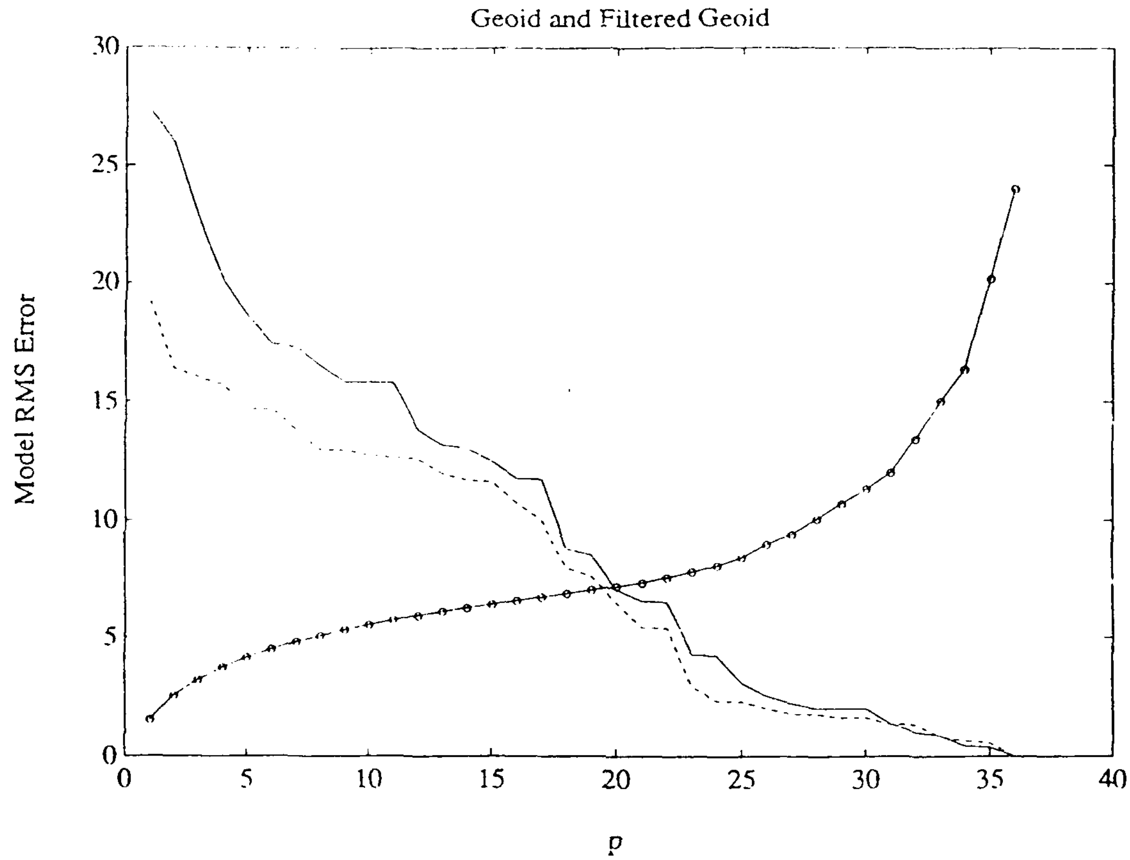

Fig. 3.31. Plot of model root mean square error [rms error], as a function of the number of singular values retained, between the observed geoid data and the geoid data predicted from the calculated coefficients. Balancing the model rms error and the model variance gives this range of p: $21 \leq p \leq 25$ (filtered and unfiltered). Line symbols: —— = unfiltered model rms error, - - - - = filtered model rms error, o—o— = model variance.

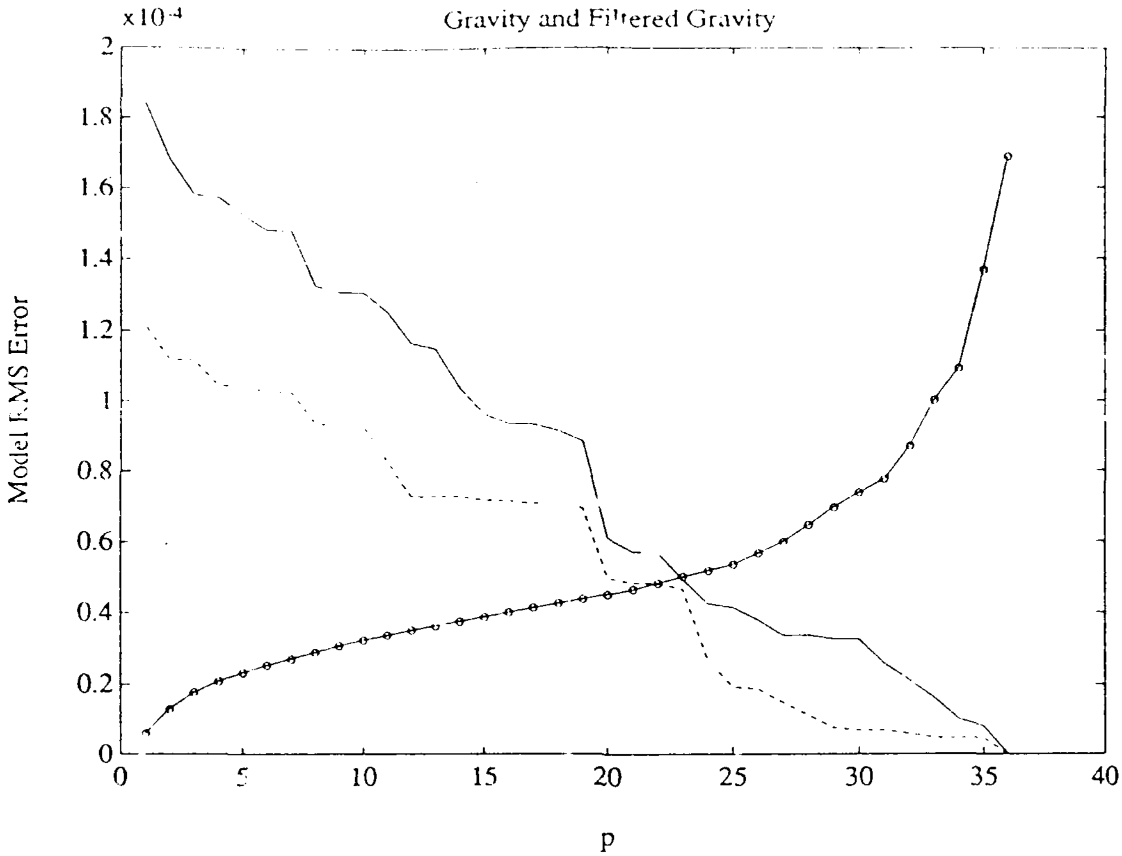

Fig. 3.32. Plot of model root mean square error [rms error], as a function of the number of singular values retained, between the observed gravity data and the gravity data predicted from the calculated coefficients. Balancing the model rms error and the model variance gives this range of p: $20 \leq p \leq 25$ (filtered and unfiltered). Line symbols: —— = unfiltered model rms error, - - - - = filtered model rms error, o—o— = model variance.

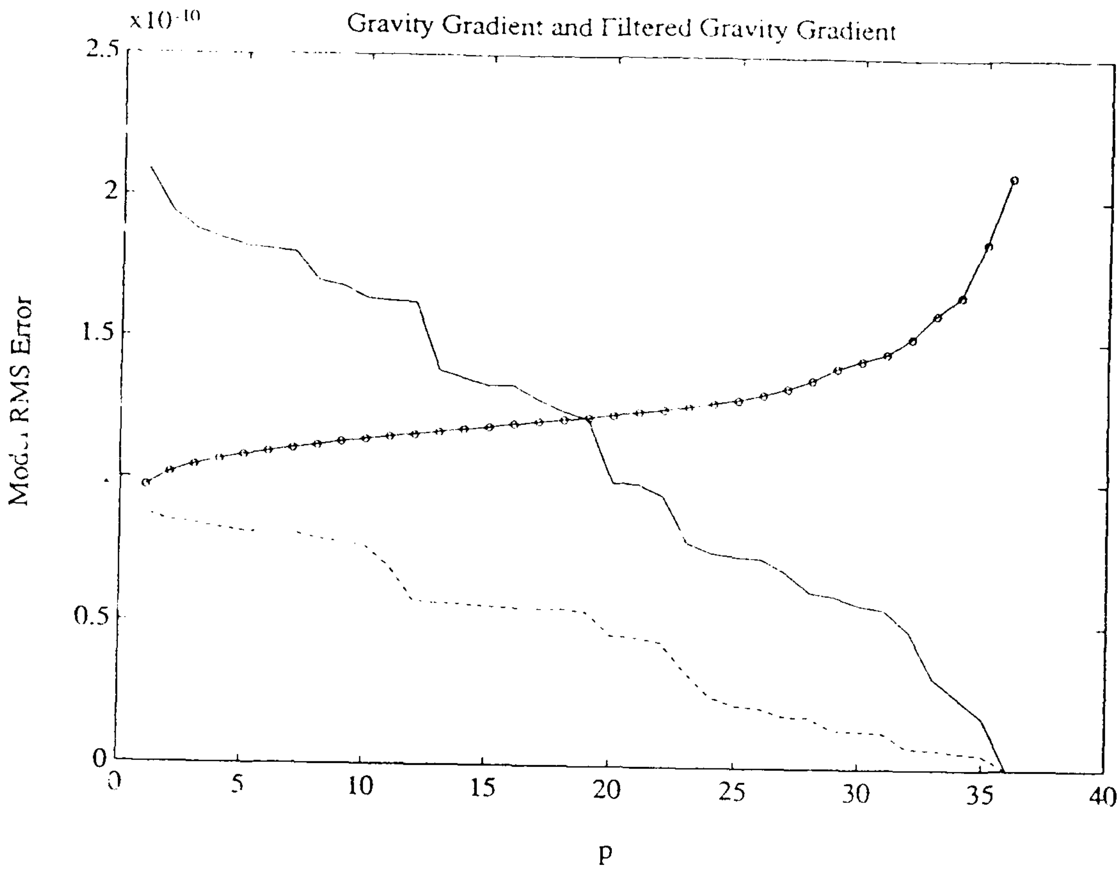

Fig. 3.33. Plot of model root mean square error [rms error], as a function of the number of singular values retained, between the observed gravity gradient data and the gravity gradient data predicted from the calculated coefficients. Balancing the model rms error and the model variance gives this range for p: $20 \leq p \leq 25$ (filtered and unfiltered). Line symbols: —— = unfiltered model rms error, - - - - = filtered model rms error, o—o— = model variance.

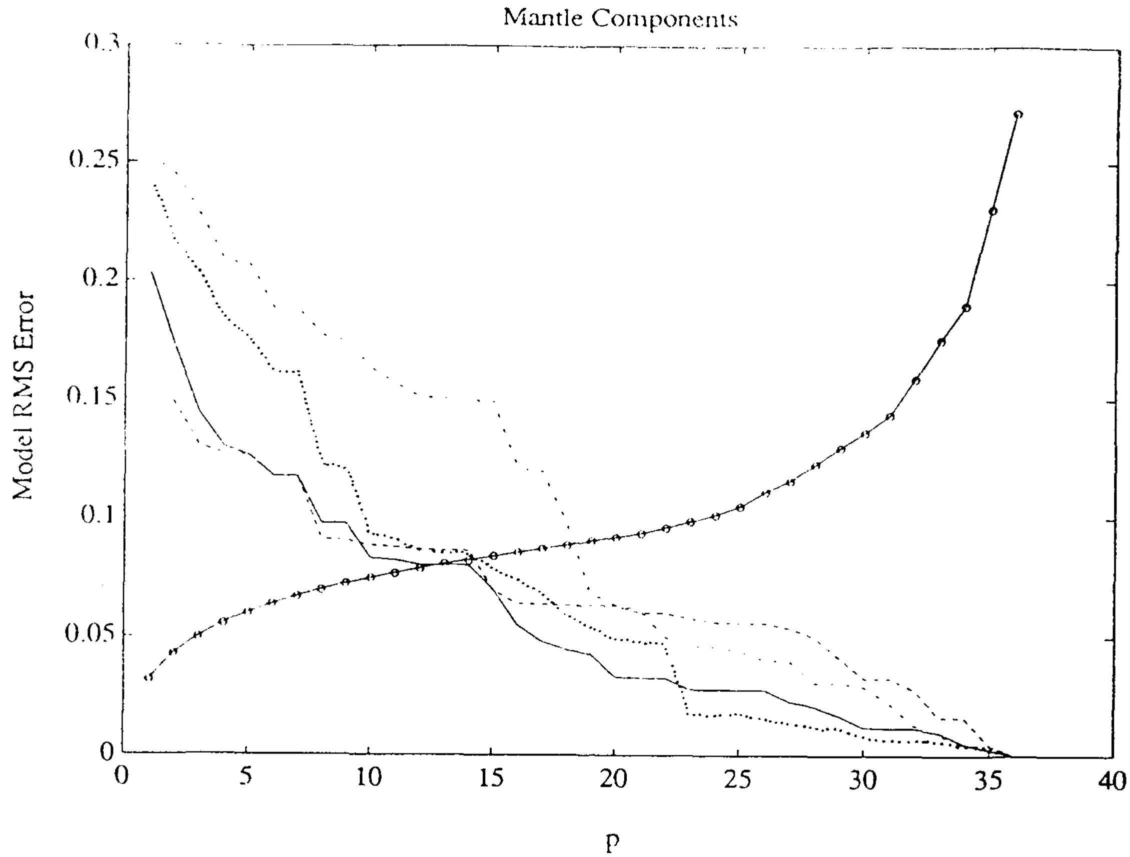

Fig. 3.34. Plot of model root mean square error [rms error], as a function of the number of singular values retained, between the observed mantle component data and the mantle component data predicted from the calculated coefficients. Balancing the model rms error and the model variance gives this range for p: $16 \leq p \leq 21$ (filtered EMI), $16 \leq p \leq 20$ (EMII), $18 \leq p \leq 23$ (filtered HIMU), $19 \leq p \leq 22$ (DMM). Line symbols: —— = filtered EMI, - - - - = EMII, · · · · = filtered HIMU, - · - · = DMM, o—o— = model variance.

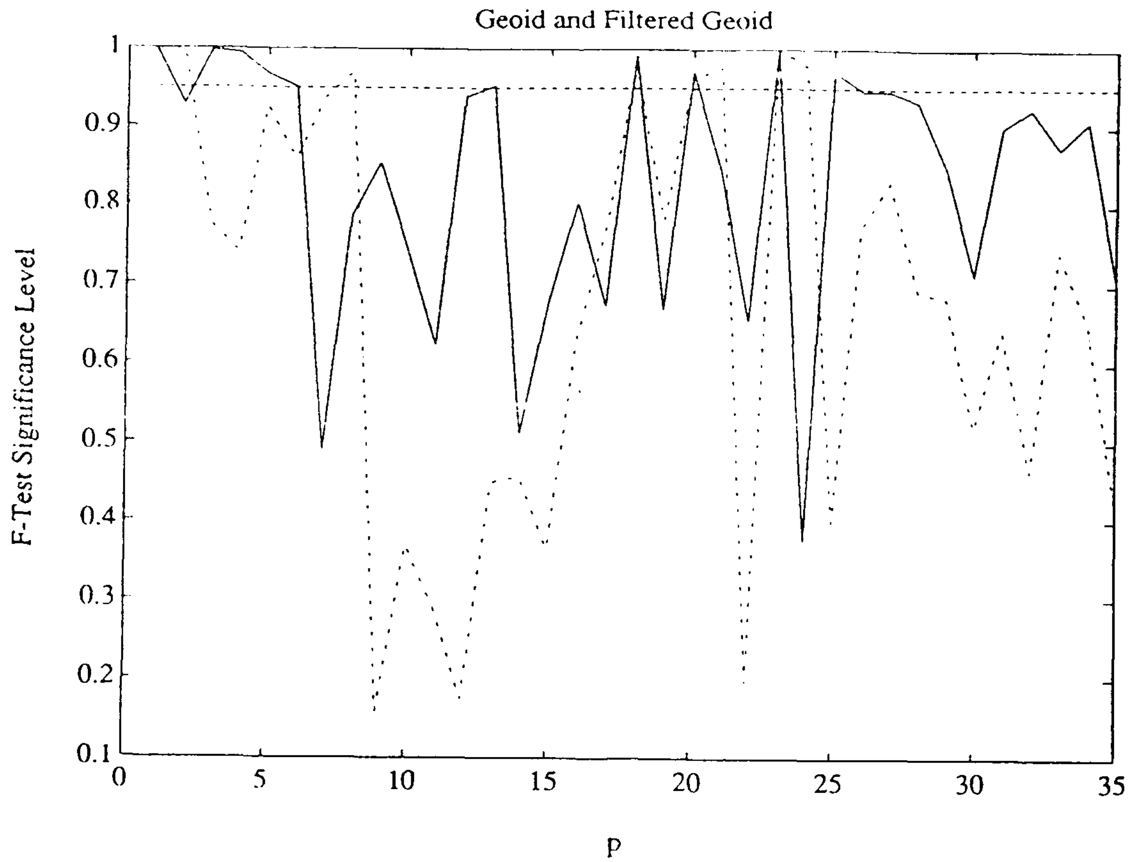

Fig. 3.35. Plot of F-test significance level as a function of the number of singular values retained for the geoid and filtered geoid data sets. Basically, the test determines whether additional parameters [singular values] make a significant contribution to the model fit of the observed data values. Optimal p values [for 95% significance] are: $p = 25$ [geoid] and $p = 24$ [filtered geoid]. Line symbols: —— = geoid, - · - · = filtered geoid, - - - - = 95% significance level.

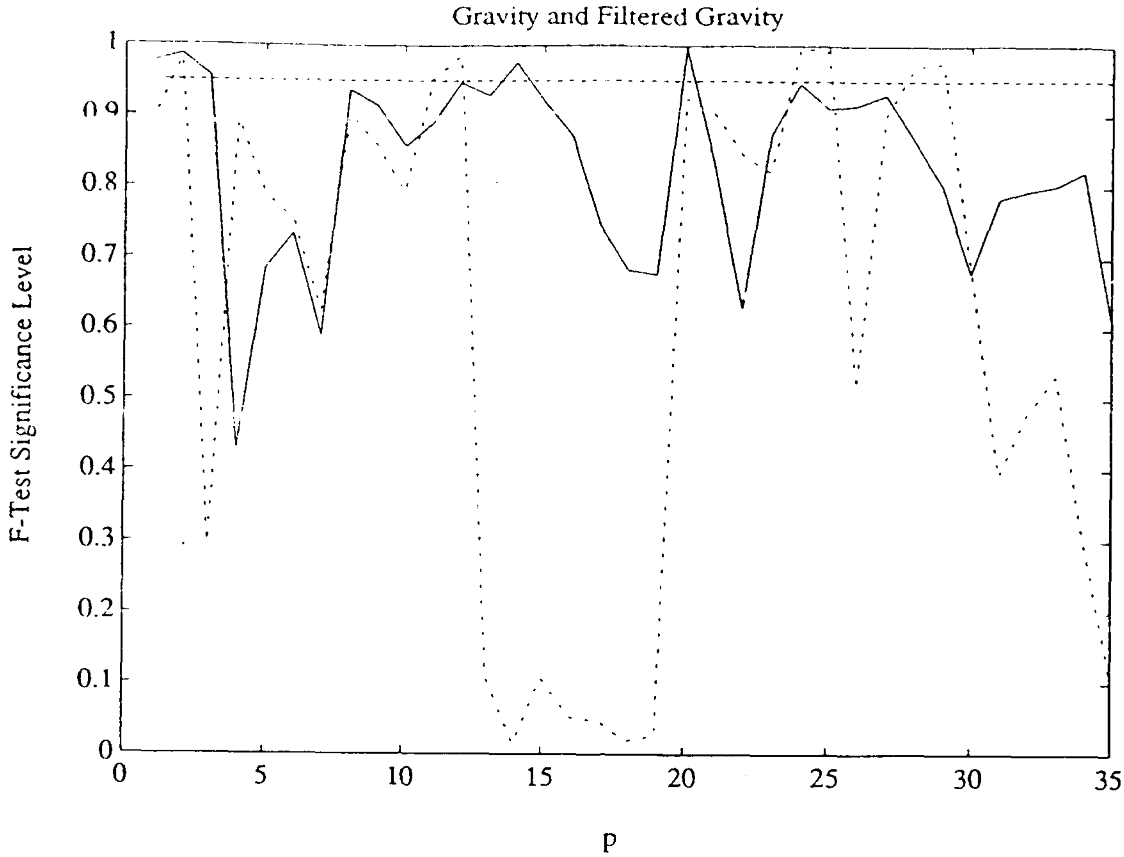

Fig. 3.36. Plot of F-test significance level as a function of the number of singular values retained for the gravity and filtered gravity data sets. Basically, the test determines whether additional parameters [singular values] make a significant contribution to the model fit of the observed data values. Optimal *p* values [for 95% significance] are: *p* = 20 [gravity] and *p* = 29 [filtered gravity]. Line symbols: —— = gravity, - · - · = filtered gravity, - - - - = 95% significance level.

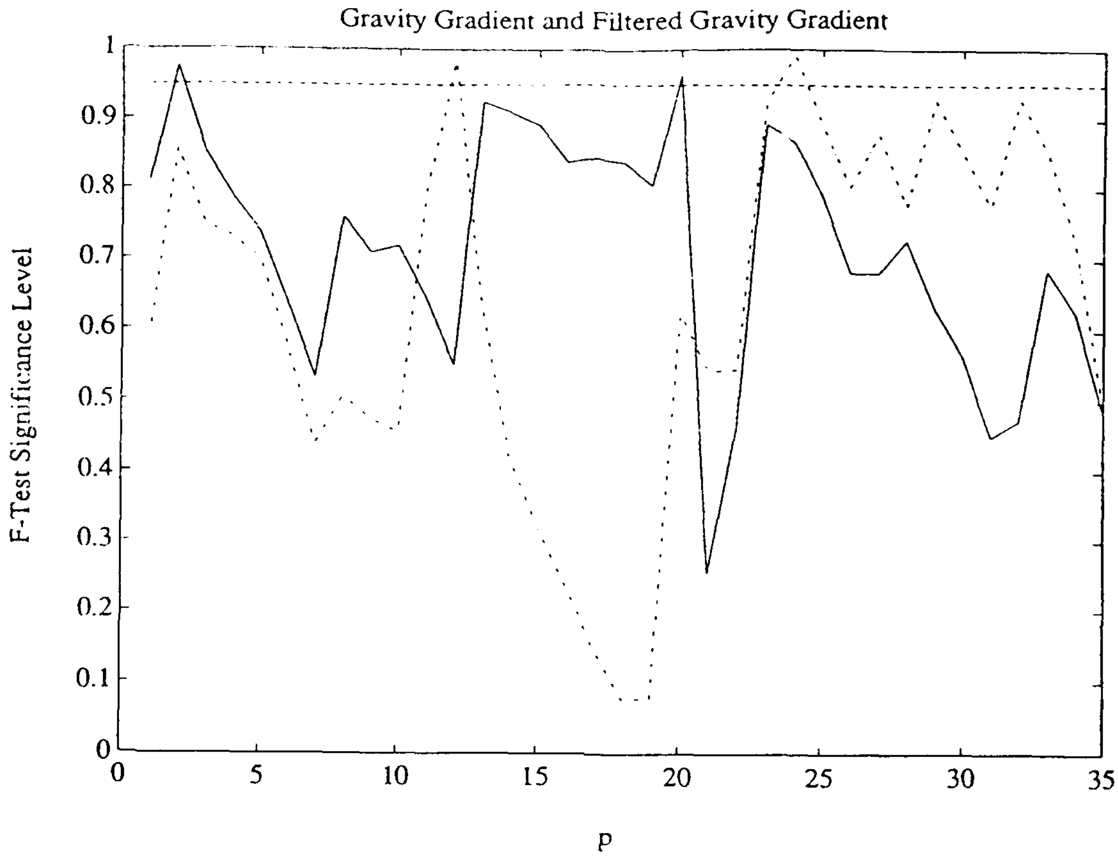

Fig. 3.37. Plot of F-test significance level as a function of the number of singular values retained for the gravity gradient and filtered gravity gradient data sets. Basically, the test determines whether additional parameters [singular values] make a significant contribution to the model fit of the observed data values. Optimal p values [for 95% significance] are: $p = 20$ [gravity gradient] and $p = 24$ [filtered gravity gradient]. Line symbols: ——— = gravity gradient, - · - · = filtered gravity gradient, - - - - = 95% significance level.

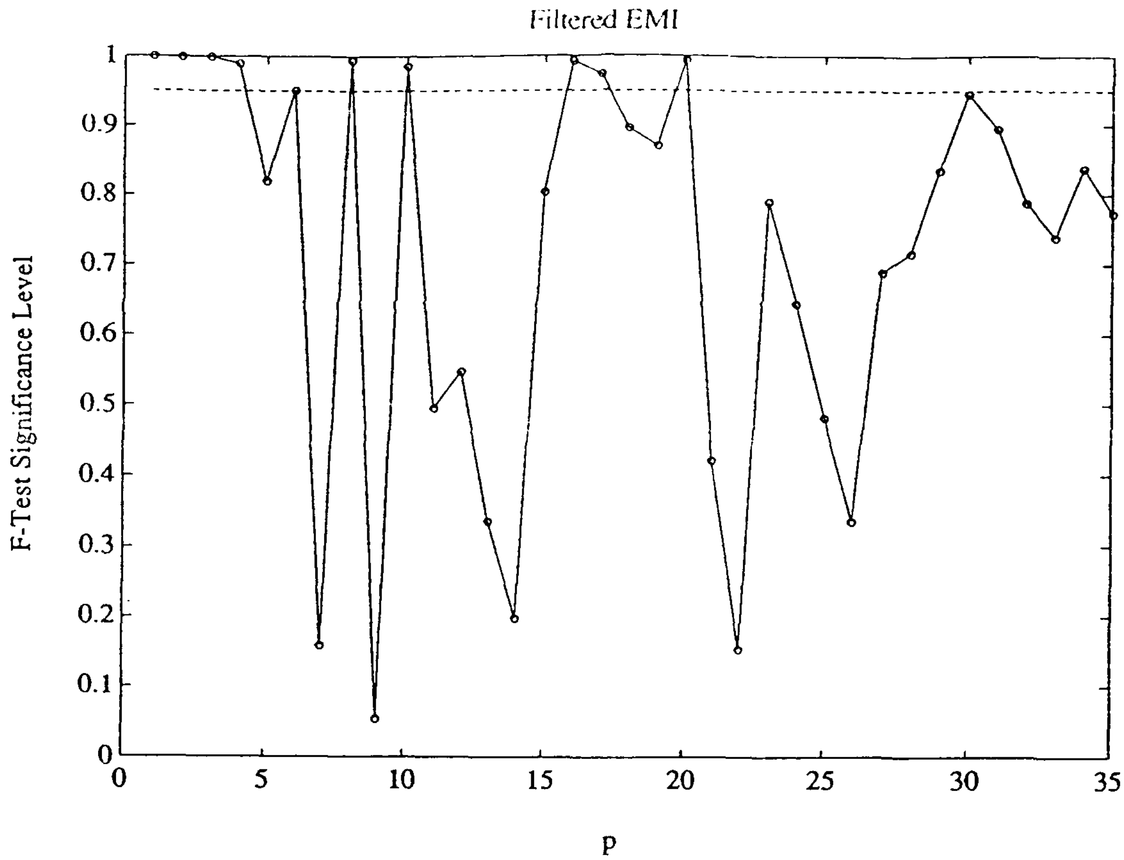

Fig. 3.38. Plot of F-test significance level as a function of the number of singular values retained for the filtered EMI data set. Basically, the test determines whether additional parameters [singular values] make a significant contribution to the model fit of the observed data values. For filtered EMI, the optimal p value [for 95% significance] is: $p = 20$. Line symbols: o——o = filtered EMI, - - - - = 95% significance level.

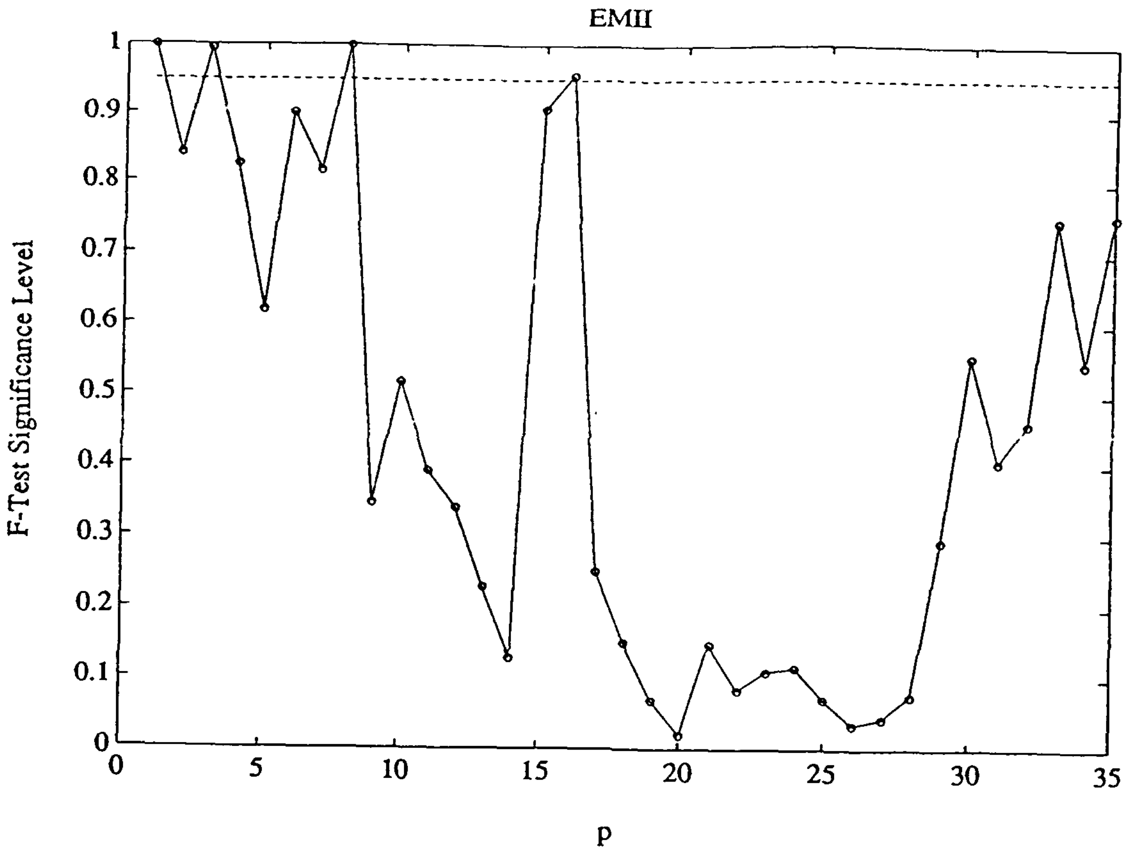

Fig. 3.39. Plot of F-test significance level as a function of the number of singular values retained for the EMII data set. Basically, the test determines whether additional parameters [singular values] make a significant contribution to the model fit of the observed data values. For EMII, the optimal p value [for 95% significance] is: $p = 16$. Line symbols: o—o = EMII, - - - - = 95% significance level.

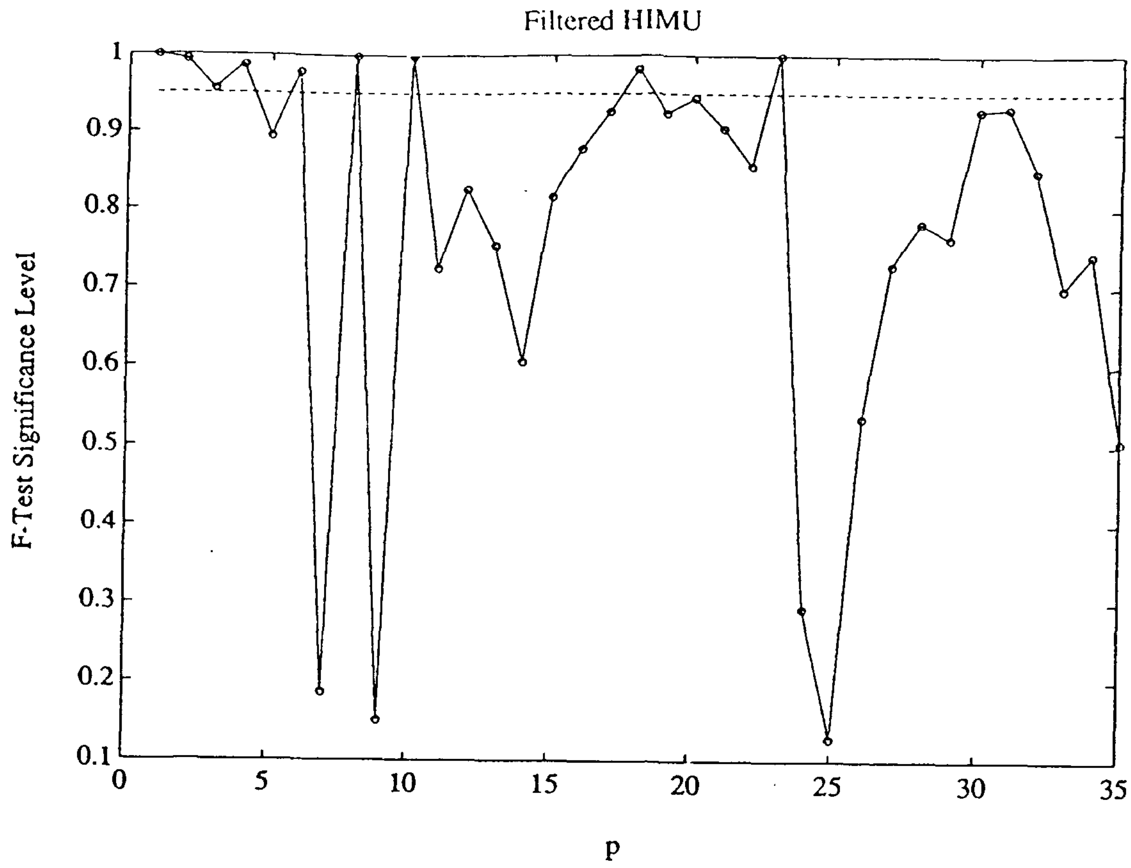

Fig. 3.40. Plot of F-test significance level as a function of the number of singular values retained for the filtered HIMU data set. Basically, the test determines whether additional parameters [singular values] make a significant contribution to the model fit of the observed data values. For filtered HIMU, the optimal p value [for 95% significance] is: $p = 23$. Line symbols: o——o = filtered HIMU, - - - - = 95% significance level.

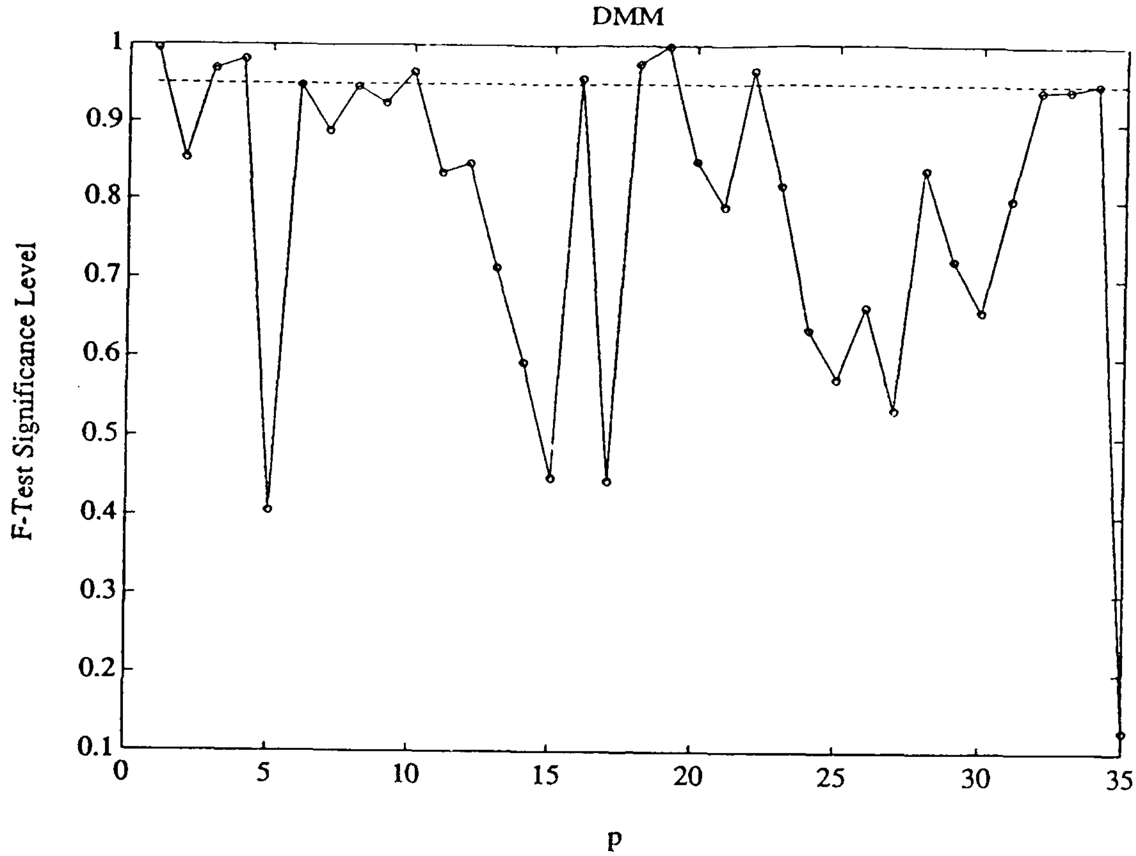

Fig. 3.41. Plot of F-test significance level as a function of the number of singular values retained for the DMM data set. Basically, the test determines whether additional parameters [singular values] make a significant contribution to the model fit of the observed data values. For DMM, the optimal p value [for 95% significance] is: $p = 22$. Line symbols: o—o = DMM, - - - - = 95% significance level.

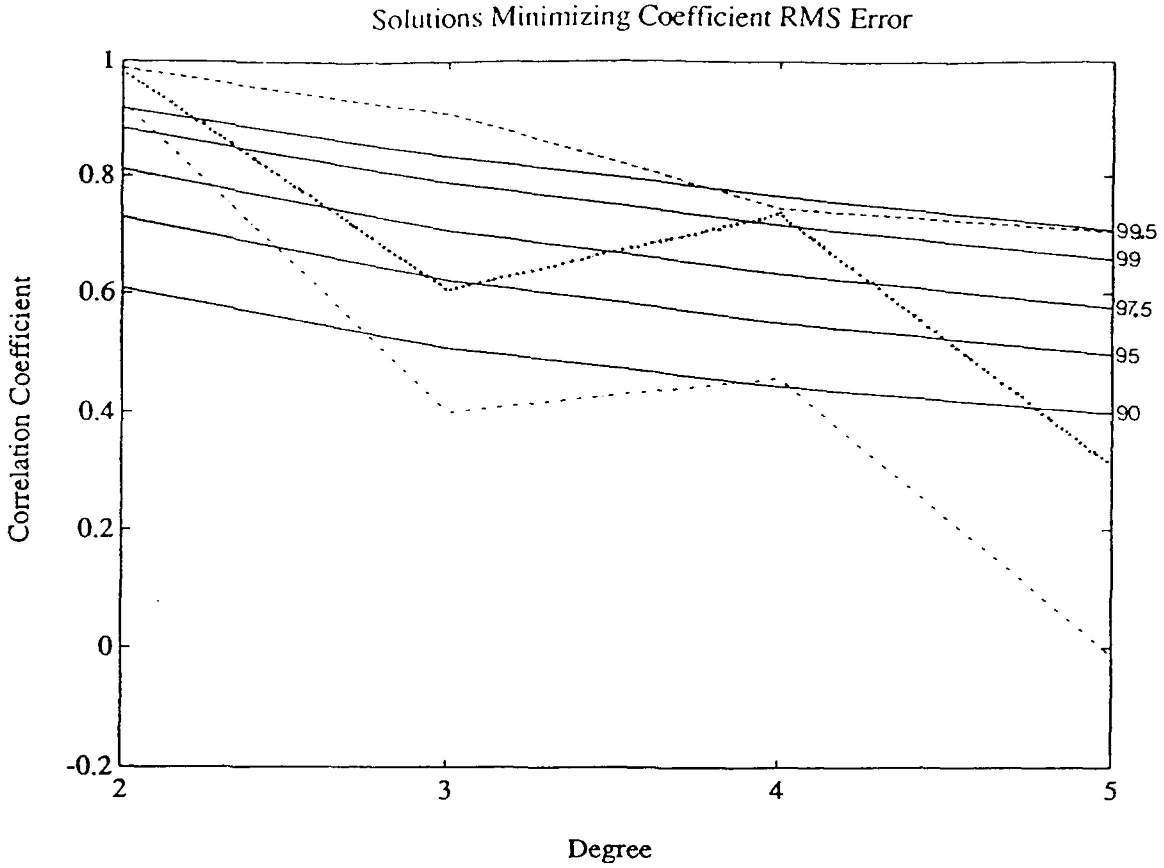

Fig. 3.42. Correlation of geophysics coefficient solutions, that minimize the coefficient rms error, with the actual GEM-L2 coefficients. Line symbols: - - - - = geoid, ... = gravity, - . - . = gravity gradient. Confidence levels are determined by a t-test with $2l$ degrees of freedom.

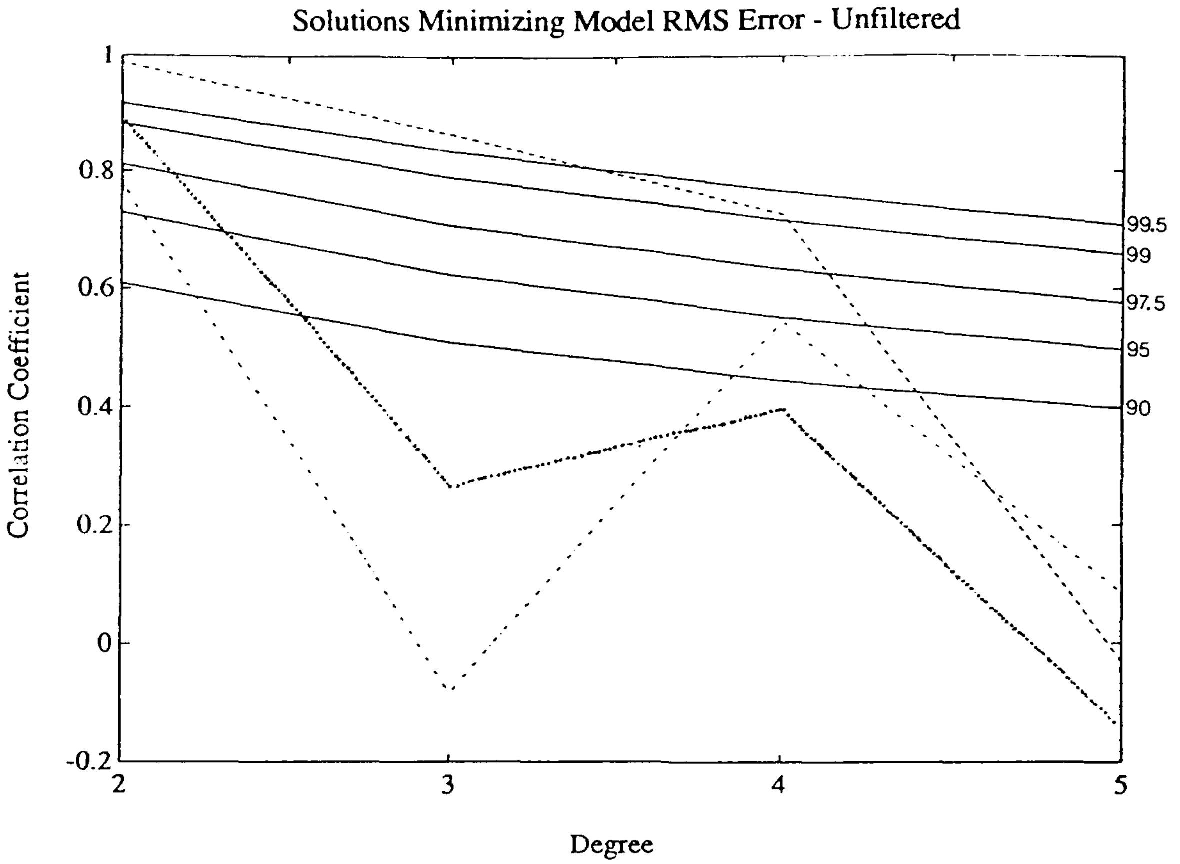

Fig. 3.43. Correlation of geophysics coefficient solutions, that minimize the model rms error for the unfiltered data, with the actual GEM-L2 coefficients. Line symbols: - - - - = geoid, ... = gravity, - . - . = gravity gradient. Confidence levels are determined by a t-test with $2l$ degrees of freedom.

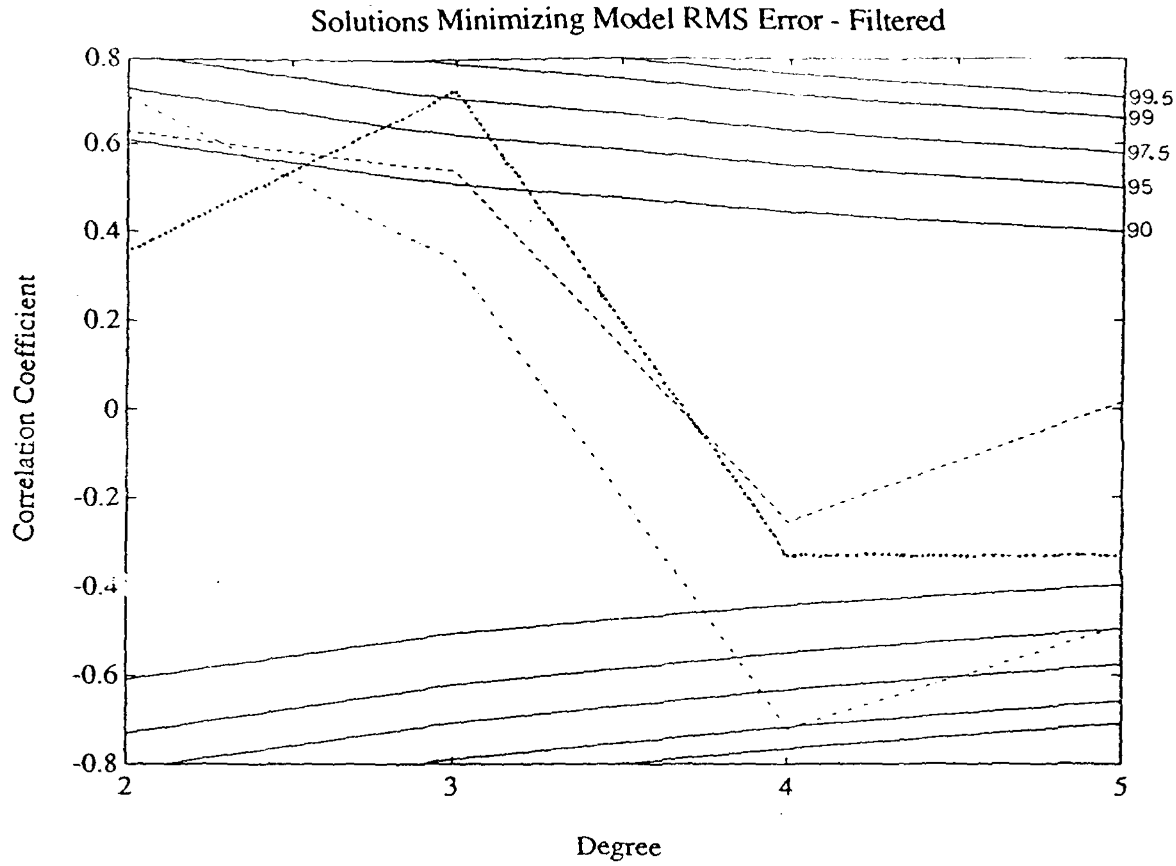

Fig. 3.44. Correlation of geophysics coefficient solutions, that minimize the model rms error for the filtered data, with the actual GEM-L2 coefficients. Line symbols: - - - - = geoid, ... = gravity, - . - . = gravity gradient. Confidence levels are determined by a *t*-test with $2l$ degrees of freedom.

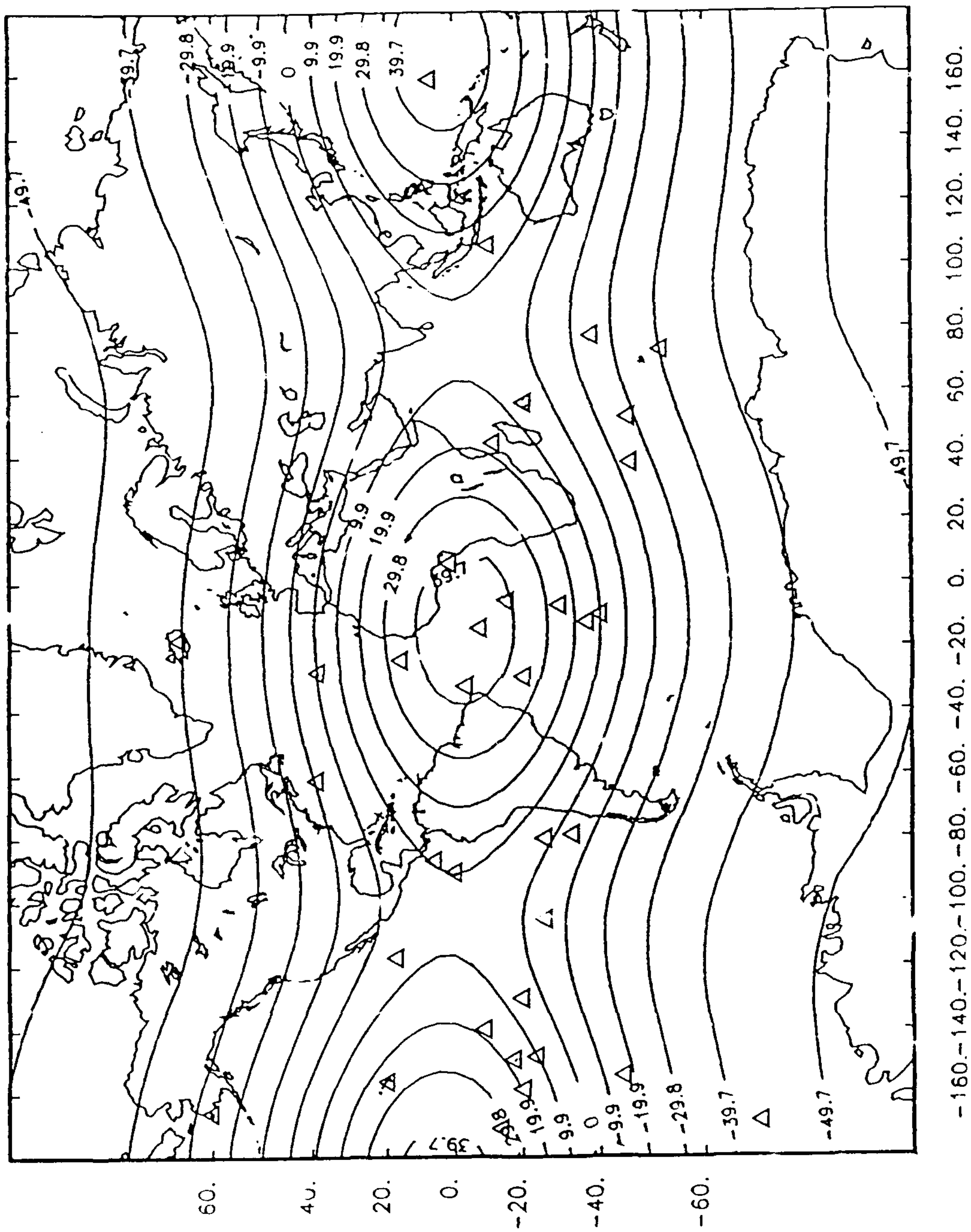

CONTINUOUS LAYER MODEL DEGREE 2 GEOID

Fig. 3.45. Reconstruction [on a 5° grid] of the continuous layer model spherical harmonic degree 2 function for the constructed geoid data set. Values [in meters] are deviations from the average constructed geoid [13.7 m]. Feature locations are designated by triangles.

CONTINUOUS LAYER MODEL DEGREE 2 EMI

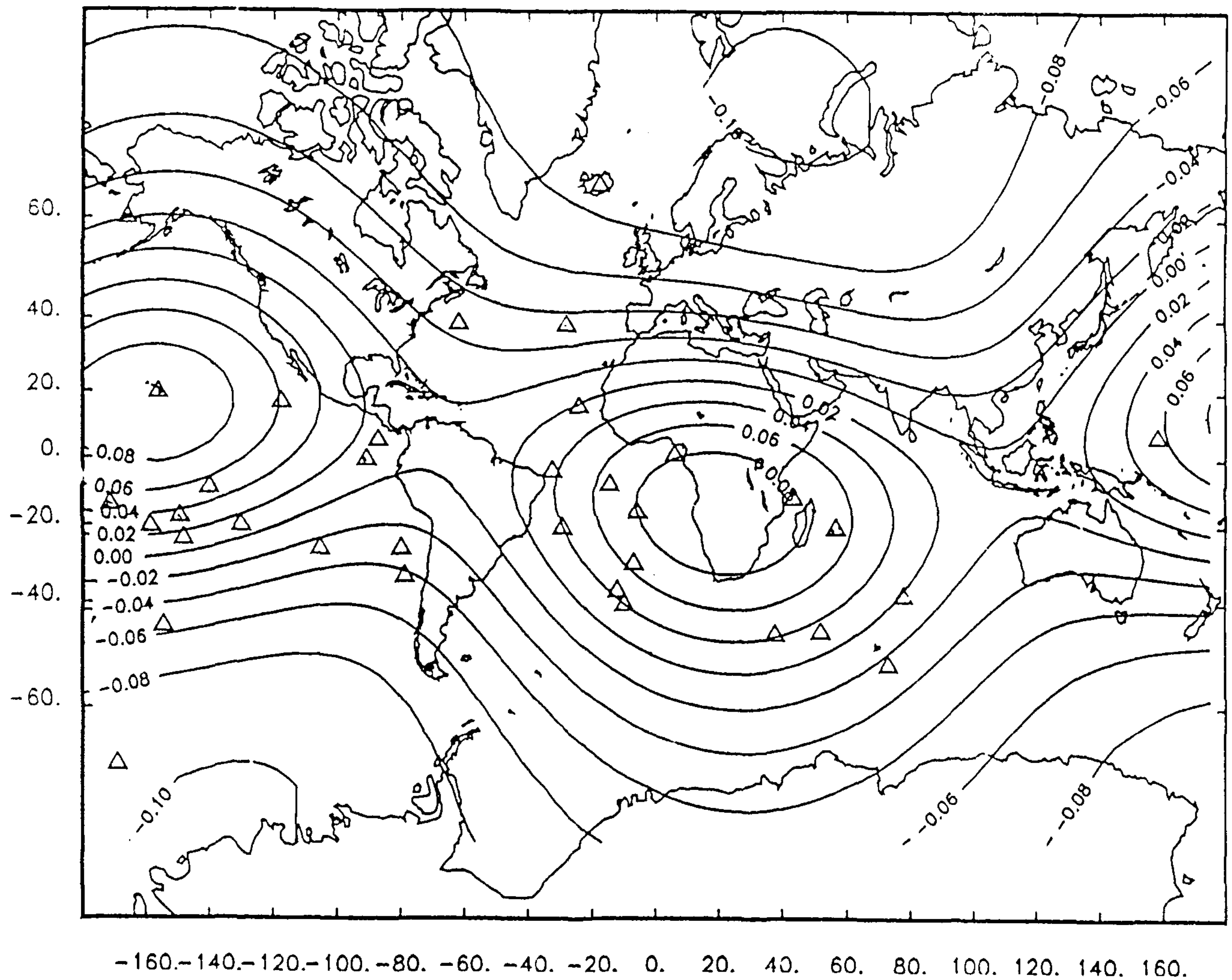

Fig. 3.46. Reconstruction [on a 5° grid] of the continuous layer model spherical harmonic degree 2 function for the filtered EMI data set. Values are deviations from the average filtered EMI percentage [0.27]. Feature locations are designated by triangles.

CONTINUOUS LAYER MODEL DEGREE 2 EMII

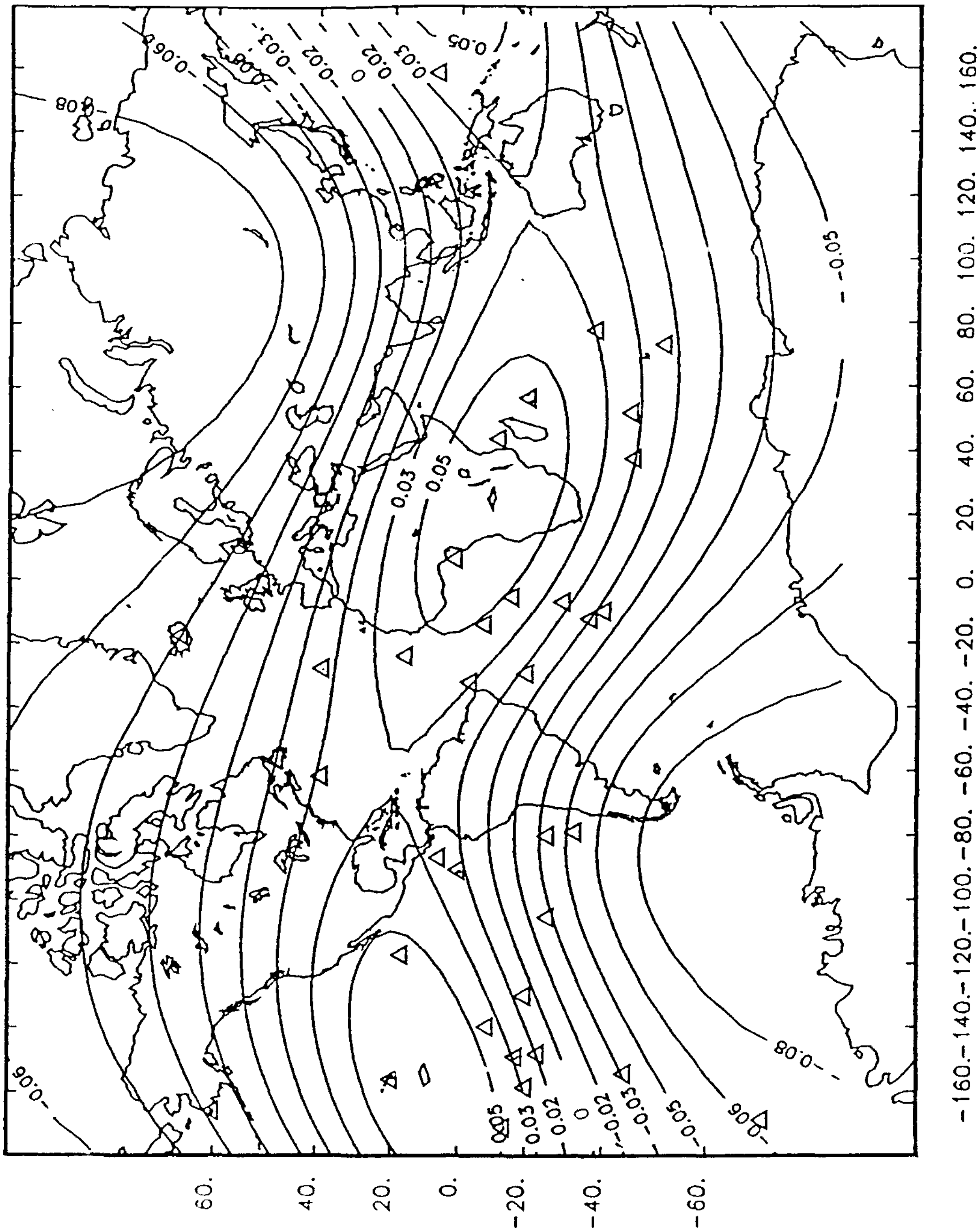

Fig. 3.47. Reconstruction [on a 5° grid] of the continuous layer model spherical harmonic degree 2 function for the EMII data set. Values are deviations from the average EMII percentage [0.17]. Feature locations are designated by triangles.

CONTINUOUS LAYER MODEL DEGREE 2 HIMU

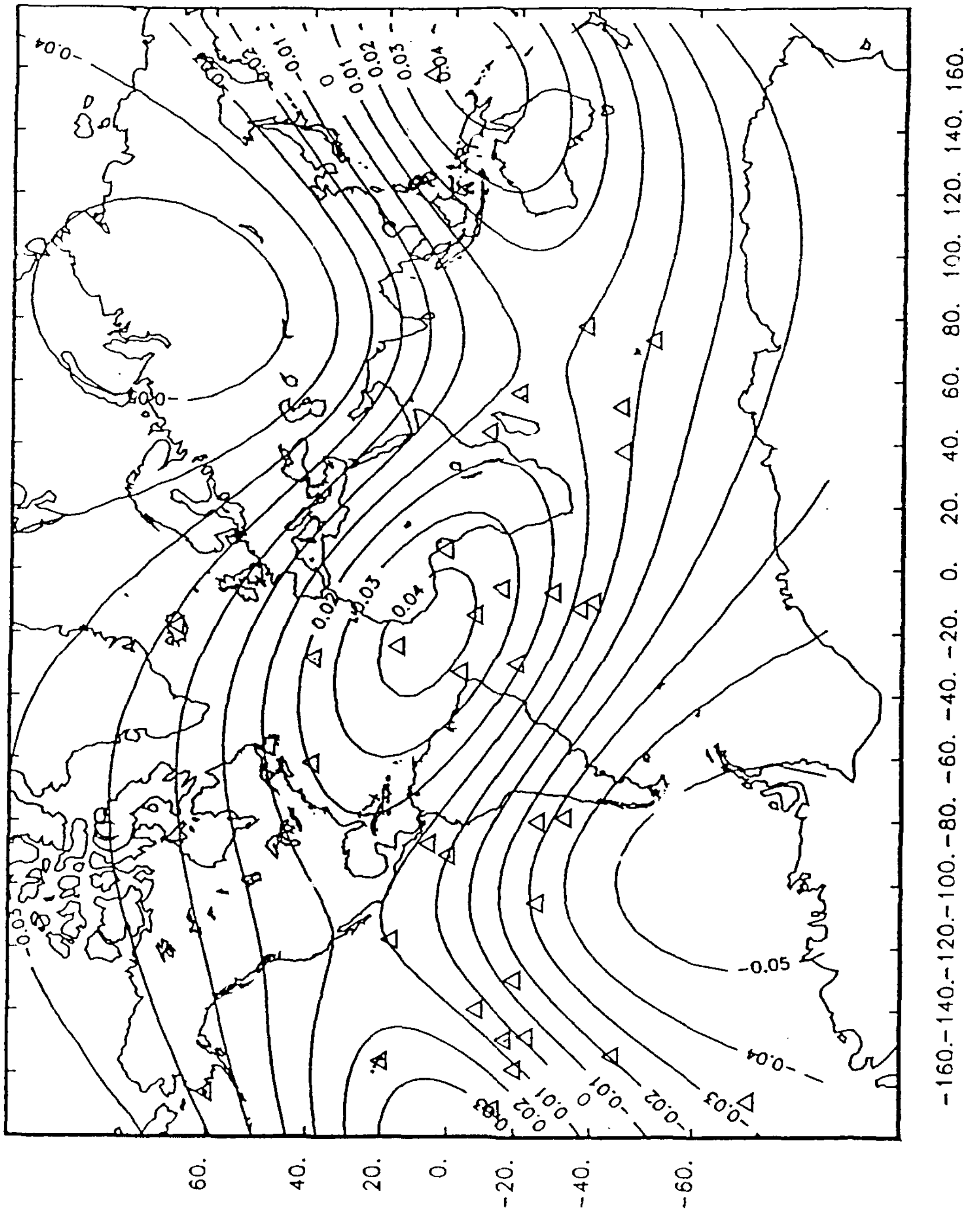

Fig. 3.48. Reconstruction [on a 5° grid] of the continuous layer model spherical harmonic degree 2 function for the filtered HIMU data set. Values are deviations from the average filtered HIMU percentage [0.31]. Feature locations are designated by triangles.

CONTINUOUS LAYER MODEL DEGREE 2 DMM

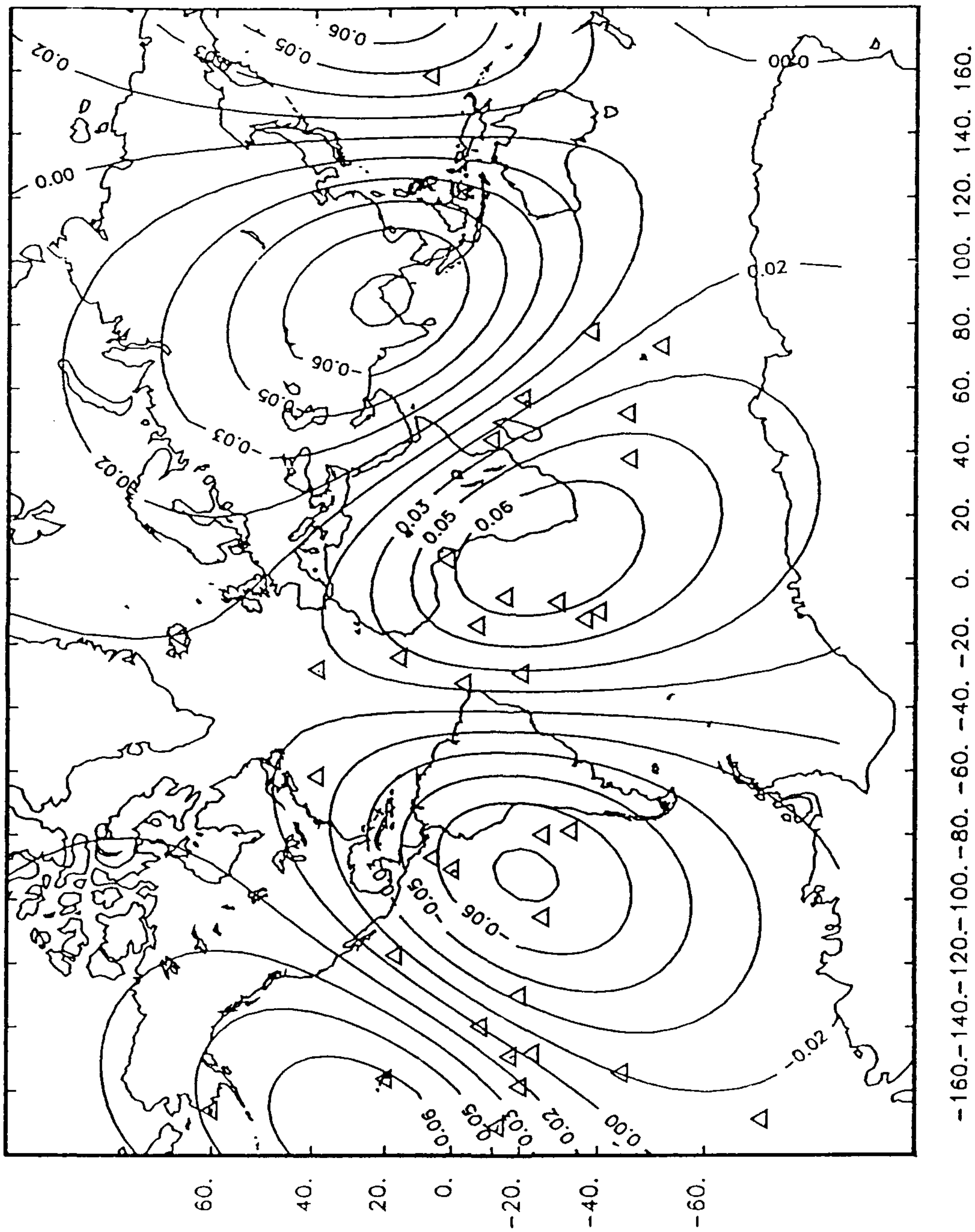

Fig. 3.49. Reconstruction [on a 5° grid] of the continuous layer model spherical harmonic degree 2 function for the DMM data set. Values are deviations from the average DMM percentage [0.25]. Feature locations are designated by triangles.

DEGREE 2 GEOID

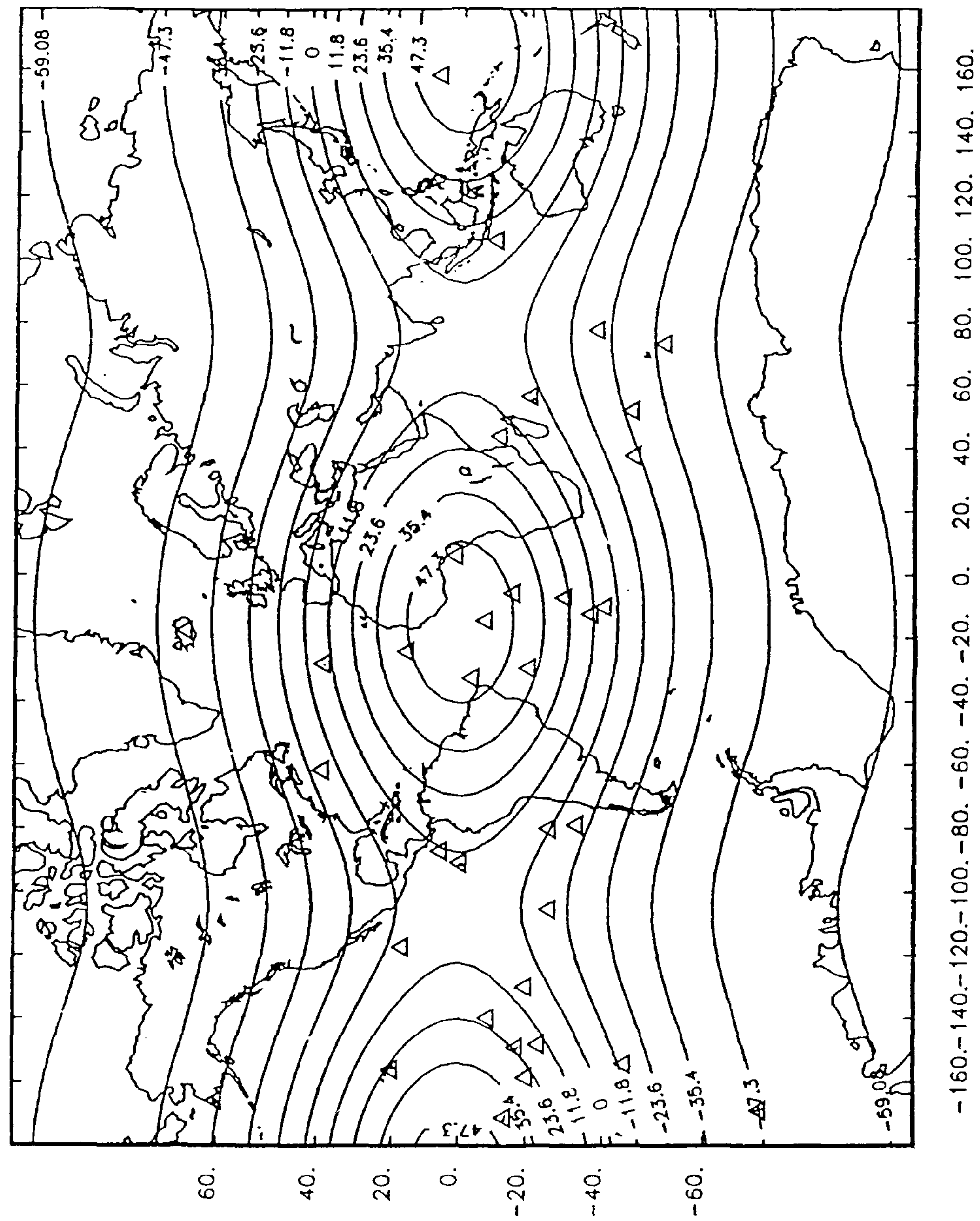

Fig. 3.50. Reconstruction [on a 5° grid] of the spherical harmonic degree 2 geoid from the GEM-L2 coefficients [degrees 0-20]. Values [in meters] are deviations from the average geoid [0.0 m]. Feature locations are designated by triangles.

CONTINUOUS LAYER MODEL DEGREES 2-3 HIMU

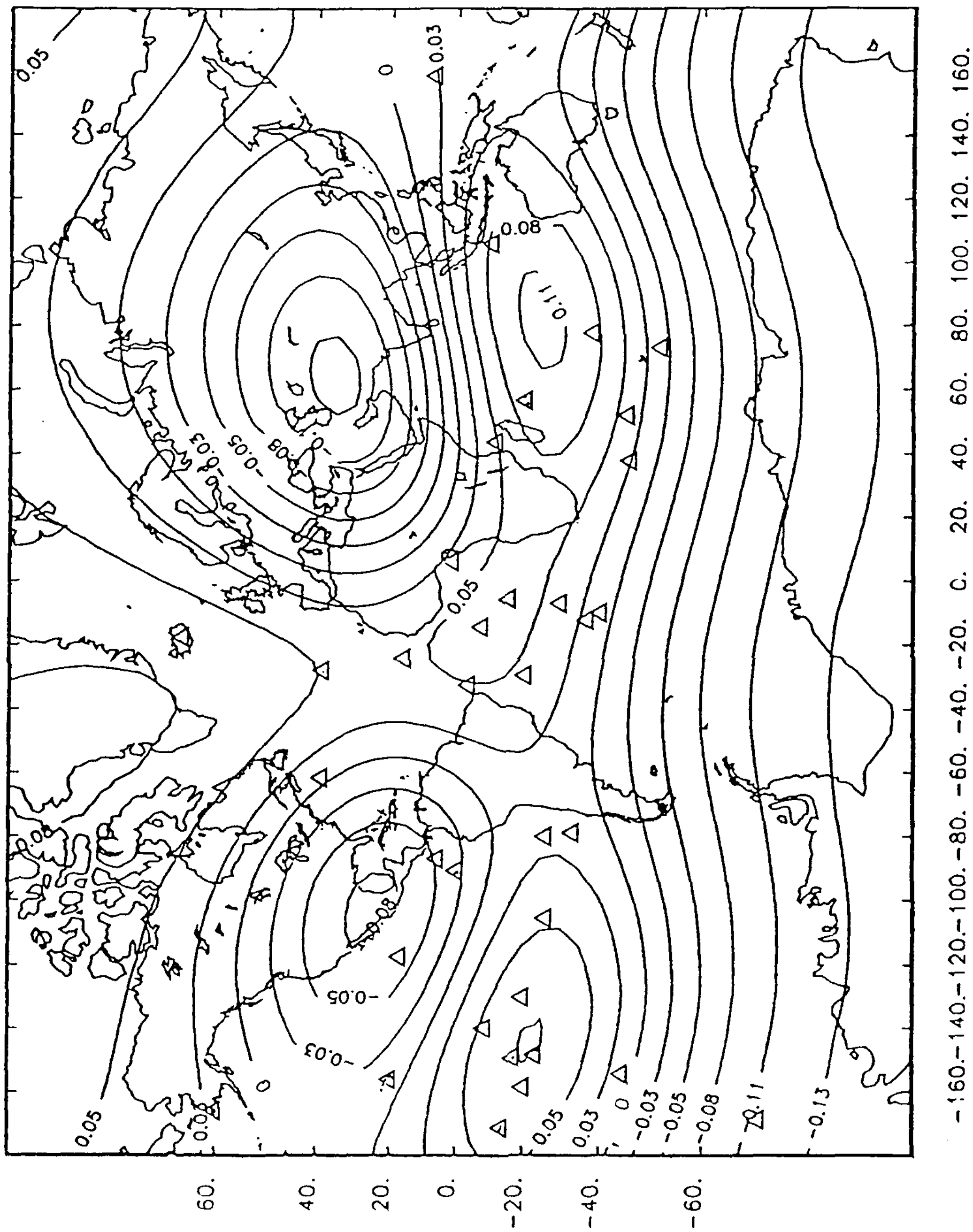

Fig. 3.51. Reconstruction [on a 5° grid] of the continuous layer model spherical harmonic degrees 2-3 function for the filtered HIMU data set. Values are deviations from the average filtered HIMU percentage [0.31]. Feature locations are designated by triangles.

DEGREES 2–3 GEOID

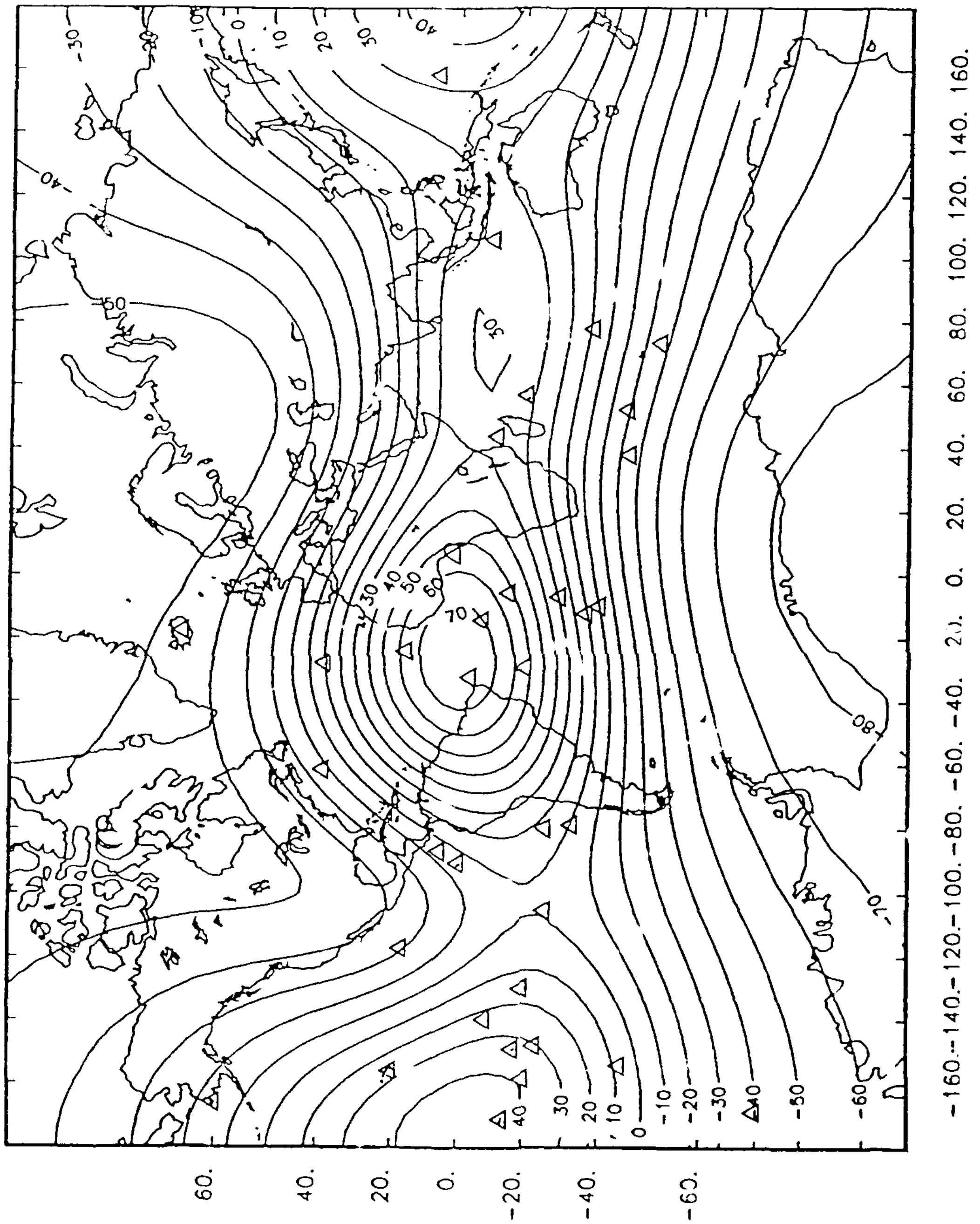

Fig. 3.52. Reconstruction [on a 5° grid] of the spherical harmonic degrees 2-3 geoid from the GEM-L2 coefficients [degrees 0-20]. Values [in meters] are deviations from the average geoid [0.0 m]. Feature locations are designated by triangles.

CHAPTER 4

SPHERICAL HARMONIC REPRESENTATION OF ISOTOPIC SIGNATURES: THE DELTA-FUNCTION MODEL

INTRODUCTION

As mentioned in Chapter 3, the delta-function model represents the OIB reservoir as a series of point sources, each feeding a separate plume. This may seem unphysical, but could be a good approximation of actual conditions if the source boundary layer is not continous, but patchy, as indicated in some seismic studies of D" (Lay *et al.*, 1990).

Representing the geographic features as delta-functions [scaled by the corresponding geoid anomaly or mantle component percentage] has two advantages, mathematically, over the approximation methods used in Chapter 3. First, the spherical harmonic coefficients can be found easily with the simplification from integration over the globe to summation over the feature locations allowed by the delta-functions. Second, representing the OIB reservoir as a known function removes the problem of aliasing; the values of the spherical harmonic coefficients are not dependent upon the truncation point of the expansion [they are dependent upon the number and location of the geographic features]. For delta-functions, which have energy at all degrees, the expansions can be carried out to infinity, but for this study, will only be carried out to degree 5, for comparison with the continuous layer model.

THEORY

As before, any function $f(\theta,\varphi)$ can be expanded in spherical harmonics:

$$f(\theta,\varphi) = \sum_{l=0}^{L} \sum_{m=0}^{l} \sqrt{\frac{(2l+1)(l-m)!}{4\pi(l+m)!}}\; P_l^m(\cos\theta)\left[A_l^m \cos m\varphi + B_l^m \sin m\varphi\right]$$

Due to the orthogonality of the spherical harmonics, the equations for the coefficients are:

$$A_l^m = \int_{-\pi}^{\pi} d\varphi \int_{-1}^{1} f(\theta,\varphi) \sqrt{\frac{(2l+1)(l-m)!}{4\pi(l+m)!}}\ P_l^m(\cos\theta) \cos m\varphi \ d(\cos\theta)$$

$$B_l^m = \int_{-\pi}^{\pi} d\varphi \int_{-1}^{1} f(\theta,\varphi) \sqrt{\frac{(2l+1)(l-m)!}{4\pi(l+m)!}}\ P_l^m(\cos\theta) \sin m\varphi \ d(\cos\theta)$$

For the delta-function model, the function being expanded is a series of delta-functions:

$$f(\theta,\varphi) = k_i\delta(\theta-\theta_i,\varphi-\varphi_i)$$

where k_i is one of the four mantle component percentages [or the value of the geoid anomaly] and $\delta(\theta-\theta_i,\varphi-\varphi_i)$ indicates a delta-function at the particular location (θ_i,φ_i). Mathematically, the delta-function is a "spike" of infinite height, infinitesimal width and unit area:

$$\int d\varphi \int \delta(\theta-\theta_i,\varphi-\varphi_i)\ d\theta = 1$$

The key property of the delta-function is that the integral of a function $g(\theta,\varphi)$ times a delta-function is just the value of g at the delta-function location:

$$\int d\varphi \int g(\theta,\varphi)\ \delta(\theta-\theta_i,\varphi-\varphi_i)\ d\theta = g(\theta_i,\varphi_i)$$

This simplifies the coefficient equations from integration over the globe to summation over the geographic feature locations:

$$A_l^m = \sum_{i=1}^{N} k_i \sqrt{\frac{(2l+1)(l-m)!}{4\pi(l+m)!}}\ P_l^m(\cos\theta_i) \cos m\varphi_i$$

$$B_l^m = \sum_{i=1}^{N} k_i \sqrt{\frac{(2l+1)(l-m)!}{4\pi(l+m)!}}\; P_l^m(\cos\theta_i)\,\sin m\varphi_i$$

The coefficient equations for the constructed data sets of geoid, gravity and gravity gradient anomalies at the feature locations have additional factors. As an example, for gravity the equations are:

$$A_l^m = \frac{R^2}{GM(l+1)} \sum_{i=1}^{N} k_i \sqrt{\frac{(2l+1)(l-m)!}{4\pi(l+m)!}}\; P_l^m(\cos\theta_i)\,\cos m\varphi_i$$

$$B_l^m = \frac{R^2}{GM(l+1)} \sum_{i=1}^{N} k_i \sqrt{\frac{(2l+1)(l-m)!}{4\pi(l+m)!}}\; P_l^m(\cos\theta_i)\,\sin m\varphi_i$$

with the additional factor of $\frac{R^2}{GM(l+1)}$. Geoid and gravity gradient additional factors are $\frac{1}{R}$ and $\frac{R^3}{GM(l+1)(l+2)}$, respectively.

APPLICATION

As before, the constructed geophysics data sets are used as a control to gauge the level of accuracy expected from the mantle component data sets. Correlating the coefficients from these data sets with the GEM-L2 coefficients (Fig. 4.1) yields good agreement for all three at degree 2. Whereas the continuous layer model showed a fairly consistent pattern of decreasing correlation from the geoid coefficient estimates to the gravity and gravity gradient estimates (Fig. 3.43), the delta-function model shows equal correlation at degree 2 and a switch to increasing correlation from the geoid estimates to the gravity and gravity gradient estimates at degree 4. Overall, it appears that the delta-function model is less accurate at reproducing the coefficients for long wavelength data sets [geoid] and more accurate at reproducing the coefficients for the short wavelength data sets [gravity gradient] than the continuous layer model. Both models are consistent, though, in showing strong correlation for all three data sets at degree 2, implying that the mantle component degree 2 coefficients are also viable. In addition, the mantle component data sets have even more high degree [short wavelength] energy than the gravity gradient data set, so their coefficients are probably reasonably accurate out to degree 4.

Since each of the different geophysics data sets approximate the GEM-L2 coefficients equally well at degree 2, it appears that there is some additional controlling factor affecting the estimates of the degree 2 coefficients, aside from the data values themselves. The location of the features, and thus the delta-functions, is the most likely candidate. A plot of the constructed degree 2 "function" for the delta-function model geoid (Fig. 4.2) shows the obvious relationship between the two main clusters of oceanic islands and the two highs in the geoid. Since the continuous layer model geophysics coefficients all agreed well with the degree 2 GEM-L2 coefficients, it appears that the location effect merely enhances an already existing correlation and is not solely responsible for the correlation. Presumably the same is true of any degree 2 correlation of delta-function model geochemistry coefficients with the GEM-L2 coefficients.

Degree 2 "functions" for the mantle component percentages are reconstructed, as before, for comparison with those of the continuous layer model (Figs. 4.3-4.6). The contoured values of the delta-fuction geoid (Fig. 4.2) and the mantle component functions are large enough to be the actual geoid and component percentages, instead of deviations from the average values, as for the continuous layer model. This is due to the arbitrary scaling that comes into play when using delta-functions. A delta-function has unit area, so the average value of a delta-function over the sphere is:

$$\langle\delta\rangle = \frac{1}{(\Delta\varphi \sin\theta)\,\Delta\theta} = \frac{1}{4\pi}$$

where $(\Delta\varphi \sin\theta)\,\Delta\theta$ is a sectional area on the sphere (Fig. 4.7), which for the whole sphere is 4π. If there is only one delta-function involved in the reconstruction, the contoured values will be off by a factor of $1/(4\pi)$. Since there are 36 features, there are 36 delta-functions involved in the reconstruction, so the contoured values are off by a factor of $36/(4\pi) = 2.86$ or ~3.

Qualitatively, the four reconstructed mantle component degree 2 functions show good agreement with each other. All four have two highs: one over central Africa and the other over the central Pacific. Slight differences include the width of the highs [from narrowest to widest width: HIMU, EMI, EMII and DMM] and the amount of displacement [from 0° to 15°] of the highs above and below the equator [from least to most displacement: HIMU, EMII, EMI and DMM]. With respect to the GEM-L2 degree 2 geoid (Fig. 3.50), all of the mantle component highs are shifted longitudinally to the east by varying amounts [HIMU ~30°, EMI ~30°, EMII ~35° and DMM ~40°].

Degrees 2-3 functions for the four components (Figs. 4.8-4.11) are constructed for comparison with the geoid (Fig. 5.32) and the HIMU continuous layer model reconstruction (Fig. 5.31).

SUMMARY

Viewing the distribution of the OIB reservoir as a series of point sources that can be represented as delta-functions yields the following results:

- With respect to the behavior of geophysics control data sets, at least the degree 2 spherical harmonic coefficients for the mantle components can be estimated with confidence, if not the degrees 3 and 4 as well.

- The location of the features, and thus the delta-functions, biases the calculated degree 2 coefficients due to the correlation between the oceanic island locations and the degree 2 geoid.

- Scaling of delta-function models reconstructed over the globe is dependent upon the number of delta-functions used in the approximation [N] and varies as $N/(4\pi)$.

- Degree 2 HIMU, EMI, EMII and DMM all show a degree 2 geoid pattern phase-shifted 30°-40° to the east, with varying widths of the highs and displacements from the equator.

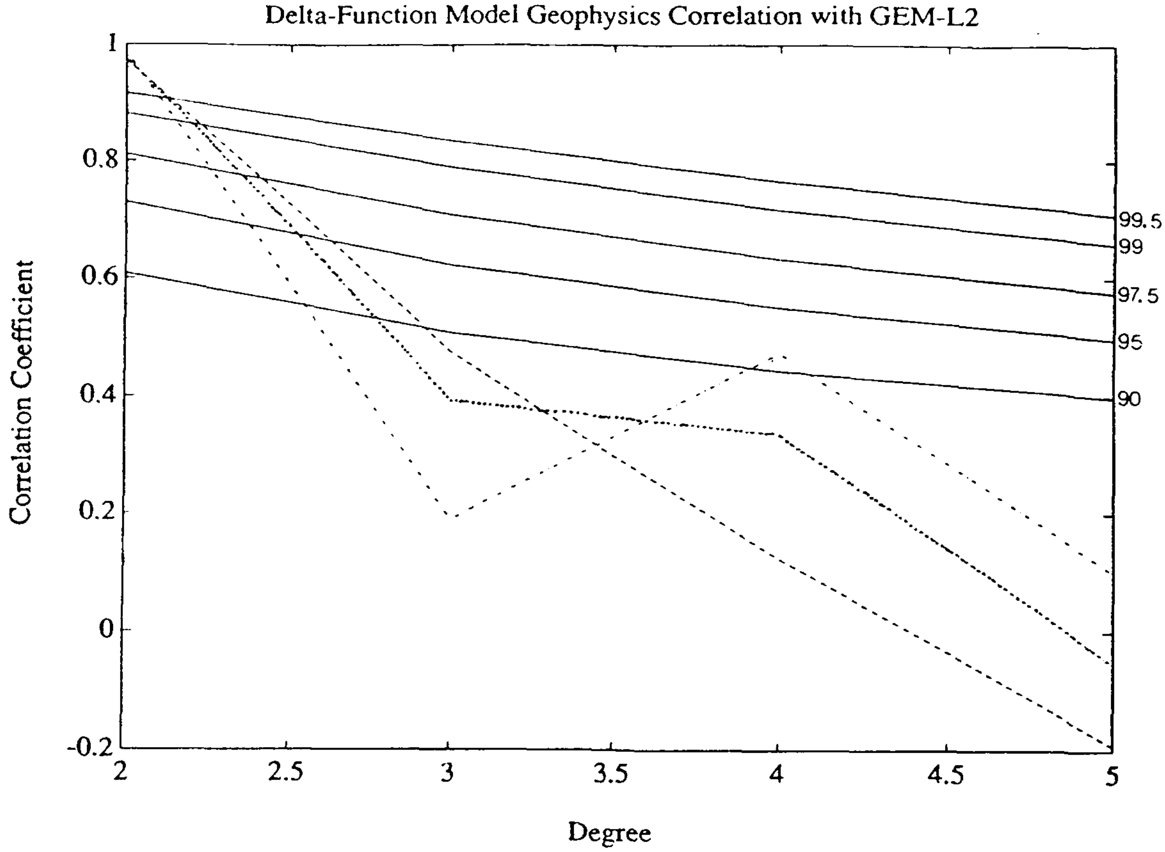

Fig. 4.1. Correlation of the delta-function model geophysics coefficient solutions with the actual GEM-L2 coefficients. Line symbols: - - - - = geoid, ... = gravity, - . - . = gravity gradient. Confidence levels are determined by a t-test with $2l$ degrees of freedom.

DELTA-FUNCTION MODEL DEGREE 2 GEOID

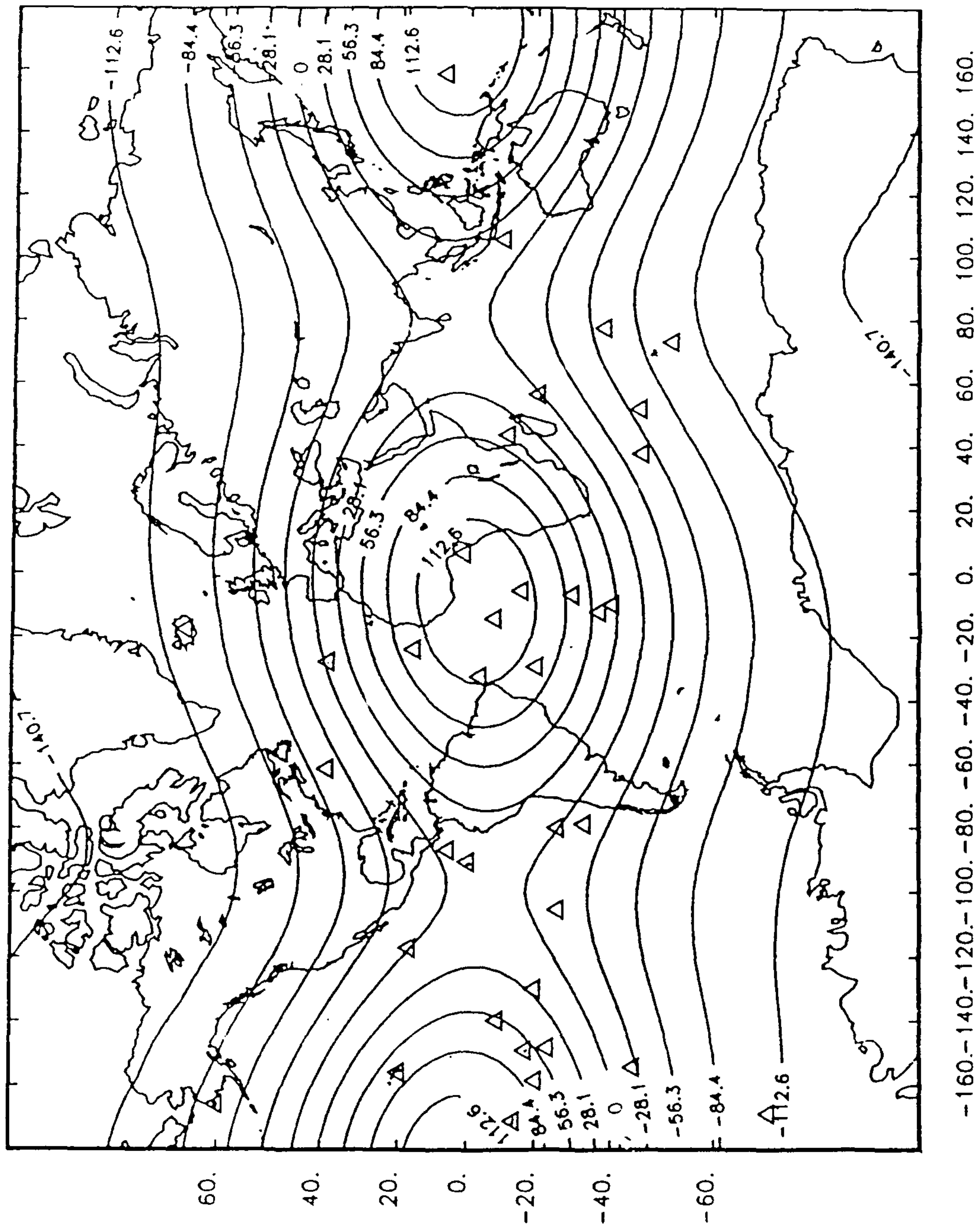

Fig. 4.2. Reconstruction [on a 5° grid] of the delta-function model spherical harmonic degree 2 function for the constructed geoid data set. Values are NOT direct deviations from the average constructed geoid [0.0 m], but are off by a factor of ~3. Feature locations are designated by triangles.

DELTA-FUNCTION MODEL DEGREE 2 EMI

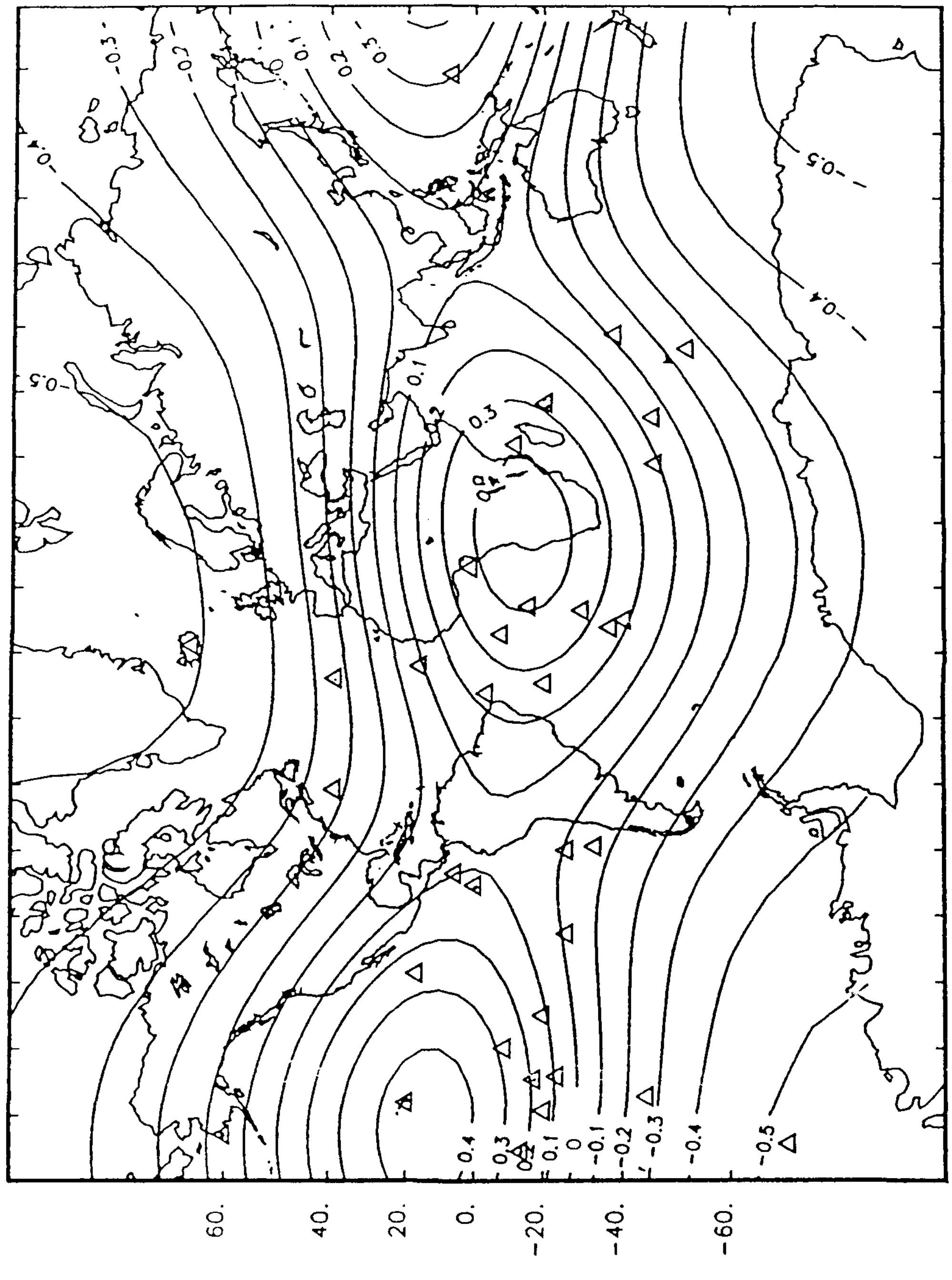

Fig. 4.3. Reconstruction [on a 5° grid] of the delta-function model spherical harmonic degree 2 function for the EMI data set. Values are NOT direct deviations from the average EMI percentage [0.27], but are off by a factor of ~3. Feature locations are designated by triangles.

DELTA-FUNCTION MODEL DEGREE 2 EMII

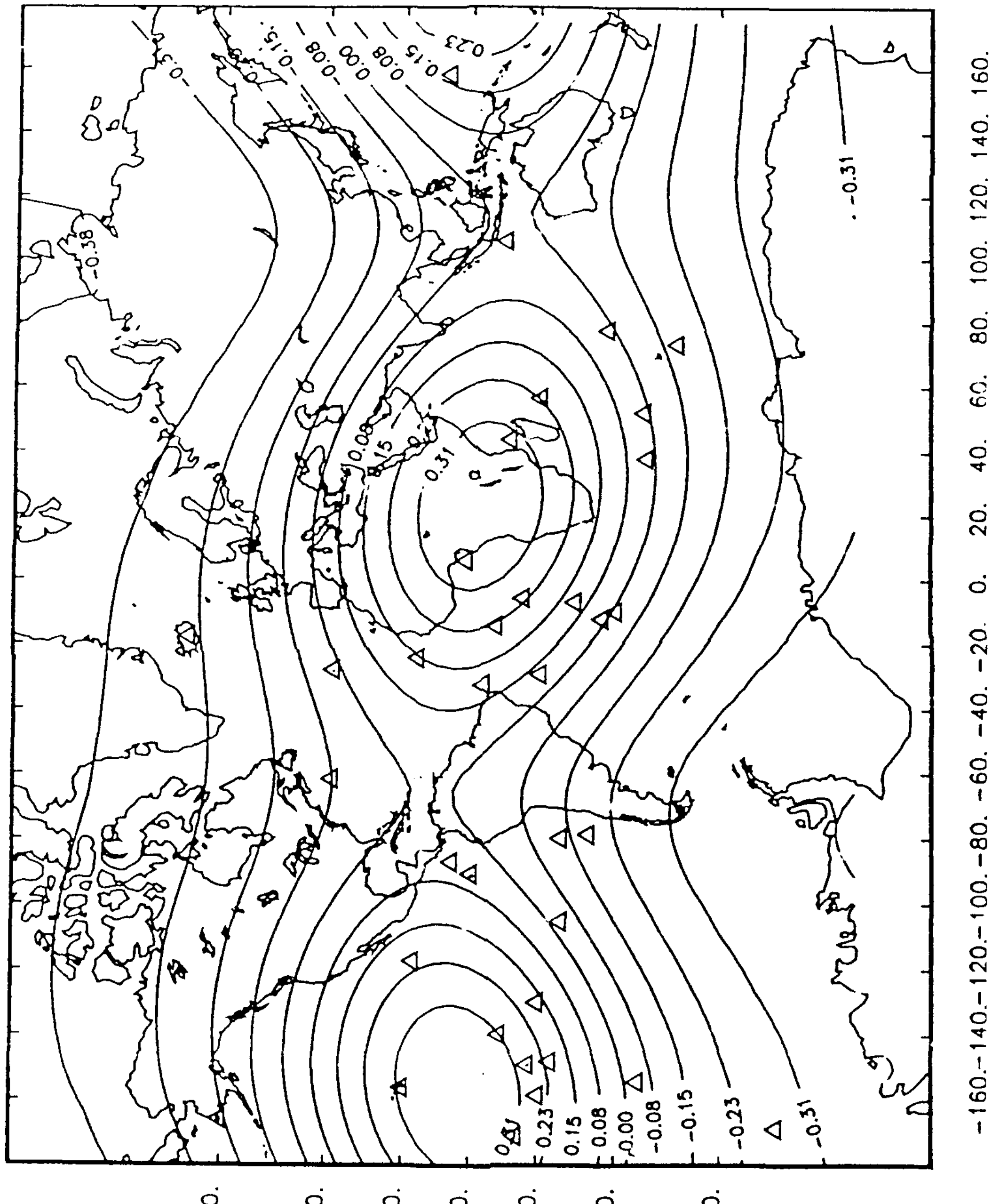

Fig. 4.4. Reconstruction [on a 5° grid] of the delta-function model spherical harmonic degree 2 function for the EMII data set. Values are NOT direct deviations from the average EMII percentage [0.17], but are off by a factor of ~3. Feature locations are designated by triangles.

DELTA–FUNCTION MODEL DEGREE 2 HIMU

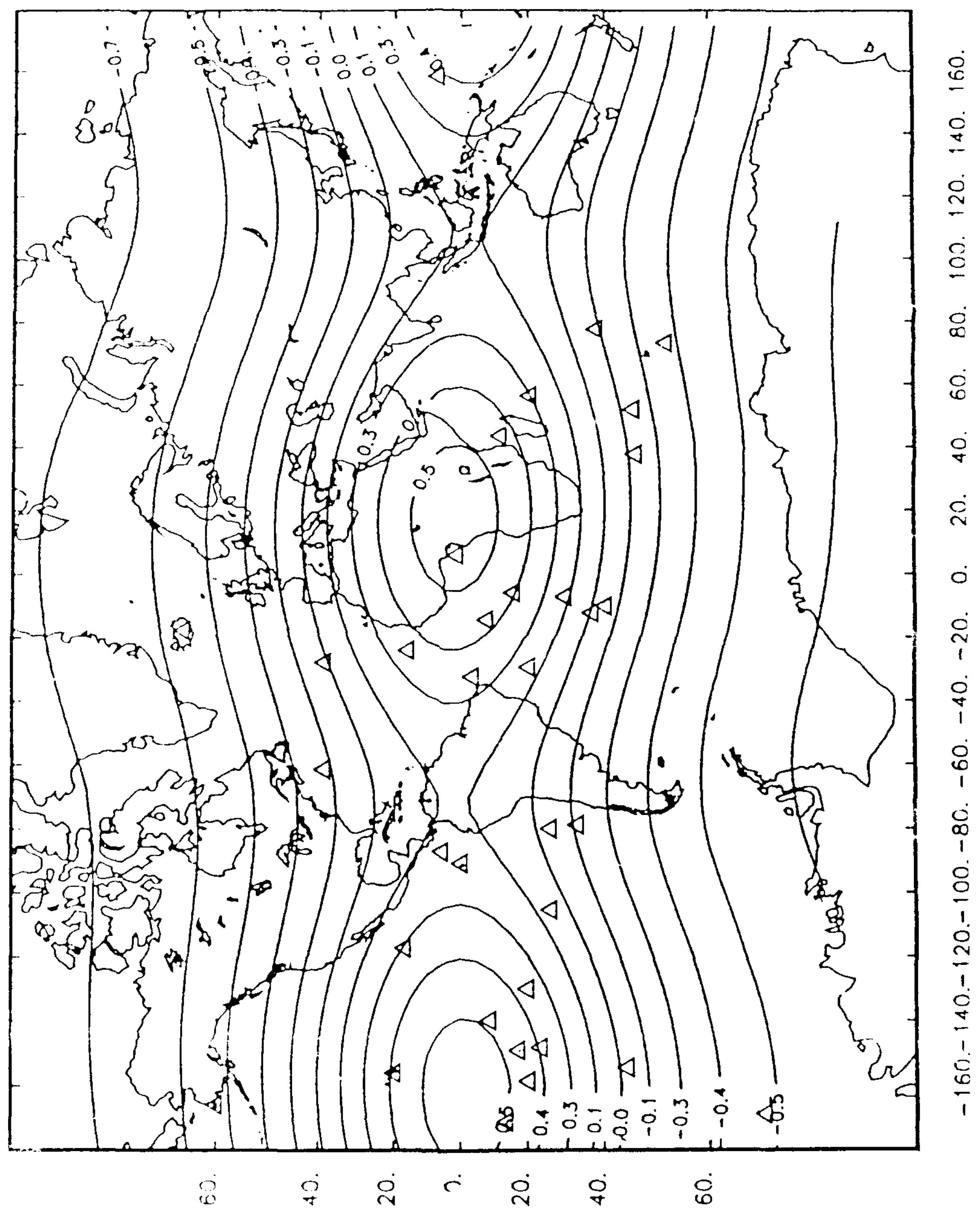

Fig. 4.5. Reconstruction [on a 5° grid] of the delta-function model spherical harmonic degree 2 function for the HIMU data set. Values are NOT direct deviations from the average HIMU percentage [0.31], but are off by a factor of ~3. Feature locations are designated by triangles.

DELTA-FUNCTION MODEL DEGREE 2 DMM

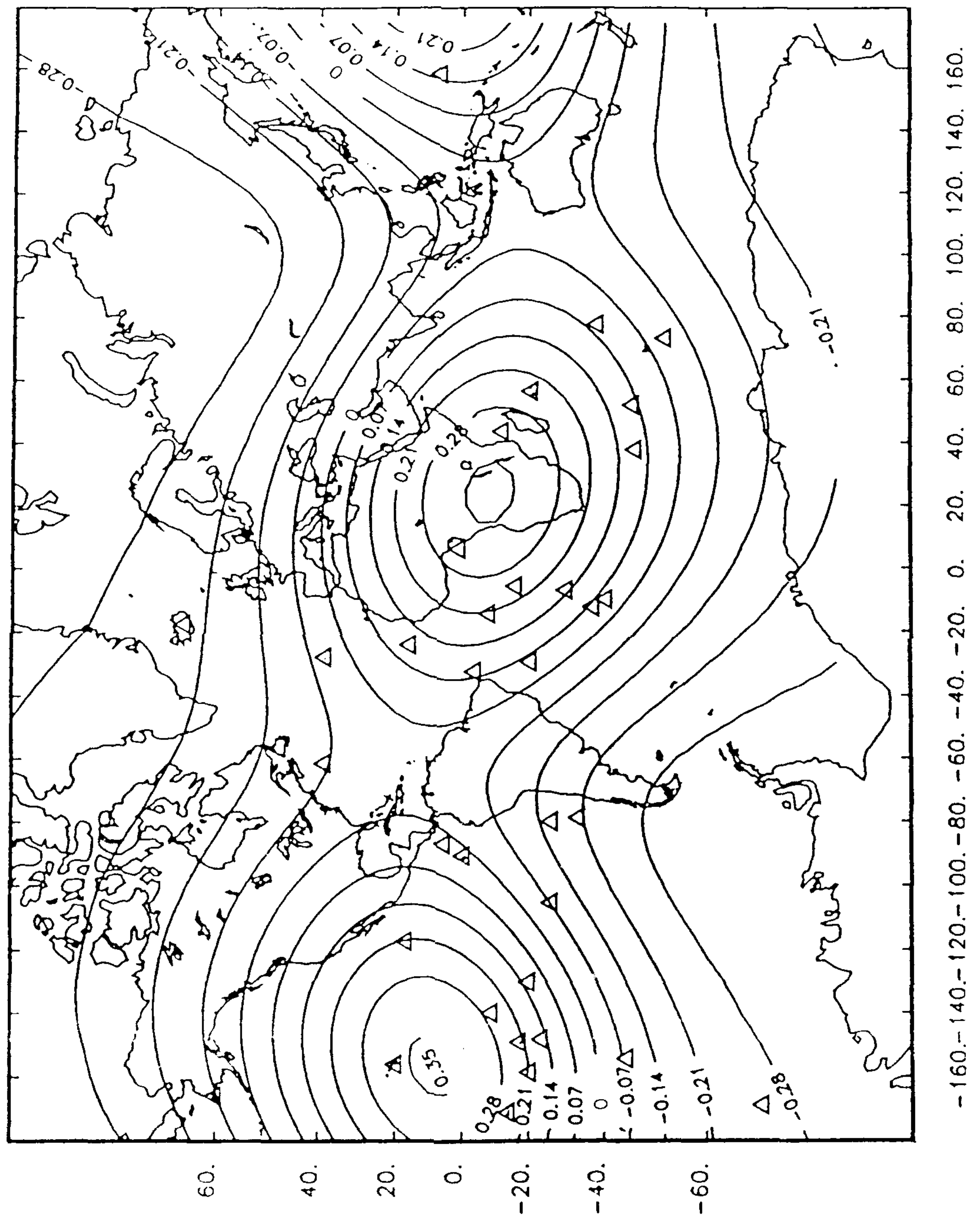

Fig. 4.6. Reconstruction [on a 5° grid] of the delta-function model spherical harmonic degree 2 function for the DMM data set. Values are NOT direct deviations from the average DMM percentage [0.25], but are off by a factor of ~3. Feature locations are designated by triangles.

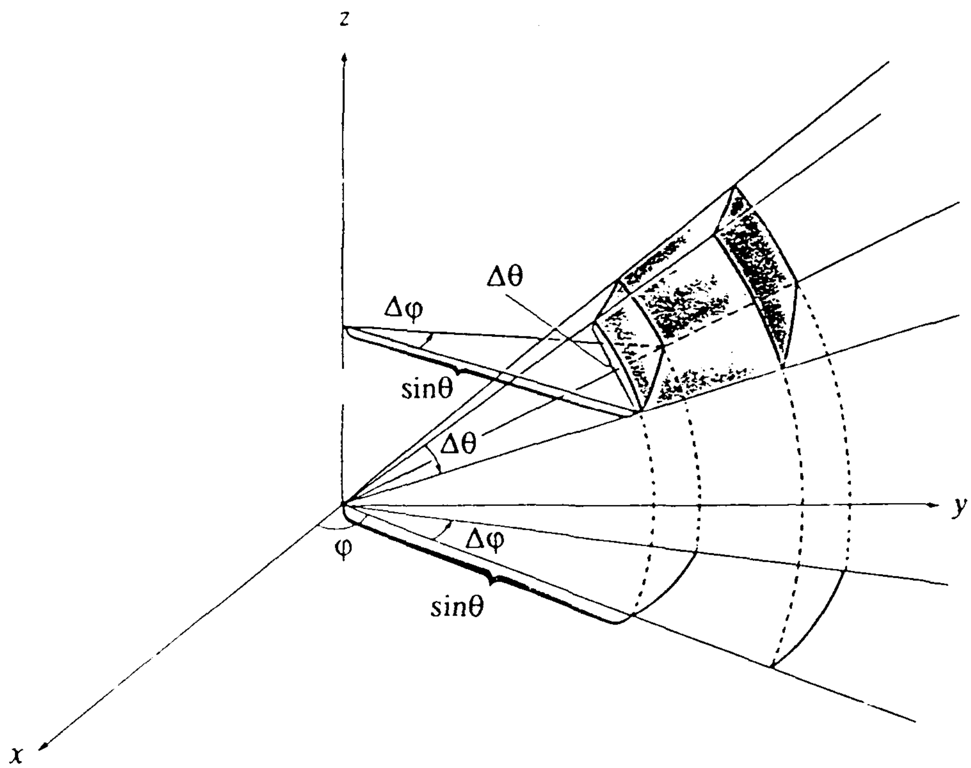

Fig. 4.7. Geometry of a sectional area on a sphere, where θ is colatitude and φ is longitude.

DELTA-FUNCTION MODEL DEGREES 2-3 EMI

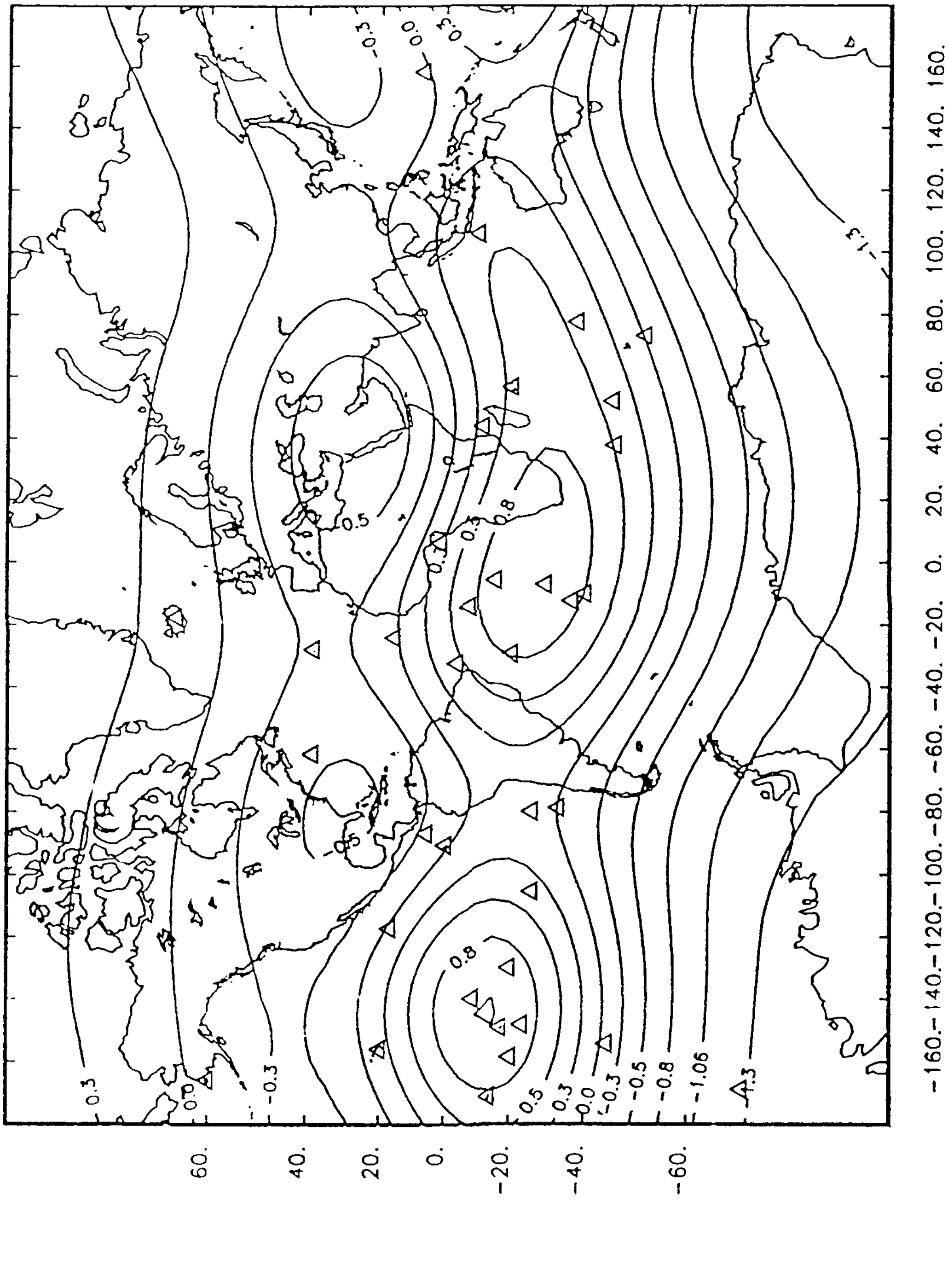

Fig. 4.8. Reconstruction [on a 5° grid] of the delta-function model spherical harmonic degrees 2-3 function for the EMI data set. Values are NOT direct deviations from the average EMI percentage [0.27], but are off by a factor of ~3. Feature locations are designated by triangles.

DELTA–FUNCTION MODEL DEGREES 2–3 EMII

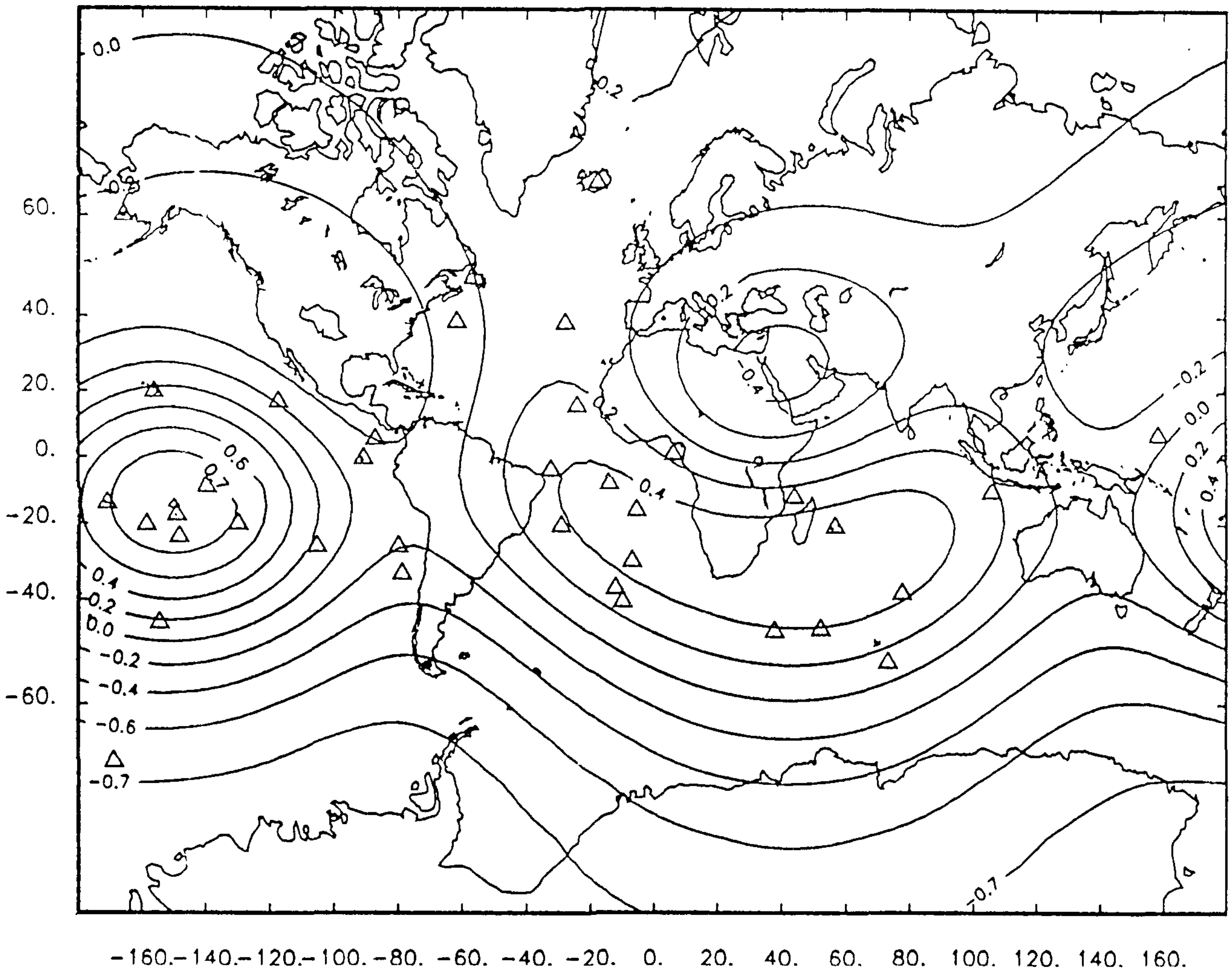

Fig. 4.9. Reconstruction [on a 5° grid] of the delta-function model spherical harmonic degrees 2-3 function for the EMII data set. Values are NOT direct deviations from the average EMII percentage [0.17], but are off by a factor of ~3. Feature locations are designated by triangles.

DELTA-FUNCTION MODEL DEGREES 2-3 HIMU

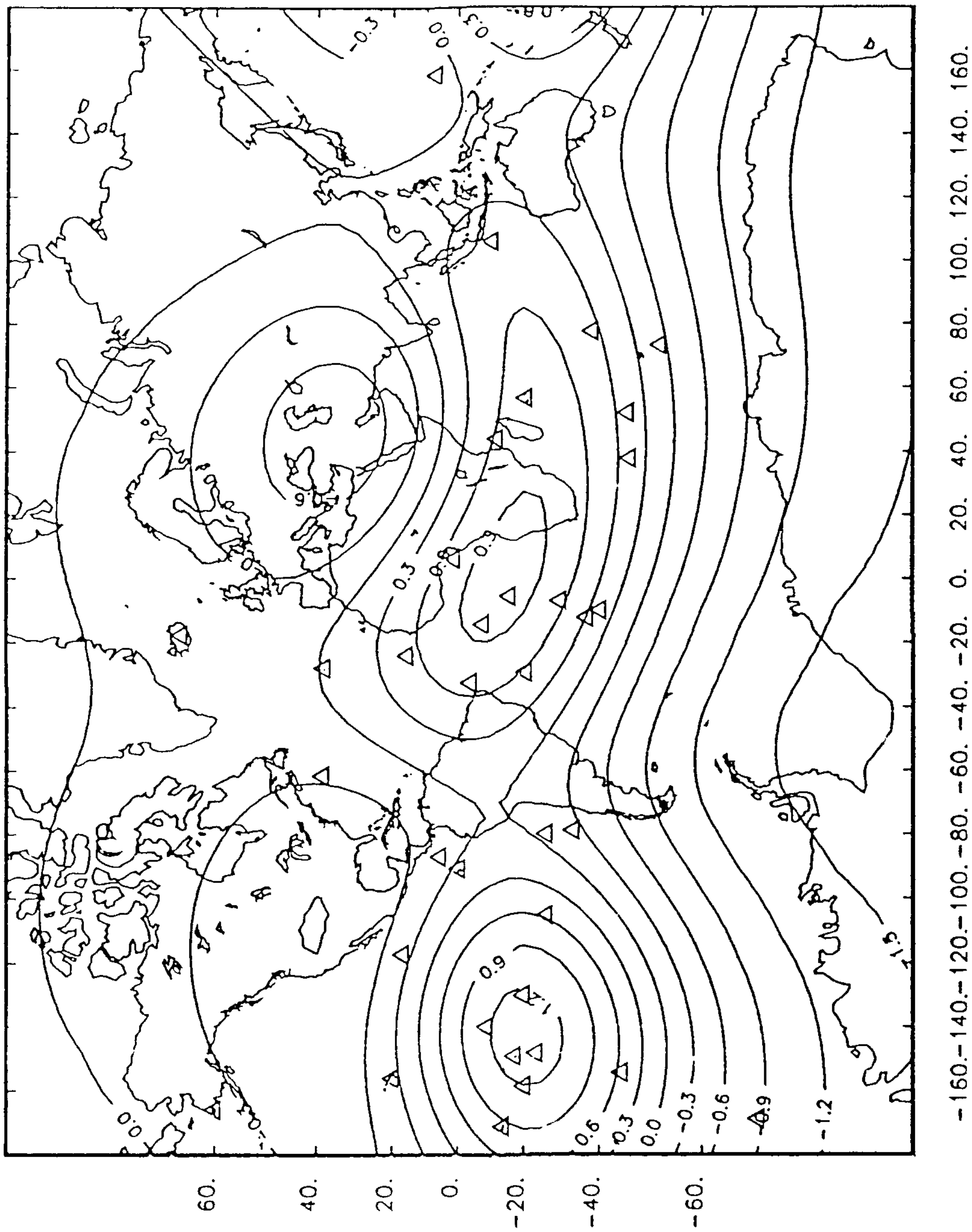

Fig. 4.10. Reconstruction [on a 5° grid] of the delta-function model spherical harmonic degrees 2-3 function for the HIMU data set. Values are NOT direct deviations from the average HIMU percentage [0.31], but are off by a factor of ~3. Feature locations are designated by triangles.

DELTA-FUNCTION MODEL DEGREES 2-3 DMM

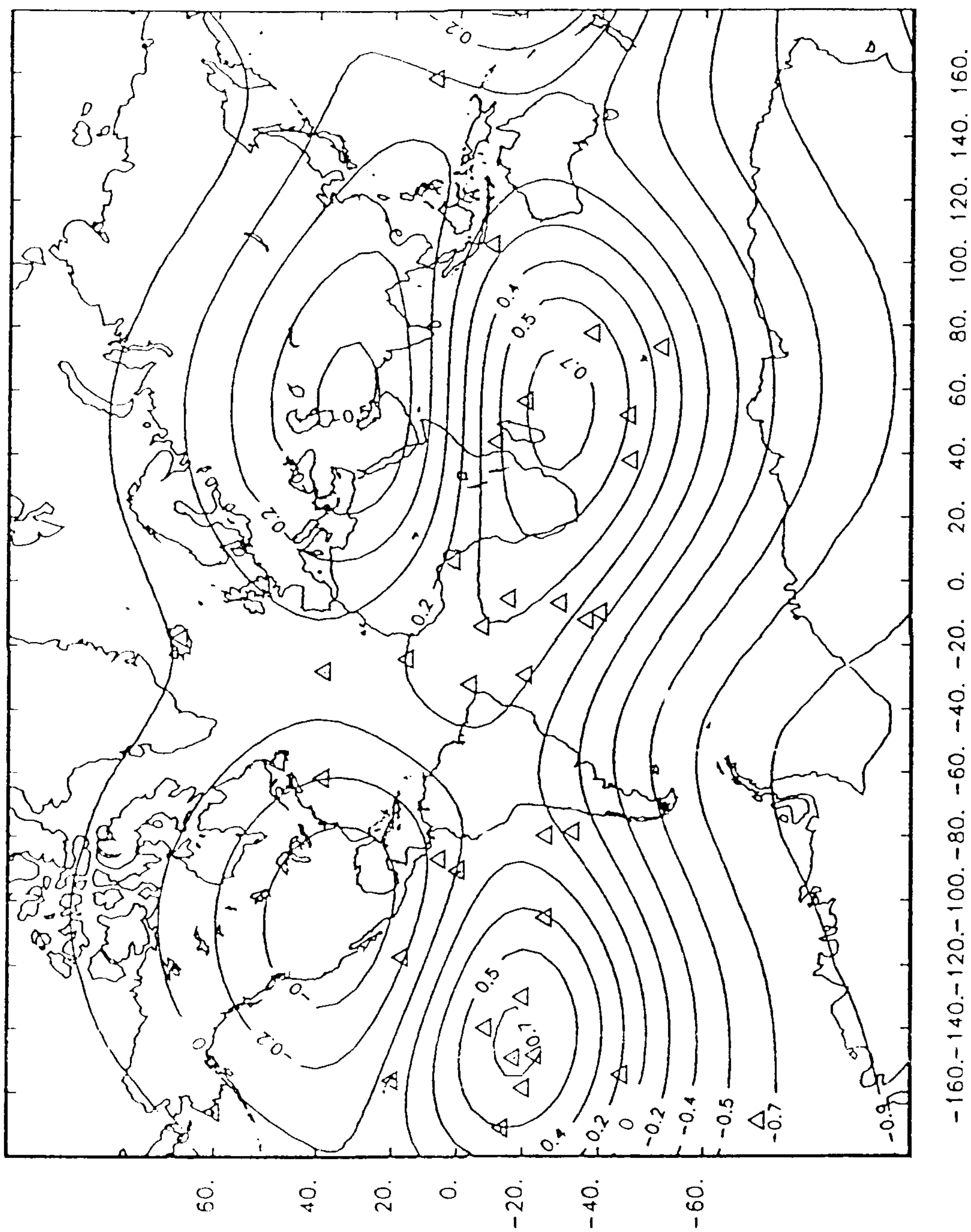

Fig. 4.11. Reconstruction [on a 5° grid] of the delta-function model spherical harmonic degrees 2-3 function for the DMM data set. Values are NOT direct deviations from the average DMM percentage [0.25], but are off by a factor of ~3. Feature locations are designated by triangles.

CHAPTER 5

RESULTS AND DISCUSSION

INTRODUCTION

Geophysical control data sets are used to judge the dependability of spherical harmonic coefficient solutions for the mantle end-member components from the continuous layer and the delta-function models. A careful comparison of the two models can further enhance or reduce the significance assigned to the various solutions. In this chapter, the two models are compared in terms of their amplitude spectra, how well they correlate with the geoid, how they are affected by nonuniform feature distribution and how well they correlate with the Clayton-Comer seismic tomography model. The significance of the correlations with the geoid and the seismic tomography model is discussed, along with suggestions for further research.

AMPLITUDE SPECTRA

Spectral amplitude plots show the relative power at each degree for the different mantle component expansions. Following Richards and Hager (1988), the root mean square harmonic coefficient amplitude at each degree is given by:

$$S_l^{rms} = \sqrt{\frac{V_l^2}{(2l+1)}} = \sqrt{\frac{\sum_{m=0}^{L}\left[(A_l^m)^2 + (B_l^m)^2\right]}{(2l+1)}}$$

where V_l^2 is the variance at each degree for a given set of harmonic coefficients. Richards and Hager (1988) include the factor of $1/(2l+1)$ because random noise on a sphere will have a flat spectrum with this normalization. On plots of S_l^{rms} versus l, low-degree or long-wavelength effects will show up as a negative slope.

Amplitude spectra of the calculated geoid coefficients from the two models agree well with the negative [long-wavelength] slope of the actual geoid coefficients (Figs. 5.1 and 5.2). For the mantle component expansions, amplitude spectra reveal no such clear cut negative slope pattern to indicate dominant long-wavelength effects (Figs. 5.3 and 5.4). Instead, the spectra appear "white", with energy at all degrees, and no decrease in the energy with increasing degree. In addition, HIMU is the only mantle component that shows any consistency in behavior between the two models. Thus, in general, the expansion of the mantle components is model dependent.

CORRELATION WITH THE GEOID

Plotting the mantle component percentages point by point against the full geoid value at the geographic feature locations is not a valid way to compare the mantle component signatures with the geoid. When correlating them by degree using spherical harmonic coefficients, it is apparent that the mantle components may correlate with the geoid at some degrees [wavelengths] and not others. In a pointwise comparison, the different patterns at the different degrees are obscured as they are added together to produce the whole, making an accurate comparison impossible. Pointwise plots done with the current data show no correlation between the mantle components and the geoid (Figs. 5.5-5.8).

In contrast, correlating the geoid coefficients and the mantle component coefficients by degree reveals a good corrrelation [90% significance level and higher] at degree 2 for the DUPAL components [EMI, EMII and HIMU] for both models (Figs. 5.9 and 5.10). Note that positive correlations indicate high concentrations of mantle components correlating with geoid highs and vice versa. HIMU has the best correlation for both models, showing better than 95% significance at degree 2 and 90% significance at degree 3. The remaining mantle components show a consistent decreasing correlation from EMII to EMI to DMM for both models.

IMPLICATIONS OF NONUNIFORM FEATURE DISTRIBUTION

Oceanic island distribution is not uniform about the globe. As indicated in Chapter 4, the two main clusters of oceanic islands correspond to the two highs of the degree 2 geoid. It can be argued, then, that any correlation between the degree 2 mantle component expansions and the degree 2 geoid is due solely to the nonuniform distribution of the oceanic islands and not to any pattern in the geochemistry values. To test this, the percentages of the HIMU mantle component at the 36 geographic features, filtered [continuous layer model] and unfiltered [delta-function model], are randomly assigned to different feature locations five times. HIMU percentages are used since the degree 2 HIMU, for both models, correlates best with the degree 2 geoid. The five randomly generated data sets for each model are then used to compute new coefficients that can be compared to the degree 2 geoid. For the continuous layer model, the number of singular values retained for the new data sets is determined by the F-test at the 95% significance level. The random number generator used for this test is nonlinear, but repeatable, since it starts with a given seed that is updated for successive calls in a predictable manner. This means that for a given randomization, the filtered and unfiltered HIMU percentages are being randomized in the same way, so the results of the two models can be compared. Five iterations is not enough to quantify the effect of the feature distribution on the degree 2 correlation for the two models, but it is enough to indicate if it has any control at all.

Concentrating on the degree 2 coefficients, three of the randomizations that result in strong correlations with the geoid for delta-function model [well above the 90% confidence level] result in negligible correlations with the geoid for the continuous layer model (Table 5.1). Reconstructed degree 2 functions of the randomized data sets show graphically how little the delta-function model changes, with respect to the continuous layer model, when the geochemical signatures of the features are mixed up (Figs. 5.11-5.20). For the delta-function model, this indicates that the values of coefficients are not so much dependent upon the scaling factors multiplying the delta-functions as the location of the delta-functions themselves. This location effect makes it difficult to trust strong correlations of the delta-function model with the geoid unless there is additional confirmation by the continuous layer model.

CORRELATION WITH SEISMIC TOMOGRAPHY

Correlating the mantle component expansions with the geoid gives an estimate of the general OIB source region [ie. lower mantle versus upper mantle], but is incapable of resolving a more precise depth range for the source since the geoid is affected by mass anomalies at all depths in the Earth. A way to select a probable depth range for the OIB source[s] is to compare the mantle component expansions to seismic tomography models. Seismic tomography models map the global distribution of lateral velocity variations in the mantle at different depths based upon the inversion of travel time anomaly data from seismic waves that travel through the Earth's interior (Hager and Clayton, 1989).

In this study, the mantle component expansions are correlated with the Clayton-Comer seismic tomography model, discussed in Hager and Clayton (1989). The Clayton-Comer model inverts for slowness [inverse of velocity] anomalies, in a given shell, that are converted to velocity anomalies by multiplying by the average shell velocity. There are 29 shells in the model, each 100 km thick, spanning the entire mantle from the core-mantle boundary [CMB], at a depth of 2900 km, to the surface. Shells 23-29 [covering the uppper mantle] are not used in this analysis since coverage in the top 700 km of the mantle is poor because of the near vertical seismic ray paths in this region. The spherical harmonic coefficients of the remaining 22 shells [covering the lower mantle] are averaged together, to dampen model noise, to produce 5 layers: 2900-2500 km [layer 1], 2500-2100 km [layer 2], 2100-1700 km [layer 3], 1700-1200 km [layer 4] and 1200-700 km [layer 5].

The geoid is correlated with the Clayton-Comer tomography model first (Fig. 5.21) to serve as a guide for interpreting the correlation of the tomography model with the mantle component expansions. Note that a negative correlation indicates geoid highs correlating with low velocity regions [and vice versa] and a positive correlation indicates geoid highs correlating with high velocity regions [and vice versa]. In layers 1-3, the strong negative correlations at degrees 2 and 3 confirm that long wavelength geoid highs are due to low density [warmer and thus slower velocity] mantle upwellings. This long wavelength upwelling signature is also present in the upper lower mantle, as shown by the strong negative correlations at degrees 2, 3 and 4 for layer 4 and at degree 2 for layer 5. Of interest is the strong positive correlations for layers 4 and 5, at degree 5 and degrees 4 and 5, respectively. Bowin (1991a) indicates the correspondence of the degrees 4-10 geoid highs with plate convergence zones. He believes that the mass anomalies responsible for the highs lie in the lower mantle, beneath plate convergence zones, below the teleseismically downgoing subducted slabs. The positive correlations in layers 4 and 5 support this theory and imply that subducted slabs extend below the 670 km discontinuity.

Correlation of the mantle component expansions with the Clayton-Comer tomography layers for the two models yields interesting results (Figs. 5.22-5.29). Due to the limitations of both models [ie. the uncertainties in the coefficient estimates for the continuous layer model and the location dependence in the delta-function model], it is more likely that a significant correlation is accurate if it is present in both models. With this in mind, the interpretation of the correlation results will be based upon common correlations of 90% significance [or very close to it] or higher (Table 5.2).

The common degree 2 correlations with layers 3-5 for all the mantle components are indicative of large scale upwelling, as for the geoid. Good degree 3 correlations with layer 1 points to a deep source for all four components, like the geoid which shows a much stronger correlation at degree 3 with layer 1 than it does at degree 2. This correlation is not unexpected for the DUPAL components, whose correlation with the degree 2 geoid also suggest a deep origin, but it is surprising for the DMM component. There are two possible solutions for the dilemma posed by the supposedly upper mantle DMM component correlating with deep mantle tomography. First, it is possible that the DMM component expansion does correlate better with upper mantle tomography, which is, unfortunately, not available for the Clayton-Comer model. Second, it is possible that the DMM component is representative of both the upper and lower mantle composition. Hart (1991) shows that all the hotspots that have elongated isotopic arrays indicate mixing between one of the DUPAL components and something that is not a MORB composition. Since 3/4 of a plume's ascent is spent in the lower mantle, the composition of the DMM component may be largely controlled by lower mantle entrainment (Hart, 1991).

Another interesting correlation common to both models is the positive correlation at degree 5 for EMII in layer 5. With respect to Bowen's model (1991a) this indicates a correlation between the EMII component and subducted slabs. This finding agrees with the geochemical evidence suggesting the EMII component is derived from recycling of subducted sediments (Hart, 1988).

DISCUSSION

As indicated in Chapter 3, the average value of the geoid anomaly at the 36 feature locations is 13.7 m, not zero as it should be if the features were located randomly with respect to the geoid. This is a simple indication that the feature locations [hotspots] correlate with geoid highs. Naturally, then, the bulk chemical signatures unique to oceanic island basalts should also correlate with geoid highs. What is significant is that the expansions of all three DUPAL mantle end-member components [EMI, EMII and HIMU], that comprise 3/4 of the bulk chemical signature, individually correlate with geoid highs. More importantly, the DUPAL components correlate with the degree 2 geoid highs, indicating a deep origin for the components since the degrees 2-3 geoid field is inferred to result from topography at the core-mantle boundary (Bowen, 1991a).

It can be argued that the correlation of the DUPAL components with the degree 2 geoid is not an indication of geochemical patterns within the earth, but a direct result of the nonuniform distribution of the oceanic islands, whose two largest population densities correspond to the degree 2 geoid highs. Randomization tests indicate, however, that while this nonuniform distribution does play a role in solutions for the delta-function model, it is not the controlling factor for continuous layer model solutions. Though the continuous layer model solutions are hindered by the limited number and coverage of the oceanic islands and the delta-function model solutions are biased by the oceanic island locations, continual comparisons of the two models can be used to judge the accuracy of the solutions [in addition to judging accuracy using geophysical control sets]. Essentially, where both models agree, the solutions are more likely to be accurate.

The total geoid field is due to the contribution of different mass anomalies at different depths throughout the Earth, so it can be difficult to directly ascertain a source depth by comparing geochemical quantities with the geoid. Seismic tomography models allow the correlation of geochemical quantities with seismic velocity anomalies at different depths and serve as an independent check on the general source locations indicated by correlation with geoid anomalies. Correlating the mantle end-member components from both models with the Clayton-Comer seismic tomography model suggests a source depth range of 2500-2900 km [just above the core-mantle boundary] for the DUPAL components, due to the strong negative degree 3 correlations at this depth. In addition, a strong positive degree 5 correlation in the depth range of 700-1200 km is an indication that the EMII component is related to subduction, as previously suggested using geochemical evidence (Hart, 1988). Similarly, the geoid shows a strong positive correlation with the Clayton-Comer model at degrees 4 and 5 in the depth range 700-1200 km and at degree 5 in the depth ranges of 1200-1700 km. These subduction related patterns in the upper lower mantle indicate that subducted slabs extend beyond the 670 km seismic discontinuity and thus are supporting evidence for whole mantle convection

Further comparisons need to be made between the mantle component expansions and other seismic tomography models. It is especially important to compare the mantle components to a high resolution upper mantle tomography model, since the amplitude spectra for the components indicate power at high degrees which will become dominant at shallow depths in the mantle. Such a comparision could clarify the nature of the DMM component, which correlates well with the degree 3 deep mantle layer of the Clayton-Comer model, and could further explore the relationship between the EMII component and subduction.

SUMMARY

A comparison of the two models used to expand the mantle components in spherical harmonics yields the following results:

- Mantle end-member component amplitude spectra, for the continuous layer model and the delta-function model, show power at all degrees, with no one degree dominating.

- The DUPAL components [EMI, EMII and HIMU] for both models correlate well with the geoid at degree 2, indicating a deep origin.

- Delta-function model solutions are, to some extent, controlled by the nonuniform feature distribution, while the continuous layer model solutions are not.

- The DUPAL and DMM components, for both models, correlate well [negatively] at degree 3 with the velocity anomalies of the Clayton-Comer seismic tomography model in the 2500-2900 km depth range [immediately above the core-mantle boundary].

- The EMII component, for both models, correlates well [positively] at degree 5 with the velocity anomalies of the Clayton-Comer seismic tomography model in the 700-1200 km depth range, indicating a subduction related origin.

- Subduction related positive correlations for the geoid and the EMII component with the Clayton-Comer model in the upper lower mantle

[700-1700 km] indicate that subducted slabs extend below the 670 km seismic discontinuity, supporting a whole-mantle convection model.

Table 5.1. Summary of correlation coefficients between the GEM-L2 coefficients and coefficients calculated from five randomly generated data sets for the continuous layer model [filtered HIMU] and the delta-function model [HIMU], along with the actual correlations of the filtered HIMU and HIMU data sets.

Data Set	Degree 2	Degree 3	Degree 4	Degree 5
Continuous Layer Model				
filtered HIMU	0.752	0.502	-0.112	-0.358
random 1	0.753	0.446	-0.639	-0.157
random 2	0.560	0.196	0.467	-0.210
random 3	-0.129	0.432	-0.303	-0.069
random 4	0.225	0.448	0.386	-0.130
random 5	-0.166	0.718	-0.285	-0.230
Delta-Function Model				
HIMU	0.850	0.491	0.063	-0.505
random 1	0.726	0.332	0.036	-0.416
random 2	0.622	0.404	0.107	-0.361
random 3	0.873	0.477	0.029	-0.320
random 4	0.893	0.407	0.415	-0.385
random 5	0.761	0.383	0.107	-0.286

Table 5.2. Summary of correlations of 90% significance [or very close to it] or higher for the continuous layer model and the delta-function model when correlated with five averaged layers in the Clayton-Comer tomography model. [A "+" or "-" next to the component name indicates a positive or negative correlation, respectively.]

	Degree 2	Degree 3	Degree 4	Degree 5
Layer 5	-EMI -EMII -HIMU[1]			+EMII
Layer 4	-EMI -EMII[1] -DMM[1]			
Layer 3	-EMI -EMII[1]			
Layer 2			-DMM[2]	-EMII[1]
Layer 1	-EMI[1]	-EMI -HIMU -DMM	-EMII[1] -DMM	-EMII[1]

[1]The continuous layer model correlation is slightly less than 90% significant.
[2]The delta-function model correlation is slightly less than 90% significant.

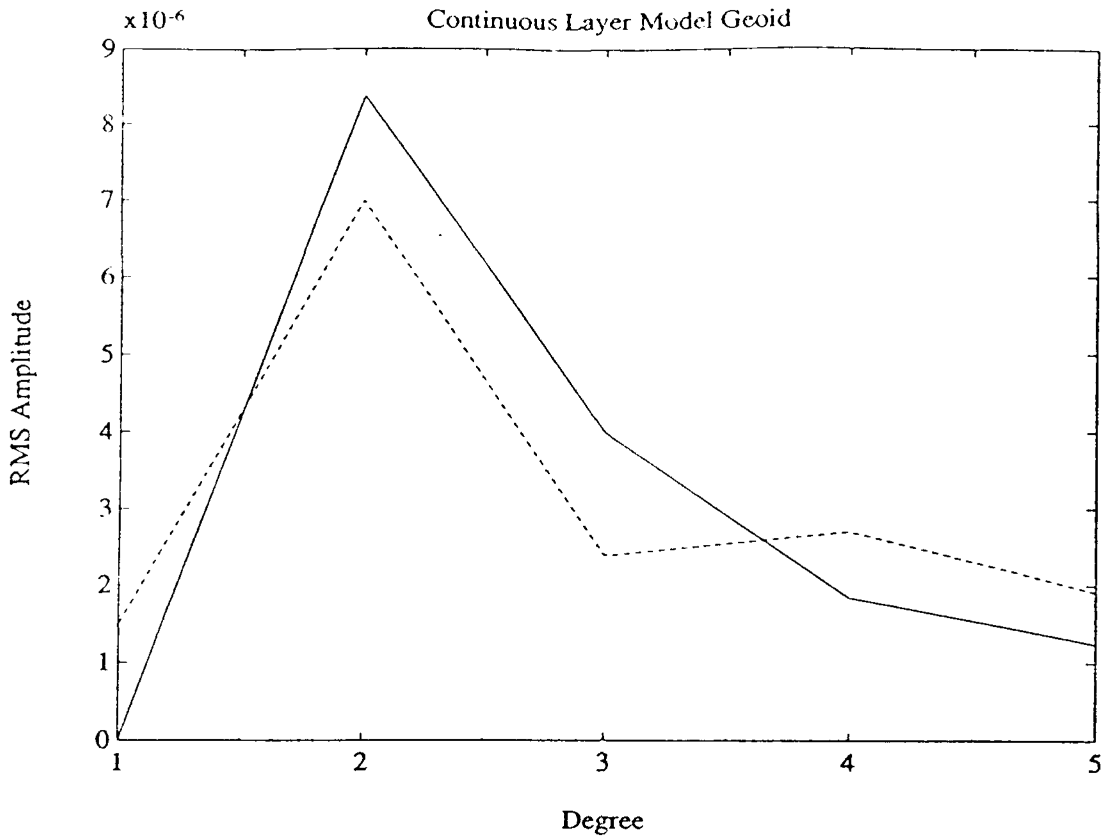

Fig. 5.1. Amplitude spectra for the continuous layer model coefficients of the constructed geoid data set, as compared to the actual geoid. Line symbols: - - - - = constructed geoid, ——– = GEM-L2 geoid.

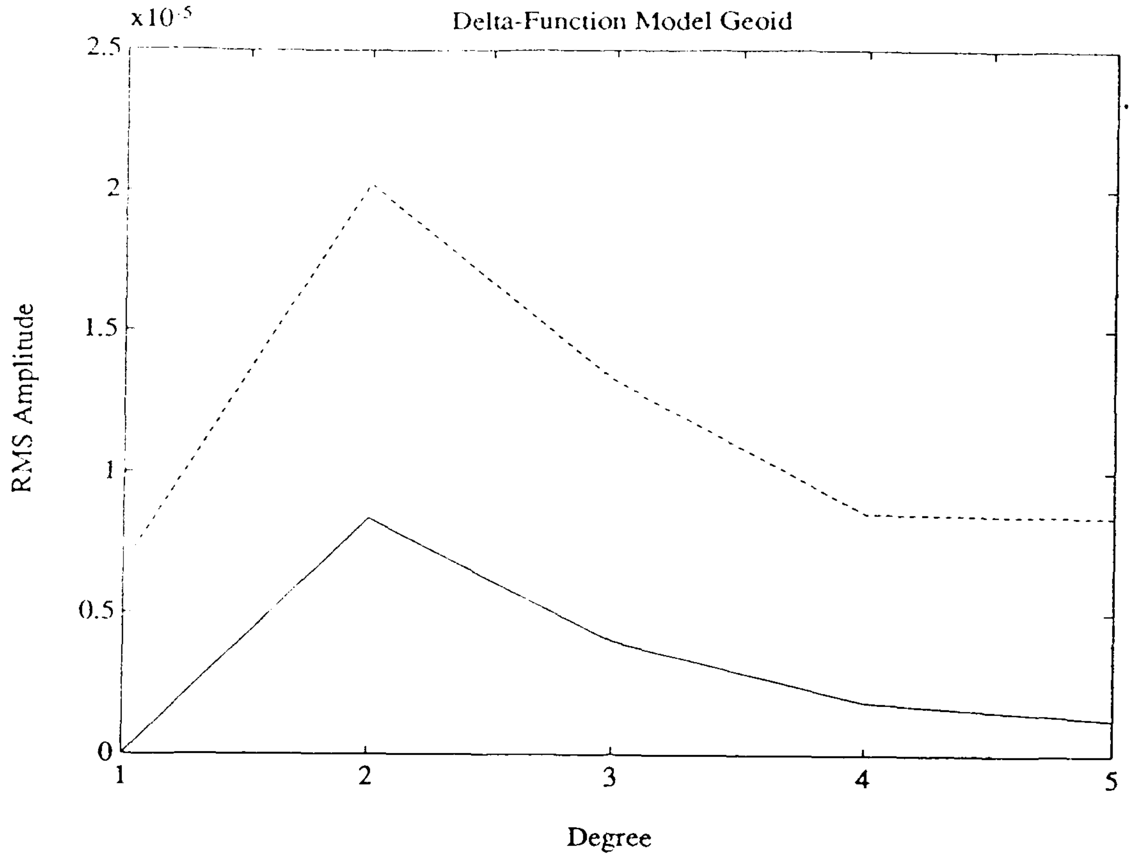

Fig. 5.2. Amplitude spectra for the delta-function model coefficients of the constructed geoid data set, as compared to the actual geoid. Line symbols: - - - - = constructed geoid, —— = GEM-L2 geoid.

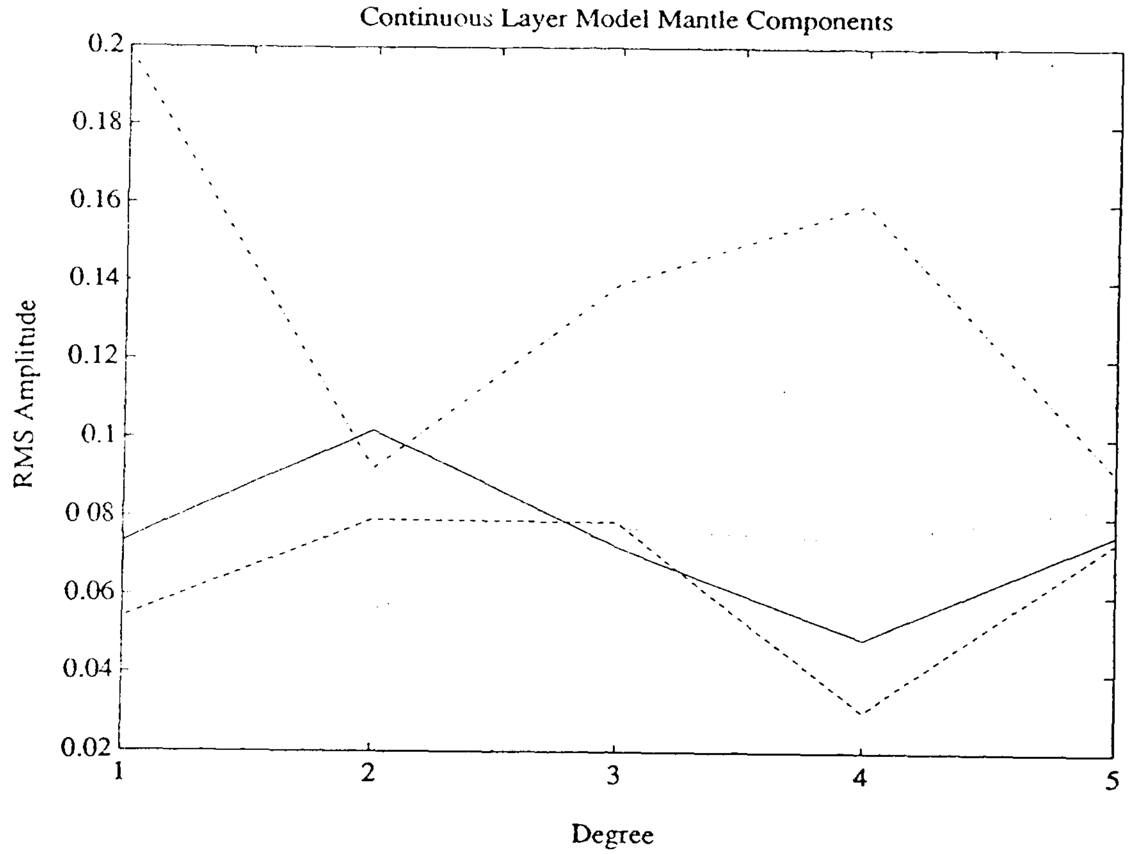

Fig. 5.3. Amplitude spectra for the continuous layer model coefficients of the mantle component data sets. Line symbols: —— = filtered EMI, - - - - = EMII, · · · · = filtered HIMU, - · - · = DMM.

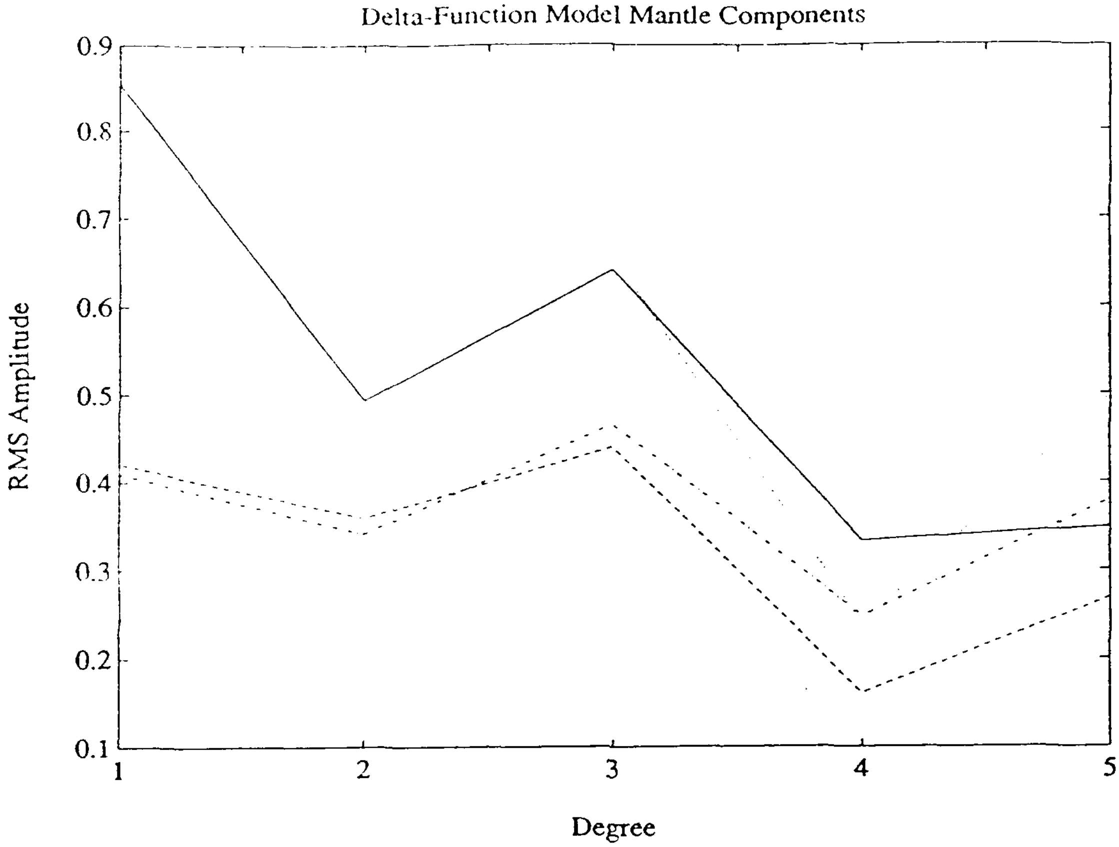

Fig. 5.4. Amplitude spectra for the delta-function model coefficients of the mantle component data sets. Line symbols: ——— = EMI, - - - - = EMII, · · · · = HIMU, - · - · = DMM.

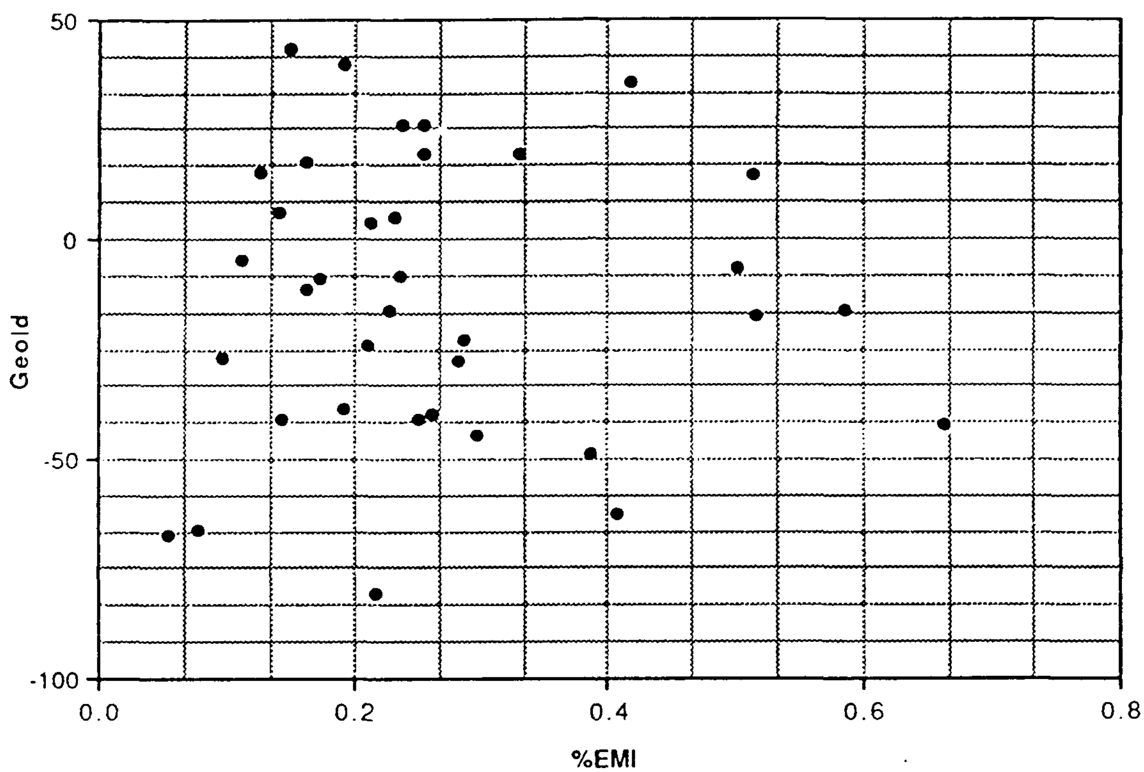

Fig. 5.5. Pointwise comparison, at each geographic feature, of the full geoid anomaly [in meters] with the EMI component percentage. This plot gives the impression that there is no correlation.

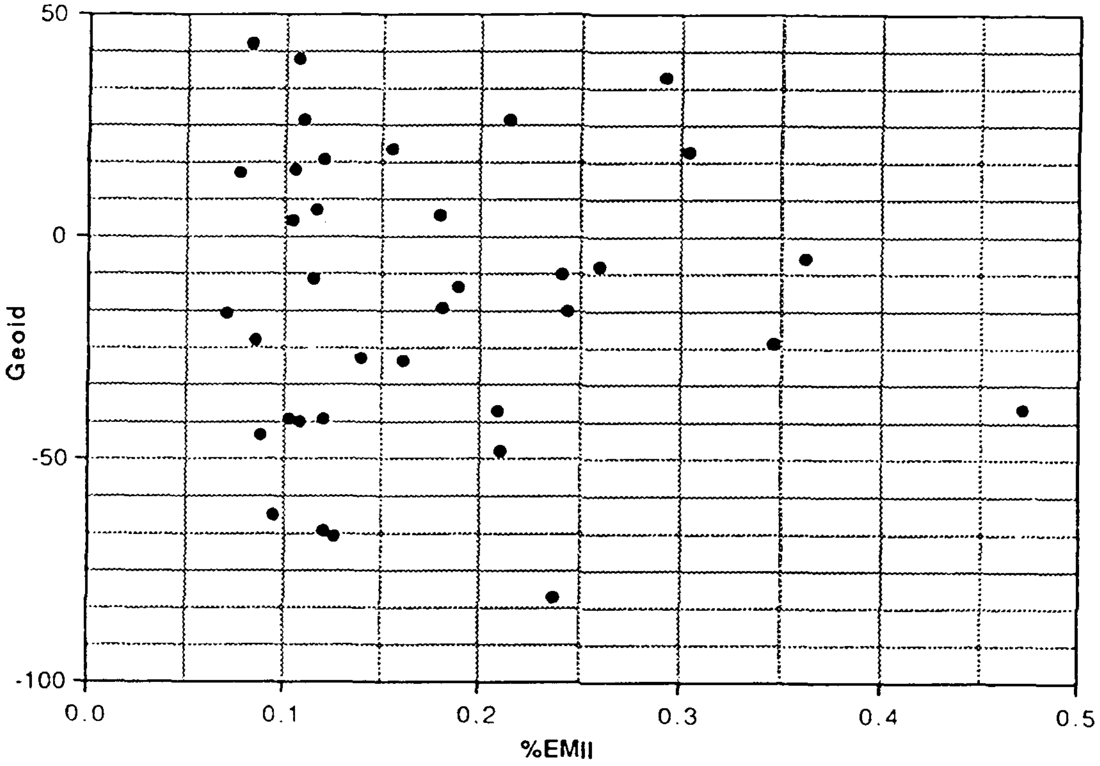

Fig. 5.6. Pointwise comparison, at each geographic feature, of the full geoid anomaly [in meters] with the EMII component percentage. This plot gives the impression that there is no correlation.

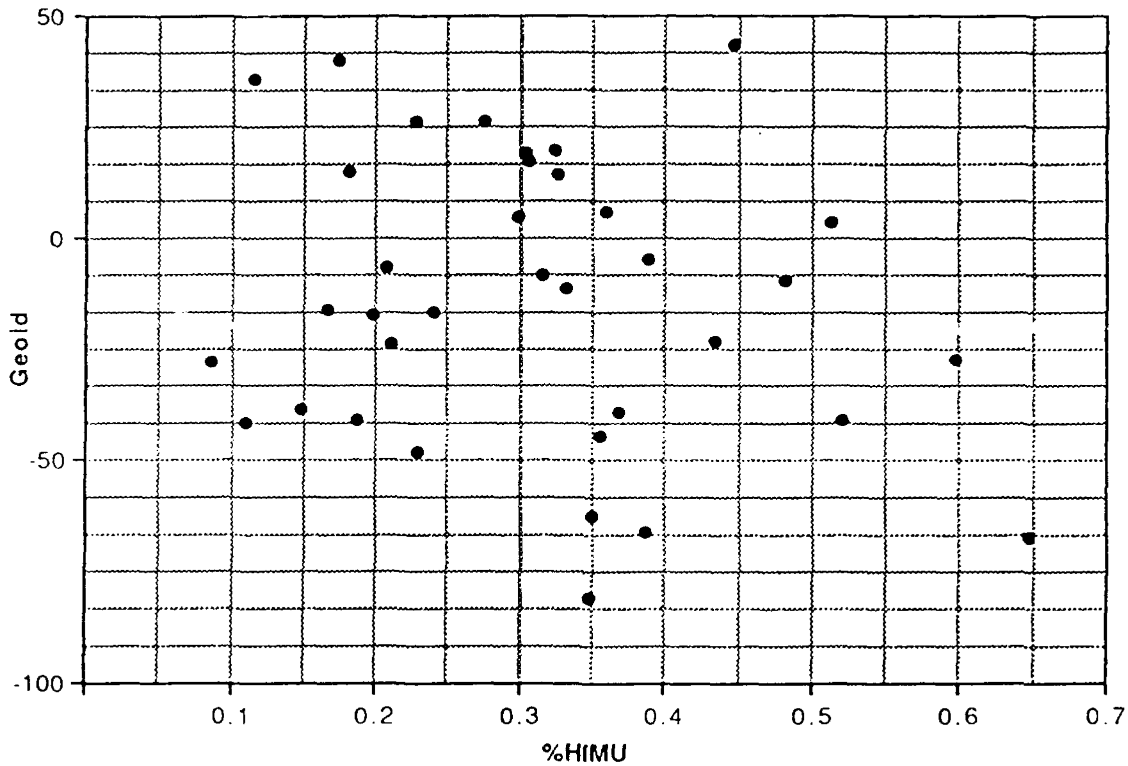

Fig. 5.7. Pointwise comparison, at each geographic feature, of the full geoid anomaly [in meters] with the HIMU component percentage. This plot gives the impression that there is no correlation.

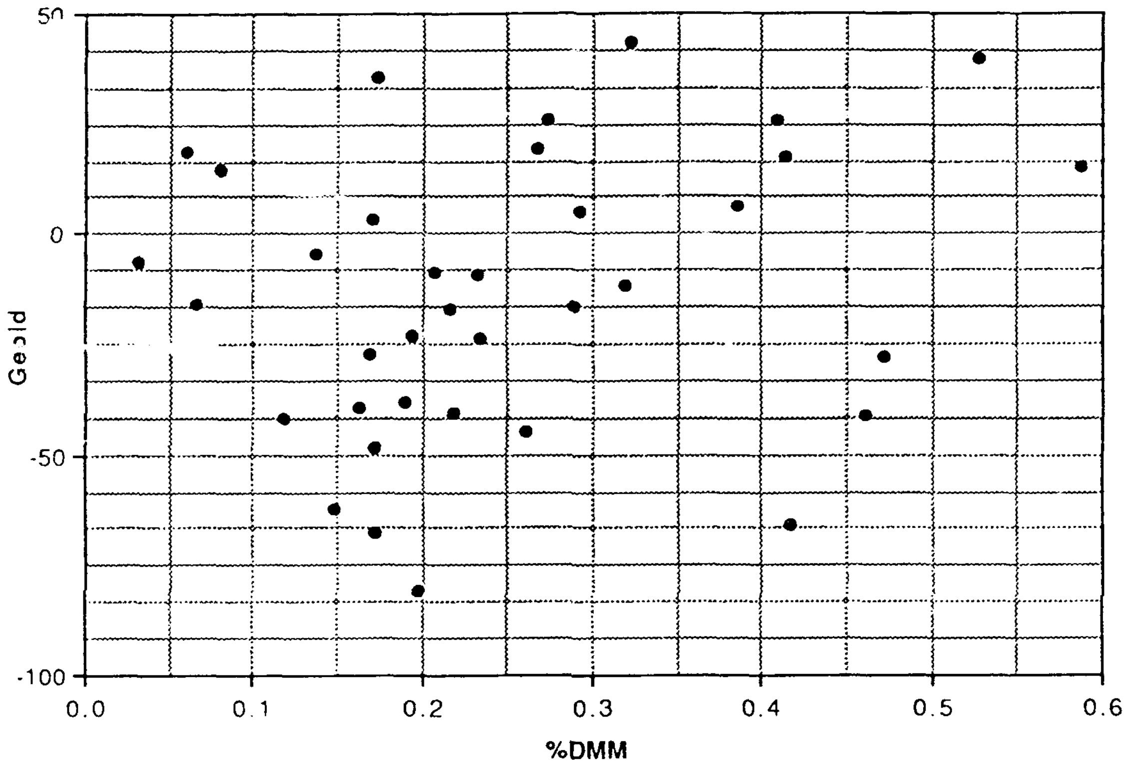

Fig. 5.8. Pointwise comparison, at each geographic feature, of the full geoid anomaly [in meters] with the DMM component percentage. This plot gives the impression that there is no correlation.

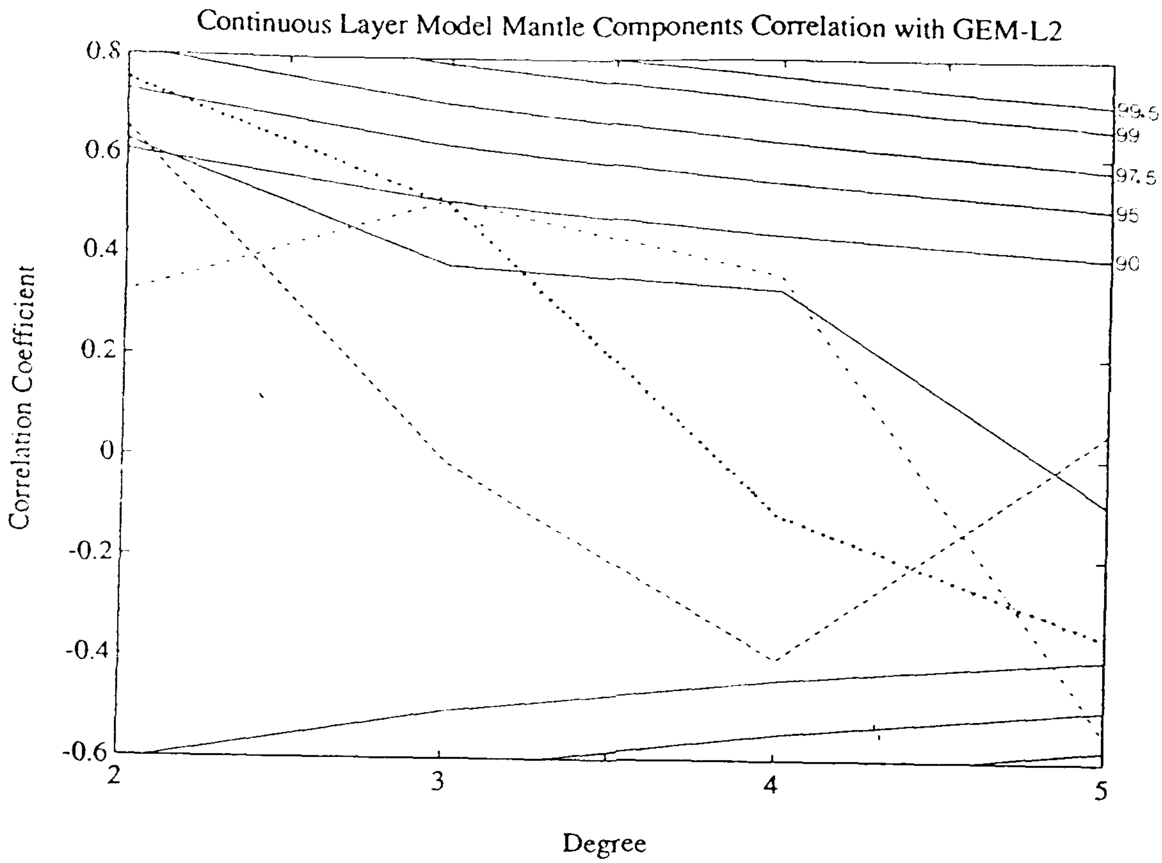

Fig. 5.9. Correlation of the continuous layer model mantle component coefficient solutions with the GEM-L2 geoid coefficients. Line symbols: —— = filtered EMI, - - - - = EMII, · · · · = filtered HIMU, - · - · = DMM. Confidence levels are determined by a t-test with $2l$ degrees of freedom.

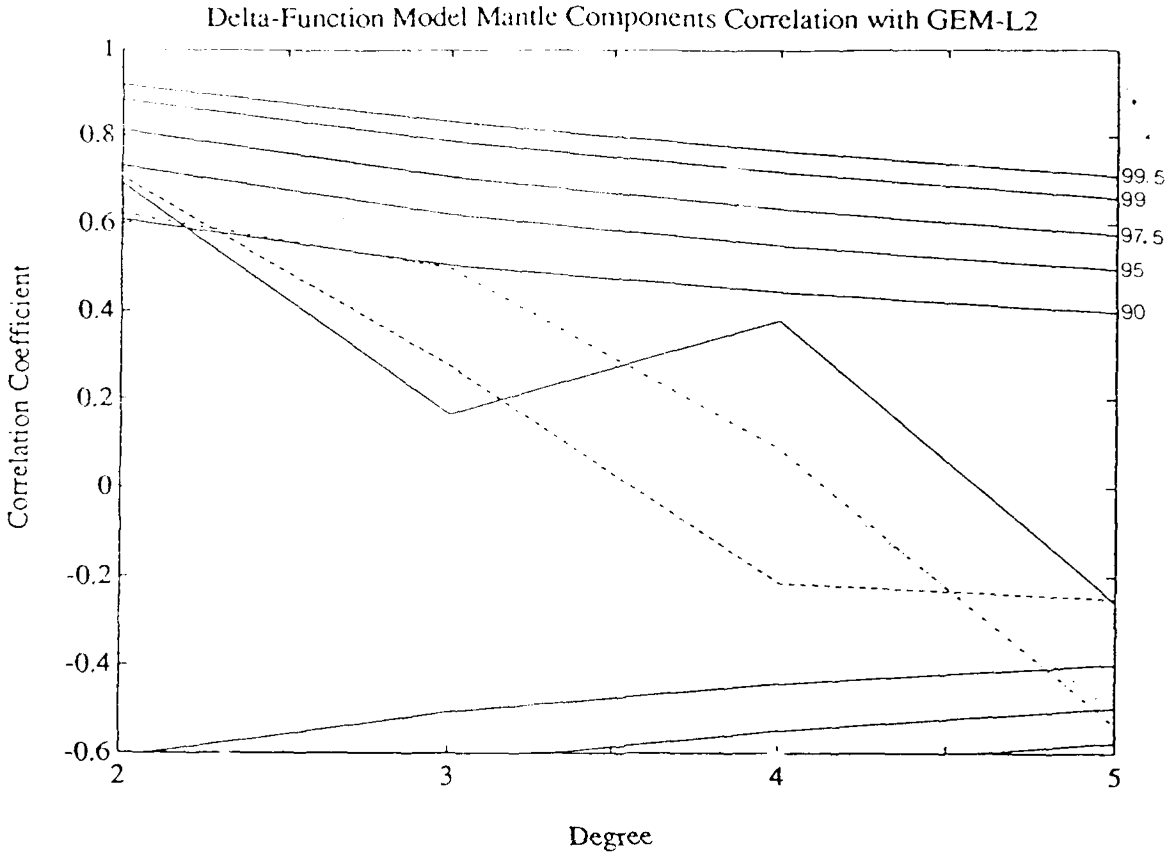

Fig. 5.10. Correlation of the delta-function model mantle component coefficient solutions with the GEM-L2 geoid coefficients. Line symbols: ——— = EMI, - - - - = EMII, · · · · = HIMU, - · - · = DMM. Confidence levels are determined by a t-test with $2l$ degrees of freedom.

CONTINUOUS LAYER MODEL RANDOM1 DEGREE 2 HIMU

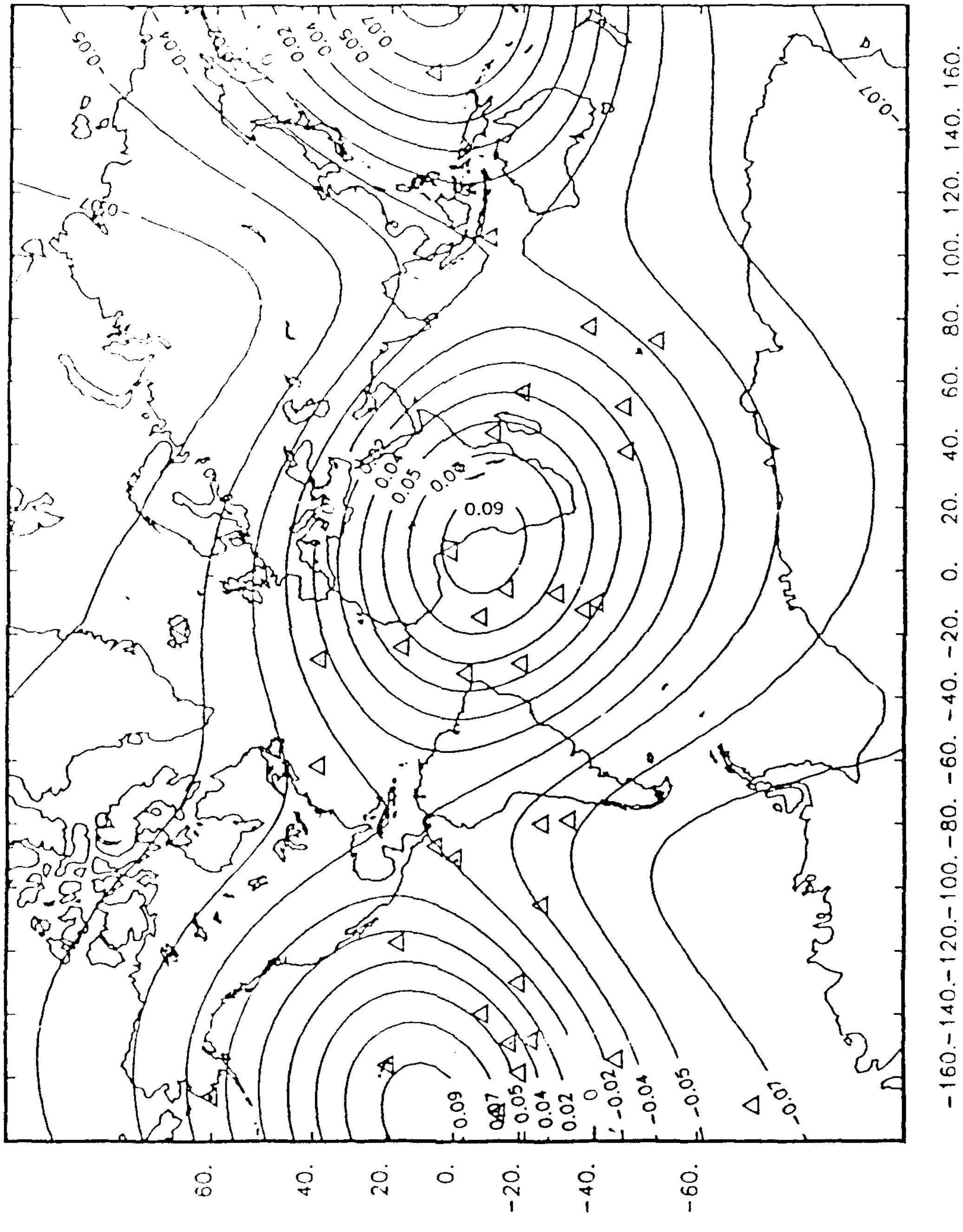

Fig. 5.11. Reconstruction [on a 5° grid] of the continuous layer model spherical harmonic degree 2 function for the first randomization of the filtered *HIMU* data set. Values are deviations from the average filtered HIMU percentage [0.31]. Feature locations are designated by triangles.

CONTINUOUS LAYER MODEL RANDOM2 DEGREE 2 HIMU

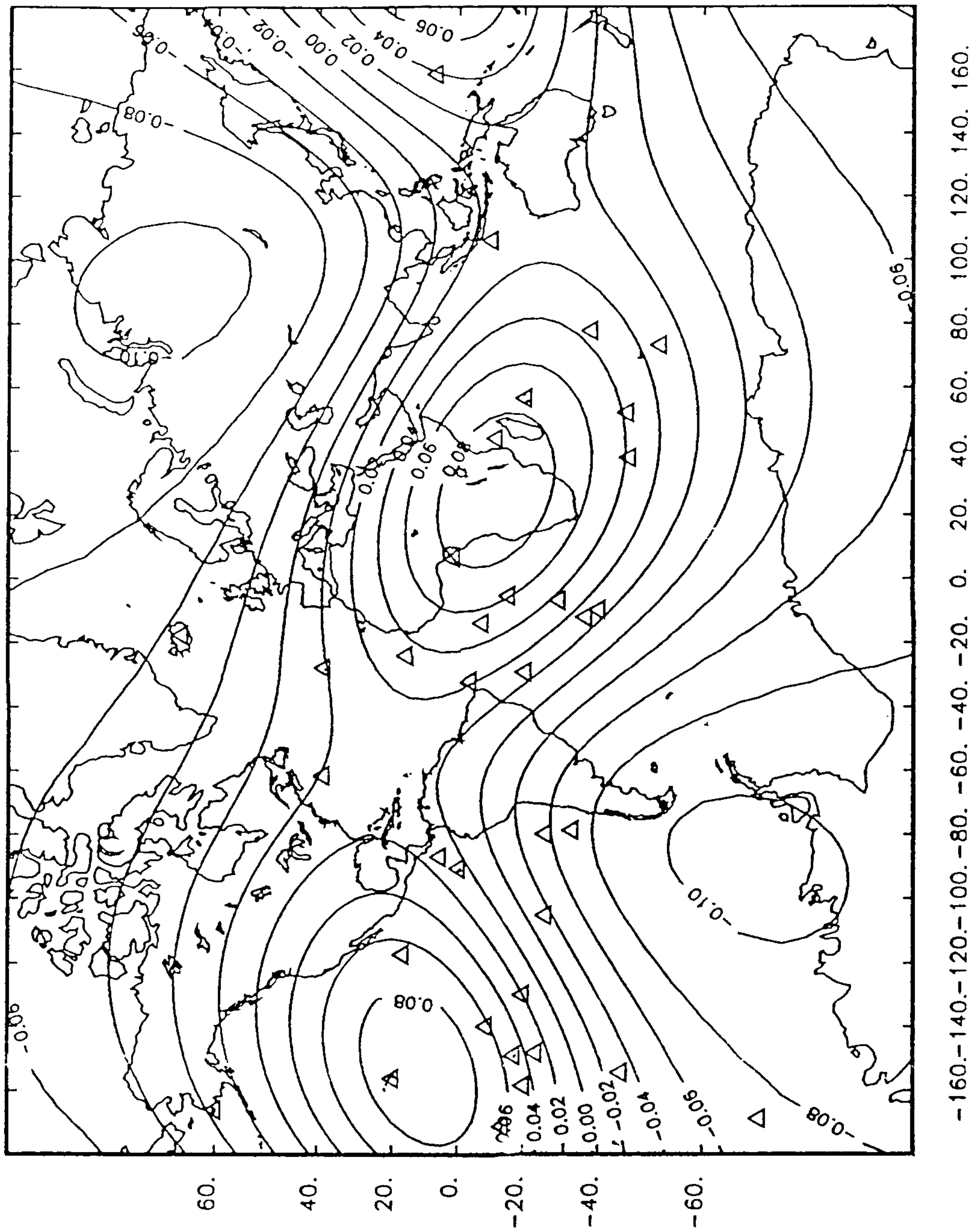

Fig. 5.12. Reconstruction [on a 5° grid] of the continuous layer model spherical harmonic degree 2 function for the second randomization of the filtered HIMU data set. Values are deviations from the average filtered HIMU percentage [0.31]. Feature locations are designated by triangles.

CONTINUOUS LAYER MODEL RANDOM3 DEGREE 2 HIMU

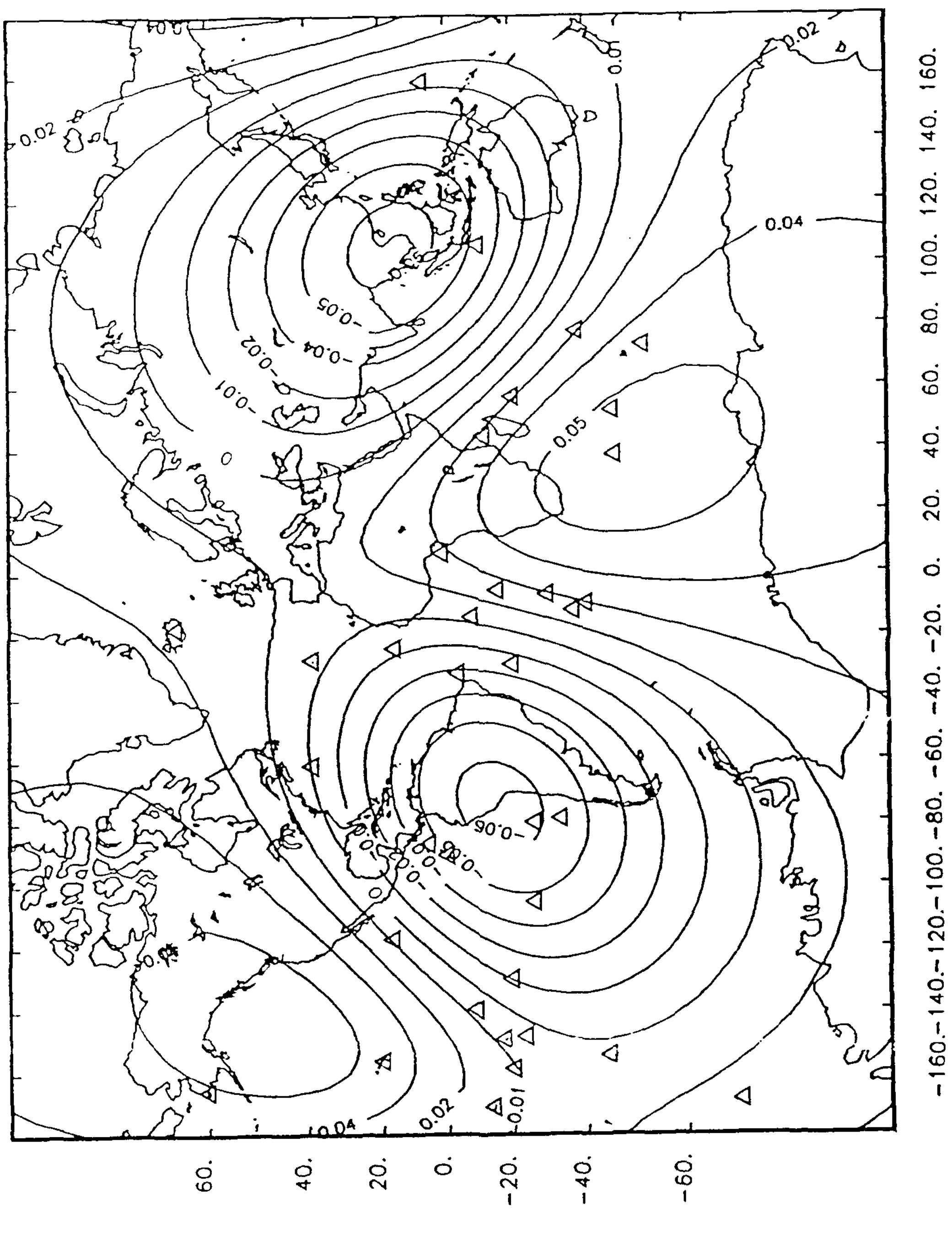

Fig. 5.13. Reconstruction [on a 5° grid] of the continuous layer model spherical harmonic degree 2 function for the third randomization of the filtered HIMU data set. Values are deviations from the average filtered HIMU percentage [0.31]. Feature locations are designated by triangles.

CONTINUOUS LAYER MODEL RANDOM4 DEGREE 2 HIMU

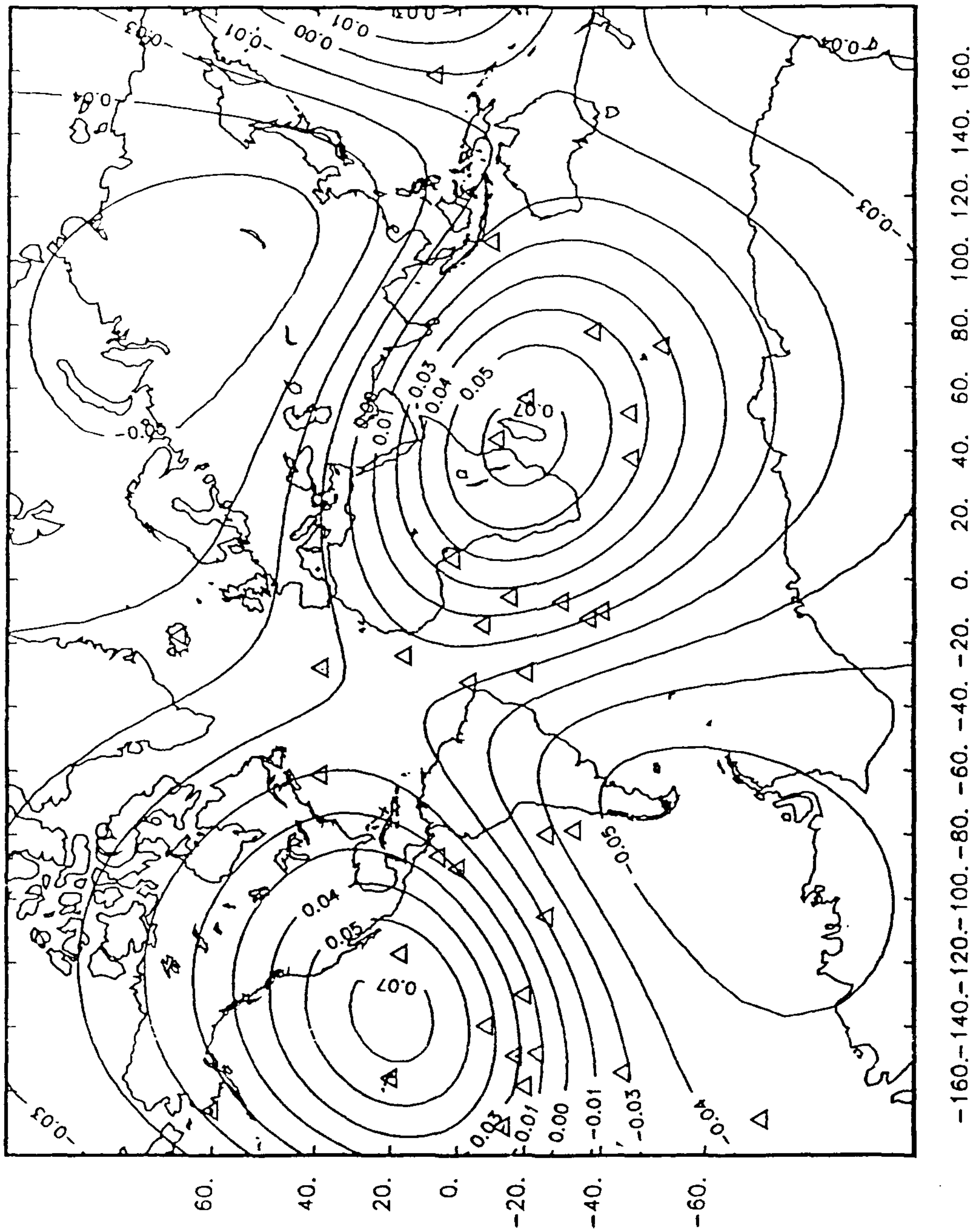

Fig. 5.14. Reconstruction [on a 5° grid] of the continuous layer model spherical harmonic degree 2 function for the fourth randomization of the filtered HIMU data set. Values are deviations from the average filtered HIMU percentage [0.31]. Feature locations are designated by triangles.

CONTINUOUS LAYER MODEL RANDOM5 DEGREE 2 HIMU

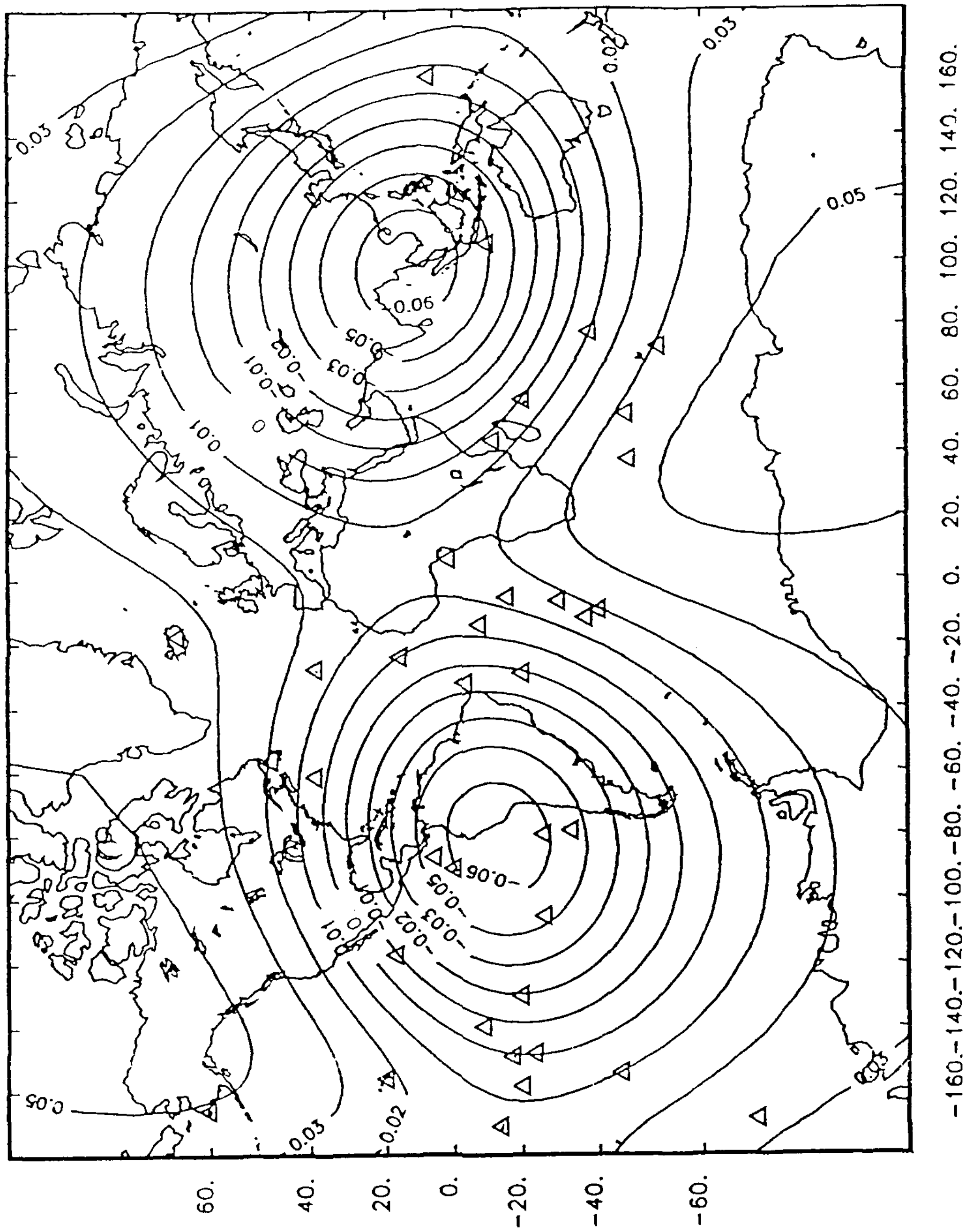

Fig. 5.15. Reconstruction [on a 5° grid] of the continuous layer model spherical harmonic degree 2 function for the fifth randomization of the filtered HIMU data set. Values are deviations from the average filtered HIMU percentage [0.31]. Feature locations are designated by triangles.

DELTA-FUNCTION MODEL RANDOM1 DEGREE 2 HIMU

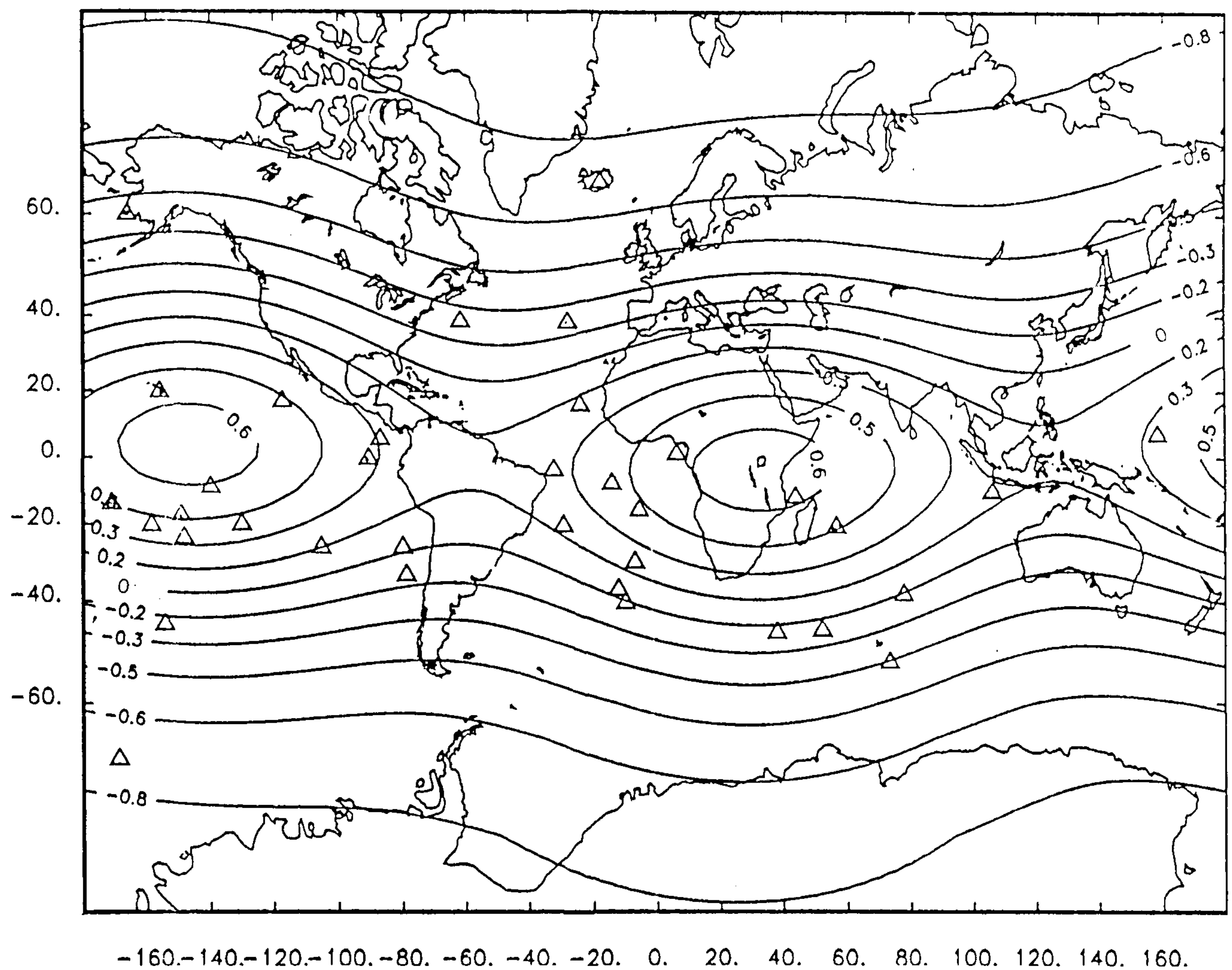

Fig. 5.16. Reconstruction [on a 5° grid] of the delta-function model spherical harmonic degree 2 function for the first randomization of the HIMU data set. Values are deviations from the average HIMU percentage [0.31]. Feature locations are designated by triangles.

DELTA-FUNCTION MODEL RANDOM2 DEGREE 2 HIMU

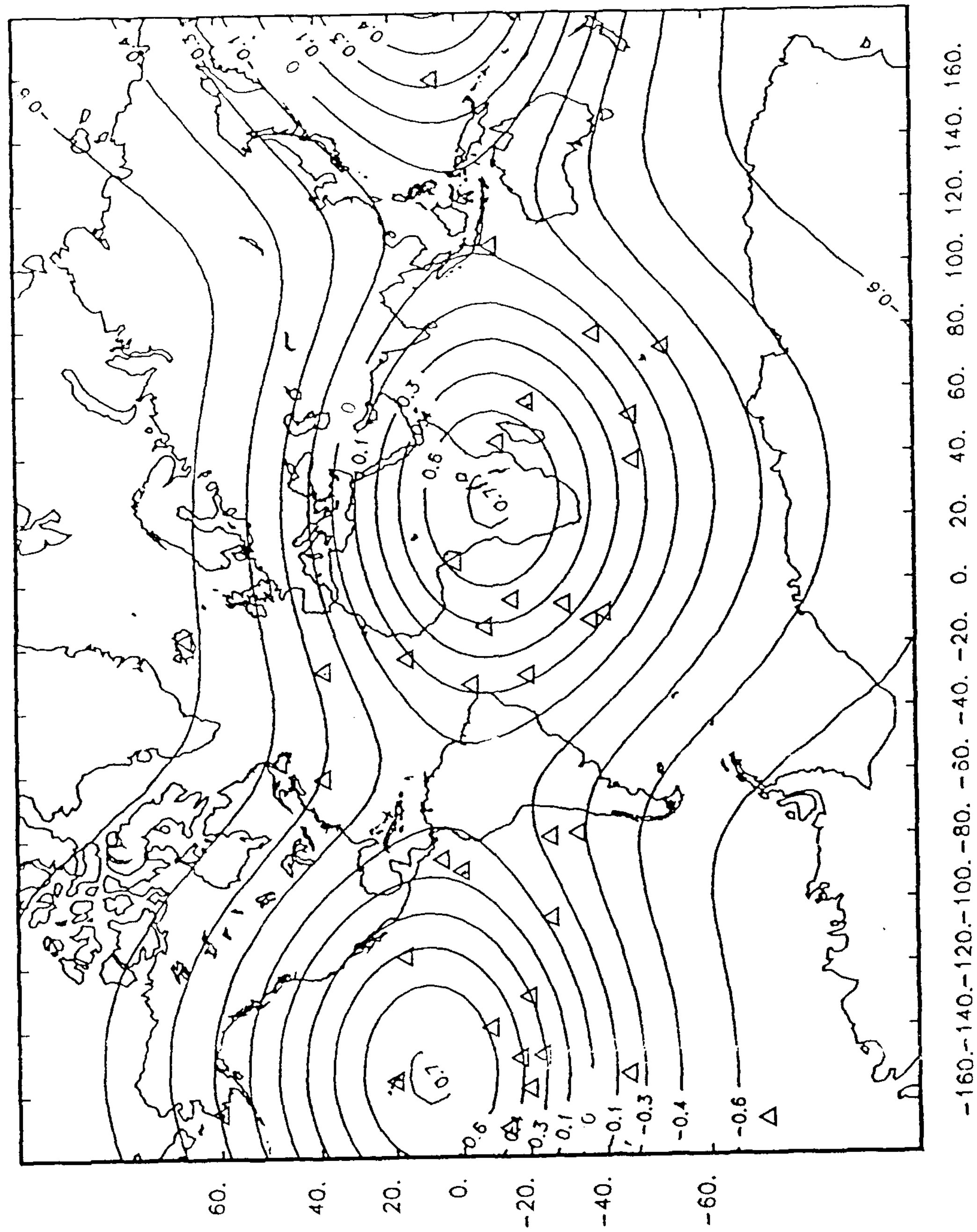

Fig. 5.17. Reconstruction [on a 5° grid] of the delta-function model spherical harmonic degree 2 function for the second randomization of the HIMU data set. Values are deviations from the average HIMU percentage [0.31]. Feature locations are designated by triangles.

DELTA-FUNCTION MODEL RANDOM3 DEGREE 2 HIMU

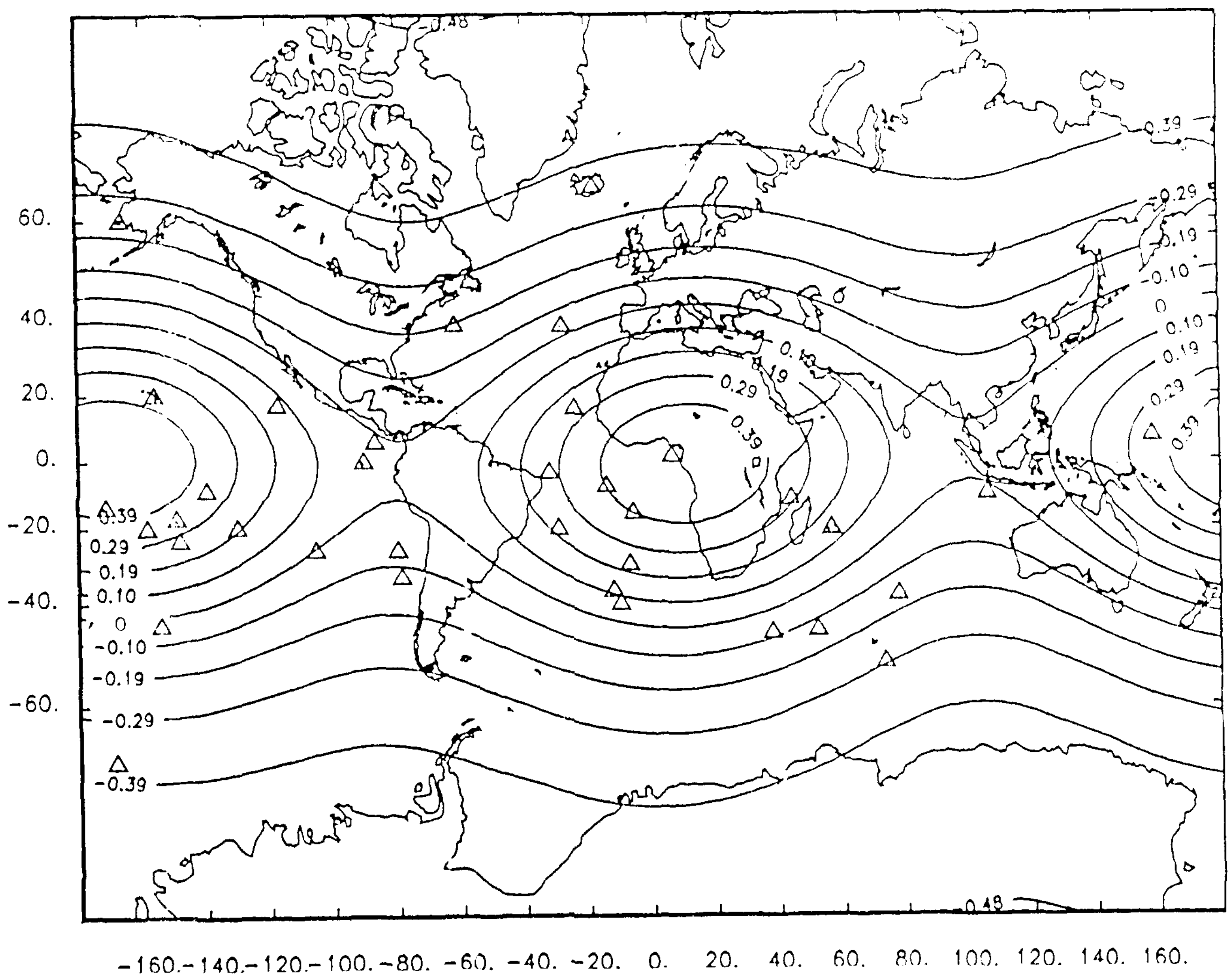

Fig. 5.18. Reconstruction [on a 5° grid] of the delta-function model spherical harmonic degree 2 function for the third randomization of the HIMU data set. Values are deviations from the average HIMU percentage [0.31]. Feature locations are designated by triangles.

DELTA-FUNCTION MODEL RANDOM4 DEGREE 2 HIMU

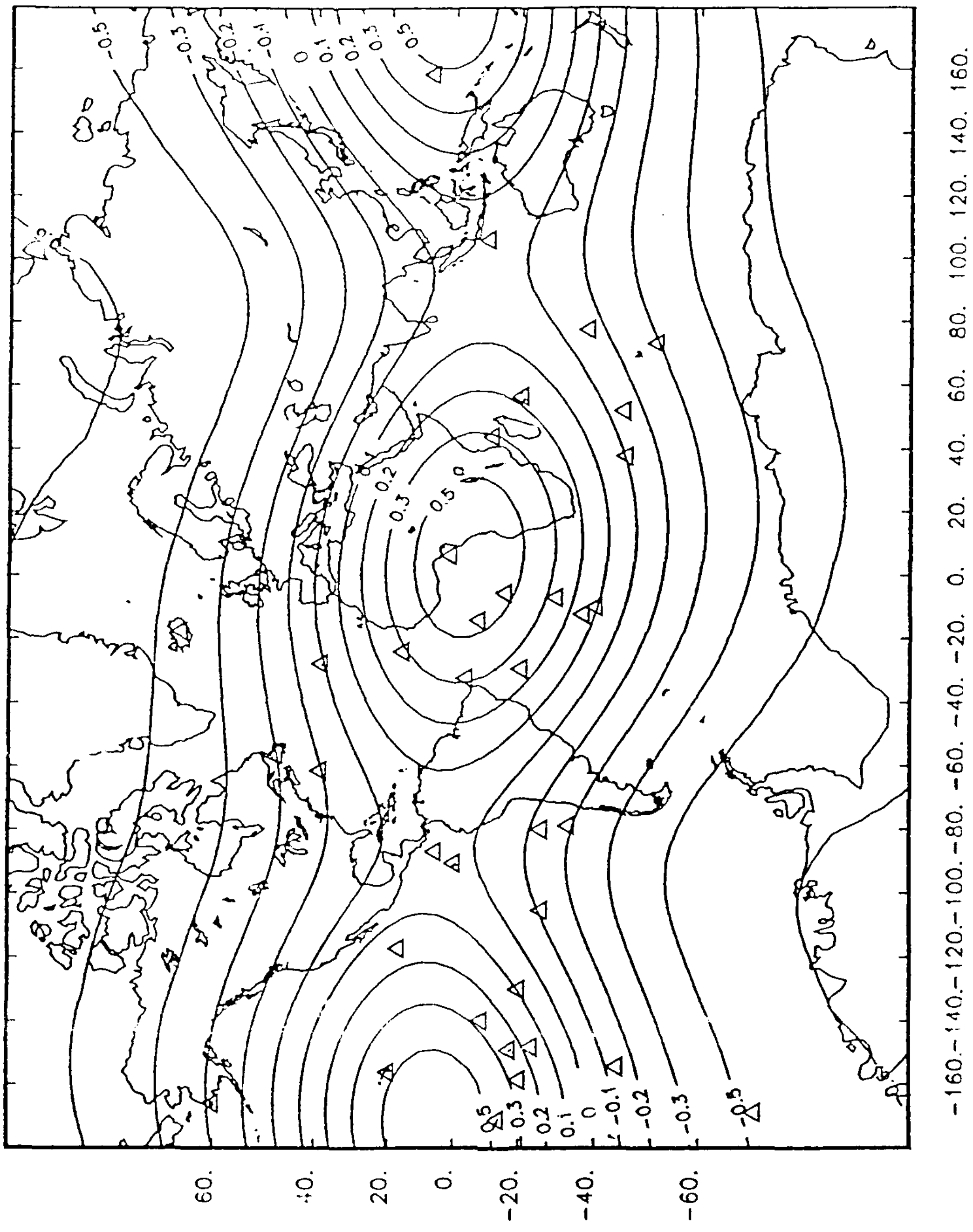

Fig. 5.19. Reconstruction [on a 5° grid] of the delta-function model spherical harmonic degree 2 function for the fourth randomization of the HIMU data set. Values are deviations from the average HIMU percentage [0.31]. Feature locations are designated by triangles.

DELTA-FUNCTION MODEL RANDOM5 DEGREE 2 HIMU

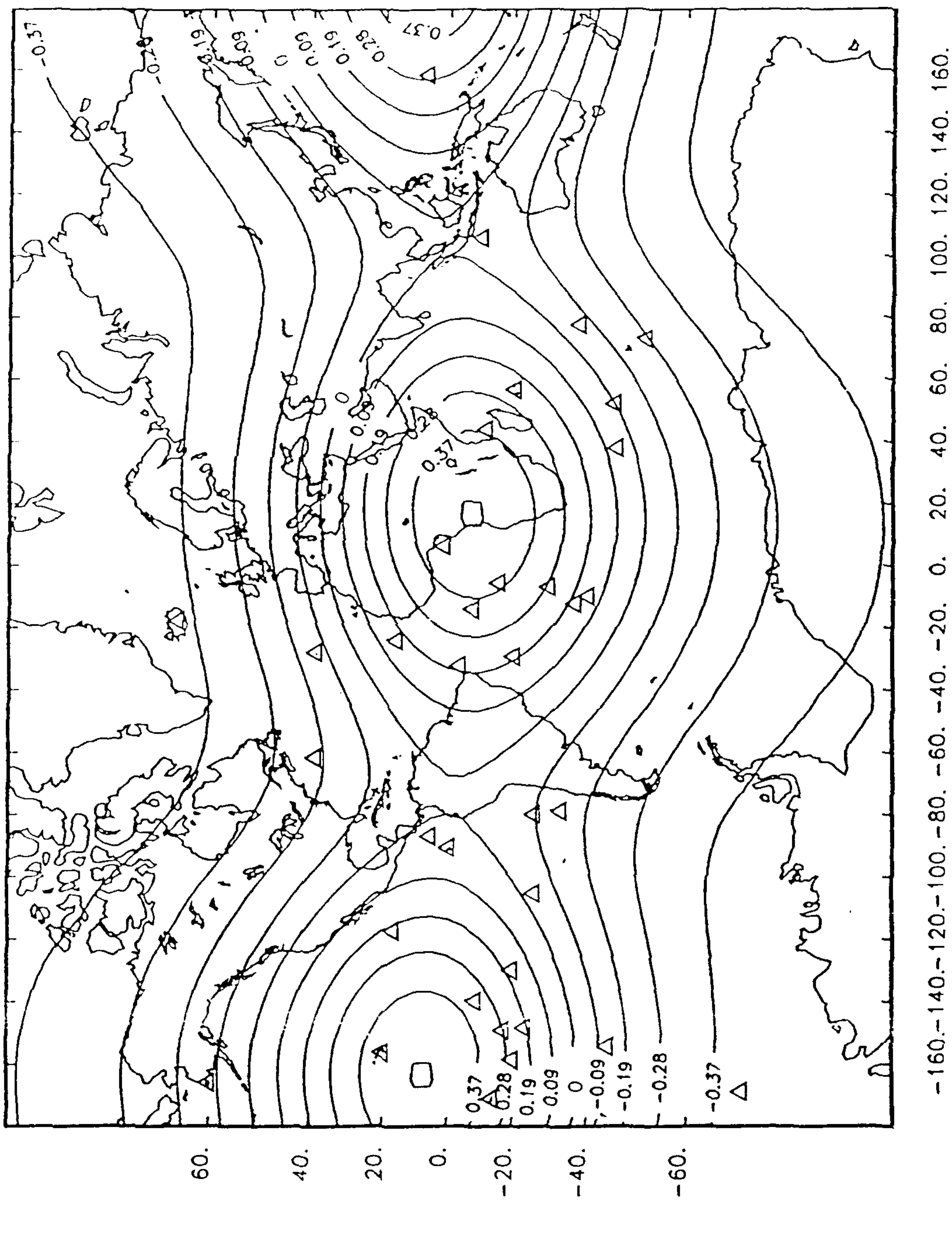

Fig. 5.20. Reconstruction [on a 5° grid] of the delta-function model spherical harmonic degree 2 function for the fifth randomization of the HIMU data set. Values are deviations from the average HIMU percentage [0.31]. Feature locations are designated by triangles.

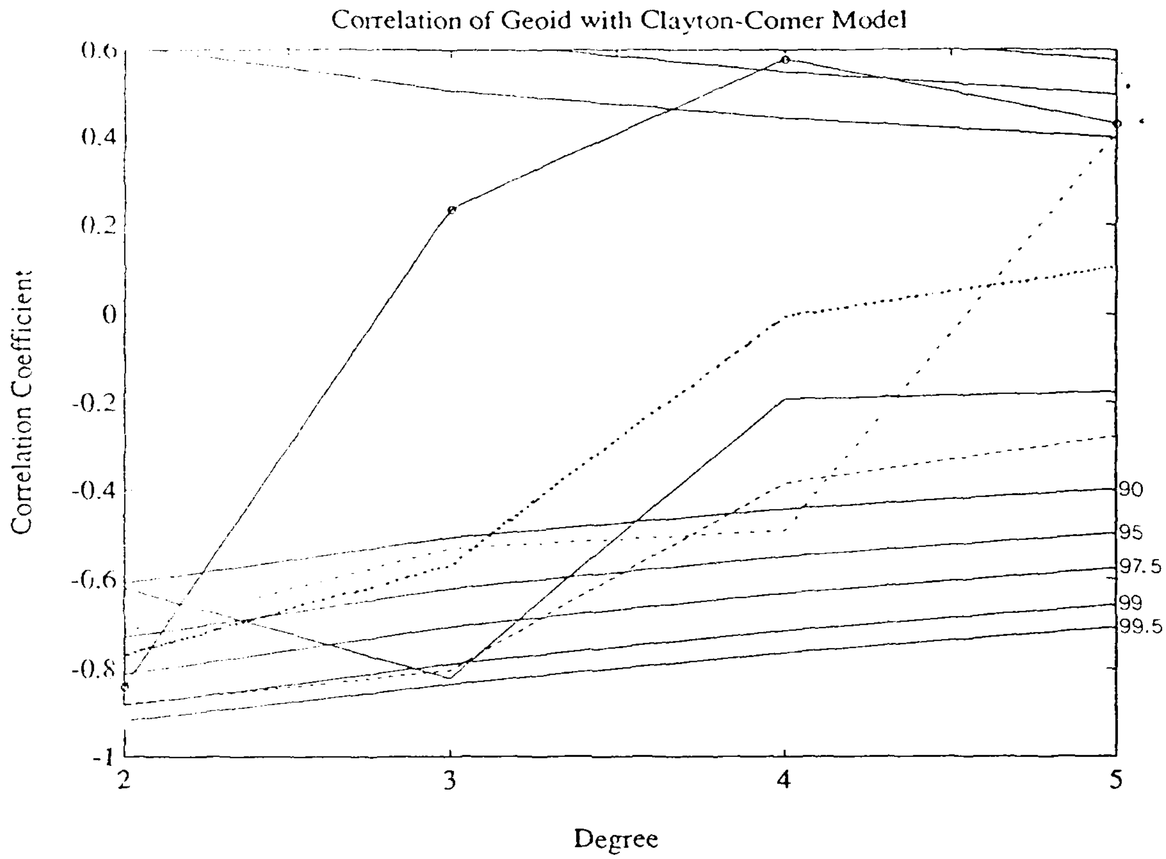

Fig. 5.21. Correlation of the GEM-L2 geoid coefficients with the five layers of the Clayton-Comer seismic tomography model. Line symbols: —— = layer 1 [2500-2900 km], - - - - = layer 2 [2100-2500 km], · · · · = layer 3 [1700-2100 km], - · - · = layer 4 [1200-1700 km], o—o = layer 5 [700-1200 km]. Confidence levels are determined by a t-test with $2l$ degrees of freedom.

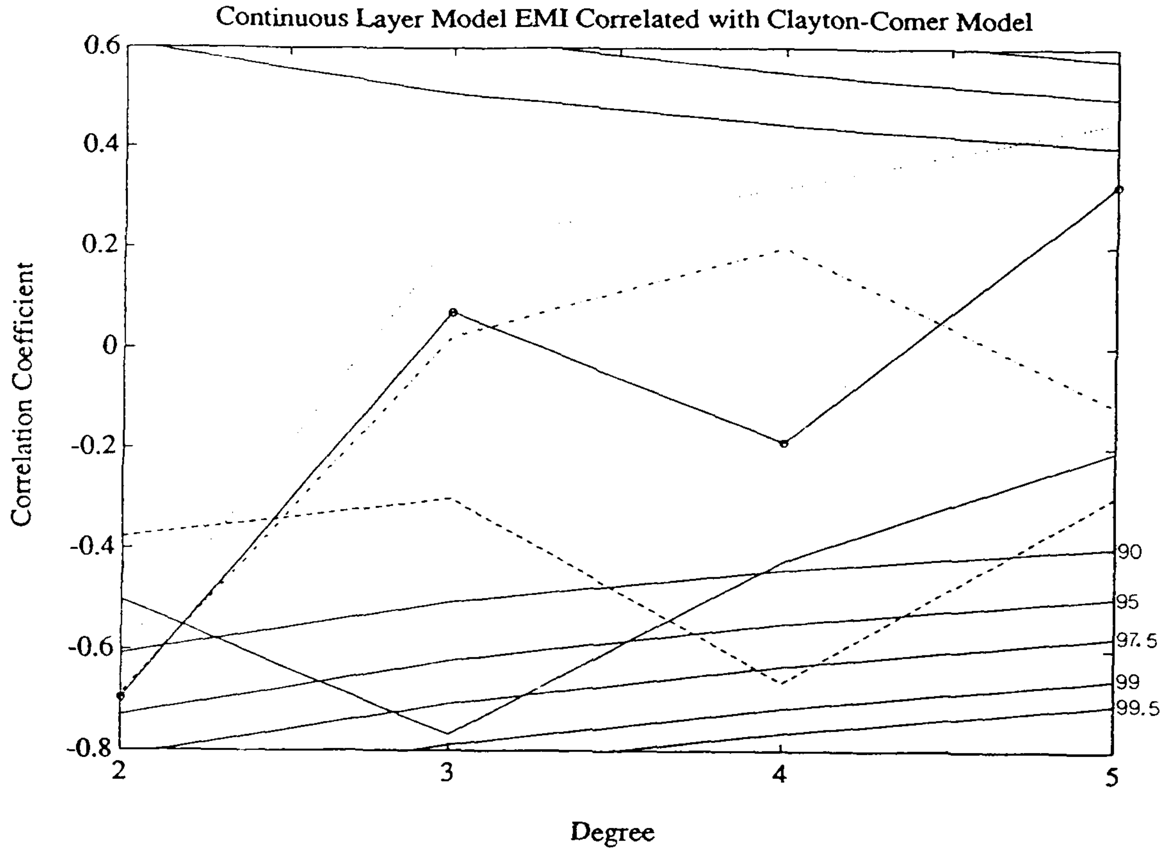

Fig. 5.22. Correlation of the continuous layer model filtered EMI coefficients with the five layers of the Clayton-Comer seismic tomography model. Line symbols: —— = layer 1 [2500-2900 km], - - - - = layer 2 [2100-2500 km], · · · · = layer 3 [1700-2100 km], - · - · = layer 4 [1200-1700 km], o—o = layer 5 [700-1200 km]. Confidence levels are determined by a t-test with $2l$ degrees of freedom.

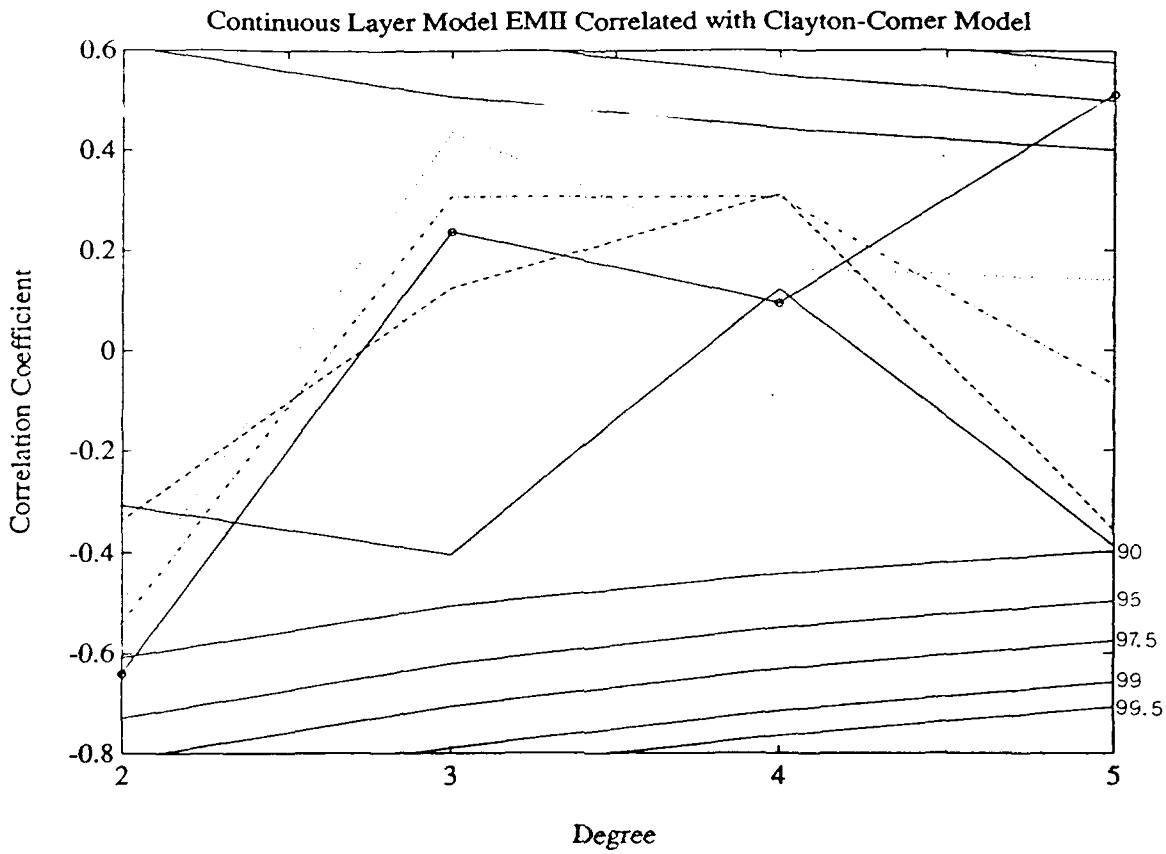

Fig. 5.23. Correlation of the continuous layer model EMII coefficients with the five layers of the Clayton-Comer seismic tomography model. Line symbols: —— = layer 1 [2500-2900 km], - - - - = layer 2 [2100-2500 km], · · · · = layer 3 [1700-2100 km], - · - · = layer 4 [1200-1700 km], o—o = layer 5 [700-1200 km]. Confidence levels are determined by a t-test with $2l$ degrees of freedom.

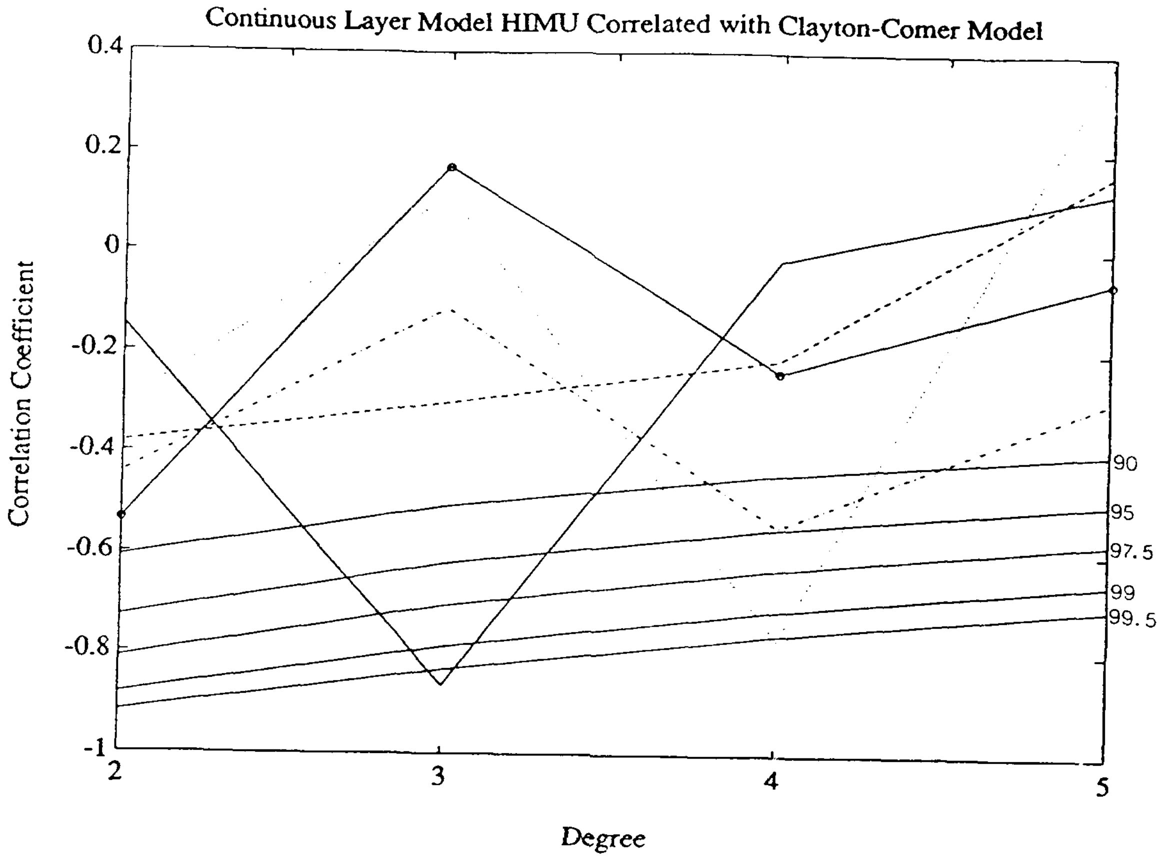

Fig. 5.24. Correlation of the continuous layer model filtered HIMU coefficients with the five layers of the Clayton-Comer seismic tomography model. Line symbols: —— = layer 1 [2500-2900 km], - - - - = layer 2 [2100-2500 km], · · · · = layer 3 [1700-2100 km], - · - · = layer 4 [1200-1700 km], o—o = layer 5 [700-1200 km]. Confidence levels are determined by a t-test with $2l$ degrees of freedom.

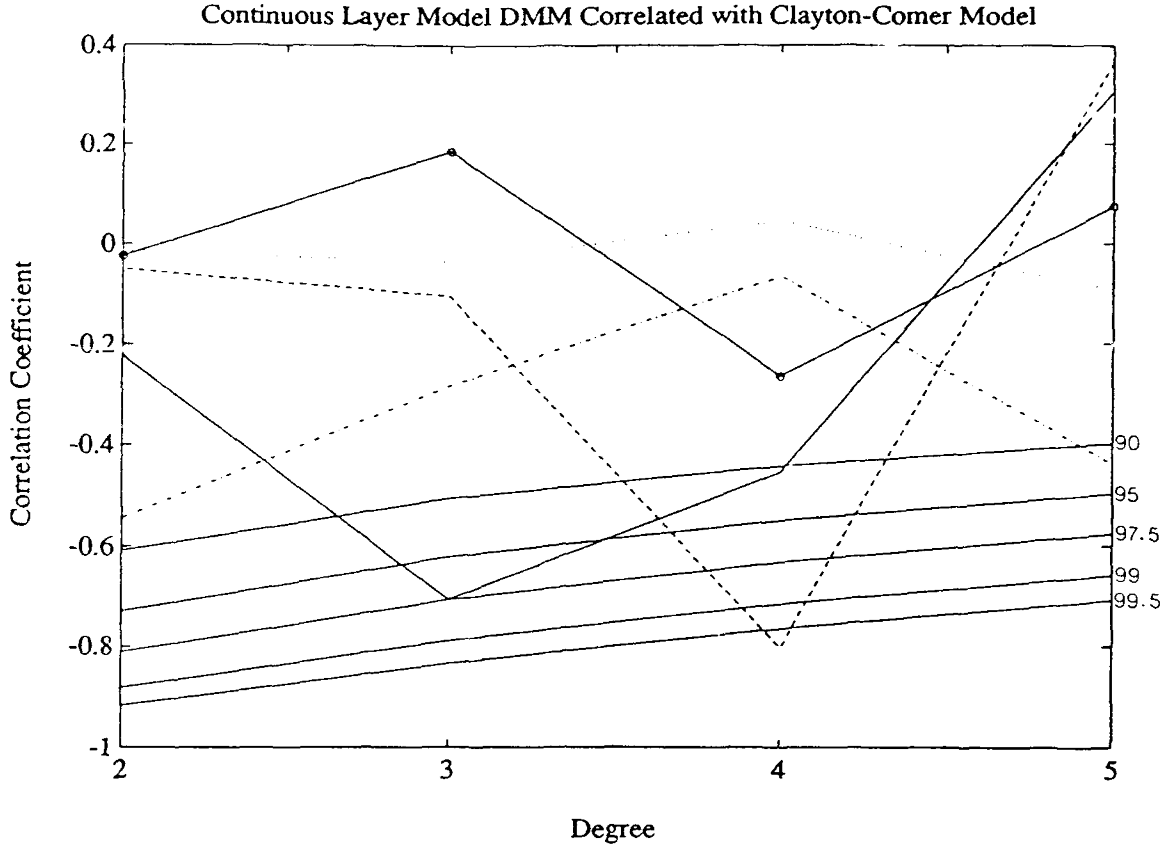

Fig. 5.25. Correlation of the continuous layer model DMM coefficients with the five layers of the Clayton-Comer seismic tomography model. Line symbols: ——— = layer 1 [2500-2900 km], - - - - = layer 2 [2100-2500 km], · · · · = layer 3 [1700-2100 km], - · - · = layer 4 [1200-1700 km], o—o = layer 5 [700-1200 km]. Confidence levels are determined by a t-test with $2l$ degrees of freedom.

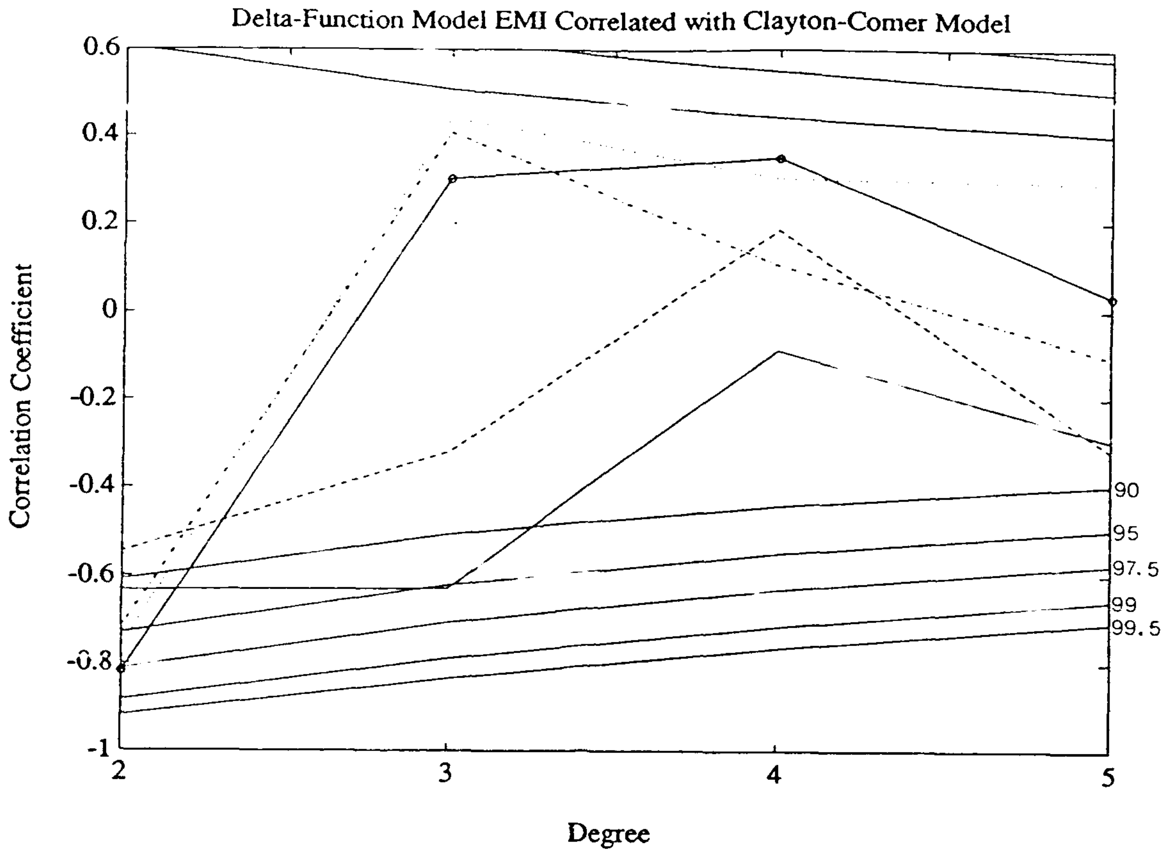

Fig. 5.26. Correlation of the delta-function model EMI coefficients with the five layers of the Clayton-Comer seismic tomography model. Line symbols: —— = layer 1 [2500-2900 km], - - - - = layer 2 [2100-2500 km], · · · · = layer 3 [1700-2100 km], - · - · = layer 4 [1200-1700 km], o—o = layer 5 [700-1200 km]. Confidence levels are determined by a t-test with $2l$ degrees of freedom.

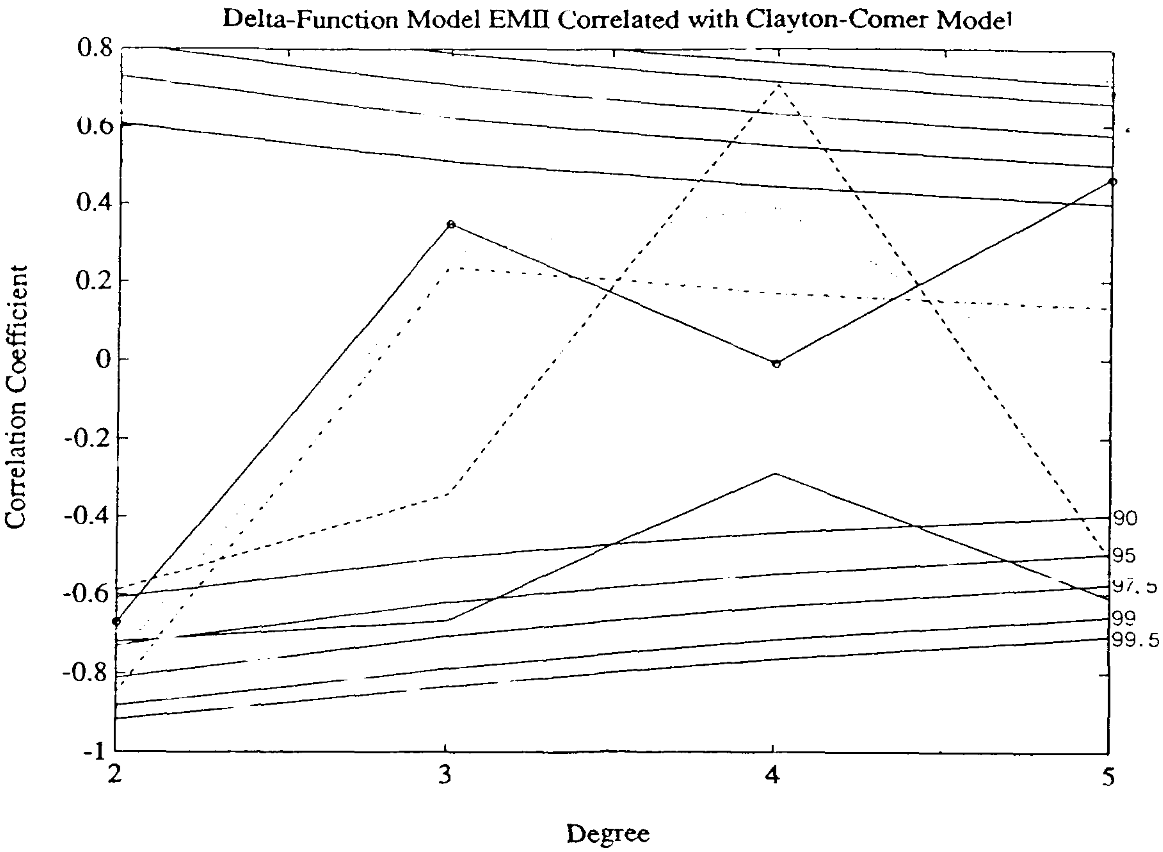

Fig. 5.27. Correlation of the delta-function model EMII coefficients with the five layers of the Clayton-Comer seismic tomography model. Line symbols: ——— = layer 1 [2500-2900 km], - - - - = layer 2 [2100-2500 km], · · · · = layer 3 [1700-2100 km], - · - · = layer 4 [1200-1700 km], o—o = layer 5 [700-1200 km]. Confidence levels are determined by a t-test with $2l$ degrees of freedom.

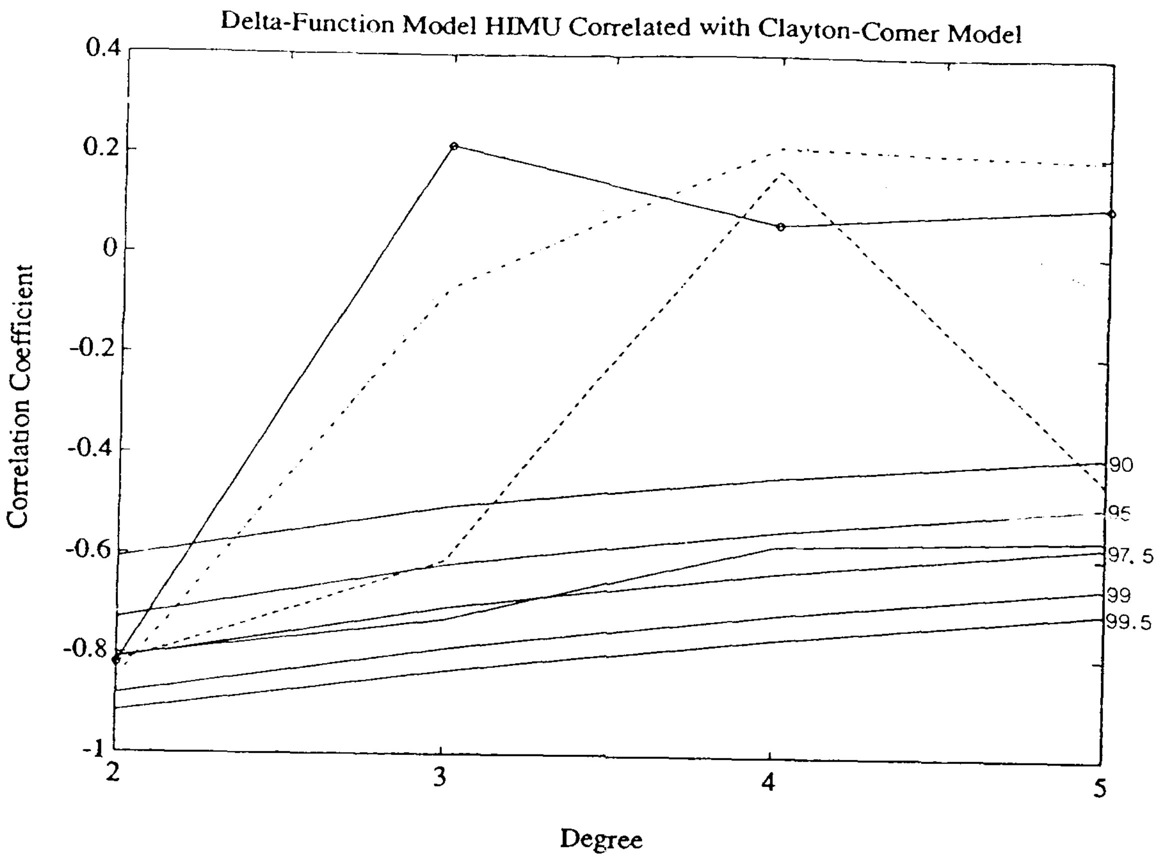

Fig. 5.28. Correlation of the delta-function model HIMU coefficients with the five layers of the Clayton-Comer seismic tomography model. Line symbols: ------ = layer 1 [2500-2900 km], - - - - = layer 2 [2100-2500 km], · · · · = layer 3 [1700-2100 km], - · - · = layer 4 [1200-1700 km], o—o = layer 5 [700-1200 km]. Confidence levels are determined by a t-test with $2l$ degrees of freedom.

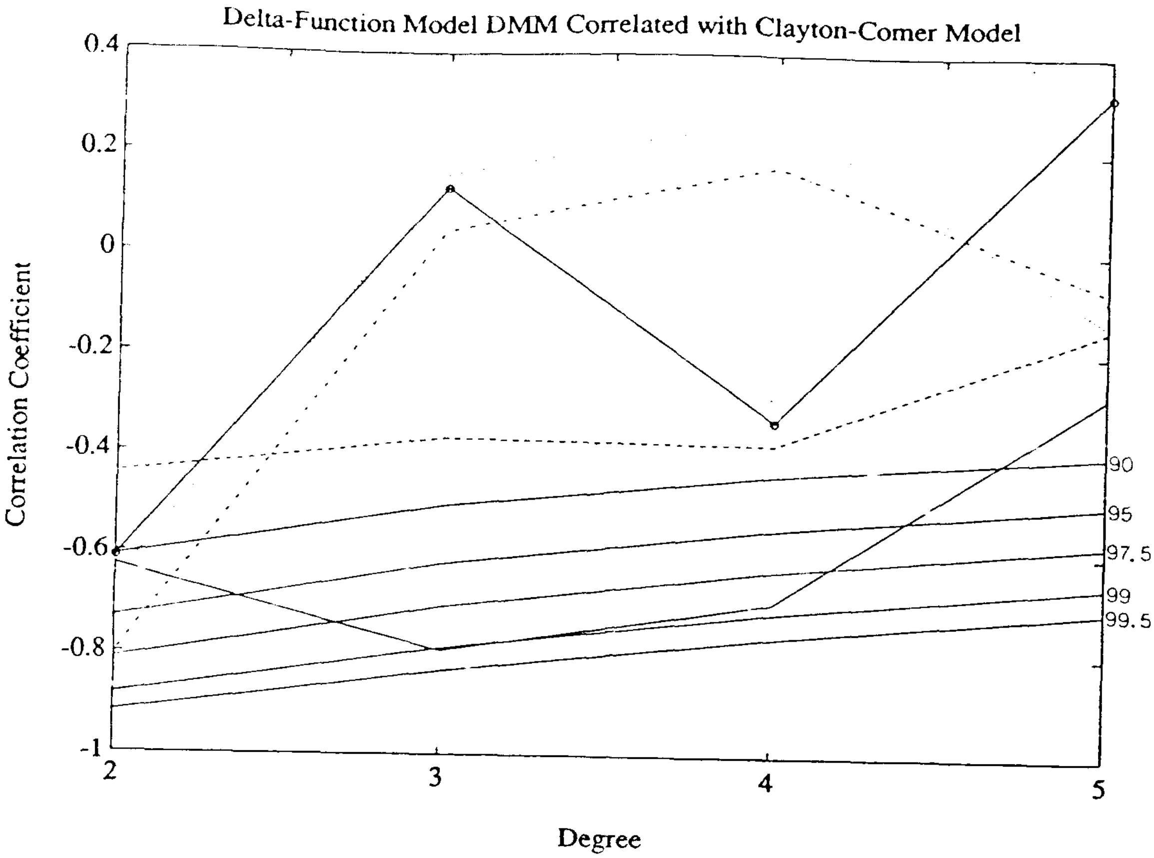

Fig. 5.29. Correlation of the delta-function model DMM coefficients with the five layers of the Clayton-Comer seismic tomography model. Line symbols: — -— = layer 1 [2500-2900 km], - - - - = layer 2 [2100-2500 km], · · · · = layer 3 [1700-2100 km], - · - · = layer 4 [1200-1700 km], o—o = layer 5 [700-1200 km]. Confidence levels are determined by a t-test with $2l$ degrees of freedom.

REFERENCES

ALLEGRE, C. J. and D. L. TURCOTTE. 1985. Geodynamic mixing in the mesosphere boundary layer and the origin of oceanic islands. Geophysical Research Letters 12:207-210.

ALLEGRE, C. J., B. HAMELIN, A. PROVOST and B. DUPRE. 1987. Topology in isotopic multispace and origin of mantle chemical heterogeneities. Earth and Planetary Science Letters 81:319-337.

ANDERSON, D. L. 1985. Hotspot magmas can form by fractionation and contamination of MORB. Nature 318:145-149.

BARLING, J. and S. L. GOLDSTEIN. 1990. Extreme isotopic variations in Heard Island lavas and the nature of mantle reservoirs. Nature 348:59-62.

BOWIN, C. 1991a. The Earth's gravity field and plate tectonics. Tectonophysics 187:69-89.

BOWIN, C. 1991b. Deep structure of the Earth from new techniques for analysis of spatial variability of potential fields combined with seismic tomography results. Submitted to the Journal of Geophysical Research.

CASTILLO, P., R. BATIZA, D. VANKO, E. MALAVASSI, J. BARQUERO and E. FERNANDEZ. 1988. Anomalously young volcanoes on old hot-spot traces; I: Geology and petrology of Cocos Island. Geological Society of America Bulletin 100:1400-1414.

CHAFFEY, D. J., R. A. CLIFF and B. M. WILSON. 1989. Characterization of the St. Helena magma source. In A. D. Saunders and M. J. Norry (eds.), *Magmatism in the Ocean Basins*. Geological Society Special Publication 42:257-276.

CHAUVEL, C., A. W. HOFMANN and P. VIDAL. 1991. HIMU - EM, the French Polynesian connection. Earth and Planetary Science Letters (in press).

CHENG, Q., K.-H. PARK, J. D. MACDOUGALL, A. ZINDLER, G. W. LUGMAIR, H. STAUDIGEL, J. HAWKINS and P. LONSDALE. 1988. Isotopic evidence for a hotspot origin of the Louisville seamount chain. In B. H. Keating, P. Fryer, R. Batiza and G. W. Boehlert (eds.), *Seamounts, Islands and Atolls*. American Geophysical Union Geophysical Monogram 43:283-296.

COHEN, R. S. and R. K. O'NIONS. 1982a. Identification of recycled continental material in the mantle from Sr, Nd and Pb isotope investigations. Earth and Planetary Science Letters 61:73-84.

COHEN, R. S. and R. K. O'NIONS. 1982b. The lead, neodymium and strontium isotopic structure of ocean ridge basalts. Journal of Petrology 23:299-324.

COHEN, R. S., N. M. EVENSON, P. J. HAMILTON and R. K. O'NIONS. 1980. U-Pb, Sm-Nd and Rb-Sr systematics of mid-ocean ridge basalt glasses. Nature 283:149-153.

CREAGER, K. C. and T. H. JORDAN. 1986. Aspherical structure of the core-mantle boundary from PKP travel times. Geophysical Research Letters 13:1497-1500.

DAVIES, G. R., M. J. NORRY, D. C. GERLACH and R. A. CLIFF. 1989. A combined chemical and Pb-Sr-Nd isotope study of the Azores and Cape Verde hot spots: the geodynamic implications. In A. D. Saunders and M. J. Norry (eds.), *Magnetism in the Ocean Basins*. Geological Society Special Publication 42:231-256.

DAVIS, J. C. 1986. *Statistics and Data Analysis in Geology*, 646 p., John Wiley & Sons, Inc., New York.

DEVEY, C. W., F. ALBAREDE, J. L. CHEMINEE, A. MICHARD, R. MUHE and P. STOFFERS. 1990. Active submarine volcanism on the Society hotspot swell (West Pacific): a geochemical study. Journal of Geophysical Research 95:5049-5066.

DUNCAN, R. A., M. T. MCCOLLOCH, H. G. BARSCZUS and D. R. NELSON. 1986. Plume versus lithospheric sources for melts at Ua Pou, Marquesas Islands. Nature 322:534-538.

DUPRE, B. and C. J. ALLEGRE. 1983. Pb-Sr isotope variation in Indian Ocean basalts and mixing phenomena. Nature 303:142-146.

DUPUY, C., P. VIDAL, H. G. BARSCZUS and C. CHAUVEL. 1987. Origin of basalts from the Marquesas Archipelago (south central Pacific Ocean): isotope and trace element constraints. Earth and Planetary Science Letters 82:145-152.

DZIEWONSKI, A. M. 1984. Mapping the lower mantle: determination of lateral heterogeneity in P velocity up to degree and order 6. Journal of Geophysical Research 89:5929-5952.

GAUTIER, I., A. GIRET, P. VIDAL, M. LOUBET, G. DI DONATO, and D. WEIS. 1990. Petrology and geochemistry of Kerguelen basalts (South Indian Ocean): Evolution of a hotspot from a ridge to an intraplate position. Preprint.

GERLACH, D. C., J. C. STORMER, JR. and P. A. MUELLER. 1987. Isotopic geochemistry of Fernando de Noronha. Earth and Planetary Science Letters 85:129-144.

GERLACH, D. C., R. A. CLIFF, G. R. DAVIES, M. NORRY and N. HODGSON. 1988. Magma sources of the Cape Verdes Archipelago: isotopic and trace element constraints. Geochimica et Cosmochimica Acta 52:2979-2992.

GERLACH, D. C., S. R. HART, V. W. J. MORALES and C. PALACIOS. 1986. Mantle heterogeneity beneath the Nazca plate: San Felix and Juan Fernandez islands. Nature 322:165-169.

GRAHAM, D. W. 1987. Helium and lead isotope geochemistry of oceanic volcanic rocks from the East Pacific and South Atlantic. Ph.D. Dissertation, MIT/WHOI Joint Program in Oceanography and Oceanographic Engineering (unpublished).

HAGER, B. H. 1984. Subducted slabs and the geoid: contraints on mantle rheology and flow. Journal of Geophysical Research 89:6003-6015.

HAGER, B. H. and R. W. CLAYTON. 1989. Contraints on the structure of mantle convection using seismic observations, flow models and the geoid. In W. R. Peltier (ed.), *Mantle Convection: Plate Tectonics and Global Dynamics*, 881 p., Gordon and Breach Science Publishers, New York.

HALLIDAY, A. N., J. P. DAVIDSON, P. HOLDEN, C. DEWOLF, D.-C. LEE and J. C. FITTON. 1990. Trace-element fractionation in plumes and the origin of HIMU mantle beneath the Cameroon Line. Nature 347:523-528.

HALLIDAY, A. N., A. P. DICKIN, A. E. FALLICK and J. G. FITTON. 1988. Mantle dynamics: A Nd, Sr, Pb and O isotope study of the Cameroon Line volcanic chain. Journal of Petrology 29:181-211.

HAMELIN, B. and C. J. ALLEGRE. 1985. Large-scale regional units in the depleted upper mantle revealed by an isotope study of the South-West Indian Ridge. Nature 315:196-199.

HAMELIN, B., B. DUPRE and C. J. ALLEGRE. 1986. Pb-Sr-Nd isotopic data of Indian Ocean ridges: new evidence of large-scale mapping of mantle heterogeneities. Earth and Planetary Science Letters 76:288-298.

HART, S. R. 1991. Mantle plumes: interpreting the isotopic record. Caltech Plume Symposium Abstract Volume.

HART, S. R. 1988. Heterogeneous mantle domains: signatures, genesis and mixing chronologies. Earth and Planetary Science Letters 90:273-296.

HART, S. R. 1984. A large-scale isotope anomaly in the Southern Hemisphere mantle. Nature 309:753-757.

HART, S. R., D. C. GERLACH and W. M. WHITE. 1986. A possible new Sr-Nd-Pb mantle array and consequences for mantle mixing. Geochimica et Cosmochimica Acta 50:1551-1557.

HOFMANN, A. W. and W. M. WHITE. 1982. Mantle plumes from ancient oceanic crust. Earth and Planetary Science Letters 57:421-436.

ITO, E., W. M. WHITE and C. GOPEL. 1987. The O, Sr, Nd, and Pb isotope geochemistry of MORB. Chemical Geology 62:157-176.

JACKSON, J. D. 1975. *Classical Electrodynamics*, 2nd edition, John Wiley & Sons, New York.

JACOBSON, R. S. and P. R. SHAW. 1991. Using the F-test for eigenvalue decompositon problems to find the statistically 'optimal' solution. Geophysical Research Letters 18:1075-1078.

KLEIN, E. M., C. H. LANGMUIR, A. ZINDLER, H. STAUDIGEL and B. HAMELIN. 1988. Isotopic evidence of a mantle convection boundary at the Australian-Antarctic Discordance. Nature 333:623-629.

LAY, T., T. J. AHRENS, P. OLSON, J. SMYTH and D. LOPER. 1990. Studies of the Earth's deep interior: goals and trends. Physics Today 43:44-52.

LE MOUEL, J. L., C. GIRE and T. MADDEN. 1985. Motions at core surface in the geostrophic approximation. Physics of the Earth and Planetary Interiors 39:270-287.

LERCH, F. J., S. M. KLOSKO and G. B. PATEL. 1982. A refined gravity model from Lagoes (GEM-L2). Geophysical Research Letters 9:1263-1266.

LI, S., Y. XIAO and X. HU. 1991. The recognition of components in oceanic basalts based on data distribution in isotopic multispace: Two new approaches. Submitted.

MANLY, B. F. J. 1986. *Multvariate Statistical Methods: A Primer*, Chapman & Hall, London.

MANTEL, N. 1967. The detection of disease clustering and a generalized regression approach. Cancer Research 27:209-220.

MENKE, W. 1989. *Geophysical Data Analysis: Discrete Inverse Theory*, revised edition, 285 p., Academic Press, Inc., San Diego.

NAKAMURA, Y. and M. TATSUMOTO. 1988. Is mantle plume homogeneous? Pb, Nd, Sr isotopic evidence for multi-component source for Cook-Austral island rocks. Geochimica et Cosmochimica Acta 52:2909-2924.

NEWSOM, H. E., W. M. WHITE, K. P. JOCHUM and A. W. HOFMANN. 1986. Siderophile and chalcophile element abundances in oceanic basalts, Pb isotope evolution and growth of the Earth's core. Earth and Planetary Science Letters 80:299-313.

PALACZ, Z. A. and A. D. SAUNDERS. 1986. Coupled trace element and isotope enrichment in the Cook-Austral-Samoa islands, southwest Pacific. Earth and Planetary Science Letters 79:270-280.

RICHARDS, M. A. and B. H. HAGER. 1988. The earth's geoid and the large-scale structure of mantle convection. In S. K. Runcorn (ed.), *The Physics of the Planets*, John Wiley & Sons Ltd.

RICHARDS, M. A., B. H. HAGER and N. H. SLEEP. 1988. Dynamically supported geoid highs over hotspots: observation and theory. Journal of Geophysical Research 93:7690-7708.

RICHARDSON, S. H., A. J. ERLANK, A. R. DUNCAN and D. L. REID. 1982. Correlated Nd, Sr and Pb isotope variation in Walvis Ridge basalts and implications for the evolution of their mantle source. Earth and Planetary Science Letters 59:327-342.

RODEN, M. F. 1982. Geochemistry of the earth's mantle, Nunivak Island, Alaska and other areas: evidence from xenolith studies. Ph.D. Dissertation, Massachusetts Institute of Technology (unpublished).

SALTERS, V. J. M. 1989. The use of Hf-isotopes and high field strength elements to constrain magmatic processes and magma sources. Ph.D. Dissertation, Massachusetts Institute of Technology (unpublished).

SOLOW, A. R. 1990. A randomization test for misclassification probability in discriminant analysis. Ecology 7:2379-2382.

STACEY, F. D. 1977. *Physics of the Earth*, 2nd edition, 414 p., John Wiley & Sons, Inc., New York.

STAUDIGEL, H., A. ZINDLER, S. R. HART, T. LESLIE, C.-Y. CHEN and D. CLAGUE. 1984. The isotope systematics of a juvenile intraplate volcano: Pb, Nd, and Sr isotope ratios of basalts from Loihi Seamount, Hawaii. Earth and Planetary Science Letters 69:13-29.

STILLE, P., D. M. UNRUH and M. TATSUMOTO. 1986. Pb, Sr, Nd and Hf isotopic constraints on the origin of Hawaiian basalts and evidence for a unique mantle source. Geochimica et Cosmochimica Acta 50:2303-2319.

STILLE, P., D. M. UNRUH and M. TATSUMOTO. 1983. Pb, Sr, Nd and Hf isotopic evidence of multiple sources for Oahu, Hawaii basalts. Nature 304:25-29.

STOREY, M., A. D. SAUNDERS, J. TARNEY, P. LEAT, M. F. THIRLWALL, R. N. THOMPSON, M. A. MENZIES and G. F. MARRINER. 1988. Geochemical evidence for plume-mantle interactions beneath Kerguelen and Heard Islands, Indian Ocean. Nature 336:371-374.

TARAS, B. D. and S. R. HART. 1987. Geochemical evolution of the New England seamount chain: isotopic and trace-element constraints. Chemical Geology 64:35-54.

TATSUMOTO, M. 1978. Isotopic composition of lead in oceanic basalt and its implication to mantle evolution. Earth and Planetary Science Letters 38:63-87.

TURCOTTE, D. L. and G. SCHUBERT. 1982. *Geodynamics: Application of Continuum Physics to Geological Problems*, 450 p., John Wiley & Sons, Inc., New York.

VIDAL, P., C. CHAUVEL and R. BROUSSE. 1984. Large mantle heterogeneity beneath French Polynesia. Nature 307:536-538.

WEIS, D. 1983. Pb isotopes in Ascension Island rocks: oceanic origin for the gabbroic to granite plutonic xenoliths. Earth and Planetary Science Letters 62:273-282.

WEIS, D., D. DEMAIFFE, S. CAUET and M. JAVOY. 1987. Sr, Nd, O and H isotopic ratios in Ascension Island lavas and plutonic inclusions; cogenetic origin. Earth and Planetary Science Letters 82:255-268.

WEIS, D., J. F. BEAUX, I. GAUTIER, A. GIRET and P. VIDAL. 1989. Kerguelen Archipelago: geochemical evidence for recycled material. In S. R. Hart (ed.), *Crust/Mantle Recycling at Convergence Zones*. NATO

Advanced Study Institute Series, Series C, Mathematical and Physical Science 258:59-63.

WEST, H. B., D. C. GERLACH, W. P. LEEMAN and M. O. GARCIA. 1987. Isotopic constraints on the origin of Hawaiian lavas from the Maui Volcanic Complex, Hawaii. Nature 330:216-220.

WHITE, W. M. 1985. Sources of oceanic basalts: Radiogenic isotopic evidence. Geology 13:115-118.

WHITE, W. M. and A. W. HOFMANN. 1982. Sr and Nd isotope geochemistry of oceanic basalts and mantle evolution. Nature 296:821-825.

WHITE, W. M., A. W. HOFMANN and H. PUCHLET. 1987. Isotope geochemistry of Pacific mid-ocean ridge basalt. Journal of Geophysical Research 92:4881-4893.

WHITE, W. M., K. HARPP, L. LEVY, M. CHEATHAM, R. A. DUNCAN and M. R. FISK. 1989. Hawaiian style volcanic evolution on Tahaa, Societies Islands. EOS 70:1385.

WOODHEAD, J. D. and M. T. MCCULLOCH. 1989. Ancient seafloor signals in Pitcairn Island lavas and evidence for large amplitude, small length-scale mantle heterogeneities. Earth and Planetary Science Letters 94:257-273.

WRIGHT, E. and W. M. WHITE. 1987. The origin of Samoa: new evidence from Sr, Nd, and Pb isotopes. Earth and Planetary Science Letters 81:151-162.

ZINDLER, A. and S. R. HART. 1986. Chemical geodynamics. Annual Review of Earth and Planetary Science 14:493-571.

ZINDLER, A., E. JAGOUTZ and S. GOLDSTEIN. 1982. Nd, Sr and Pb isotopic systematics in a three-component mantle: a new perspective. Nature 298:519-523.

APPENDIX

OCEANIC BASALT DATA SET

	A	B	C	D	E	F	G	H	I	J
1	Sample Number		87/86Sr	143/144Nd	206/204Pb	207/204Pb	208/204Pb	REFERENCES	Latitude	Longitude
2										
3	ASCENSION		#N/A	#N/A	#N/A	#N/A	#N/A		#N/A	#N/A
4	A15085		0.702820	0.512970	19.520	15.610	39.060	Cohen,O'Nions, 1982a	-7.95	-14.37
5	A15176		0.702760	0.513030	19.560	15.620	39.070		-7.95	-14.37
6	A17308		0.702690	0.513050	19.430	15.570	38.850		-7.95	-14.37
7	Asc10		0.702980	0.513050	19.190	15.630	38.634	Pb-Weis, 1983	-7.95	-14.37
8	Asc15150		0.702900	0.513080	19.403	15.630	38.964	Sr,Nd-Weis et al., 1987	-7.95	-14.37
9	AITUTAKI		#N/A	#N/A	#N/A	#N/A	#N/A		#N/A	#N/A
10	AKI1		0.704629	0.512715	18.647	15.544	38.685	Allègre et al., 1987	-18.57	-159.77
11	AIT-22B		0.704370	0.512778	18.700	15.573	38.753	Nakamura,Tatsumoto, 1988	-18.57	-159.77
12	AIT-24B		0.704810	0.512786	18.858	15.552	38.958		-18.57	-159.77
13	AIT-64A		0.704850	0.512769	18.922	15.576	39.019		-18.57	-159.77
14	AMSTERDAM		#N/A	#N/A	#N/A	#N/A	#N/A		#N/A	#N/A
15			0.703773	0.512860	19.098	15.609	39.471	White, unpublished	-37.92	77.67
16			0.703734	0.512886	19.113	15.603	39.470		-37.92	77.67
17			0.703864	0.512857	19.115	15.604	39.470		-37.92	77.67
18			0.703877	0.512849	19.058	15.608	39.425		-37.92	77.67
19			0.703865	0.512858	19.049	15.607	39.411		-37.92	77.67
20	ATUI		#N/A	#N/A	#N/A	#N/A	#N/A		#N/A	#N/A
21	ATU4		0.704515	0.512805	19.573	15.635	39.473	Allègre et al., 1987	-20.00	-158.12
22	ATU2		0.705005	0.512770	20.044	15.723	40.215		-20.00	-158.12
23	AT-50C		0.704310	0.512784	19.673	15.631	39.593	Nakamura,Tatsumoto, 1988	-20.00	-158.12
24	AT-54D		0.704070	0.512772	19.343	15.591	39.083		-20.00	-158.12
25	AT-83A		0.704600	0.512766	19.573	15.635	39.534		-20.00	-158.12
26	AT-87A		0.704890	0.512784	19.512	15.617	39.518		-20.00	-158.12
27	AZORES		#N/A	#N/A	#N/A	#N/A	#N/A		#N/A	#N/A
28	F-33	Faial	0.703930	0.512843	19.312	15.634	39.151	Newsom et al., 1986	38.50	-28.00
29	SM1D	Sao Miguel	0.705130	0.512699	20.000	15.780	40.330	Allègre et al., 1987	38.50	-28.00
30	SM2D		0.705350	0.512712	19.960	15.750	40.190		38.50	-28.00
31	AZ1704		0.703480	0.512920	19.333	15.601	39.130	Davies et al., 1989	38.50	-28.00
32	SM30		0.704320	0.512850	19.750	15.699	39.890		38.50	-28.00
33	SM49		0.705220	0.512810	19.884	15.754	40.170		38.50	-28.00
34	BALLENY		#N/A	#N/A	#N/A	#N/A	#N/A		#N/A	#N/A
35			0.702967	0.512956	19.856	15.605	39.482	Hart, 1988	-66.88	-163.33
36			0.702997	0.512956	19.762	15.594	39.399		-66.83	-163.37
37			0.702849	0.512989	19.638	15.601	39.197		-67.53	-179.95
38	CAMERCON LINE		#N/A	#N/A	#N/A	#N/A	#N/A		#N/A	#N/A
39	FP32	Bioko	0.703410	0.512776	20.368	15.667	40.210	Halliday et al., 1990	3.64	8.75
40	FP1		0.703230	0.512846	20.032	15.652	39.860		3.64	8.75
41	FP23		0.703210	0.512850	20.298	15.691	40.050		3.64	8.75

	A	B	C	D	E	F	G	H	I	J
42	FP38		0.703170	0.512867	20.044	15.646	39.800		3.64	8.75
43	FP44		0.703220	0.512840	20.353	15.675	40.170	Halliday et al., 1988	3.64	8.75
44	P17	Principe	0.702870	0.512911	19.953	15.671	39.630		1.59	2.75
45	P18		0.703240	0.512891	20.060	15.699	39.920		1.59	2.75
46	P19		0.702980	0.512921	20.112	15.691	39.770		1.59	2.75
47	ST93	São Tomé	0.703180	0.512896	20.064	15.666	39.790	Halliday et al., 1990	0.23	7.00
48	ST72		0.703160	0.512926	19.997	15.683	39.720		0.23	7.00
49	ST106		0.703130	0.512906	19.944	15.653	39.360		0.23	7.00
50	ST100		0.703100	0.512932	20.014	15.659	39.680		0.23	7.00
51	ST73		0.703050	0.512960	20.074	15.720	39.800		0.23	7.00
52	ST109		0.702970	0.513005	19.954	15.676	39.570		0.23	7.00
53	ST19		0.702920	0.512974	20.011	15.656	39.620	Halliday et al., 1988	0.23	7.00
54	ST96		0.703440	0.512848	20.009	15.707	39.930		0.23	7.00
55	ST107		0.703020	0.512956	20.045	15.674	39.700		0.23	7.00
56	AN15	Pagalu	0.703280	0.512906	19.032	15.607	38.860		-1.36	5.88
57	CAPE VERDE		#N/A	#N/A	#N/A	#N/A	#N/A		#N/A	#N/A
58	nf8	Fogo	0.703693	0.512786	18.932	15.554	38.801	Gerlach et al., 1988	15.00	-24.30
59	nf34		0.703419	0.512752	18.929	15.551	38.822		15.00	-24.30
60	nf16		0.703646	0.512779	18.943	15.544	38.794		15.00	-24.30
61	zf30		0.703647	0.512786	18.934	15.552	38.778		15.00	-24.30
62	zf29		0.703522	0.512783	18.949	15.554	38.817		15.00	-24.30
63	nf60		0.703223	0.512978	19.881	15.640	39.454		15.00	-24.30
64	zm69	Maio	0.703653	0.512811	19.185	15.583	39.014		15.10	-23.20
65	zm63		0.703754	0.512785	19.199	15.578	39.078		15.10	-23.20
66	zm60		0.703720	0.512813	19.201	15.564	39.061		15.10	-23.20
67	zm53		0.703386	0.512886	19.267	15.575	39.016		15.10	-23.20
68	zm32		0.703299	0.512897	19.173	15.586	38.972		15.10	-23.20
69	zm159		0.703749	0.512712	19.033	15.560	39.115		15.10	-23.20
70	zm189		0.703795	0.512694	18.954	15.520	38.816		15.10	-23.20
71	zm191		0.703600	0.512735	19.260	15.582	39.281		15.10	-23.20
72	zl50	Sao Tiago	0.703748	0.512692	18.970	15.560	38.843		15.00	-23.60
73	zl53		0.703512	0.512790	19.207	15.570	38.974		15.00	-23.60
74	zl47		0.703934	0.512606	18.744	15.537	38.686		15.00	-23.60
75	zl46		0.703844	0.512693	18.930	15.546	38.8[illegible]8		15.00	-23.60
76	nl7		0.703648	0.512752	19.013	15.564	38.858		15.00	-23.60
77	nl4		0.703721	0.512761	18.999	15.550	38.849		15.00	-23.60
78	zl60		0.703192	0.512908	19.438	15.595	39.100		15.00	-23.60
79	zl59		0.703278	0.512862	19.118	15.577	38.966		15.00	-23.60
80	zl13		0.703224	0.512854	19.124	15.577	38.987		15.00	-23.60
81	nl185		0.703511	0.512828	19.135	15.573	38.888		15.00	-23.60
82	nl78		0.703515	0.512711	19.195	15.574	38.961		15.00	-23.60

	A	B	C	D	E	F	G	H	I	J
83	ni176		0.703875	0.512674	18.883	15.550	38.797		15.00	-23.60
84	n17		0.703650	0.512770	19.013	15.560	38.860	Davies et al., 1989	17.00	-25.10
85	nv6	ao Vicente	0.703205	0.512984	19.143	15.571	38.750		16.90	-25.00
86	hv85		0.703085	0.512935	19.554	15.608	39.241		16.90	-25.00
87	nv9		0.702922	0.513000	19.434	15.593	39.094		16.90	-25.00
88	na2	Sao Antao	0.703096	0.512873	19.715	15.626	39.334		17.00	-25.10
89	na15		0.702919	0.513045	19.607	15.622	39.191		17.00	-25.10
90	na48		0.703192	0.512914	19.669	15.619	39.320		17.00	-25.10
91	na51		0.703167	0.512868	19.651	15.623	39.282		17.00	-25.10
92	na60		0.703019	0.512967	19.685	15.621	39.285		17.00	-25.10
93	na63		0.703086	0.512901	19.732	15.624	39.335		17.00	-25.10
94	na69		0.703050	0.513009	19.670	15.611	39.256		17.00	-25.10
95	na73		0.703157	0.512916	19.767	15.622	39.445		17.00	-25.10
96	na79		0.703105	0.512974	19.609	15.615	39.185		17.00	-25.10
97	na80		0.702943	0.513012	19.275	15.587	38.902		17.00	-25.10
98	zm55		0.703250	0.512920	19.287	15.581	39.060		15.10	-23.20
99	CHRISTMAS		#N/A	#N/A	#N/A	#N/A	#N/A		#N/A	#N/A
100	XI-1		0.703987	0.512796	18.869	15.597	38.835	Hart, 1988	-10.50	105.67
101	XI-2		0.703938	0.512761	19.123	15.627	39.180		-10.50	105.67
102	XI-3		0.703995	0.512779	18.900	15.623	39.017		-10.50	105.67
103	XI-4		0.703966	0.512789	18.914	15.623	38.979		-10.50	105.67
104	XI-5		0.703987	0.512776	18.869	15.591	38.871		-10.50	105.67
105	70452		0.704090	0.512702	18.955	15.644	39.125		-10.50	105.67
106	70453		0.705420	0.512498	17.846	15.566	38.071		-10.50	105.67
107	70457		0.705360	0.512544	18.043	15.566	38.128		-10.50	105.67
108	70461		0.705390	0.512511	17.905	15.573	38.134		-10.50	105.67
109	70462		0.705430	0.512460	17.904	15.568	38.118		-10.50	105.67
110	70471		0.703770	0.512827	18.918	15.577	38.784		-10.50	105.67
111	70472		0.703980	0.512806	19.151	15.675	39.334		-10.50	105.67
112	70480		0.703930	0.512724	18.915	15.637	39.071		-10.50	105.67
113	OCOS		#N/A	#N/A	#N/A	#N/A	#N/A		#N/A	#N/A
114	PC77		0.703020	0.512984	19.236	15.596	38.922	Castillo et al., 1988	5.54	-87.08
115	RB43		0.703080	0.512979	19.251	15.593	39.036		5.54	-87.08
116	E10		0.702990	0.513009	19.214	15.579	38.961		5.54	-87.08
117	OMORES		#N/A	#N/A	#N/A	#N/A	#N/A		#N/A	#N/A
118	al7-6		0.703244	0.512888	20.216	15.654	39.917	White, unpublished	-12.22	44.17
119	al21-9		0.703191	0.512878	20.418	15.681	40.072		-12.22	44.17
120	mo105		0.703343	0.512837	19.453	15.607	39.338		-12.30	43.72
121	mo110		0.703208	0.512832	19.339	15.602	39.197		-12.30	43.72
122	mo107		0.703316	0.512826	19.219	15.573	39.081		-12.30	43.72
123	72gc-5		0.703879	0.512715	19.500	15.602	39.575		-11.75	43.38

	A	B	C	D	E	F	G	H	I	J
124	72gc-1		0.703950	0.512718	19.554	15.591	39.624		-11.75	43.38
125	ka-77		0.703888	0.512645	19.392	15.566	39.484		-11.75	43.38
126	72gc-14		0.703838	0.512701	19.425	15.578	39.474		-11.75	43.38
127	AJ10-1		0.703152	0.512874	20.046	15.643	39.706		-12.22	44.17
128	AJ4-2		0.703165	0.512894	20.043	15.647	39.765		-12.22	44.17
129	AJ29-4		0.703203	0.512886	19.625	15.620	39.379		-12.22	44.17
130	GC-37		0.703237	0.512870	19.192	15.573	39.033		-11.75	43.38
131	GC-33		0.703194	0.512868	19.192	15.591	39.055		-11.75	43.38
132	CROZET		#N/A	#N/A	#N/A	#N/A	#N/A		#N/A	#N/A
133			0.704030	0.512840	18.846	15.572	38.984	White, unpublished	-46.45	52.00
134			0.704008	0.512851	18.902	15.571	39.007		-46.45	52.00
135			0.703930	0.512870	19.184	15.623	39.160		-46.45	52.00
136			0.704051	0.512836	18.857	15.573	38.973		-46.45	52.00
137			0.704003	0.512831	18.793	15.568	38.956		-46.45	52.00
138			0.703963	0.512859	19.019	15.607	39.089		-46.45	52.00
139			0.703971	0.512856	18.930	15.588	38.913		-46.45	52.00
140			0.704010	0.512865	18.892	15.583	39.034		-46.45	52.00
141			0.704007	0.512830	18.936	15.600	39.216		-46.45	52.00
142	FERNANDO		#N/A	#N/A	#N/A	#N/A	#N/A		#N/A	#N/A
143	36		0.703900	0.512865	19.423	15.626	39.290	Gerlach et al., 1987	-3.83	-32.42
144	25		0.704647	0.512785	19.132	15.569	38.940		-3.83	-32.42
145	104		0.703945	0.512828	19.565	15.652	39.466		-3.83	-32.42
146	98		0.703861	0.512817	19.473	15.626	39.414		-3.83	-32.42
147	10		0.704578	0.512811	19.199	15.620	39.139		-3.83	-32.42
148	76		0.703989	0.512773	19.507	15.683	39.602		-3.83	-32.42
149	72		0.703969	0.512849	19.559	15.657	39.450		-3.83	-32.42
150	84		0.704854	0.512712	19.145	15.571	39.054		-3.83	-32.42
151	31		0.703821	0.512851	19.354	15.623	39.230		-3.83	-32.42
152	33		0.703766	0.512897	19.317	15.599	39.077		-3.83	-32.42
153	74		0.703946	0.512797	19.470	15.648	39.493		-3.83	-32.42
154	106		0.703855	0.512851	19.445	15.647	39.488		-3.83	-32.42
155	79		0.704181	0.512798	19.553	15.663	39.481		-3.83	-32.42
156	20		0.703957	0.512821	19.644	15.679	39.472		-3.83	-32.42
157	FN10		0.704710	0.512711	19.233	15.645	39.253	Allègre et al., 1987	-3.83	-32.42
158	FN15		0.703791	0.512777	19.522	15.637	39.447		-3.83	-32.42
159	GALAPAGOS		#N/A	#N/A	#N/A	#N/A	#N/A		#N/A	#N/A
160	FL3		0.703950	0.512909	19.879	15.632	39.559	White,Hoffman, 1982	-1.30	-90.45
161	FI26		0.703430	0.512933	19.535	15.583	39.114		-1.30	-90.45
162	Sc163		0.702670	0.513068	18.555	15.508	38.016		-0.62	-90.33
163	E134		0.703270	0.513001	18.263	15.524	37.956		-0.88	-91.17
164	E63		0.702780	0.513005	18.744	15.545	38.308		-0.88	-91.17

	A	B	C	D	E	F	G	H	I	J
165	E76		0.702860	0.513064	18.881	15.533	38.390		-0.22	-90.77
166	E103		0.702820	0.513096	18.838	15.536	38.386		-0.88	-89.50
167	E15		0.702760	0.513051	18.840	15.526	38.399		0.33	-90.47
168	E8		0.703350	0.512812	19.124	15.566	38.927		0.58	-90.75
169	E42		0.703120	0.512941	19.068	15.526	38.607		-0.37	-91.55
170	E35		0.703290	0.512985	20.114	15.730	39.947		-0.18	-91.28
171	GOUGH		#N/A	#N/A	#N/A	#N/A	#N/A		#N/A	#N/A
172	10		0.705030	0.512515	18.579	15.643	39.090	Allègre et al., 1987	-40.33	-10.00
173	51		0.705160	0.512560	18.311	15.604	38.890		-40.33	-10.00
174	HAWAIIAN ISLANDS		#N/A	#N/A	#N/A	#N/A	#N/A		#N/A	#N/A
175	OA1	Honolulu	0.703290	0.513052	18.038	15.443	37.689	Stille et al., 1983	21.40	-157.75
176	OA3		0.703260	0.513033	18.170	15.468	37.822		21.40	-157.75
177	OA4		0.703330	0.513062	18.202	15.451	37.815		21.40	-157.75
178	OA5		0.703250	0.513052	18.154	15.461	37.773		21.40	-157.75
179	OA6		0.703360	0.513042	18.099	15.463	37.754		21.40	-157.75
180	OA11		0.703330	0.513051	18.103	15.438	37.686		21.40	-157.75
181	1801	Hualalai	0.703640	0.512914	17.903	15.429	37.747	Stille etal.,86,Tatsumoto,78	19.71	-155.90
182	ID-872-2	Kauai	0.703620	0.512962	18.447	15.512	37.962	Stille et al., 1986	22.01	-159.58
183	KAU-1		0.703820	0.512967	18.070	15.442	37.803		22.01	-159.58
184	1921	Kilauea	0.703440	0.513057	18.647	15.491	38.192	Sr/Nd-Stille et al., 1986	19.40	-155.21
185	1955		0.703650	0.513040	18.485	15.475	38.108	Pb-Tatsumoto, 1978	19.40	-155.21
186	1960		0.703560	0.513024	18.533	15.486	38.155		19.40	-155.21
187	1963		0.703560	0.513009	18.541	15.481	38.155		19.40	-155.21
188	C-53	Kohala	0.703620	0.513044	18.136	15.457	37.760		20.16	-157.78
189	C-62		0.703555	0.512986	18.156	15.463	37.831		20.16	-157.78
190	C-66		0.703670	0.513017	18.267	15.471	37.916		20.16	-157.78
191	C-70		0.703595	0.513032	18.211	15.458	37.828		20.16	-157.78
192	oa2	Koo au	0.704080	0.512732	17.826	15.440	37.763	Stille et al., 1983	21.40	-157.75
193	oa7		0.704110	0.512704	17.898	15.448	37.779		21.40	-157.75
194	oa8		0.704190	0.512702	18.000	15.462	37.842		21.40	-157.75
195	oa9		0.704210	0.512703	17.929	15.484	37.803		21.40	-157.75
196	oa11		0.704110	0.512701	17.912	15.445	37.749		21.40	-157.75
197	69Tan2		0.704550	0.512673	17.686	15.406	37.735	Hart, 1988	21.40	-157.75
198	WW9991		0.703800	0.512880	17.909	15.471	37.758		21.40	-157.75
199	KW24	Kahoolawe	0.704131	0.512868	18.025	15.429	37.759	West et al., 1987	20.50	-156.67
200	25		0.704162	0.512848	18.047	15.428	37.786		20.50	-156.67
201	1		0.704136	0.512809	17.954	15.445	37.805		20.50	-156.67
202	2		0.704211	0.512784	17.921	15.439	37.733		20.50	-156.67
203	7		0.703833	0.512975	18.337	15.450	37.990		20.50	-156.67
204	6		0.704039	0.512887	18.120	15.431	37.842		20.50	-156.67
205	5		0.703785	0.512929	18.367	15.455	38.023		20.50	-156.67

	A	B	C	D	E	F	G	H	I	J
206	23		0.704090	0.512901	18.036	15.430	37.800		20.50	-156.67
207	19		0.704399	0.512731	17.946	15.454	37.836		20.50	-156.67
208	16		0.704149	0.512897	18.149	15.445	37.845		20.50	-156.67
209	18		0.704159	0.512900	18.092	15.439	37.866		20.50	-156.67
210	H1440		0.704257	0.512864	18.005	15.447	37.817		20.50	-156.67
211	KW14		0.704032	0.512921	18.027	15.466	37.770		20.50	-156.67
212	0x067	Lanai	0.704249	0.512729	17.853	15.420	37.702		20.83	-156.92
213	ox068		0.704111	0.512784	17.871	15.436	37.701		20.83	-156.92
214	ox069		0.704352	0.512721	17.886	15.431	37.742		20.83	-156.92
215	ox078		0.704239	0.512768	17.712	15.428	37.738		20.83	-156.92
216	16-1	Loihi	0.703530	0.512941	18.222	15.478	38.088	Staudigel et al.,1984	19.01	-155.27
217	20-14		0.703520	0.512949	18.347	15.469	38.143		18.86	-155.26
218	23-3		0.703580	0.512982	18.433	15.492	38.164		18.90	-155.27
219	29-10		0.703580	0.512962	18.266	15.474	38.015		18.90	-155.25
220	18-4		0.703700	0.512954	18.443	15.475	38.173		18.94	-155.28
221	18-8		0.703680	0.512940	18.448	15.477	38.189		18.94	-155.28
222	25-4		0.703650	0.512946	18.418	15.477	38.118		18.83	-155.25
223	21-2		0.703520	0.513059	18.504	15.499	38.160		18.91	-155.26
224	24-7		0.703530	0.513048	18.384	15.490	38.107		18.89	-155.26
225	27-4		0.703410	0.512981	18.373	15.502	38.159		18.84	-155.26
226	31-12		0.703350	0.513047	18.255	15.477	38.054		18.93	-155.31
227	17-2		0.703510	0.513045	18.447	15.488	38.177		18.97	-155.27
228	20-4		0.703580	0.512902	18.372	15.463	38.139		18.86	-155.26
229	15-4		0.703590	0.512949	18.392	15.463	38.123		18.97	-155.27
230	17-17		0.703520	0.513009	18.462	15.482	38.221		18.97	-155.27
231	C107	West Maui	0.703460	0.513072	18.438	15.499	37.948	Stille et al., 1986	20.88	-156.57
232	C114		0.703440	0.513097	18.416	15.468	37.907		20.88	-156.57
233	HMT79-28		0.703500	0.513007	18.474	15.535	37.974		20.88	-156.57
234	C-74	Mauna Kea	0.703580	0.513018	18.401	15.476	37.923	Sr/Nd-Stille et al., 1986	19.86	-155.50
235	79MK1		0.703450	0.513030	18.398	15.490	38.017	Pb-Tatsumoto, 1978	19.86	-155.50
236	1907	Mauna Loa	0.703780	0.512925	18.173	15.469	37.898		19.50	-155.78
237	1926		0.703805	0.512915	18.113	15.458	37.817		19.50	-155.78
238	1950		0.703795	0.512905	18.089	15.449	37.824		19.50	-155.78
239	C46	Walanae	0.703590	0.513007	18.158	15.449	37.762	Stille et al., 1983	21.46	-158.17
240	C48		0.703650	0.512976	18.114	15.454	37.735		21.46	-158.17
241	C30		0.703740	0.512961	18.143	15.457	37.754		21.46	-158.17
242	C52		0.703650	0.512973	18.082	15.439	37.692		21.46	-158.17
243	WAIK 8F	E. Molokai	0.703640	0.512982	18.516	15.491	37.990	Stille et al., 1986	21.17	-156.85
244	c162	W. Molokai	0.703758	0.512910	18.071	15.444	37.731		21.17	-157.25
245	WMOL-1		0.704090	0.512945	18.133	15.455	37.751		21.17	-157.25
246	WMOL-3		0.703740	0.512942	18.167	15.460	37.754		21.17	-157.25

	A	B	C	D	E	F	G	H	I	J
247	C44		0.703660	0 513018	18.391	15.489	37.952		21.17	-157.25
248	ICELAND		#N/A	#N/A	#N/A	#N/A	#N/A		#N/A	#N/A
249	I-13		0.703300	0.512930	18.130	15.430	37.900	Hart, unpublished	65.10	-13.70
250	I-16		0.703300	0.512980	18.460	15.450	38.100		65.10	-14.70
251	R-14		0.703040	0.513040	18.350	15.450	37.840		64.80	-19.70
252	RE-15		0.703150	0.512990	18.762	15.506	38.371		64.00	-22.50
253	RE-21		0.703200	0.512995	18.707	15.516	38.359		64.00	-22.50
254	RE-36		0.702776	0.513158	18.574	15.516	38.187		64.00	-22.50
255	RE-46		0.702976	0.513168	18.190	15.523	37.988		64.00	-22.50
256	JUAN FERNANDEZ		#N/A	#N/A	#N/A	#N/A	#N/A		#N/A	#N/A
257			0.703512	0.512882	19.094	15.595	38.899	Gerlach et al., 1986	-33.62	-78.83
258			0.703779	0.512818	19.214	15.627	39.099		-33.62	-78.83
259			0.703581	0.512835	19.045	15.597	38.886		-33.62	-78.83
260			0.703762	0.512831	19.130	15.595	38.958		-33.62	-78.83
261	KERGUELEN PLATEAU		#N/A	#N/A	#N/A	#N/A	#N/A		#N/A	#N/A
262	(Kerg Isl.)	Courbet	0.705260	0.512671	18.452	15.549	39.058	White, unpublished	-49.25	70.00
263		Foch Isl	0.703980	0.512907	18.399	15.542	38.473		-49.00	69.28
264		Courbet	0.705310	0.512645	18.460	15.560	39.075		-49.25	70.00
265			0.705320	0.512631	18.396	15.561	39.037		-49.25	70.00
266		Foch Isl	0.704070	0.512870	18.483	15.521	38.693		-49.00	69.28
267			0.703880	0.512878	18.459	15.520	38.479		-49.00	69.28
268			0.705310	0.512640	18.385	15.544	38.981		-49.00	69.28
269		Courbet	0.706616	0.512615	18.543	15.568	39.167		-49.25	70.00
270			0.704926	0.512669	18.486	15.556	39.051		-49.25	70.00
271	BM64878	(Kerg Isl.)	0.704610	0.512794	18.112	15.481	38.290	Storey et al., 1988	-48.75	69.00
272	BM75059		0.704400	0.512831	18.313	15.592	38.477		-48.75	69.00
273	BM1967	P8(5)	0.705410	0.512545	18.086	15.532	38.710		-49.50	70.00
274	BM 75190		0.705660	0.512502	18.060	15.537	38.884		-48.75	69.00
275	BM64986	(Heard Isl.	0.705530	0.512586	18.009	15.547	38.461		-56.10	73.50
276	DR02/12	(Kerg. Plat	0.705900	0.512530	17.539	15.467	37.875	Weis et al., 1989	-56.67	78.00
277	DR05		0.704740	0.512790	18.068	15.596	38.336		-57.29	77.00
278	DR06		0.704270	0.512710	18.182	15.579	38.277		-57.50	77.00
279	DR08		0.706120	0.512540	17.938	15.549	38.521		-50.20	75.00
280	DR08/05		0.704170	0.512700	18.419	15.542	38.767		-50.20	75.00
281	65171	(Heard Isl.	0.705328	0.512598	18.211	15.567	38.508	Barling,Goldstein, 1990	-56.10	73.50
282	65085	Big Ben	0.705458	0.512598	18.110	15.564	38.590		-56.10	73.50
283	65151		0.705980	0.512516	17.953	15.550	38.420		-56.10	73.50
284	H10		0.705224	0.512622	18.189	15.566	38.646		-56.10	73.50
285	65002	Laurens	0.704772	0.512734	18.527	15.558	38.608		-56.10	73.50
286	65054		0.704793	0.512722	18.656	15.577	38.980		-56.10	73.50
287	56015		0.704806	0.512733	18.796	15.578	39.120		-56.10	73.50

	A	B	C	D	E	F	G	H	I	J
288	69244		0.704852	0.512707	18.776	15.588	39.170		-56.10	73.50
289	747c-12r-4-45-46		0.705508	0.512435	17.466	15.461	37.977	Salters, 1989	-54.81	74.79
290	747c-16r-2-85-87		0.705895	0.512452	18.275	15.643	38.459		-54.81	74.79
291	747c-16r-2-81-84		0.705866	0.512410	17.608	15.508	38.072		-54.81	74.79
292	748c-79r-7-65-67		0.705157	0.512491	18.305	15.613	38.495		-58.44	78.98
293	749-15r-2-35-37		0.704237	0.512763	18.200	15.625	38.435		-58.72	76.41
294	749c-15r-5-127-130		0.704306	0.512764	17.978	15.587	38.213		-58.72	76.41
295	750-16r-3-134-136		0.705012	0.512902	18.112	15.585	38.405		-57.59	81.24
296	81-18	Loranchet	0.704710	0.512660	18.504	15.550	38.957	Gautier et al., 1990	-48.93	69.00
297	81-19		0.704300	0.512740	18.302	15.558	38.391		-48.93	69.00
298	85-12	ateauCent	0.704880	0.512730	18.377	15.539	38.813		-49.39	69.33
299	85-55		0.704830	0.512750	18.467	15.528	38.817		-49.39	69.33
300	77-211	ItsChateau	0.705080	0.512620	18.444	15.565	39.007		-49.25	70.00
301	80-135	Ouest	0.705380	0.512540	18.334	15.552	38.807		-49.25	68.75
302	80-71		0.705640	0.512500	18.234	15.545	38.978		-49.25	68.75
303	LOUISVILLE(<40my)		#N/A	#N/A	#N/A	#N/A	#N/A		#N/A	#N/A
304	mthn7d1		0.703744	0.512946	19.203	15.615	38.921	Cheng et al., 1988	-50.44	-139.17
305	mthn6d1		0.703735	0.512888	19.422	15.625	39.239		-48.20	-148.80
306	msn110-1		0.703648	0.512932	19.332	15.626	39.127		-41.45	-164.27
307	lv-2		0.703178	0.512897	19.128	15.574	38.676		-40.78	-165.35
308	MANGAIA		#N/A	#N/A	#N/A	#N/A	#N/A		#N/A	#N/A
309	MGA1		0.702853	0.512864	21.141	15.771	40.068	Allègre et al., 1987	-21.93	-157.93
310	MAN-82C		0.702820	0.512886	21.624	15.793	40.459	Nakamura,Tatsumoto, 1988	-21.93	-157.93
311	MAN-88A		0.702870	0.512871	21.631	15.796	40.329		-21.93	-157.93
312	MAN-96A		0.702730	0.512878	21.755	15.802	40.619		-21.93	-157.93
313	MAN-101		0.702830	0.512845	21.647	15.825	40.602		-21.93	-157.93
314	MARION/P.E.		#N/A	#N/A	#N/A	#N/A	#N/A		#N/A	#N/A
315	WJE21		0.703050	0.513020	18.574	15.541	38.302	Hart, 1988	-46.92	37.75
316	WJE39		0.703360	0.512919	18.506	15.541	38.329		-46.92	37.75
317	WJM43		0.703390	0.512883	18.560	15.546	38.395		-46.92	37.75
318	AJE1M		0.703391	0.512899	18.608	15.532	38.440		-46.92	37.75
319	MAROTIRI		#N/A	#N/A	#N/A	#N/A	#N/A		#N/A	#N/A
320	113F		0.703693	0.512826	19.290	15.580	39.100	Chauvel et al., 1991	-23.10	-144.00
321	MARQUESAS		#N/A	#N/A	#N/A	#N/A	#N/A		#N/A	#N/A
322	UP73f	(AOB)	0.705120	0.512710	19.230	15.620	39.230	Vidal et al., 1984	-9.42	-140.00
323	UH68f2	(AOB)	0.705614	0.512741	19.150	15.650	39.290		-8.92	-139.53
324	NH78a	(thol)	0.703780	0.512889	19.110	15.570	38.880		-8.93	-140.00
325	NH10e	(thol?)	0.703040	0.512971	19.130	15.580	39.130		-8.93	-140.00
326	uap11	(thol)	0.702880	0.512919	19.858	15.536	39.383	Dupuy et al., 1987	-9.42	-140.00
327	uap17	(thol)	0.702930	0.512921	19.978	15.559	39.619		-9.42	-140.00
328	uap24	(thol)	0.703180	0.512904	19.617	15.553	39.188		-9.42	-140.00

	A	B	C	D	E	F	G	H	I	J
329	up-74h	(AOB)	0.705220	0.512724	19.228	15.635	39.260		-9.42	-140.00
330	uap010	(AOB)	0.705090	0.512674	19.180	15.650	39.310	Duncan et al., 1986	-9.42	-140.00
331	uap026	(AOB)	0.704970	0.512683	19.140	15.640	39.200		-9.42	-140.00
332	uap015	(Haw.)	0.704810	0.512714	19.360	15.650	39.350		-9.42	-140.00
333	MAUKE		#N/A	#N/A	#N/A	#N/A	#N/A		#N/A	#N/A
334	MKE3		0.704356	0.512753	19.697	15.629	39.510	Allègre et al., 1987	-20.08	-157.25
335	MK-73		0.704350	0.512829	19.728	15.589	39.522	Nakamura,Tatsumoto, 1988	-20.08	-157.25
336	MK-75F		0.704400	0.512823	19.746	15.612	39.579		-20.08	-157.25
337	MAURITIUS		#N/A	#N/A	#N/A	#N/A	#N/A		#N/A	#N/A
338	MAU-1		0.703740	0.512924	18.704	15.532	38.660	Allègre et al., 1987	-20.33	57.50
339	N.E.SEAMOUNTS		#N/A	#N/A	#N/A	#N/A	#N/A		#N/A	#N/A
340			0.703500	0.512798	20.651	15.665	40.035	Taras,Hart, 1987	35.30	-57.55
341			0.703550	0.512933	20.242	15.637	40.340		36.83	-58.82
342			0.703330	0.512950	20.297	15.630	39.544		38.92	-60.98
343			0.703180	0.512793	19.993	15.631	40.028		38.42	-63.25
344			0.703290	0.512789	20.102	15.608	39.986		38.42	-63.25
345			0.703389	0.512837	19.643	15.603	39.507		39.83	-67.45
346	NUNIVAK		#N/A	#N/A	#N/A	#N/A	#N/A		#N/A	#N/A
347	B-5		0.702980	0.513149	18.539	15.473	38.031	Roden, 1982	60.00	-166.00
348	B-10		0.702820	0.513071	18.637	15.469	38.144		60.00	-166.00
349	PITCAIRN		#N/A	#N/A	#N/A	#N/A	#N/A		#N/A	#N/A
350	P3	Tedside	0.704756	0.512495	17.782	15.477	38.872	Woodhead,McCulloch, 1989	-20.07	-130.10
351	P4		0.704487	0.512603	17.827	15.486	38.898		-20.07	-130.10
352	P5		0.704493	0.512613	17.832	15.477	38.908		-20.07	-130.10
353	P7		0.704746	0.512517	17.761	15.464	38.823		-20.07	-130.10
354	P8		0.704865	0.512462	17.635	15.460	38.725		-20.07	-130.10
355	P9		0.704694	0.512538	17.795	15.475	38.844		-20.07	-130.10
356	P10		0.705132	0.512432	17.640	15.459	38.913		-20.07	-130.10
357	P11	damstown	0.703519	0.512848	18.449	15.492	38.896		-20.07	-130.10
358	P12		0.703525	0.512859	18.427	15.501	38.876		-20.07	-130.10
359	P18		0.703534	0.512859	18.515	15.523	39.047		-20.07	-130.10
360	P20		0.703637	0.512828	18.424	15.494	38.912		-20.07	-130.10
361	P22		0.703531	0.512846	18.475	15.517	39.035		-20.07	-130.10
362	P26		0.703548	0.512860	18.489	15.498	38.958		-20.07	-130.10
363	P28		0.703518	0.512854	18.484	15.502	39.009		-20.07	-130.10
364	P30		0.703505	0.512851	18.406	15.499	38.900		-20.07	-130.10
365	P31		0.703495	0.512880	18.459	15.494	38.920		-20.07	-130.10
366	P34	Chr. Cave	0.703509	0.512840	18.419	15.499	38.967		-20.07	-130.10
367	642	Pulwana	0.703702	0.512648	17.832	15.508	38.503		-20.07	-130.10
368	647		0.703693	0.512725	17.849	15.477	38.698		-20.07	-130.10
369	PONAPE		#N/A	#N/A	#N/A	#N/A	#N/A		#N/A	#N/A

	A	B	C	D	E	F	G	H	I	J
370			0.703287	0.512973	18.462	15.489	38.289	Hart, 1988	6.93	158.32
371	RAEVAVAE		#N/A	#N/A	#N/A	#N/A	#N/A		#N/A	#N/A
372	RVV5		0.703058	0.512980	19.472	15.570	39.144	Allègre et al., 1987	-23.87	-147.67
373	RAPA		#N/A	#N/A	#N/A	#N/A	#N/A		#N/A	#N/A
374	198(4)		0.703888	0.512802	19.355	15.706	38.903	Palacz,Saunders, 1986	-27.58	-144.33
375	198(30)		0.703887	0.512789	19.996	15.862	39.170		-27.58	-144.33
376	RA31		0.704288	0.512764	18.970	15.560	38.870	Chauvel et al., 1991	-27.58	-144.33
377	RARATONGA		#N/A	#N/A	#N/A	#N/A	#N/A		#N/A	#N/A
378	R-38A		0.704354	0.512701	18.381	15.595	38.971	Palacz,Saunders, 1986	-21.25	-159.75
379	RTG4		0.704566	0.512629	18.256	15.518	38.724	Allègre et al., 1987	-21.25	-159.75
380	R-1		0.704260	0.512747	18.975	15.564	38.798	Nakamura,Tatsumoto, 1988	-21.25	-159.75
381	R-6		0.704210	0.512716	18.499	15.528	38.934		-21.25	-159.75
382	R-8B		0.704150	0.512720	18.756	15.532	38.994		-21.25	-159.75
383	R-8C		0.704170	0.512678	18.745	15.520	38.945		-21.25	-159.75
384	R-11B		0.704160	0.512716	18.570	15.512	38.847		-21.25	-159.75
385	R-12B		0.704090	0.512743	18.685	15.530	38.979		-21.25	-159.75
386	REUNION		#N/A	#N/A	#N/A	#N/A	#N/A		#N/A	#N/A
387			0.704279	0.512846	18.792	15.575	38.888	White, unpublished	-21.17	55.50
388			0.704245	0.512825	18.994	15.593	39.053		-21.17	55.50
389			0.704157	0.512848	18.966	15.588	39.016		-21.17	55.50
390			0.704146	0.512851	18.794	15.584	38.915		-21.17	55.50
391			0.704187	0.512834	18.812	15.577	38.887		-21.17	55.50
392			0.704196	0.512848	18.981	15.597	39.026		-21.17	55.50
393			0.704197	0.512844	18.799	15.595	38.907		-21.17	55.50
394	RIMATARA		#N/A	#N/A	#N/A	#N/A	#N/A		#N/A	#N/A
395			0.703100	0.512840	21.230	15.810	40.400		-22.67	-152.75
396			0.702750	0.513080	19.700	15.610	39.150		-22.67	-152.75
397	RIM-100A		0.702840	0.512868	21.184	15.781	40.334	Nakamura,Tatsumoto, 1988	-22.67	-152.75
398	RIM-100B		0.703240	0.512864	21.205	15.776	40.311		-22.67	-152.75
399	RURUTU		#N/A	#N/A	#N/A	#N/A	#N/A		#N/A	#N/A
400	199(6)		0.702798	0.512860	20.972	15.784	40.148	Palacz,Saunders, 1986	-22.42	-151.33
401	199(11)		0.702726	0.512872	20.091	15.791	39.183		-22.42	-151.33
402	199(4)		0.703205	0.512928	20.151	15.772	39.672		-22.42	-151.33
403	RUR-90A		0.703190	0.512907	20.255	15.645	39.662	Nakamura,Tatsumoto, 1988	-22.42	-151.33
404	SALA Y GOMEZ		#N/A	#N/A	#N/A	#N/A	#N/A		#N/A	#N/A
405	y734		0.703220	0.512898	19.865	15.640	39.670		-26.47	-105.47
406	SAMOA		#N/A	#N/A	#N/A	#N/A	#N/A		#N/A	#N/A
407		Upolu	0.705950	0.512760	18.940	15.630	39.070	Palacz,Saunders, 1986	-13.90	-171.75
403			0.705598	0.512669	18.590	15.620	38.780		-13.90	-171.75
409		Tutuila	0.704730	0.512811	19.340	15.650	39.150		-14.35	-170.75
410			0.705950	0.512760	18.940	15.630	39.070		-14.35	-170.75

	A	B	C	D	E	F	G	H	I	J
411			0.705076	0.512836	19.080	15.590	39.270		-14.35	-170.75
412	Shields	Manu'a	0.704610	0.512810	19.201	15.598	39.329	Wright,White, 1987	-14.35	-169.58
413			0.704710	0.512811	19.234	15.599	39.386		-14.35	-169.58
414			0.704650	0.512813	19.297	15.597	39.459		-14.35	-169.58
415			0.704650	0.512854	19.170	15.591	39.305		-14.35	-169.58
416		Tutuila	0.705170	0.512871	18.856	15.572	38.783		-14.35	-170.75
417			0.705000	0.512821	19.149	15.598	39.263		-14.35	-170.75
418			0.706680	0.512667	19.221	15.628	39.586		-14.35	-170.75
419			0.707400	0.512640	19.103	15.622	39.463		-14.35	-170.75
420			0.704720	0.512827	19.161	15.599	39.240		-14.35	-170.75
421		Upolu	0.704830	0.512831	18.987	15.579	39.001		-13.90	-171.75
422			0.705310	0.512776	18.979	15.581	39.067		-13.90	-171.75
423			0.705530	0.512818	18.955	15.589	39.050		-13.90	-171.75
424			0.704910	0.512933	18.881	15.566	38.778		-13.90	-171.75
425		Saval'i	0.705960	0.512715	18.810	15.611	39.027		-13.73	-172.30
426	P. Erosion	Tutulla	0.705000	0.512664	18.597	15.610	38.755		-14.35	-170.75
427		Upolu	0.705770	0.512740	18.881	15.602	39.073		-13.90	-171.75
428			0.705850	0.512720	18.882	15.606	39.088		-13.90	-171.75
429			0.705510	0.512622	18.572	15.605	38.759		-13.90	-171.75
430			0.705730	0.512721	18.722	15.617	38.904		-13.90	-171.75
431			0.706670	0.512702	18.757	15.622	38.952		-13.90	-171.75
432			0.705520	0.512626	18.587	15.651	38.886		-13.90	-171.75
433			0.705620	0.512659	18.767	15.609	38.966		-13.90	-171.75
434		Saval'i	0.705580	0.512763	18.801	15.613	39.049		-13.73	-172.30
435			0.705960	0.512699	18.762	15.616	39.005		-13.73	-172.30
436			0.705910	0.512726	18.808	15.611	39.042		-13.73	-172.30
437			0.705590	0.512749	18.724	15.604	38.917		-13.73	-172.30
438			0.705940	0.512764	18.886	15.601	39.094		-13.73	-172.30
439			0.706190	0.512744	18.738	15.597	38.939		-13.73	-172.30
440			0.705910	0.512694	18.692	15.627	38.909		-13.73	-172.30
441	SAN FELIX/S.A.		#N/A	#N/A	#N/A	#N/A	#N/A		#N/A	#N/A
442		San Felix	0.704120	0.512585	18.960	15.569	38.871	Gerlach et al., 1986	-26.42	-79.98
443			0.704122	0.512552	19.312	15.602	39.329		-26.42	-79.98
444		San Ambrosio	0.703983	0.512732	18.913	15.569	38.844		-26.42	-79.98
445	99655	San Felix	0.704120	0.512562	19.253	15.604	39.240		-26.42	-79.98
446	99654		0.704100	0.512621	18.956	15.560	38.860		-26.42	-79.98
447	SHIMADA Seamount		#N/A	#N/A	#N/A	#N/A	#N/A		#N/A	#N/A
448			0.704843	0.512640	19.046	15.681	39.354	Graham, 1987	16.87	-117.47
449	SOCIETY		#N/A	#N/A	#N/A	#N/A	#N/A		#N/A	#N/A
450	P1-1	Mehetia	0.704622	0.512779	19.095	15.567	38.949	Devey et al., 1990	-17.88	-148.08
451	P3-4		0.704243	0.512879	19.057	15.561	38.751		-17.88	-148.08

	A	B	C	D	E	F	G	H	I	J
452	(2-1)	Dredge 2	0.704433	0.512856	19.098	15.587	38.876		-17.38	-148.83
453	(3-1)	Teahitia	0.704607	0.512745	19.128	15.594	38.890		-17.58	-148.80
454	(3-3)		0.704514	0.512817	19.037	15.589	38.809		-17.58	-148.80
455	(3-5)		0.704803	0.512799	19.108	15.612	39.032		-17.58	-148.80
456	(9-1)		0.705473	0.512739	19.117	15.624	38.983		-17.58	-148.80
457	(29-1)	Moua Pihaa	0.703676	0.512964	19.222	15.540	38.744		-18.33	-148.50
458	St.HELENA		#N/A	#N/A	#N/A	#N/A	#N/A		#N/A	#N/A
459	SH4		0.702880	0.512963	20.571	15.743	39.870	Allègre et al., 1987	-15.97	-5.72
460	SH20		0.702840	0.512828	20.622	15.740	39.914		-15.97	-5.72
461	NMNH109984		0.702960	0.512842	20.816	15.778	40.072	Newsom et al., 1986	-15.97	-5.72
462	NMNH99653		0.702850	0.512871	20.820	15.801	40.133		-15.97	-5.72
463	55470		0.702910	0.512870	20.960	15.810	40.180	Cohen,O'Nions, 1982a	-15.97	-5.72
464	2882		0.702920	0.512847	20.896	15.791	40.131	?	-15.97	-5.72
465	2928		0.702870	0.512873	20.908	15.810	40.161		-15.97	-5.72
466	37		0.702854	0.512985	20.442	15.759	39.841	Chaffey et al., 1989	-15.97	-5.72
467	38		0.702826	0.512990	20.401	15.708	39.736		-15.97	-5.72
468	69		0.702818	0.512943	20.448	15.711	39.754		-15.97	-5.72
469	125		0.702818	0.512946	20.440	15.724	39.820		-15.97	-5.72
470	56		0.702840	0.512915	20.609	15.753	39.929		-15.97	-5.72
471	80		0.702852	0.512931	20.745	15.755	39.995		-15.97	-5.72
472	111		0.702856	0.512892	20.617	15.759	39.977		-15.97	-5.72
473	134		0.703090	0.512862	20.781	15.770	40.037		-15.97	-5.72
474	8		0.702885	0.512942	20.545	15.760	39.901		-15.97	-5.72
475	64		0.702951	0.512916	20.735	15.769	40.020		-15.97	-5.72
476	168		0.702837	0.512929	20.764	15.783	40.072		-15.97	-5.72
477	215		0.702826	0.512844	20.839	15.795	40.093		-15.97	-5.72
478	190		0.702867	0.512893	20.586	15.796	40.058		-15.97	-5.72
479	237		0.702831	0.512983	20.488	15.744	39.822		-15.97	-5.72
480	238		0.702818	0.512963	20.518	15.749	39.846		-15.97	-5.72
481	216		0.702846	0.512905	20.654	15.717	39.881		-15.97	-5.72
482	114		0.702846	0.512915	20.620	15.757	39.940		-15.97	-5.72
483	119		0.702867	0.512898	20.824	15.780	40.104		-15.97	-5.72
484	13		0.702890	0.512915	20.764	15.768	40.057		-15.97	-5.72
485	14		0.702934	0.512890	20.736	15.775	40.016		-15.97	-5.72
486	139		0.702864	0.512905	20.491	15.739	39.850		-15.97	-5.72
487	74		0.702901	0.512891	20.809	15.786	40.113		-15.97	-5.72
488	75		0.702913	0.512918	20.844	15.789	40.104		-15.97	-5.72
489	85		0.702835	0.512874	20.846	15.767	40.055		-15.97	-5.72
490	St.PAUL		#N/A	#N/A	#N/A	#N/A	#N/A		#N/A	#N/A
491			0.703640	0.512900	18.651	15.556	38.776	White, unpublished	-38.73	77.50
492			0.703780	0.512853	18.701	15.573	38.875		-38.73	77.50

	A	B	C	D	E	F	G	H	I	J
493			0.703529	0.512932	18.757	15.563	38.868		-38.73	77.50
494			0.703596	0.512899	18.739	15.566	38.905		-38.73	77.50
495			0.703714	0.512905	18.705	15.579	38.906		-38.73	77.50
496			0.703691	0.512874	18.681	15.567	38.866		-38.73	77.50
497	TAHAA		#N/A	#N/A	#N/A	#N/A	#N/A		#N/A	#N/A
498			0.706930	0.512580	19.290	15.655	39.200		-16.67	-151.50
499	TRINIDADE		#N/A	#N/A	#N/A	#N/A	#N/A		#N/A	#N/A
500	UCTD7		0.703803	0.512708	19.116	15.601	39.110	Allègre et al., 1987	-20.50	-29.42
501	TRISTAN		#N/A	#N/A	#N/A	#N/A	#N/A		#N/A	#N/A
502	TR-7	Tristan	0.704540	0.512617	18.671	15.530	39.070	Newsom et al., 1986	-37.10	-12.28
503	Tr-1		0.705050	0.512534	18.534	15.546	39.049		-37.10	-12.28
504	Tr-4		0.705090	0.512526	18.516	15.526	38.988		-37.10	-12.28
505	T617		0.705170	0.512550	18.470	15.500	38.890	Cohen,O'Nions, 1982a	-37.10	-12.28
506	T369		0.705170	0.512500	18.190	15.490	38.340		-37.10	-12.28
507	TUBUAII		#N/A	#N/A	#N/A	#N/A	#N/A		#N/A	#N/A
508	5433		0.702800	0.512886	21.140	15.760	40.290	Chauvel et al., 1991	-23.38	-149.45
509	5434		0.702755	0.512882	21.070	15.760	40.330		-23.38	-149.45
510	5435		0.702781	0.512887	21.140	15.780	40.440		-23.38	-149.45
511	5436		0.702793	0.512884	21.060	15.780	40.300		-23.38	-149.45
512	5437		0.702759	0.512895	21.110	15.770	40.410		-23.38	-149.45
513	TBA09		0.703153	0.512885	21.160	15.770	40.590		-23.38	-149.45
514	TBA11		0.703178	0.512912	21.040	15.750	40.320		-23.38	-149.45
515	K109		0.702761	0.512875	21.050	15.760	40.230		-23.38	-149.45
516	110B		0.702786	0.512920	21.090	15.750	40.320		-23.38	-149.45
517	WALVIS		#N/A	#N/A	#N/A	#N/A	#N/A		#N/A	#N/A
518			0.704980	0.512461	17.648	15.472	38.120	Richardson et al., 1982	-29.07	2.98
519			0.704860	0.512456	17.641	15.477	38.149		-29.07	2.98
520			0.705120	0.512376	17.650	15.483	38.227		-29.07	2.98
521			0.705110	0.512379	17.535	15.471	38.138		-29.07	2.98
522			0.704980	0.512555	18.029	15.491	38.820		-28.53	2.32
523			0.704230	0.512699	18.180	15.508	38.629		-28.53	2.32
524			0.704440	0.512682	18.070	15.494	38.632		-28.53	2.32
525			0.703910	0.512694	18.315	15.524	38.774		-28.05	1.77
526			0.704550	0.512566	18.160	15.507	38.760		-28.05	1.77
527	Rio Grande Rise		0.704780	0.512549	17.619	15.490	38.054		-30.28	-35.28
528	MORB		#N/A	#N/A	#N/A	#N/A	#N/A			
529	DSDP335-	Atlantic	0.703210	0.513090	19.200	15.590	38.610	Cohen et al., 1980	37.18	-35.20
530	I.O. 6243.4	Ind. Ocean	0.702900	0.512950	18.720	15.530	38.460	Cohen, O'Nions, 1982b	12.35	47.66
531	45°N56	Atlantic	0.703140	0.513090	19.280	15.540	38.830	Cohen et al., 1980	45.15	-28.00
532	AD3-3		0.702300	0.513290	17.840	15.470	37.330		-5.47	-11.42
533	D1	SW In. Ridg	0.702820	0.512908	17.525	15.416	37.235	Hamelin, Allègre, 1985	-31.69	57.84

	A	B	C	D	E	F	G	H	I	J
534	D2		0.702760	0.512981	18.114	15.505	37.839		-33.76	56.27
535	D4		0.703030	0.513068	17.764	15.467	37.632		-40.98	43.70
536	D5		0.704720	0.512448	16.943	15.497	37.316		-43.89	40.65
537	D6		0.702870	0.513071	18.373	15.509	38.096		-44.18	38.80
538	D7		0.702870	0.513041	18.237	15.499	37.976		-44.81	36.30
539	03/01D1	E In. Ridge	0.703150	0.512941	17.692	15.442	37.654	Hamelin et al., 1986	-26.91	72.24
540	05/03D1		0.703050	0.513053	17.635	15.457	37.493		-29.81	75.18
541	07/04D1		0.703000	0.513022	17.854	15.429	37.728		-32.67	77.62
542	22/07D1		0.703070	0.512986	18.270	15.508	38.279		-34.38	78.02
543	18/06D2		0.704670	0.512813	18.039	15.555	38.636		-38.98	78.14
544	18/06D3		0.705360	0.512575	17.777	15.549	38.477		-38.96	78.16
545	13/05D1		0.702950	0.513122	17.960	15.446	37.912		-40.36	77.89
546	VG768	J. de Fuca	0.702440	0.513027	18.766	15.547	38.226	White et al., 1987	46.39	-130.22
547	VG44		0.702580	0.513062	18.751	15.563	38.568		44.66	-130.33
548	D10-1		0.702560	0.513169	18.486	15.485	37.852		44.66	-130.33
549	D10-2		0.702560	0.513138	18.448	15.466	37.786		44.66	-130.33
550	D10-3		0.702520	0.513158	18.471	15.500	37.903		44.66	-130.33
551	VG348		0.702490	0.513243	18.470	15.457	37.867		44.27	-129.55
552	A1407-B1	Gorda	0.702320	0.513228	18.161	15.419	37.521		42.73	-126.44
553	W7605B-DR-94		0.702390	0.513181	18.335	15.473	37.765		42.55	-126.85
554	W7605B-DR5-301		0.702490	0.513136	18.453	15.477	37.851		42.47	-126.92
555	A1406		0.702470	0.513180	18.530	15.481	37.926		42.28	-127.12
556	A1406-2B11		0.702490	0.513173	18.528	15.473	37.920		42.28	-127.12
557	KK2-83-D9-1		0.702490	0.513189	18.348	15.470	37.756		42.24	-127.08
558	A1405-B5		0.702520	0.513217	18.317	15.453	37.759		41.53	-127.43
559	L6-83-31-1		0.702840	0.513105	18.679	15.545	38.294		41.00	-127.04
560	K28A-D23	EPR	0.702440	0.513186	17.975	15.442	37.478		-3.70	-102.73
561	K10A-D33A		0.702460	0.513154	18.321	15.484	37.798		-20.36	-114.02
562	D12A-D38AA		0.702450	0.513149	18.408	15.490	37.906		-20.39	-113.76
563	VG798		0.702520	0.513090	18.616	15.518	37.957		-31.00	-113.12
564	K42A-D20	Galapagos	0.702470	0.513117	18.269	15.479	37.797		2.18	-100.67
565	K46A-D202F		0.702430	0.513150	18.228	15.453	37.697		2.08	-100.34
566	K62-D143G		0.702830	0.513034	18.744	15.562	38.566		2.62	-95.20
567	VG1235		0.702800	0.513036	18.743	15.540	38.548		2.70	-95.25
568	VG1234		0.702830	0.513068	18.749	15.560	38.550		2.70	-95.24
569	VG1202		0.702800	0.513039	18.736	15.550	38.576		2.70	-95.24
570	VG1223		0.702810	0.513048	18.752	15.564	38.568		2.70	-95.24
571	K71A-D130H		0.702540	0.513094	18.574	15.515	38.132		0.74	-85.58
572	VG1747		0.702490	0.513135	18.336	15.500	37.911		1.04	-85.12
573	K73A-D123H		0.702400	0.513191	18.287	15.481	37.816		1.45	-85.10
574	VG962	Atlantic	0.703150	0.513162	18.343	15.503	37.792	Ito et al., 1987	70.17	-15.26

	A	B	C	D	E	F	G	H	I	J
575	VG367		0.703160	0.513139	18.344	15.475	37.870		52.67	-34.94
576	VG965		0.702850	0.513202	18.339	15.499	37.830		49.81	-28.65
577	VG200		0.703340	0.512985	19.690	15.608	39.299		42.96	-29.20
578	521-1B		0.702900	0.513070	18.814	15.541	38.404		36.82	-33.27
579	528-3		0.702850	0.513059	18.846	15.534	38.361		36.81	-33.26
580	534-2-1		0.702880	0.513072	18.899	15.545	38.435		36.80	-33.27
581	VG968		0.702870	0.513055	18.589	15.529	38.108		28.90	-43.32
582	VG744		0.702610	0.513138	18.320	15.501	37.807		25.40	-45.30
583	VG205		0.702810	0.513123	18.275	15.485	37.842		22.92	-13.51
584	VG296		0.702320	0.513207	18.317	15.485	37.710		22.24	-45.02
585	VG937		0.702500	0.513213	18.338	15.481	37.700		22.24	-45.02
586	VG249		0.702450	0.513142	18.408	15.490	37.906		11.22	-43.06
587	VG260		0.702530	0.513120	18.359	15.504	37.845		11.02	-43.67
588	P6906-28B		0.702760	0.513043	19.444	15.588	39.037		6.01	-33.28
589	GS7309-94		0.702610	0.513108	18.845	15.575	38.256		-0.02	-24.58
590	GS7309-75		0.702550	0.513093	18.775	15.568	38.320		-0.55	-16.07
591	VG198		0.702290	0.513175	18.375	15.518	37.842		-21.87	-11.85
592	VG192		0.702320	0.513175	18.299	15.489	37.726		-21.93	-11.81
593	R3-3-D30	EPR	0.702560	0.513123	18.336	15.495	37.837		13.83	-104.14
594	R3-3-D10		0.702480	0.513114	18.337	15.501	37.840		12.14	-103.83
595	VG1214	Galapagos	0.702820	0.513055	18.741	15.559	38.552		2.70	-95.24
596	VG1001		0.703130	0.513112	18.554	15.558	38.215		0.71	-85.50
597	VG1770		0.702770	0.513111	18.644	15.548	38.236		1.04	-85.12
598	VG1583	Ind. Ocean	0.702950	0.513136	18.084	15.452	37.804		5.35	68.69
599	VG5262		0.702830	0.513067	17.978	15.451	37.760		3.78	63.87
600	VG5269		0.702740	0.513089	18.009	15.473	37.846		3.70	63.89
601	VG5284		0.702840	0.513107	17.997	15.460	37.816		-1.65	67.77
602	VG5294		0.702760	0.513121	18.100	15.474	37.900		-5.28	68.53
603	VG5291		0.702740	0.513102	18.170	15.500	38.064		-5.36	68.62
604	VG3095		0.703030	0.513065	17.315	15.443	37.251		-24.98	69.99
605	AII93-11-103		0.703040	0.513076	17.325	15.456	37.287		-24.98	70.01
606	AII93-15-23		0.703110	0.513070	17.469	15.449	37.456		-25.78	70.23
607	D4-1	E In. Ridge	0.702530	0.513129	18.816	15.505	38.155	Klein et al., 1988	-50.22	137.55
608	D3-4		0.702570	0.513064	18.979	15.590	38.416		-50.42	135.08
609	D2-19		0.702610	0.513048	18.911	15.514	38.319		-50.27	132.55
610	D1-2		0.702640	0.513113	18.805	15.499	38.262		-50.40	131.00
611	D6-1		0.702590	0.513092	18.617	15.480	38.095		-50.30	130.05
612	D5-5		0.702550	0.513103	18.572	15.482	38.097		-48.73	127.08
613	D7-3		0.702900	0.513027	18.057	15.439	37.859		-49.03	124.00
614	D7-7		0.703000	0.512997	18.008	15.462	37.794		-49.03	124.00
615	D8-8		0.703140	0.512962	18.223	15.465	38.212		-49.47	121.03

	A	B	C	D	E	F	G	H	I	J
616	D9-2		0.702930	0.513026	18.248	15.489	38.003		-49.82	119.18
617	D11-6		0.702835	0.513031	17.944	15.409	37.743		-49.85	118.00
618	D10-10		0.703450	0.512977	17.764	15.483	37.803		-49.92	115.38